UNIVERSITY OF SOUTHAMPTON

Faculty of Engineering and Physical Sciences

Department of Mechanical Engineering

Fabrication of Robust Bifunctional Composite Coatings by Electrodeposition

By

Xingyu Wang

Thesis for the degree of Doctor of Philosophy

ORCID: 0009-0001-4544-1702

April 2025

UNIVERSITY OF SOUTHAMPTON

ABSTRACT

FACULTY OF ENGINEERING AND PHYSICAL SCIENCES
Department of Mechanical Engineering

Thesis for the degree of Doctor of Philosophy

Fabrication of Robust Bifunctional Composite Coatings by Electrodeposition

By

Xingyu Wang

Solid lubrication shows promising potential for advanced applications in automotive and aerospace industries where the challenging environment of high vacuum and extreme temperature have rendered it unpractical for traditional liquid lubrication. Transition metal dichalcogenides (TMD) such as molybdenum disulphide (MoS_2) and tungsten disulphide (WS_2) are well-known solid lubricants and exhibit excellent friction reduction due to their unique lamellar structure. Incorporating these TMD particles into a metal matrix (e.g. nickel, cobalt, copper) via electrodeposition has been a facile and versatile method for self-lubricating composite coating synthesis. Electrodeposited Ni-MoS_2 coatings demonstrate a lower coefficient of friction than electroplated nickel coatings. Under dry sliding conditions, the friction coefficient of electrodeposited nickel ranges from 0.4 to 0.6, while that of Ni-MoS_2 can be as low as 0.1. However, during electroplating, the conductive nature of co-deposited TMD particles resulted in an enhanced electric field in the vicinity of particle-absorbed sites. In consequence, more metal ions would be attracted towards these sites due to greater Coulomb force, which accelerated the reduction of ions at these locations and created composite coatings with non-compact and porous structures. These porous structures become a major challenge to achieving long-term durability as they can be easily sheared off during sliding contact motion. One of the research purposes of this thesis is to develop a robust electrodeposited metal-TMD coating achieved by densifying the structure of these existing coatings.

On the other hand, TMD particles with low surface energy are also good candidates for developing superhydrophobic coatings through electro-co-deposition. However, the lack of mechanical robustness and abrasion resistance has become the major challenge inhibiting their practical industrial applications. This work presents a strategy to develop robust nickel-based hybrid composite coatings via the co-deposition of TMD and reinforcing ceramic particles (i.e., SiC and TiO_2). The size of the added ceramic particle was found to have a significant effect on the surface morphology, co-deposited WS_2 content and wettability of the as-deposited hybrid composite coatings. Nickel-based hybrid coating deposited from an electrolyte containing WS_2 and micron-sized SiC particles showed a rough surface with uniformly distributed protrusions. The as-deposited nickel-hybrid coating exhibited excellent water repellence with a water contact angle of $166.2 \pm 0.7°$ and a sliding angle of 3.2°. Moreover, the electrochemical tests in 3.5 wt% NaCl solution showed that the nickel hybrid coating exhibited good corrosion resistance ($E_{corr} = -0.14$ V and $I_{corr} = 4.29 \times 10^{-7}$ A/cm^2) and high corrosion inhibition efficiency ($\eta = 97.1\%$.). Furthermore, the linear abrasion test proved that nickel hybrid superhydrophobic coating has one of the best abrasion resistance compared with literature (water contact angle remained above 150° after 2000 cm abrasion distance under the pressure of 2.2 kPa), indicating such coating has promising potential in robust industrial applications.

Table of Contents

List of Figures

List of Tables

Research Thesis: Declaration of Authorship

Xingyu Wang

‘Fabrication of Robust Bifunctional Coatings by Electrodeposition’

I declare that this thesis and the work presented in it is my own and has been generated by me as the result of my own original research.

I confirm that:

1. This work was done wholly or mainly while in candidature for a research degree at this University;
2. Where any part of this thesis has previously been submitted for a degree or any other qualification at this University or any other institution, this has been clearly stated;
3. Where I have consulted the published work of others, this is always clearly attributed;
4. Where I have quoted from the work of others, the source is always given. With the exception of such quotations, this thesis is entirely my own work;
5. I have acknowledged all main sources of help;
6. Where the thesis is based on work done by myself jointly with others, I have made clear exactly what was done by others and what I have contributed myself;
7. None of this work has been published before submission;

Signature: Date:

Acknowledgements

I would like to express my sincere gratitude to my supervisors Dr. Shuncai Wang and Dr. Nong Gao and Dr. Zheng Jiang. Without their guidance, I would not have been able to complete this project. Foremost, I am deeply indebted to my primary supervisor Dr. Shuncai Wang for his his patience, motivation, encouragement, and immense inspiration for research. I am lucky that he became my MSc mentor in 2017, and after one year of MSc study, he found opportunities for me to pursuit my PhD degree and continued as my PhD project supervisor.

Moreover, special thanks are due to Dr. Carlos Ponce De Leon Albarran for his valuable advice on electrochemistry and corrosion science.

My sincere thanks also goes to my colleagues in Faculty of Engineering and Physical Sciences: Dr. Terry J Harvey, Dr. Puiki Leung, Dr. Ping Lu, Dr. Tao Zhu and Dr. Peng Jiang who offered me help as and when required.

I also highly appreciated my parents who provided financial support to study aboard helped me to overcome depression during COVID lockdown period.

Last but not least, the completion of the thesis would not be possible without support given by my beloved wife Xiaolin. I would like to thank you for always being there for me.

Definitions and symbols

Abbreviations

Al_2O_3	aluminium oxide
BAS	benzyl ammonium salts
CoF	coefficient of friction
CTAB	cetyltrimethylammonium bromide
CVD	chemical vapour deposition
DC	direct current
EDS	energy dispersive X-ray spectroscopy
H_3BO_3	boric acid
HPB	hexadecylpyridinium bromide
MoS_2	molybdenum disulphide
PC	pulse current
PRC	pulse reverse current
PTFE	polytetrafluoroethylene
PVD	physical vapor deposition
Ra	average roughness
RDE	rotation disk electrode
SEM	scanning electron microscope
SiC	silicon carbide
SDS	sodium dodecyl sulphate
SLS	sodium lauryl sulphate
TiO_2	titanium dioxide
WC	tungsten carbide
WS_2	tungsten disulphide

Symbols

A	area of deposition
dx/dt	deposition rate
I	current density
n	number of electrons
F	Faraday’s constant
M	Molar mass of the metal deposited
γ	surface tension
θ	contact angle
θ^*_w	apparent Wenzel contact angle
r	roughness factor
f_{SL}	area fraction of solid in contact with liquid
f_{LA}	area fraction of air in contact with liquid
γ	duty cycle
T_{ON}	on-time
T_{OFF}	off-time
f	frequency
I_A	average current density
I_P	peak current density
I_C	cathodic current density
I_AA	anodic current density
T_AA	anodic (reverse) time
T_C	cathodic (forward) time
Φ	diameter of ball
V_E	electrophoretic velocity
E	intensity of electric field
μE	electrophoretic mobility
q	charge of particle
η	viscosity of the suspension

1 Introduction

1.1 Background

Friction, wear, and corrosion are the main causes leading to low machine efficiency, high energy consumption and component deterioration [1]. In the UK, corrosion and wear are estimated to cost the economy around £ 80 billion per annum [2]. In many cases, it may not be realistic to use high-performance materials for bulk components due to the high cost. Alternatively, enhancing the properties of component surfaces by depositing a layer of coating is a more practical and economical way to combat friction, wear and corrosion.

Liquid lubricants such as grease and oil have been traditionally used to solve friction and wear issues. However, when the working environment becomes demanding (e.g. high vacuum and extreme temperature in the aerospace industry), liquid lubrication could be problematic. Alternatively, transition metal dichalcogenides (TMD) such as molybdenum disulphide (MoS_2) and tungsten disulphide (WS_2) show promising potential to reduce wear and friction in harsh working conditions. Since TMD materials are used in the form of powder and film, they are also known as solid lubricants. The successful cases of applying solid lubricants are mainly reported by vapour deposition techniques, though the disadvantages of high capital cost and low deposition rate limit their commercial promotion in a broad range of engineering applications [3].

On the other hand, incorporating solid lubricants (MoS_2 and WS_2) into a metal matrix (nickel, copper, nickel-cobalt) via electrodeposition has been successfully used for self-lubricating composite coating synthesis [4, 5]. However, during electroplating, the conductive nature of co-deposited MoS_2 or WS_2 particles resulted in the non-uniform growth of deposits, leading to a porous coating structure and limiting long-term durability[6, 7]. Therefore, this thesis aims to develop a robust coating achieved by densifying the structure of these existing coatings.

The susceptibility to corrosion is largely dependent on the wettability of component surfaces. In general, surfaces with low wettability demonstrate excellent corrosion resistance due to the low chance of direct contact with corrosive liquid. As an extreme aspect of wettability, superhydrophobicity exhibits exceptional water repellency with contact angle (CA) greater than 150° and sling angle (SA) lower than 10°. The term "superhydrophobicity" was first reported in 1936, as Fogged published his observation that water droplets could form spherical shapes on the leaves of Triticum (wheat) plants [8]. Since then, natural non-wetting surfaces such as lotus leaves, strider legs and bird feathers [9, 10] have become the template for researchers to mimic and develop artificial superhydrophobic surfaces. By studying these natural superhydrophobic surfaces, researchers concluded that hierarchical surface roughness and low surface energy are two key factors contributing to superhydrophobicity. Based on this finding, various biomimetic superhydrophobic surfaces have been developed through a strategy of first creating a hierarchical surface structure and then modifying the surface with low surface energy chemicals.

TMD materials (i.e. MoS_2 and WS_2 particles) are also good candidates for fabricating superhydrophobic surfaces due to their low surface energy (65-120 mJ/cm^2). Although they are traditionally used for self-lubrication [11, 12], the studies of co-deposition of MoS_2 or WS_2 particles with composite coatings for preparing superhydrophobic surfaces have increased in the last five years. Successful cases include Ni-WS_2 [13], Ni-P-WS_2 [14], Ni-Co-WS_2 [15] and Cu-MoS_2 [16]. However, a major challenge is that such coatings have very poor abrasion resistance. MoS_2 and WS_2 are soft solid lubricant materials. The co-deposition of these particles may result in weak mechanical robustness of composite coatings. Consequently, during real applications, the delicate hierarchical surface structure could easily be damaged even with a slight fingernail scratch, therefore shortening their service life. To overcome this challenge, adding a third-phase hard ceramic particle into the metal-TMD system to develop hybrid composite coatings seems feasible. The method of mixing different particles has been used in electrodeposited metal-TMD coatings for self-lubricating applications [17, 18], while almost no study has explored hybrid composite coatings in superhydrophobic applications.

1.2 Motivation and objectives

The electro-co-deposition of solid lubricant particles (MoS_2 or WS_2) with metal is a facile and economical method to prepare self-lubricating coatings. However, the conductive nature of co-deposited MoS_2 or WS_2 particles resulted in the non-uniform growth of deposits, leading to a porous coating structure and limiting long-term durability. The aim of this work is to develop a robust self-lubricating coating achieved by densifying the structure of these existing coatings. On the other hand, electrodeposited metal-TMD coating also exhibits superhydrophobicity, which can be used for anti-corrosion applications. However, lack of abrasion resistance is the major challenge for commercial promotion. Therefore, this work also aims to enhance the abrasion wear resistance of superhydrophobic coatings by including third-phase ceramic particles into existing metal-TMD coating systems. In this research, nickel was selected as the metal matrix for composite electroplating due to its excellent mechanical properties and corrosion resistance. Moreover, the co-deposition of particles with nickel further tailors its surface properties, making it suitable for demanding applications such as those in the aerospace and automotive industries.

Specifically, the objectives of this project are:

(1) Develop nickel single-particle composite coatings by electro-co-deposition of TMD particles (MoS_2 or WS_2) with nickel and examine their surface morphologies, coating structures, surface wettability and self-lubrication performance.

(2) Investigate the effect of electroplating parameters including particle size, deposition time and surfactant concentration on developed composite coatings.

(3) Develop nickel hybrid composite coatings by adding ceramic particles (SiC or TiO_2) into existing nickel-TMD particle coating systems and investigate the effect of different particle combinations on the surface morphologies, surface topographies and structures of the composite coatings.

(4) Investigate surface wettability and self-lubricating performance of developed nickel hybrid composite coatings.

(5) Evaluate the long-term durability and abrasion resistance of developed superhydrophobic composite coatings.

(6) Investigate the corrosion resistance of electrodeposited superhydrophobic coatings and elucidate the corrosion mechanism.

1.3 Thesis structure

This thesis is divided into seven main chapters, namely Chapter 1 – Introduction; Chapter 2 – Literature review; Chapter 3 – Experimental methodology; Chapter 4, 5 and 6 – Result and discussion; Chapter 6 – Conclusions and future work.

Chapter 2 is a literature review. First, it provides an overview of electrodeposition. Then, the review focuses on studies of self-lubricating coatings and superhydrophobic coatings. Finally, previous attempts to densify coating structures are summarised.

Chapter 3 describes the methodologies of composite coating deposition, surface and structural characterisation, surface wettability test, electrochemical test and tribological test.

Chapter 4 presents the results and discussion of superhydrophobic coatings. The effect of particle size, deposition time and different particle combinations on the surface morphologies, surface topographies, coating structures, surface wettability electrochemical performance and abrasion resistance were investigated.

Chapter 5 presents the tribological performance of composite coatings. Effects of process parameters, including particle concentration, surfactant CTAB (cetyltrimethylammonium bromide) concentration and different particle combinations were studied.

Finally, conclusions and future work are presented in Chapter 6, followed by the reference list.

2 Literature review

2.1 Overview of electrodeposition

Coatings can be deposited by the reduction of metal ions in an aqueous solution. Generally, the reduction of ions can be realized by two main methods, namely electrodeposition and electroless deposition. In the electrodeposition, the coating is deposited by passing an electric current between two electrodes immersed in an electrolyte. The positively charged electrode is known as the anode, while the negatively charged electrode is the cathode. The electrolyte contains metal ions to be plated. When an electrical potential or voltage is applied between the electrodes, these metal ions migrate towards the cathode and are reduced to form a metal layer. At the cathode surface, two possible reactions, namely metal reduction (equation 2.1) and hydrogen evolution (equation 2.2), might take place at the cathode.

$$M^{Z+} + ze^- \rightarrow M \quad \ldots\ldots\ldots\ldots\ldots\ldots\ldots\ldots\ldots 2.1$$

$$2H^+ + 2e^- \rightarrow H_2 \ldots\ldots\ldots\ldots\ldots\ldots\ldots\ldots\ldots 2.1$$

Based on the material of the anode, two possible oxidation reactions might take place. If the anode is made of the same metal as the one being deposited on the cathode surface, the metal will be oxidised to metal ions, which go into the electrolyte.

$$M \rightarrow M^{Z+} + ze^- \ldots\ldots\ldots\ldots\ldots\ldots\ldots\ldots\ldots 2.2$$

If the anode is made of a material that resists electrochemical oxidation (e.g. platinum, lead), the water will be oxidised to oxygen gas, which escapes from the electrolyte.

$$2H_2O \rightarrow 4H^+ + O_2 + 4e^- \ldots\ldots\ldots\ldots\ldots\ldots\ldots\ldots 2.3$$

In the above equations (2.1 to 2.4), M^{z+} is the metal cation to be plated; z is the number of electrons required for metal reduction, e^- is the electron; M is the metal deposited at the cathode, H^+ is the hydrogen ion in the electrolyte; H_2 is the hydrogen gas evolved at the cathode; H_2O is the water to be oxidised; O_2 is the escaped oxygen.

Numerous pure metal (e.g. nickel, copper, zinc etc.) and alloy (e.g. nickel-phosphorus, tin-copper etc.) coatings can be produced via electrodeposition. Based on Faraday's law, the deposition rate (*dx/dt*) can be predicted and calculated by the following equation.

$$\frac{dx}{dt} = \frac{M \times I}{\rho \times A \times n \times F} \ldots\ldots\ldots\ldots\ldots\ldots\ldots\ldots 2.4$$

Where M is the Molar mass of metal deposited on the cathode, I is the current density, ρ is the density of metal, A is the area of deposition, n is the number of electrons involved in reduction reaction, and F is the Faraday's constant (96,487 C/mol). From equation 2.5, it can be noted that current density and deposition time are the basic parameters affecting coating thickness.

However, in actual electrodeposition, especially on shaped components (or cathodes), the coating thickness will not normally be uniform. The actual thickness at any point on the cathode surface is referred to as the local thickness [19]. The local thickness depends primarily on the current density at that point. The current distribution is determined by geometric factors such as the shape of the cathode and the location of the cathode relative to the anode. In general, cathodes can be divided into two categories based on their geometries, namely parallel plate cathode and irregular shape cathode. The current density distribution in a cell with a parallel plated cathode is shown in **Figure 2.1 (a)**. It can be noted that a uniform current density distribution is present over the entire electrode surface up to the very edge of the electrode, where the current density increases abruptly. This phenomenon is also called the "edge effect", which is believed to be caused by the current flow partially passing around the rectangular space between the electrodes [20]. The increased current density at the edges can attract more metal ions, which leads to a higher deposition rate at the edge than the central area. In consequence, the coating in the central part of the cathode may be compact and flat, whereas the occurrence of dendrites is observed at the edges. When an irregular shape cathode is used, the current density distribution becomes even more complicated. As shown in **Figure 2.1 (b)**, the current density is higher on prominences and areas closer to the anodes. Conversely, the current density becomes lower in recesses and areas facing away from the anodes. These variations in current density inevitably mean that the coating deposited on the prominences is thicker than the coating deposited on the recessed areas. Therefore, to obtain a smooth coating with uniform thickness, a parallel plate cathode will be used in this research.

According to the research conducted by Tan and Lim [21], the "edge effect" can be mitigated by appropriate bath agitation. For laboratory research, magnetic stirring, ultrasonic agitation and rotating disk electrode are applied for bath agitation. These techniques demonstrate high reproducibility due to their controllable hydrodynamics. For industrial applications, air agitation is commonly used. However, its reproducibility is relatively low due to localised turbulence near air outlets.

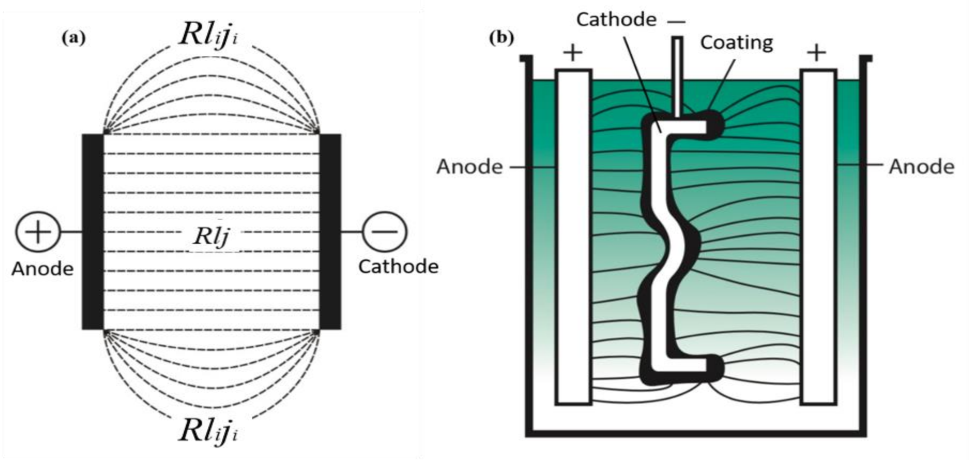

Figure 2.1 (a) current density distribution on a parallel plate cathode, dash line is the current line, R is the specific resistivity of the electrolyte, l is the distance between two electrodes, j is the current density, l_i is the length of the i-th current line, and j_i is the current density corresponding to the i-th current line; (b) current density distribution on an irregular shape cathode, the solid line is the current line. [20, 22].

Compared with other coating technologies, electrodeposition has the advantages of (i) low cost, (ii) easy operation, (iii) not requiring high working temperature and (iv) reliable stability [23]. However, electrodeposition has the following disadvantages.

(1) Substrate material must be conductive.

(2) Current distribution can be non-uniform, leading to inhomogeneous.

(3) The disposal of electroplating solutions is a cause of environmental concern.

Opposite to electrodeposition, electroless deposition requires no power source. Instead, the bath solution needs to contain a reducing agent, normally hypophosphite ions ($H_2PO_2^-$), to react with metal ions. Since electroless deposition is not a line-of-sight process, uniform coating thickness and desired deposition rate can be realised by controlling bath composition, temperature and proper bath agitation [24, 25]. Additionally, by not requiring conductive material as substrates, the range of electroless deposition options expands beyond those for electrodeposition. However, the major disadvantage of using electroless deposition is the low deposition rate, which makes it unsuitable for depositing thick coatings.

Apart from pure metal and alloy electrodeposition, many studies have also reported that the coating properties can be further enhanced by co-depositing second-phase particles with the growing metal matrix. In the following subsection, composite electrodeposition and its working mechanism will be reviewed.

2.1.1 Composite electrodeposition

The advantages of composite electrodeposition are very clear since it offers an elegant method to combine the properties of two different materials in a controlled manner [26]. Historically, the origin of this technique can be traced back to 1928 in a study of a copper-graphite coating for car engine components [27]. Then, a major development has been witnessed in this subject throughout the 1960s and 1970s. Most studies in this period focused on the development of wear-resistant coatings by embedding hard ceramic particles such as SiC and WC into nickel or cobalt layers. Nowadays, the science and technology of composite electrodeposition has matured into a sub-field of material surface finishing. A wide range of micron or submicron particles with various properties has been co-deposited with metal matrix to enhance coating qualities. For instance, soft lubricants such as graphite [28], WS_2 [29, 30], MoS_2 [7, 31] are co-deposited to improve self-lubrication, metal oxides, including Al_2O_3 [32-34] and TiO_2 [35, 36], are incorporated to obtain better corrosion resistance. Section 2.2 and Section 2.3 will provide a detailed review of self-lubricating coatings and superhydrophobic coatings produced by composite electrodeposition techniques for the purpose to combat wear and corrosion issues. Compared with other composite coating fabrication methods (e.g., powder metallurgy, pressure infiltration, stirring casting, etc.), composite electrodeposition has the advantages of low cost and easy operation. The process of composite electrodeposition is schematically depicted in **Figure 2.2**.

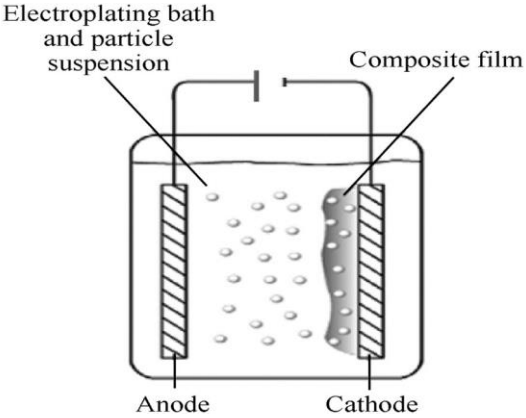

Figure 2.2 Schematic diagram of composite electrodeposition.

2.1.2 Theoretical models of composite electrodeposition

Many theoretical models have been proposed to understand the mechanism of composite electroplating. **Table 2.1** provides an overview of the existing models. In general, many models suggest that the particle incorporation during electrodeposition can be divided into five consecutive steps: (1) ionic clouds are formed on the surface of particles due to adsorption of metal ions and surfactants, (2) convection of particles towards cathode induced by bath agitation, (3) diffusion through a hydrodynamic boundary layer, (4) diffusion through a concentration layer, and (5) particle embedment with the reduction of metal ions. **Figure 2.3** schematically illustrates the co-deposition process of particles. It should be noted that, during electro-co-deposition, particles in close proximity to the cathode are consumed more rapidly than they can be replenished through convection and diffusion. Therefore, a decrease in particle concentration can be observed from bulk electrolyte to the cathode surface. Although many existing models have included mathematical expression to predict the incorporated particle content, the necessary process parameters to achieve particular coatings are still hard to be determined without experimental trials.

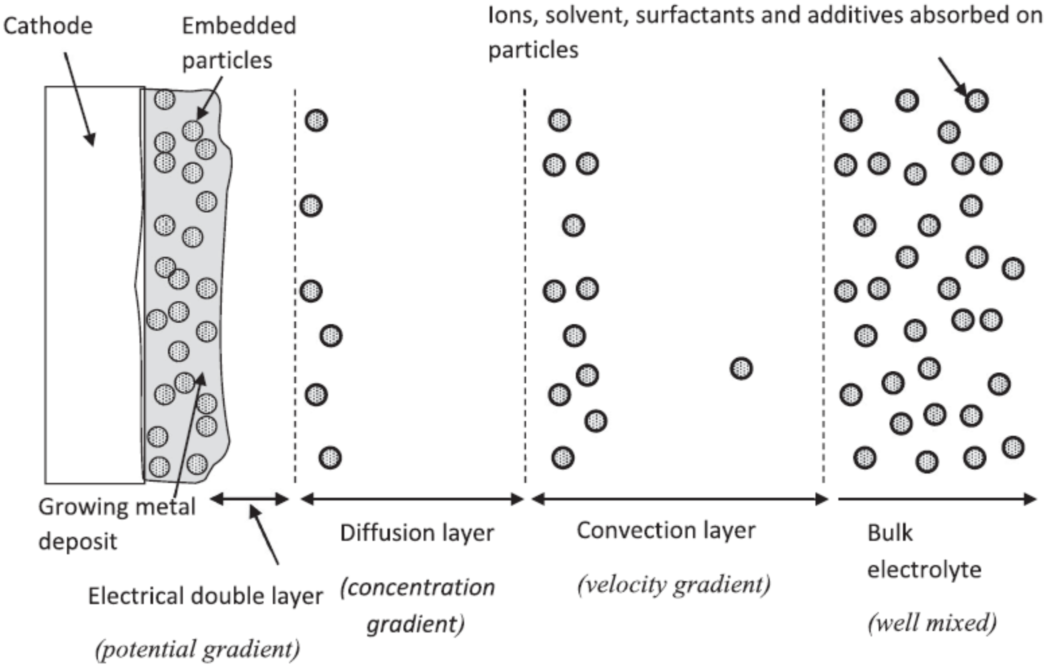

Figure 2.3 Processes involved in the co-deposition of particles into growing metallic layers [37].

Table 2.1 Theoretical models developed to describe the growing mechanism of composite electrodeposition after Low, Wills and Walsh [38].

Author & year	Description, hypothesis and limitations of the model	Coatings of investigation	Ref
Guglielmi, 1972	- Particle incorporation consists of two successive steps. The first step produces a layer of loosely adsorbed particles, and the second step produces irreversible adsorption of particles on the electrode with the assistance of an electrical field. - The quantitative (mathematical) treatment of the proposed model is developed and verified by experiments. - However, the model does not take the hydrodynamic effect of the plating bath into consideration.	Ni-TiO_2 Ni-SiC	[39]
Celis, Roos and Buelens, 1972	- Particle incorporation would only be achieved when a certain amount of adsorbed ions, depending on the plating system itself, is reduced. - Model uses probability to determine the amount of particles that are likely to be embedded under a given current density. - Mass transport of particles is proportional to the mass transport of ions to the working electrode.	Cu-Al_2O_3 Au-Al_2O_3	[40]
Fransaer, Celis and Ross, 1992	- Trajectory theory is applied to describe the co-deposition of non-Brownian particles. - Particles in the electrolyte are driven by adhesion force, hydrodynamic force and friction force. Particle incorporation can be realised when the friction force is greater or equal to the shear force (one type of hydrodynamic force).	Cu-polystyrene	[41]
Hwang and Hwang, 1993	- An improvement of Guglielmil's model. - Three modes of current density (low, intermediate and high) are used to distinguish the metal ions reduction around particles. -Particle incorporation consists of three steps: forced convection of particles to the cathode, loose adsorption of ions on the particle surface and irreversible particle embedment due to the reduction of adsorbed ions.	Co-SiC	[42]
Vereecken, Shao, and Searson,	- Particle incorporation is simulated by a kinetic model based on the particle diffusion process.	Ni-Al_2O_3	[43]

Author & year	Description, hypothesis and limitations of the model	Coatings of investigation	Ref
2000	- Under certain conditions, the gravitational force can affect the kinetics of particle co-deposition significantly. - However, this model is only valid when the particle size is smaller than the thickness of the diffusion layer.		
Bercot, Pena-Munoz and Pagetti, 2002	- The modification of Guglielmi's model by considering the bath agitation. - However, the model uses magnetic stirring as bath agitation, which is not an adequate method to carry out fundamental study due to poor reproducibility.	Ni-PTFE	[44]

2.2 Self-lubricating coating

Friction and wear can result in catastrophic machinery failure. In order to cope with the demanding working environments, many engineering components require superior surface properties, especially wear resistance, compared to their bulk [45]. One approach to combating wear is self-lubricating coatings. Since the shear strength of the self-lubricating coating is much smaller than that of the substrate, the friction between the component surface and counter body can be significantly reduced. Therefore, self-lubricating coatings can provide lubrication and reduce wear without any external lubrications [46]. Nowadays, the most common way to develop self-lubricating coatings is using solid lubricants. In the following subsections, different types of solid lubricants and the methods of applying them will be reviewed.

2.2.1 Solid lubricants and low friction materials

Traditionally, liquid lubricants and greases are used to combat friction and wear in most tribological applications. However, under extremely severe operating conditions, liquid lubricants can no longer provide sufficient lubrication. For instance, in aerospace applications, where temperature of jet engine components can exceed 500 °C, liquid lubricants often fail due to evaporation and oxidation. Similarly, in vacuum environments, such as those in satellite or spacecraft mechanisms, liquid lubricants evaporate due to low pressure. Furthermore, in nuclear reactors, liquid lubricants degrade under radiation. Alternatively, solid lubricants have shown promising potentials to reduce friction and wear under these harsh environments [47].

By definition, solid lubricants can be described as materials that provide lubrication under dry conditions [48, 49]. When present at a sliding interface, they can provide low friction and prevent wear damage between the sliding surfaces. In general, solid lubricants can be categorised into several subclasses based on the properties and crystal structures (**Table 2.2**).

Table 2.2 Typical solid lubricants and their self-lubricating capability [47].

Classification	**Key examples**	**Friction coefficient**	**Main features**
Lamellar solids	WS_2 MoS_2 Boric acid (H_3BO_3)	0.002-0.25 0.01-0.2 0.02-0.2	- Layered crystal structures. - High load bearing capacity. - Effective in harsh environment. - Susceptible to moisture.
Soft metals	Sliver (Ag) Lead (Pb) Gold (Au) Indium (In) Tin (Sn)	0.2-0.35 0.15-0.2 0.2-0.3 0.15-0.25 0.2	- Ideal for electrical contact and sliding components due to good electrical conductivity. - Prone to wear under extreme pressures due to soft nature.
Organic materials or polymers	PTFE Waxes Soaps	0.04-0.15 0.2-0.4 0.15-0.25	- Weak intermolecular force provides intrinsic lubrication. - Ideal lubricants for bearing, bushing, gasket and seal. - Limited load bearing capacity and thermal stability.
Carbon-based solids	Diamond Diamond-like carbon	0.02-1 0.003-0.5	- Excellent wear resistance due to high hardness. - Resistant to most chemicals, suitable for harsh environment. - High cost of production.

Classification	Key examples	Friction coefficient	Main features
Bulk or thick-film (>50 µm) composites	Metal-, polymer- and ceramic matrix composites consisting of graphite, WS_2, MoS_2, Ag, etc.	0.05-0.4	- Tailored for specific applications by adjusting composition of lubricants and matrix. - Not ideal for weight sensitive applications as bulk materials can be heavy.

2.2.2 Lamellar solids and their lubrication mechanism

Among all the solid lubricants mentioned above, lamellar solids such as TMDs (MoS_2, WS_2), graphite and boric acid (H_3BO_3) are the class that has been mostly studied and applied in both academia and industry. Their lubrication mechanism can be explained by unique crystal structures. As shown in **Figure 2.4**, lamellar solids are composed of stacked layers. Within each layer, atoms are closely packed and strongly bonded to each other (covalent bonds). However, the layers themselves are relatively far apart, and the forces that bond them (van der Waals) are weak. When shear forces are applied, the weak interlayer bonding results in an easy slip of layers over each other, leading to a low coefficient of friction [50]. On the other hand, strong covalent bonds within each layer will provide these solids with very high in-plane strength to resist wear damage and prolong service life. Moreover, lamellar solids can be sheared to form a tribofilm during sliding contact, which helps separate sliding surfaces and reduces direct wear between sliding surfaces [51].

Although graphite, boric acid, and TMDs (MoS_2, WS_2) are all classified as lamellar solid lubricants, their applications and optimal working environments differ significantly. Graphite exhibits enhanced self-lubricating properties in the presence of moisture. The adsorbed water molecules act as boundary lubricants, facilitating the sliding between its layers. However, in dry or vacuum environments, the absence of moisture reduces graphite's lubricating efficiency [52]. In contrast, moisture is detrimental to TMDs, as it promotes the formation of oxides, which are abrasive and impair lubrication. Boric acid, unlike the other two, performs effectively in both humid and dry conditions but decomposes above 300°C into boron oxides, which lack lubricating properties. Compared to graphite and boric acid, TMDs are particularly suitable for extreme conditions, excelling in high vacuum, high-pressure environments, and temperatures up to 1100°C in inert atmospheres [3].

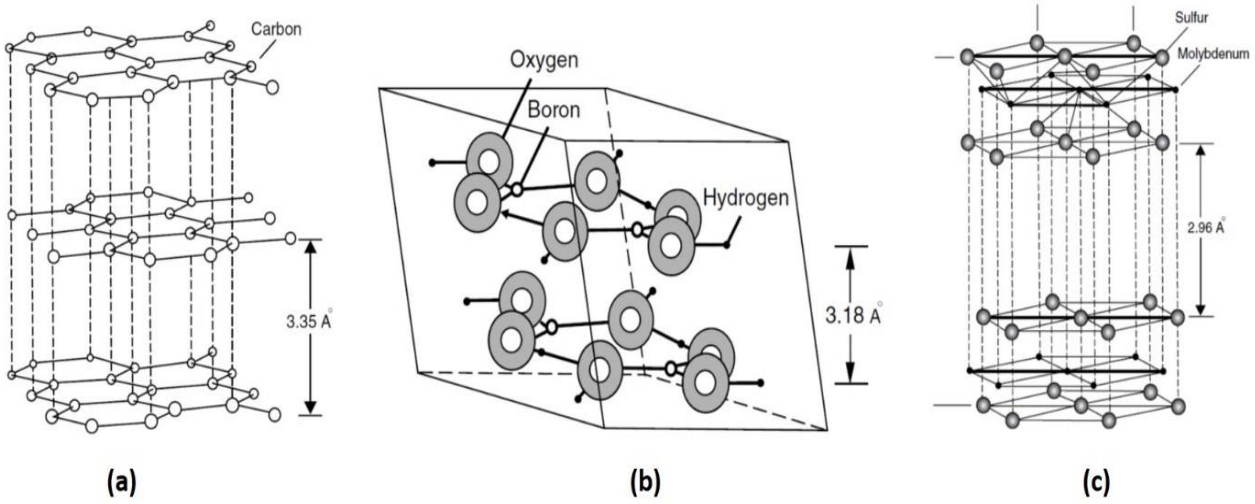

Figure 2.4 Schematic illustration of layered structures of (a) graphite, (b) boric acid, and (c) molybdenum disulphide (representing transition-metal dichalcogenides) [46].

2.2.3 Methods of applying solid lubricants

Solid lubricants can be applied to a tribological surface in a variety of forms. The application method usually depends on the complexity of the component being lubricated and the desired location of the solid lubricants. In the following paragraphs, some commonly used methods and their characteristics will be provided.

Burnishing is the oldest and simplest method of applying solid lubricants onto substrate surfaces. In this method, solid lubricants are manually rubbed onto the component surface to form a lubrication layer [53]. The advantages of burnishing method include its simplicity, cost-effectiveness, and versatility. It is a straightforward process requiring minimal equipment, making it suitable for small-scale or localized applications. However, burnishing is the least effective in regard to bonding [54]. Obvious stratification can be observed between the solid lubricant layer and the metal surface. Therefore, this process is only suitable for applications where lubrication requirements and wear life are not stringent.

Another application method is to blend solid lubricants with epoxy resins, plastics and polymers to form thick composite coatings with anti-friction properties. Compared to the direct use of solid lubricants (burnishing), blending solid lubricants with epoxy resins can provide stronger adhesion between substrates and coatings. However, the bonding materials usually possess low mechanical strength and poor wear resistance, which may restrict their usage in high demanding applications [55].

Vapour deposition techniques, including physical vapour deposition (PVD) and chemical vapour deposition (CVD), are more advanced methods for developing thin films of solid lubricants. The PVD process begins with the vaporisation of solid lubricant atoms from target materials. These vaporised atoms are then transported through a vapour chamber and deposited as a thin film on the substrate [56]. The advantages of PVD include precise thickness control, a dense surface structure, and strong adhesion to the substrate, which are essential for high demanding applications. However, the PVD process also presents challenges of high initial equipment costs and process complexity, requiring stringent control of deposition parameters. The CVD process, on the other hand, relies on the reaction of precursors in the vapor phase to form a solid lubricant film on the heated substrate surface. Although self-lubricating coatings prepared by CVD offer the advantage of uniform coating coverage, especially on complex geometries, the residual stresses in the deposited coating, arising from differences in thermal expansion between the substrate and the coating, can deteriorate the coating's performance and longevity.

Different from the techniques discussed above, composite electroplating is a versatile method to fabricate self-lubricating coatings by co-depositing solid lubricants with metals. The deposited metals such as nickel, copper, and aluminium can provide excellent strength and stiffness. The incorporated solid lubricants can be slowly released onto the wear track to achieve a very low friction coefficient. Owing to the advantages of precise control, cost-effectiveness, and promising potential for industrial applications, electrodeposition is an effective method for developing self-lubricating coatings. However, the challenges associated with composite electroplating cannot be ignored. Apart from the general drawbacks of electroplating discussed in Section 2.1, composite electroplating faces specific challenges, such as particle agglomeration in the electrolyte, poor adhesion between the coating and substrate, and a limited incorporation rate of solid lubricant particles. The following section will review the electrodeposited self-lubricating coatings and some related research in this field.

2.2.4 Electrodeposited self-lubricating coating

The electrodeposition of metal-solid lubricant composite coatings have been extensively studied in the past two decades. WS_2 and MoS_2 are the most commonly used solid lubricant particles to be co-deposited. For example, Lecina et al. [57] electrodeposited a Ni-WS_2 coating with a stable coefficient of friction (CoF) of 0.4 against steel. Redlich et al. [58] reported that co-depositing WS_2 particles with nickel resulted in a friction reduction of 60% compared to pure nickel coating. Cardinal et al. [59] demonstrated that the friction coefficient of Ni-W-MoS_2 coating could reach as low as 0.14 with an appropriate amount of particle embedment. Recently, the research group at the University of Southampton has successfully deposited a series of self-lubricating coatings including, Ni-P/WS_2 [14], Ni-P/MoS_2 [4], Ni-Co/WS_2 [15] and Ni-MoS_2 [6], showing a friction coefficient less than 0.2. A self-lubrication mechanism has been proposed to explain the friction reduction of composite coatings mentioned above [15]. Once counterpart (either ball or cylinder) starts sliding against composite coating, the contact area on the coating surface will experience severe plastic deformation due to high shear stress. Then, the incorporated solid lubricant particles can be released from their fixed positions and adhere to the contact area. With the accumulation of these released particles, a densely packed lubricating layer (or tribofilm) will be formed between sliding surfaces, which can not only reduce friction force but also improve wear resistance and oxidation resistance by avoiding direct metal to metal contact. However, excessive accumulation of detached solid lubricant particles should be avoided as it can result in unstable tribofilm. Instead of reducing friction, the unstable tribofilm may lead to loss of lubrication when dislodged.

The amount of embedded solid lubricant and the coating structure are two main factors influencing self-lubricating performance. According to He et al. [4, 14, 15]'s studies, the lower friction coefficient of Ni-P/WS_2 and Ni-P/MoS_2 and Ni-Co-WS_2 coatings were realised at higher particle content (**Figure 2.5 a-c**). A similar finding was also reported by Shourije and Bahrololoom [60]. In their research, the increase of MoS_2 content led to a decrease in the friction coefficient from 0.35 to 0.08. The significant friction reduction was attributed to the high abundance of solid lubricants, which can be continuously released from the coating system during sliding motions. In addition, the SEM images and EDS analysis of wear tracks on both coating surface and counterpart revealed that the wear loss and frictional oxidation could be suppressed due to the formation of complete tribofilm.

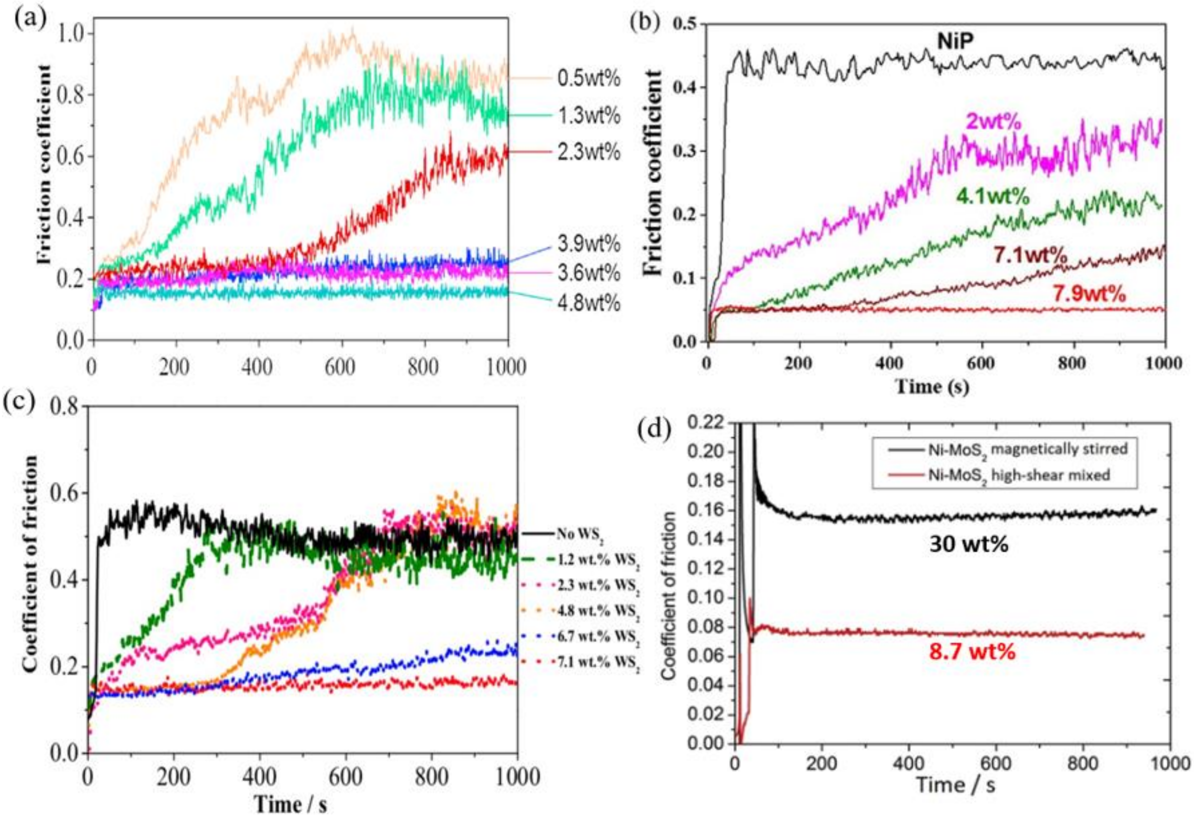

Figure 2.5 Friction coefficient of electrodeposited composite coating with different solid lubricant content (a) Ni-P/WS_2, (b) Ni-P/MoS_2, (c) Ni-Co/WS_2 (d) Ni-MoS_2 [4, 6, 14, 15].

However, increasing particle content alone may not always lead to improved tribological performance. Many studies also pointed out that self-lubricating properties are largely dependent on the composite coating structure. Zhou, Wang and Walsh [6] prepared self-lubricating Ni-MoS_2 coating with the assistance of two different particle dispersion methods, namely magnetic stirring and high shear mixing. As shown in **Figure 2.5 (d)**, Ni-MoS_2 composite coating using particle dispersion via high-shear mixing showed lower particle content (8.7 wt%) but better self-lubricating property (CoF = 0.08) compared to those of Ni-MoS_2 composite coatings using particle dispersion via magnetic stirring (particle content = 30 wt%, CoF = 0.16). The lower friction coefficient by high shear mixing can be attributed to compact and dense coating structure which provides firm support for the MoS_2 particles to allow an effective shear to occur. On the other hand, although Ni-MoS_2 coating prepared with magnetic stirring showed higher MoS_2 content, the porous and sponge-like structure induced by particle agglomeration makes coatings easily be fractured and damaged during the sliding contact. Similar results have also been reported by Cardinal et al. [59] and Cheng et al. [7]. In both studies, high particle incorporation rates resulted in rough coating surfaces and porous coating structures, which deteriorated the tribological performance. Therefore, it can be concluded that solid lubricant content in the composite coating alone should not be regarded as the only criteria for assessing coating quality. The coating structure also plays an important role in determining anti-friction performance. In Section 2.4, a detailed literature review of methods to densify electrodeposited coating structures will be given.

2.2.5 Wear mechanism

Wear is defined as the removal of material when two solid surfaces come into contact. Understanding wear mechanism is important for developing self-lubricating coatings. By identifying the dominant wear, such as adhesive wear, abrasive wear and oxidative wear, researchers are able to optimise self-lubricating coatings by tailoring their composition, coating structures and solid lubricant distribution. The mechanisms of several types wear will be reviewed in the following paragraphs.

Adhesive wear is characterised by material transfer from one surface to another due to the shearing of surface asperities at the contact interface. This type of wear originates from the adhesive bond. When the adhesive bond at the contact interface is greater than the cohesive bond within the weaker material of the contact pairs, material transfer occurs [61]. Adhesive wear usually leads to severe wear damage on the sliding surfaces.

Abrasive wear occurs when a harder surface or abrasive particles sliding or rolling against softer surface. There are two types of abrasive wear, namely two-body abrasive wear and three-body abrasive wear. The former occurs when the asperities of hard surface cut through the softer surface, while the latter arises when loose abrasive particles become entrapped at the contact interface, removing materials from both sliding surfaces [62].

Oxidative wear occurs due to the formation and subsequent removal of oxide layers on the surfaces in contact during sliding motion. The process begins with the formation of a thin oxide film due to frictional heating. With continuous sliding contact, this oxide layer may crack, and flake off, exposing fresh material that undergoes further oxidation [63]. The removal of the oxide layer generates wear debris, which can induce additional abrasive wear.

2.3 Superhydrophobic Coatings

Superhydrophobic coatings have attracted attention from both academia and industry. Due to their excellent water-repellent properties, such coatings have been widely applied in the fields of anti-corrosion [64], anti-fouling [65], anti-icing [66], and energy savings [67]. In this section, the studies about superhydrophobicity will be reviewed. However, before that, it is necessary to review basic knowledge of surface wettability and wetting models as they can help to understand the fundamental principles and mechanisms of superhydrophobic surfaces.

2.3.1 Surface wettability and wetting models

Surface wettability is the ability of a surface to get wetted by a liquid. Normally, when a water droplet is placed on a surface, it will either form a sphere or wet the surface. To characterise and quantify the wetting state of a solid surface, the concept of contact angle is introduced. As shown in **Figure 2.6**, the contact angle θ is defined as the angle formed by the intersection of the solid, liquid, and solid-gas interface. In general, a small contact angle is formed when the liquid is distributed on the surface (hydrophilic, $\theta < 90^{\circ}$), while a large contact angle is formed when there is a low contact area between solid and liquid (hydrophobic, $\theta > 90^{\circ}$).

According to previous research [68, 69], surface energy and surface roughness are two primary factors influencing solid surface wettability. Surface energy, by definition, characterises the amount of energy required to overcome the molecular cohesive forces within a bulk material to create a unit area of new surface. Surface energy arises because the molecules at the surface are surrounded by fewer molecules compared to those within the bulk material, resulting in an imbalance of forces. Surface energy is quantified in terms of energy per unit area – joules per square meter (J/m^2). Surface energy is determined by the chemical composition of the surface, and the decrease of surface energy usually leads to a hydrophobic surface. On the other hand, a surface with rough texture tends to have a hydrophobic property. Because in such surface air can be easily entrapped in the grooves between surface protrusions. When water is placed on the surface, the entrapped air will avoid further penetration of water. Therefore, water droplets will form sphere shapes and can easily roll off from the surface [70].

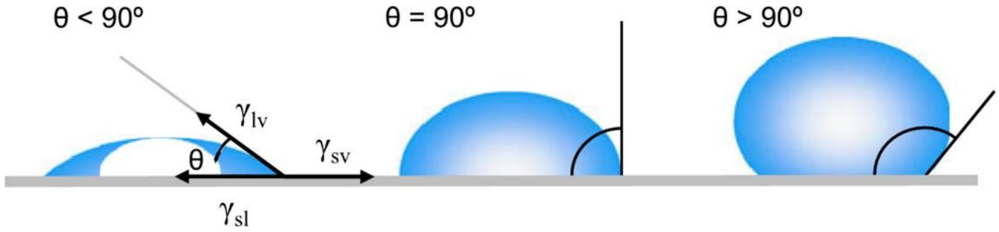

Figure 2.6 Illustration of contact angle formed by water droplets on a smooth homogeneous solid surface [71].

To further explore the mechanism of the surface wetting state, three classical models have been proposed. The first model was introduced in 1805 by Young [72]. For a drop of water placed on an ideal flat surface (**Figure 2.7 a**), the contact angle is determined by the surface free energy of a solid and derived in Equation (2.6):

$$cos\theta = \frac{\gamma_{sv}\text{-}\gamma_{sl}}{\gamma_{lv}} \ldots\ldots\ldots\ldots\ldots\ldots\ldots\ldots\ldots\ldots\ldots\ldots\ldots 2.5$$

Where θ is the water contact angle. γ_{sv}, γ_{sl}, γ_{lv} is the surface tension of solid surface, solid-liquid interface, and liquid surface, respectively. The Young equation ambiguously relates the water contact angle to the interfacial tensions (energies). However, since real surfaces usually vary in the surface conditions, most scenarios regarding contact angles in practice cannot be fully explained by the Young equation. Wenzel [73] then proposed an equation relating the contact angle to surface roughness and surface energies. As shown in **Figure 2.7 (b)**, Wenzel's model assumes full contact between the liquid and solid phase in the homogeneous regime. The calculation of the contact angle can be expressed in Equation (2.7):

$$cos\theta_w = r\frac{\gamma_{sv}\text{-}\gamma_{sl}}{\gamma_{lv}} = rcos\theta \ldots\ldots\ldots\ldots\ldots\ldots\ldots\ldots\ldots\ldots\ldots 2.6$$

Where θ_w is the apparent Wenzel contact angle, which measures the apparent contact angle influenced by the roughness of solid surfaces. r corresponds to the "roughness factor", defined by the roughness area ratio of the actual surface with respect to the geometric surface. Wenzel equation predicts that a higher roughness will increase the contact angle for a hydrophobic surface ($\theta > 90°$). But for hydrophilic surface ($\theta < 90°$), contact angle values will be lower with increasing roughness [74].

However, Wenzel's model is only workable for the homogenous interfacial areas and cannot be applied to the non-homogeneous interfaces. In this regard, Cassie and Baxter [75] in 1944 provided another model for heterogeneous surfaces (**Figure 2.7 c**). Their model consists of two parts. The first part includes f_{SL} (area fraction of solid in contact with liquid) and θ_y (static contact angle on the smooth surface). The second part includes f_{LA} (area fraction of air in contact with liquid) and θ_A (contact angle of a droplet with the gas phase, which can be considered up to 180°). Hence, in Cassie and Baxter's equation, the contact angle θ is defined as Equation (2.8):

$$cos\theta = f_{SL} cos\theta_y + f_{SA} cos\theta_A \quad \text{2.8}$$

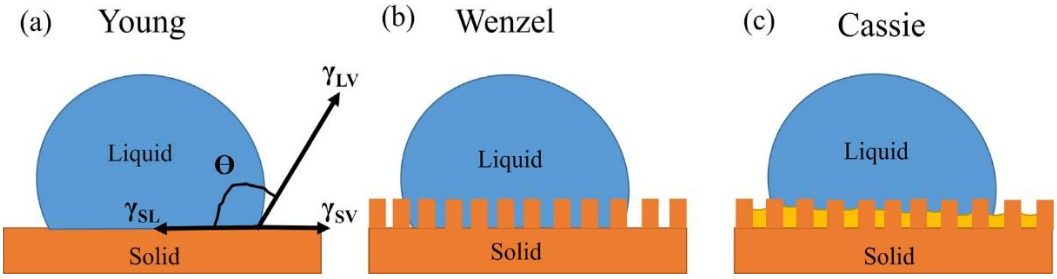

Figure 2.7 Schematics of different wetting models [4].

The above wetting models are significant to characterise the wetting states of coatings with different surface conditions. For hydrophilic coatings which can be completely wetted, the Wenzel model (for $\theta < 90°$) is suitable to calculate the contact angle value. While for hydrophobic coatings of which the surfaces are heterogeneous due to air entrapment, the Cassie-Baxter model (for $90° < \theta < 180°$) can be applied to predict the contact angle.

2.3.2 Superhydrophobic surfaces inspired by nature

A typical superhydrophobic surface has water contact angles greater than 150° and sliding angles (the minimum tilt angle that allows water droplets to roll off) less than 10°. Extremely low wettability is achievable on such superhydrophobic surfaces. In 1936, the triticum (wheat) plant was the first reported organism with a water contact angle above 150° [10]. Since then, nature has become the source of many valuable templates used to design synthetic hydrophobic surfaces. The most representative organisms exhibiting superhydrophobicity include natural plants and insects. The following paragraphs will briefly describe the wetting mechanism of several typical superhydrophobic surfaces in nature.

Among all kinds of plants showing superhydrophobicity, lotus is the most notable one as its leaves can prevent being polluted and contaminated even when the lotus is growing from muddy water, thus giving the name to the “lotus effect”. Barthlott and Neinhuis’ work [76] in 1997 attributed the “lotus effect” to the presence of hierarchical structures on the surface. The SEM images in **Figure 2.8** showed that the hierarchical surface structure is built by convex cells (> 1μm) and a much smaller superimposed layer of hydrophobic three-dimensional wax tubules (typically below 200 nm). According to the Wenzel-Cassie model, when the water droplet is placed on such hierarchical structures, air bubbles can be entrapped in the cavities of convex cell sculptures, which can avoid further water penetration. Therefore, water droplets can easily roll off the lotus leaves. Similar hierarchical structures have also been observed on taro leaves and rice leaves, which makes them extremely water-repellent.

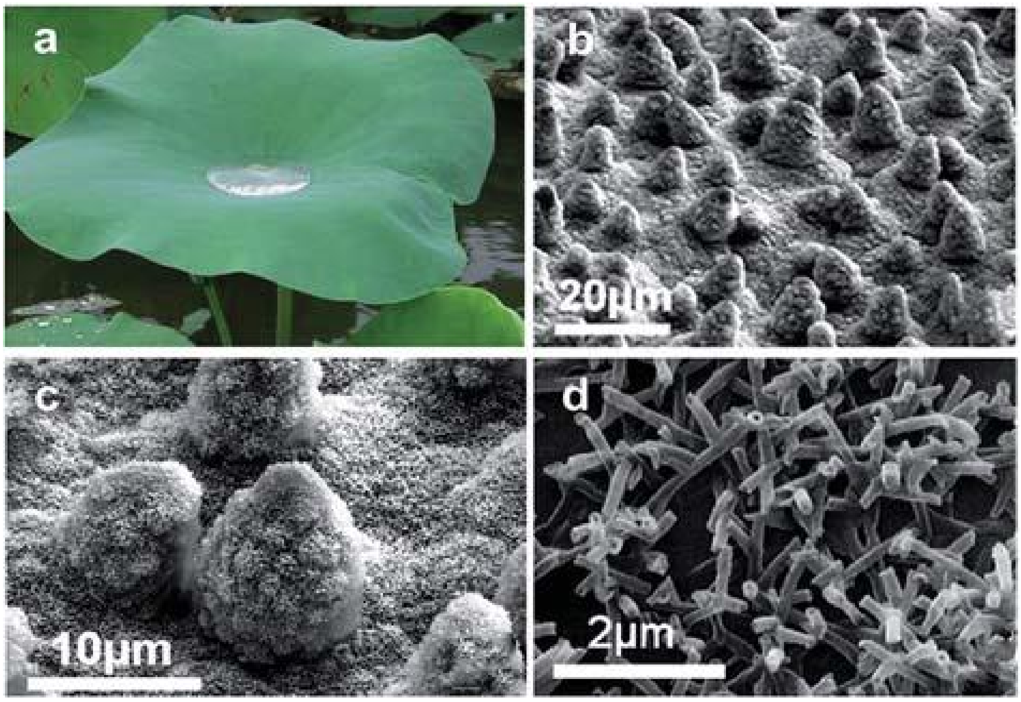

Figure 2.8 (a) self-cleaning behaviour of lotus leaves (b) the related microstructures as observed by scanning electron microscopy, (c) protrusions and (d) the wax tubules on them [77].

Unlike the lotus leaves mentioned above, another kind of plant surface with high water contact angle but the high sliding angle is existing as well, such as red rose petal. Water droplet can form a high contact angle on the rose petal surface, but it is very difficult to move freely. This special phenomenon is called the “rose petal effect” and can be explained by its microstructure. As shown in **Figure 2.9 (a)**, the rose petal surface is composed of a periodic array of microtubercle structures with an average diameter of 16 μm and a height of 7 μm. The high magnification SEM image in **Figure 2.9 (b)** reveals that these microtubercle structures have a layer of nanoscaled cuticular folds (average size of 730 nm) on their top. Similar to the “lotus effect”, rose petal surface exhibits superhydrophobicity owning to these hierarchical micro- and nanostructures. However, the different microstructure size of the lotus leaf and the rose petal results in different dynamic wetting. That is, water droplets can effortlessly roll off the surface of a lotus leaf (**Figure 2.9 c**), while they stay pinned to the surface of a red rose petal (**Figure 2.9 d**). Feng et al. [78] proposed a Cassie impregnating wetting model to explain this different dynamic wetting phenomenon. As shown in Figure **2.9 (e-f)**, the microstructure and nanostructure of the rose petal are both larger than those of lotus leaf, so the liquid tends to impregnate into the microscaled grooves but not into the nanoscaled cuticular folds, forming the Cassie impregnating wetting state. When the surface is inclined to any angle or even upside down, the liquid immersed in the micro-scale grooves will adhere to the petal surfaces, showing strong adhesion.

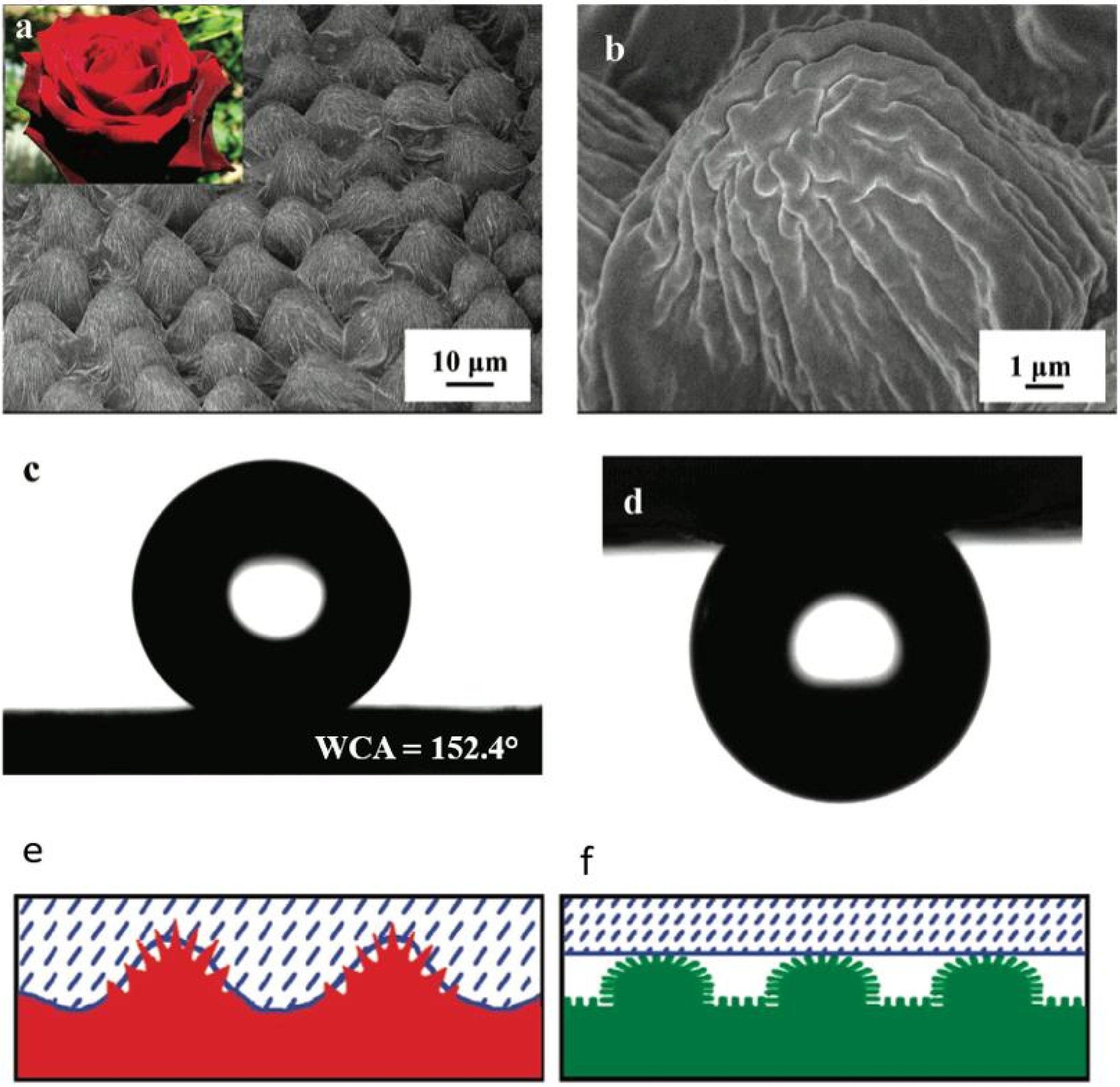

Figure 2.9 (a-b) SEM images of rose petal with low and high magnification; (c) water droplet formed on a rose petal; (d) water droplet adheres to the overturned petal surface; (e) schematic of Cassie impregnating wetting state on rose petal; (f) schematic of Cassie-Baxter wetting on lotus leaf [78].

Water striders are a type of insect with the ability to walk freely on the water for a long (**Figure 2.10 a**). The non-wetting feature was first believed to be due to a surface tension effect caused by secreted wax [79]. However, the water contact angle made with the cuticle wax secreted on a strider's leg is about 105° [80], which is not enough to explain its extreme water repellence. According to the research conducted by Gao and Jiang [81], the superhydrophobic mechanism of the water strider leg is also attributed to the special hierarchical micro/nanostructure. As shown in **Figure 2.10 (b)**, strider's leg consists of numerous oriented setae, which are needleshaped, with diameters in a few to tens of micrometres. Most setae are roughly 50 µm in length and arranged at an inclined angle of about 20° from the surface of the leg. The high-magnified SEM image in **Figure 2.10 (c)** reveals that the seta surface has groove structures with depth and width of about 100 nm. When strider leg touches water, tiny air bubbles trapped in these grooves can form a cushion at the leg/water interface that prevents the legs from being wet.

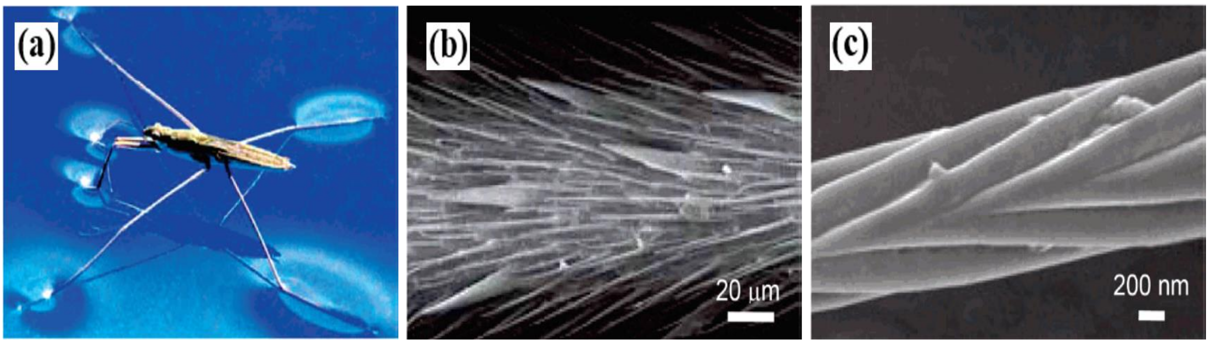

Figure 2.10 (a) Image of water strider walking on the water surface; (b) SEM image of a strider leg showing numerous setae; (c) high magnification SEM image showing nanoscaled grooves [82].

Inspired by the wetting mechanisms of organisms discussed above, it can be suggested that the realization of superhydrophobicity is due to the combination of surface hierarchal structure and low surface energy. Therefore, methods to fabricate artificial superhydrophobic surface are based on two basic rules, namely reducing material surface energy and creating surface micro-/nanostructures. In the following section, a review of currently available methods for fabricating superhydrophobic surfaces will be provided.

2.3.3 Fabrication methods of superhydrophobic coatings

Nowadays, superhydrophobic coatings can be fabricated via many advanced techniques such as lithography, sol-gel transitions, chemical vapour deposition (CVD), template, etching and electrochemical process. **Table 2.3** provides brief descriptions of these fabrication methods. Electrochemical processes seem to combine both ease of implementation and the possibility to obtain various surface morphologies among all these methods. Moreover, the electrochemical process can avoid expensive equipment and a specialised reaction environment compared to other techniques [9]. Combined with the advantages mentioned in the previous self-lubricating coating section, the electrochemical process is ideal for fabricating coatings with self-lubrication and superhydrophobicity. On the other hand, additive manufactureing, as an innovative technology, exhibits advatanges of accurate control, surface robustness, and high printing efficiency in terms of developing superhydrophobic surfaces. Although the capital investment of additive manufacturing might be a concern, a continuing falling trend in entry cost has been witnessed, making this technology affordable for industrial applications. The following section will provide a review of electrodeposited superhydrophobic coatings

Table 2.3 Fabrication methods of superhydrophobic surfaces [77]

Fabrication method	Process description	Pros and Cons
Lithography	Similar to an inked stamp, a pattern is transferred from master to a surface, producing several copies.	- High degree of control and precision, suitable for research. - Require specialised equipment and post treatment, not suitable for large-scale production.
Sol-gel	A chemical precursor, when undergoing hydrolysis and polycondensation reactions, is converted into a glassy material, which forms a layer on the substrate. Sol-gel is a low cost and simple controlled process, but the process is time-consuming.	- Cost effective as the materials (silicon oxide, titanium oxide, etc.) are affordable and the process can be performed with low-cost equipment. - Time consuming as it requires several steps and post-treatment
CVD	The phase of a chemical precursor is changed into the vapour phase and is allowed to react with the heated surface (substrate) to form a thin layer of film. CVD is able to achieve extreme wettability (contact angle = 170º).	- Ability to develop uniform coatings on complicated or irregular surfaces. Prepared surfaces are durable due to chemical bonding. - High reaction temperature is required, leading to energy

Fabrication method	**Process description**	**Pros and Cons**
		consumption. By-products are hazardous to environment.
Etching	When a surface is exposed to an etching medium, chemical reactions selectively erode/remove materials.	- Lower cost compared to CVD and lithography. - Limited control on surface uniformity and environmental and health concern.
Electroplating	It is an electrochemical reduction process where metal ions are reduced into metals and deposited. This method can produce various surface morphologies and be used on a large surface.	- Cost effective for metal coatings. Suitable for large-scale industrial application. - Limited to conductive substrates. Post-treatment such as fluorination is required to reduce surface energy.
Additive manufacturing	Selective laser melting (SLM) 3D-printed technology adopts high energy to selectively melt and fuse metallic powders, layer by layer, based on computer aided design (CAD).	- Precise control of surface texture. Suitable for a wide variety of materials (e.g. polymers, metals and ceramics). - High cost due to specialised equipment. Post-treatment is required as the freshly prepared surface is hydrophilic.

2.3.4 Superhydrophobic surfaces by electrodeposition

Electrodeposition has been successfully applied for the preparation of superhydrophobic coatings (e.g. nickel [83, 84], copper [85] and cobalt [86]). As a mature coating technique, Electrodeposition is advantageous in the aspects of low cost, high deposition rate, reliable repeatability, and accurate control [26, 87]. In the past decade, numerous successful cases of electrodeposited superhydrophobic surfaces have been reported. By controlling deposition parameters such as bath composition [88, 89], current density [90, 91], deposition time [92-94], deposition potential [85, 95-98], and bath temperature [99], hierarchical surface structures can be developed on electrodeposited pure metals (e.g. Ni, Co, Au, Cu) and alloys (Ni-Co, Ni-Zn, Cu-Zn). However, the freshly prepared surfaces of electrodeposited metals and alloys exhibited hydrophilic nature due to high surface free energy[91, 97]. To achieve the transition from hydrophilic to superhydrophobic, the freshly electrodeposited coatings need to be stored in ambient air to allow the adsorption of low surface energy airborne hydrocarbons [100]. This process of wettability transition is time-consuming. It usually takes several days to weeks to reach superhydrophobic states, which will limit the economic efficiency for practical applications [83, 88, 90, 93, 95, 101-103]. To accelerate the transition process, many researchers applied post-treatment method, in which the freshly deposited surfaces were modified by low surface energy chemicals such as silane, fluorinated compounds and organic acids. However, the additional post-treatment complicates the manufacturing process and can be harmful to the environment as these chemicals are usually non-biodegradable [104]. Moreover, chemicals such as fluorinated and silane compounds are proven to have threats to human health. The frequent exposure or inhalation can cause skin and eye irritation and even kidney damage to the operators [105, 106]. It is therefore necessary to develop superhydrophobic coatings by electrodeposition without long-term wettability transition process or additional surface modification.

Since long-term storage or post-treatment is to lower the surface energy, the co-deposition of low-surface-energy particles with metals during electroplating could achieve similar effects. **Table 2.4** below summarises the surface energy of different types of materials. From **Table 2.4**, it can be noted that the surface energy of transition metal dichalcogenides (TMD) such as molybdenum disulphide (MoS_2) and tungsten disulphide (WS_2) are lower than other types of materials. The low surface energy makes them good candidates to fabricate superhydrophobic composite coatings. Although TMD materials are traditionally used as solid lubricants to combat friction [11, 12], the studies of electrodeposited metal-TMD composite coatings for superhydrophobic surfaces has increased in the last five years.

Zhao et al. [13] reported that Ni-WS_2 coating with WCA of 158.3° and SA of 7.7° could be successfully prepared by one-step electrodeposition. The wettability of deposited Ni-WS_2 surface is determined by two factors, namely the embedded WS_2 content and surface morphology. As shown in **Figure 2.11 (a)**, superhydrophobicity can only be achieved when the WS_2 content is greater than 4 wt%. This is because co-deposited WS_2 is the main substance to reduce the surface energy of coating. The direct method to enhance WS_2 content is increasing particle concentration in the electroplating bath. SEM image under low magnification reveals that the Ni-WS_2 coating surface consists of numerous protrusions (**Figure 2.11 b**). Under high magnification, it can be observed that each protrusion has a diameter of microscale and consists of densely packed particles in the nanoscale (**Figure 2.11 c and d**). Such surface microstructure is very similar to a lotus leaf. Therefore, when the droplet is placed on the Ni-WS_2 coating surface, an air layer could remain in the micro gaps to prevent water penetration (**Figure 2.11 e**). Similar superhydrophobic surfaces were also reported on electrodeposited Ni-P-WS_2 [14] and Ni-Co-WS_2 [15]. Recently, Prado and Virtanen [16] claimed that Cu-MoS_2 coating prepared with electrodeposition showed superhydrophobicity. The as-deposited Cu-MoS_2 could maintain hydrophobic even after 20 min immersion into water. The excellent water repellence was ascribed to the unique hierarchical structure where a great amount of air can be trapped to achieve the Cassie-Baxter wetting state.

Table 2.4 Summary of surface energy of different materials

Material	Approximate surface energy (mJ/m^2)	Ref
Molybdenum Disulphide (MoS_2)	46.5	[107]
Tungsten Disulphide (WS_2)	38.5	[108]
Silicon Carbide (SiC)	718	[109]
Titanium Dioxide (TiO2)	88.9	[110]
Tungsten Carbide (WC)	126.3	[111]
Nickel	1821	[112]

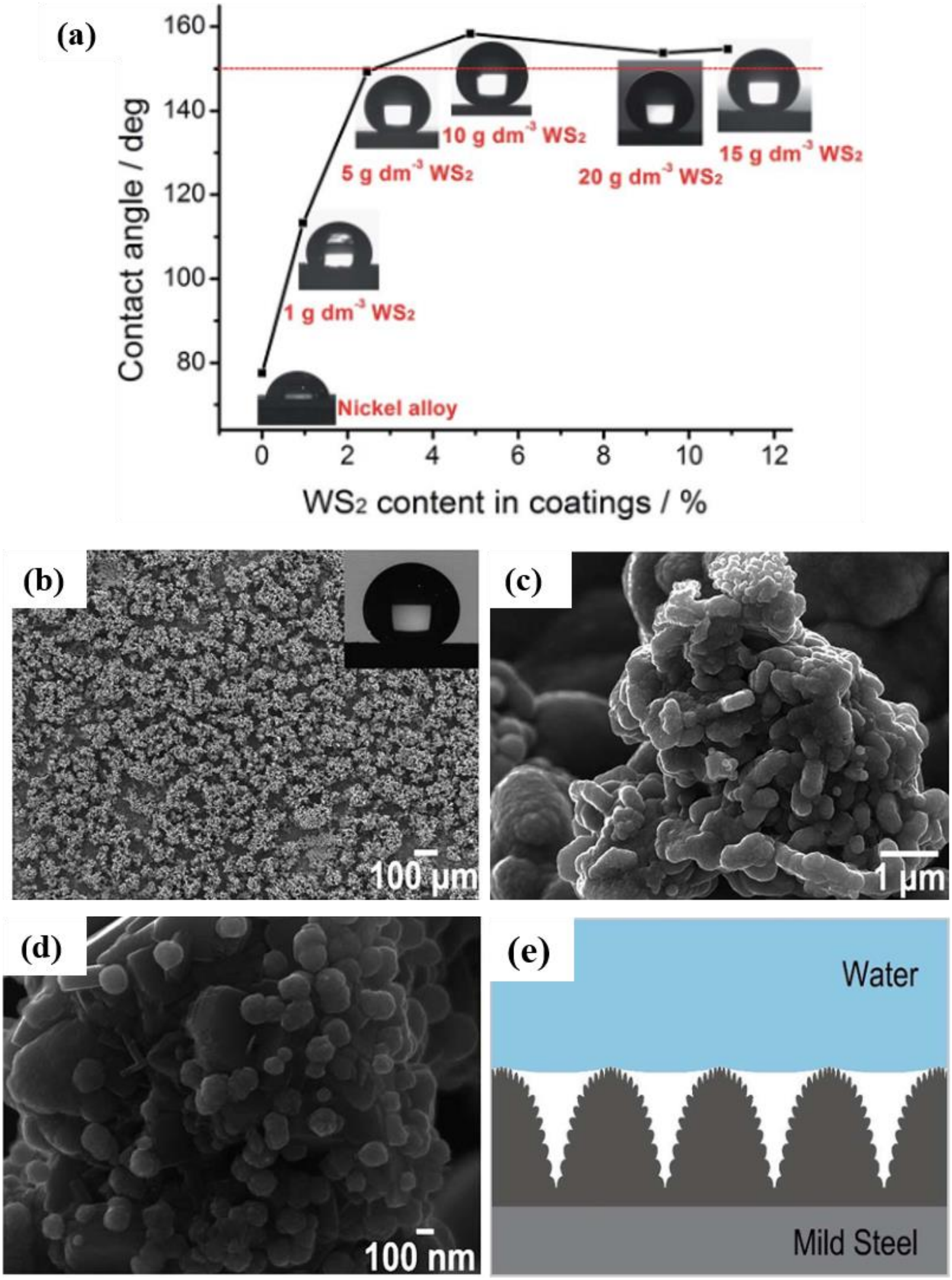

Figure 2.11 (a) Relationship between particle content and surface wettability; (b), (c) and (d) are surface morphology of superhydrophobic Ni-WS2 coating under low and high magnification; (e) is a schematic illustration of contact area, in which air is entrapped between protrusions of coating surface [13]

The co-deposition of solid lubricants with metal matrix seems to be a promising method for preparing superhydrophobic surfaces, however the weak hierarchical surface structure inhibits the long-time stability and industrial applications. According to Zhou et al. [113], most electrodeposited superhydrophobic coatings are porous and fragile. As a consequence, superhydrophobicity can be diminished quickly if the hierarchical micro and nano structures are worn by surface abrasion. To address this challenge, it is essential to densify the coating structure of superhydrophobic surfaces. The following section will explore various methods for densifying electrodeposited composite coatings.

2.4 Densification of electrodeposited coating structures

A major challenge of both pure metal and composite electroplating is that porous and rough coatings might be formed during the plating process. Many studies indicate that porous coating structures may severely deteriorate coating qualities from several aspects. Firstly, service lives might be shortened as porous coatings are prone to wear during sliding contact motion. Secondly, mechanical properties (e.g., hardness and adhesive strength) could deteriorate because the porous structures are fragile and tend to be exfoliated under bending test. Thirdly, the corrosion process would be aggravated since corrosive media could easily penetrate the porous coating and reach the substrate.

In order to enhance the durability and coating properties, it is necessary to form smooth coating surfaces and dense coating structures. Many previous studies have agreed that the operational parameters can significantly influence the appearances and structures of electrodeposited coatings. According to a review article by Walsh, Wang and Zhou [87], these operational parameters can be classified into four categories, i.e. electrode (material, geometry, surface finish, etc.), electrolyte (composition, pH, agitation, additives, etc.), particle (material, size, shape, conductivity, etc.), and current (current type, current density, current distribution). There are many review papers available discussing the influence of each parameter on the final coating properties [26, 38, 114, 115]. However, none of them gives a detailed review of how to densify the electroplated coatings by adjusting operational parameters. Therefore, the following sections will provide a comprehensive review of different methods to smoothen the coating surface and densify the coating structure. The working mechanisms and their effects on final coating properties will also be discussed.

2.4.1 Origins of coating porosity and methods to densify coating structure

The origins of porous electroplated coatings and possible methods to densify coating structures are summarised in **Figure 2.12**. Generally, the porous coating structures can be attributed to three main reasons: hydrogen evolution, particle agglomeration, and the disturbance of the electric field due to particle conductivity. In electroplating, metal deposition is always accompanied by hydrogen evolution since the reduction potential of hydrogen ion is more positive than metal ion [116]. The evolved hydrogen might adhere to the cathode surface. Therefore, some areas would be blocked from metal deposition. As a consequence, the coating structure would become porous. Additionally, in composite electroplating, due to the high surface free energy of submicron-sized particles and high ionic strength of electrolyte, particles tend to form large agglomerates in the plating bath. This prevents a homogeneous particle dispersion and may negatively affect particle co-deposition. Unstable particle dispersion can also lead to porous deposits, which are susceptible to wear and corrosion [6]. For the co-deposition of conductive particles such as graphite, carbon nanotubes (CNTs), MoS_2, WS_2 and WC, the phenomenon of porous coating is more severe. During electroplating, the electric field in the vicinity of conductive particle absorbed sites will be enhanced. More metal ions would be attracted towards these sites due to greater Coulomb force, which accelerated the reduction of ions at these locations and created composite coatings with non-compact and porous structures [59, 117, 118].

Similar to the categorization of operational parameters proposed in a previous review article [87], the methods to densify coating structures may also be classified into four aspects, namely current regime, particle modification, surfactant addition and particle dispersion and bath agitation. In the following subsections, each method will be discussed and critically reviewed.

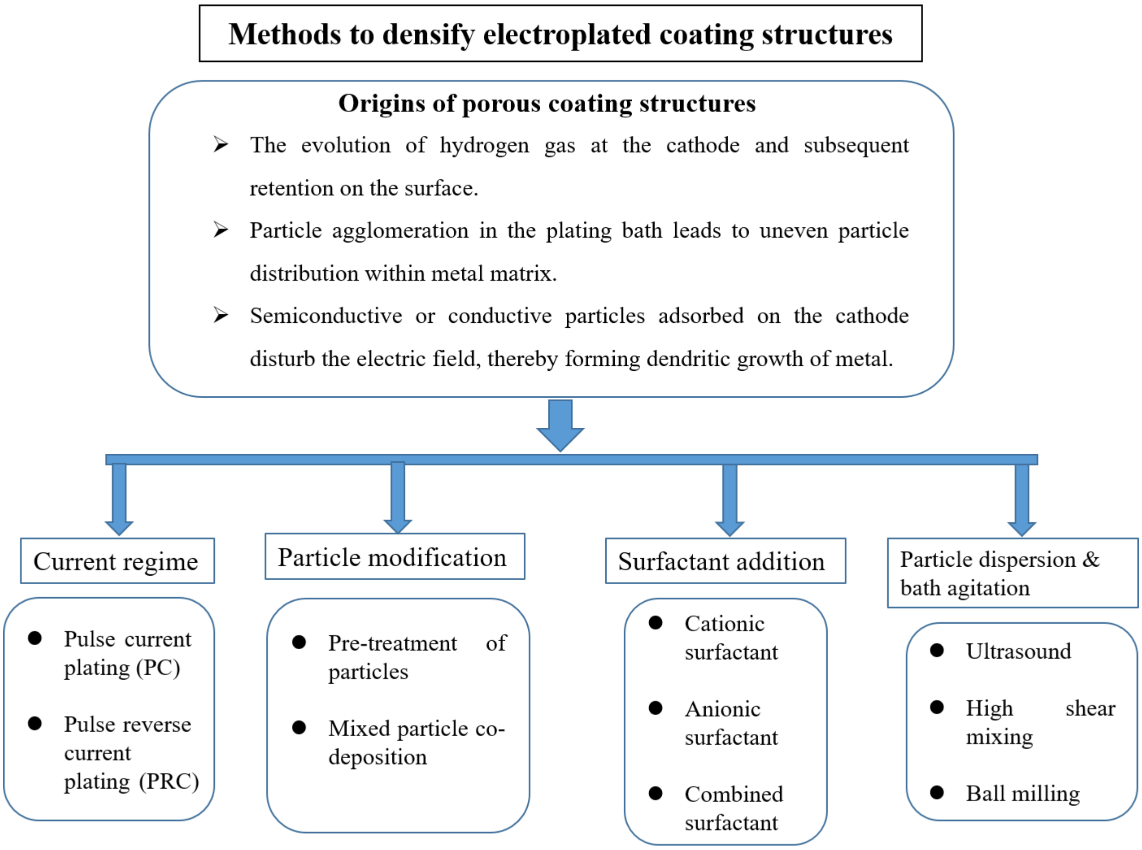

- The evolution of hydrogen gas at the cathode and subsequent retention on the surface.
- Particle agglomeration in the plating bath leads to uneven particle distribution within metal matrix.
- Semiconductive or conductive particles adsorbed on the cathode disturb the electric field, thereby forming dendritic growth of metal.

Figure 2.12 Origins of porous coating structures and possible methods to densify electrodeposited coating structures

2.4.2 Current regime

Pulse electrodeposition has been extensively applied for the deposition of metals, alloys and composite materials. Different from conventional direct current (DC) electrodeposition, which uses continuous and constant current throughout the plating process, the current in pulse methods is alternated swiftly between two different values. Based on the applied current waveform, pulse electrodeposition can be divided into two groups: (1) pulse current (PC) plating and (2) pulse reverse current (PRC) plating. In PC plating, each pulse can be divided into two periods, namely T_{ON} and T_{OFF} (**Figure 2.13 a**). T_{ON} is the period during which the current is applied. T_{OFF} is the period during which zero current is applied. Similar to PC plating, PRC plating is also comprised of two periods, which are cathodic time (T_C) and anodic time (T_{AA}). During the cathodic time, cathodic current density (I_C) is applied, and during the anodic time, anodic current (I_{AA}) is applied (**Figure 2.13 b**).

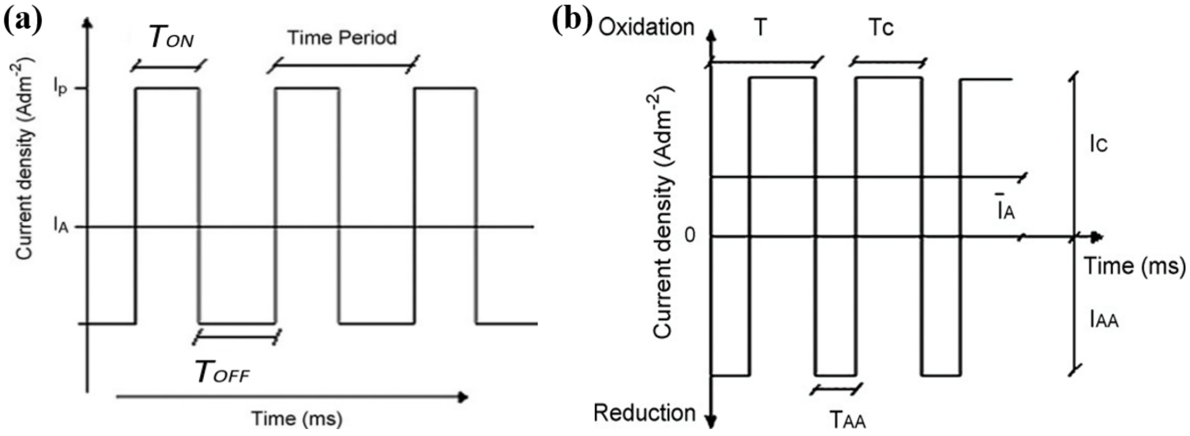

Figure 2.13 (a) Waveform of PC plating, I_P is the peak current, I_A is the average current, T_{ON} is the period with applied current, T_{OFF} is the period with no applied current; (b) Waveform of PRC plating, I_C is the cathodic current density, I_{AA} is the anodic current density, T_C is the cathodic time, T_{AA} is the anodic time [119].

The quality of deposits prepared by pulse electrodeposition is determined by three independent variables (i) period with current applied (T_{ON}), (ii) period with no current applied (T_{OFF}) and (iii) peak current density (I_P), which is more complicated than conventional DC plating where the current density is the only one parameter.

By convention, the duty cycle (γ), which corresponds to the T_{ON} percentage in a cycle, is used as a standard parameter in PC. It can be calculated by [119]:

$$Duty\ cycle\ (\gamma) = \frac{T_{ON}}{T_{ON} + T_{OFF}} = T_{ON} f \qquad 2.7$$

Where f is frequency, which is defined as the reciprocal of the cycle time (T).

$$Frequency\ (f) = \frac{1}{T_{ON} + T_{OFF}} = \frac{1}{T} \ldots\ldots\ldots\ldots\ldots\ldots\ldots\ldots\ 2.8$$

In practice, T_{ON} varies from µs to ms, and PC will deposit metal at the same rate as DC provided the average pulse current density equals the latter. The average current density (I_A), in pulse plating, is defined as:

$$I_A = peak\ current\ (I_P) \times duty\ cycle(\gamma) \ldots\ldots\ldots\ldots\ldots\ldots\ 2.9$$

In the case of the PRC technique, the average current ($\overline{I_A}$) is as given below.

$$\overline{I_A} = \frac{I_C T_C - I_{AA} T_{AA}}{T_{AA} + T_C} \ldots\ldots\ldots\ldots\ldots\ldots\ldots\ldots\ 2.10$$

Where I_C is the cathodic current density, I_{AA} is the anodic current density, T_C is the cathodic time, T_{AA} is the anodic time. In PRC, the duty cycle (γ') is given as below.

$$\gamma' = \frac{T_C}{T_C + T_{AA}} \ldots\ldots\ldots\ldots\ldots\ldots\ldots\ldots\ldots\ldots\ 2.11$$

2.4.2.1 Pulse current plating

Pulse current plating has long been applied to fabricate smooth and dense pure metal and alloy coatings. Nemes et al. [120] reported that PC plated Zn coatings exhibited smoother surface and increased compactness than DC plating. The enhanced compactness also led to an increase in hardness and corrosion resistance. Similar findings were also reported by Mangolini, Magagnin and Cavallotti [121]. In their research, Mn-Cu coatings prepared by PC plating showed brighter and more homogeneous morphologies compared with coatings deposited with DC plating. Tury, Lakatos-Varsányi and Roy [122] studied the influence of PC parameters towards Ni-Co coating and found that the most protective and compact coating was deposited at low current densities and at high off-time. The mechanism of surface morphology improvement and structure densification can be briefly explained as follows. In electroplating, some cathode areas with higher current density would become more depleted of ions than low-density regions. Thus, a non-uniform and rough surface might be deposited. The application of the PC technique can help alleviate this issue by enabling ions migration from concentrated regions to the depleted regions during T_{OFF}. When pulse T_{ON} reoccurs, more evenly distributed ions are available for deposition. Accordingly, smooth and flat surface morphology can be obtained.

Similarly, it has also been widely reported that composite electrodeposits produced by PC electrodeposition are less porous than those obtained by conventional DC plating. Stroumbouli et al. [123] reported that the application of the PC technique could deposit compact Ni-WC coatings with a high concentration of embedded particles and uniform distribution (**Figure 2.14 a**). However, composite coatings prepared under the same plating condition except using DC condition exhibited a structure full of voids and a "dendrite-like" nickel crystal growth (**Figure 2.14 b**). The formation of pores might be attributed to the simultaneous production of molecular hydrogen on the cathode. The authors suggested that the application of pulse current facilitate the removal of hydrogen during T_{OFF}.

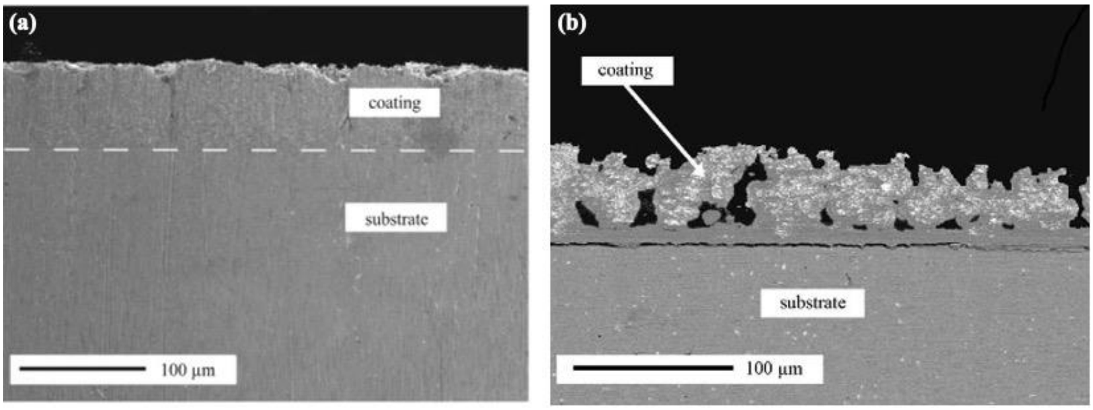

Figure 2.14 Cross-section of Ni-WC composite coating (a): under PC condition frequency f = 0.1 Hz, duty cycle γ =50%, average current density I_A = 7 A/dm^2, (b): comparative study under DC plating [123].

2.4.2.2 Pulse reverse current plating

The phenomenon of coating densification is enhanced by applying the PRC technique. During the anodic time of PRC, protrusions on the coating surface can be selectively dissolved to ensure a uniform deposit. Leisner and his co-workers [124] reported that PRC plated chromium coating showed dense coating structure, refined grains, enhanced hardness and reduced surface crack density than that plated with DC at the same density. Furthermore, by conducting a comparative study, Shao et al. [125] observed that Ni coatings produced by PRC plating exhibited smoother surface, denser structure, higher hardness and better wear resistance than Ni coatings prepared with PC plating.

For composite electroplating, Weston et al. [126] successfully deposited porosity-free Co/IF-WS_2 nanocomposite coatings by PRC technique with the addition of sodium dodecyl sulphate (SDS). Authors proposed a model to understand the particle behaviour and co-deposition mechanism. As shown in **Figure 2.15**, WS_2 particles are negatively charged in the electroplating bath by the adsorption of anionic surfactant SDS on their surfaces. Thus, during the anodic phase, the imposition of a positive pulse attracts the particles electrophoretically towards the working electrode surface, where they might be adsorbed (**Figure 2.15 (1)**). In the meantime, the roughness of the coating surface can be reduced since the positive charge in the anodic phase could dissolve cobalt protrusion formed previously (**Figure 2.15 (2)**). When the PRC shifts to the cathodic phase, the polarity of the current is then rapidly reversed (**Figure 2.15 (3)**). The Co deposition occurs, and therefore, the particles can be incorporated into the metal matrix (**Figure 2.15 (4)**). The continuous behaviours of attraction, dissolution and incorporation during PRC lead to compact and smooth composite coating with desired particle content. However, Authors also pointed out that PRC parameters, especially cathodic time (Tc), should be carefully controlled. Either excessive or insufficient T_C would result in insufficient particle content or increased pores in composite coatings

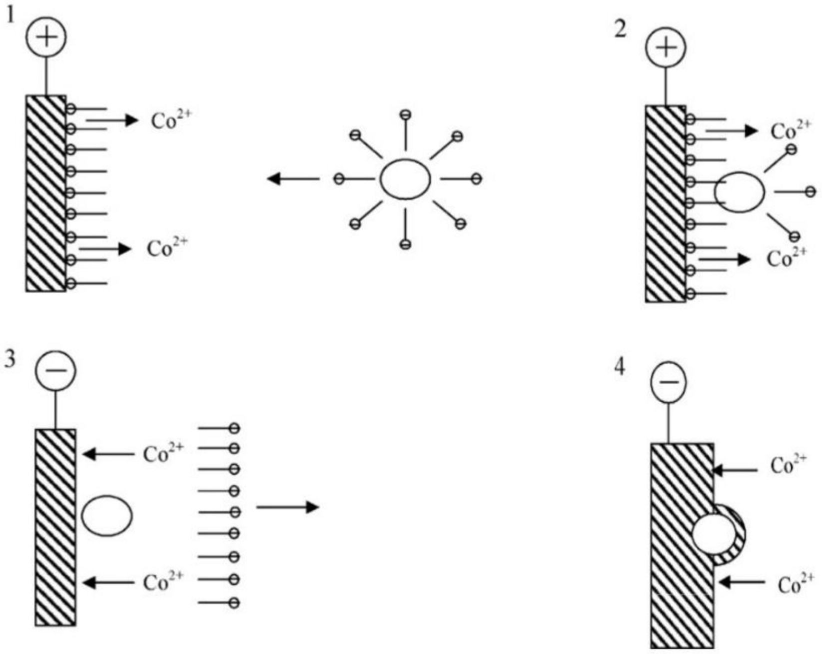

Figure 2.15 Model of particle co-deposition in PRC plating with surfactant SDS [126].

Although PC and PRC have been recognised as effective method to densify coating structures, their applications in practical use might be limited due to the following two factors. The first is the complicated nature of the PC and PRC (three independent variables). Researchers should design and plan ahead with a series of procedures to follow in order to obtain the desired coating qualities. The second is the high cost of a pulse rectifier, which is much greater than a DC power supply. Additionally, highly regulated and sophisticated design makes the capital cost even higher.

2.4.3 Particle dispersion and bath agitation

According to Walsh and his co-workers [25, 81], particle dispersion and bath agitation are significant operational parameters that influence final coating properties. After comparing the effects of different particle dispersion methods on the tribological properties of metal-MoS_2 coatings, Zhou, Wang and Walsh [6], concluded that coatings prepared in electrolytes agitated using ultrasonic or ball milling techniques exhibited a lower coefficient of friction compared to those produced with magnetic stirring. The improved tribological performance is attributed to the more homogeneous particle dispersion achieved through ultrasonic and ball milling agitation, which facilitates the formation of a dense coating structure. Thus, it can be speculated that selecting appropriate particle dispersion methods is crucial for developing smooth and dense composite coatings. Similar to particle dispersion, the aim of bath agitation is to keep particle suspended and transport them to the cathodes for co-deposition. Numerous studies also claimed that different agitation methods might result in changes in coating appearances and properties. In the following subsections, particle dispersion and bath agitation methods that show potential to achieve smooth and dense composite coatings will be discussed.

2.4.3.1 Ultrasonic bath agitation

Ultrasonic vibration is an effective processing method to agitate the solution and generate well-dispersed particles [127]. When ultrasound is applied to a liquid media, the phenomenon termed acoustic cavitation occurs [128]. Similar to many mechanical waves, sound waves that propagate through a liquid result in alternating positive pressure (compression) and negative pressure (rarefaction) cycles, with rates depending on the frequency. During the negative part of the acoustic cycles, high-intensity ultrasonic waves create small vacuum bubbles or voids in the liquid. When the bubbles attain a volume at which no more energy can be absorbed, they will collapse violently during a positive pressure cycle (**Figure 2.16**). At this point, the implosion of cavitating bubbles could produce intense local heating (about 5000 K), high pressure (about 1000 atm), along with enormous heating and cooling rates ($>10^9$ K/sec) and the formation of liquid jet streams (about 400 km/h) [129]. The cavitation induced mechanical events such as micro-jetting and micro-turbulence are the basis for the application of particle dispersion and solution agitation.

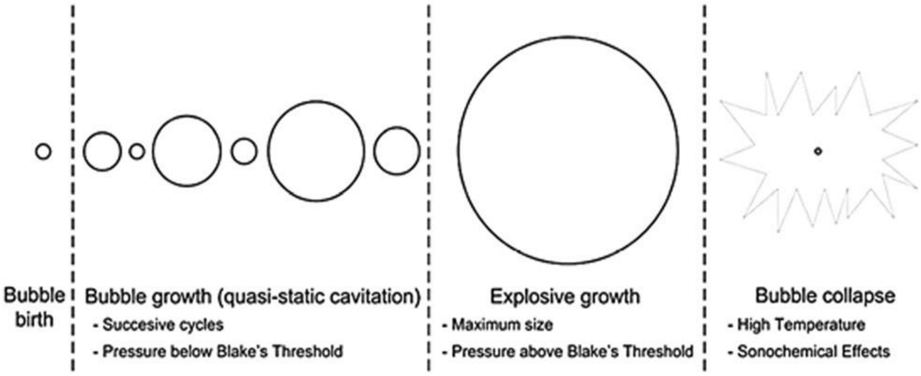

Figure 2.16 Schematic of acoustic cavitation induced by ultrasound [130].

In the field of electroplating, ultrasound has been applied for bath agitation since the 1950s. An early review by Walker and Walker [131] concluded that the use of ultrasound in electroplating of metals or alloys could bring about many benefits, not only in terms of the electrodeposition itself (improvement of current efficiency, enhancement in mass and charge transfer) but also in terms of the final properties of the deposits. It has been widely reported that electrodeposits produced in the presence of ultrasound are less porous than those obtained by conventional bath agitation methods. García-Lecina et al. [132] studied the effect of ultrasonic agitation (24 kHz, 38 W/cm^2) on the microstructure of pure nickel deposits. They found that pure nickel coating prepared with ultrasound assistance exhibited reduced porosity and enhanced hardness. In a research conducted by Barnes and Ward [133], a series of bath agitation methods including (a) solution circulation, (b) mechanical stirring, (c) air bubbling, (d) ultrasonic agitation and (e) ultrasonic agitation + mechanical stirring were studied, and their effects towards the porosity level of final gold coatings were compared. **Table 2.5** gives the results obtained. It is worth noting that the combination of ultrasound and mechanical stirring during gold plating from acid cyanide baths exhibited a dramatic reduction in residual porosity, enabling pore-free gold coating to be deposited.

It is widely believed that the reduction in porosity is achieved by the acoustic cavitation in the electrolyte near the cathode surface. According to Kristof and Pritzker [134], as bubble collapse occurs near the solid surface, a drag force created on the portion of the void nearest the surface will cause the bubble to move toward the surface. This asymmetric force results in an effective microjet oriented toward the surface, which in turn suppresses the out-of-plane growth of the films. Therefore, lateral growth rather than three-dimensional growth on the cathode surface would be promoted, which helps to form coatings with improved smoothness and compactness. Many other researchers also ascribed the reduction of porosity level to the accelerated removal of hydrogen from the cathode surface [135, 136]. During the electroplating, some cathode areas are shielded from the deposition by the generated hydrogen bubbles. With the ultrasound application, the adhered hydrogen bubbles can be removed, promoting a uniform coating deposition. What’s more, Prasad et al. [136] revealed that the reduction in porosity might also be attributed to a fine-grained, densely packed coating structure formed from the electrolytes subjected to ultrasound.

Table 2.5 Porosity density of gold plating under various bath agitation method [133].

Type of agitation	Porosity density (pores per cm^2)
No agitation	15-76
Solution circulation	3-49
Mechanical stirring	3-86
Air bubbling	2-12
Ultrasonic agitation	1-18
Ultrasonic agitation + mechanical stirring	1-8

Ultrasound has also been widely applied in composite electroplating. A review article concluded that the implementation of ultrasound could promote particle dispersion in the electroplating bath and densify the final coating structures [137]. As mentioned in the previous section, the co-deposition of particles with conductive and semi-conductive nature such as WS_2 and MoS_2 would disturb the electric field on the cathode, making metal ions preferentially deposit on the particle surface. Consequently, composite coatings with a rough surface and porous structure would be formed. A few researchers attempted to overcome this issue by applying ultrasonic agitation during the plating process. A recent study conducted by Cheng et al. [7] reported that Ni-MoS_2 coating prepared by ultrasonic agitation exhibited low surface roughness with few pores and defects. However, Ni-MoS_2 coating deposited under the same plating condition except using conventional magnetic stirring as bath agitation method demonstrated continuous dendritic gap and loose structure (**Figure 2.17**). A similar ultrasonic agitation effect was observed when co-depositing inorganic fullerene-like WS_2 (IF-WS_2) nanoparticles in the nickel matrix [57]. By applying ultrasound, Ni/IF-WS_2 coating showed a more uniform and compact structure than those prepared in the silent plating bath.

Researchers of both studies (Ni-MoS_2 and Ni/IF-WS_2) attributed the porous structure and dendritic growth pattern to the insufficient agitation level of magnetic stirring. The hydrodynamic flow generated by magnetic stirring is not strong enough to avoid re-agglomeration of previously dispersed particles during electroplating. Accordingly, the agglomerated MoS_2 or WS_2 particles adsorbed on the cathode surface would exacerbate the non-uniform distribution of current, preventing the uniform reduction of nickel ions across the cathode surface, finally forming many pores and defects. On the contrary, when ultrasound is applied to the plating bath, the phenomenon of acoustic cavitation could generate high-energy liquid jet streams due to the violent collapse of bubbles. This high-energy liquid jet stream could suppress the particle agglomeration and keep the suspended particles in a small volume. Small-sized MoS_2 or WS_2 particles, corresponding to a lower degree of current disturbance, offer nickel ions an opportunity to deposit uniformly and efficiently. The uniform nickel deposition promotes the formation of uniform and compact coating structures. Moreover, the high-energy liquid jet stream could scatter the mutual absorbed particles, reducing the continuous deposition of particles and optimizing the particle dispersion in final composite coatings. Therefore, the co-deposition of MoS_2 or WS_2 particles with ultrasound assistance acquires a compact structure with well-dispersed particles in the metal matrix.

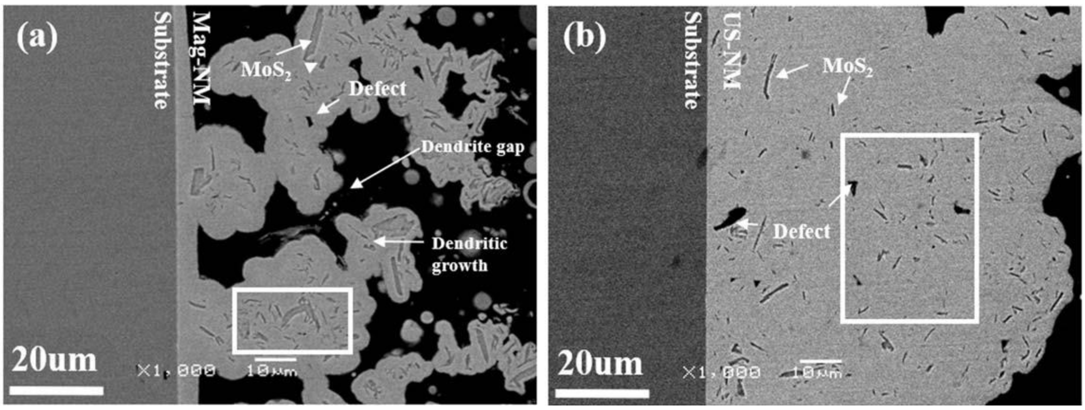

Figure 2.17 Cross-sectional image of Ni-MoS_2 coatings via (a) magnetic stirring of 120 rpm and (b) ultrasonic agitation of 40 KHz, 60 W/cm^2 [7].

2.4.3.2 High shear mixing

As shown in **Figure 2.12**, particle agglomeration is one of the origins of porous and fragile coating structures. In addition to the ultrasonic agitation mentioned above, High shear mixing has also been recognised as an advanced mechanical agitation method that shows promising potential to aid particle dispersion. This technique is traditionally applied to homogeneously disperse second phase particles into metal or polymer matrix [138-140]. A recent study carried out by Pullicino et al. [141] stated that mixing speed and time are two important parameters of high shear mixing. They also found that a high mixing speed (3000 rpm) combined with a long mixing time (2 h) could reduce the size of agglomerates by 30 % compared to that of 1000 rpm and 1 h mixing time. **Figure 2.18** below illustrates the equipment set-up and working principle of the high shear mixer. During operation, the vortex generated by the rotation of the blade can draw large agglomerates into the mixing head. In the meantime, due to the large velocity difference, an extremely high shear zone is formed at a close-clearance gap between the high-speed rotor blade and stator, thereby breaking down large agglomerates at the exit holes of the stator.

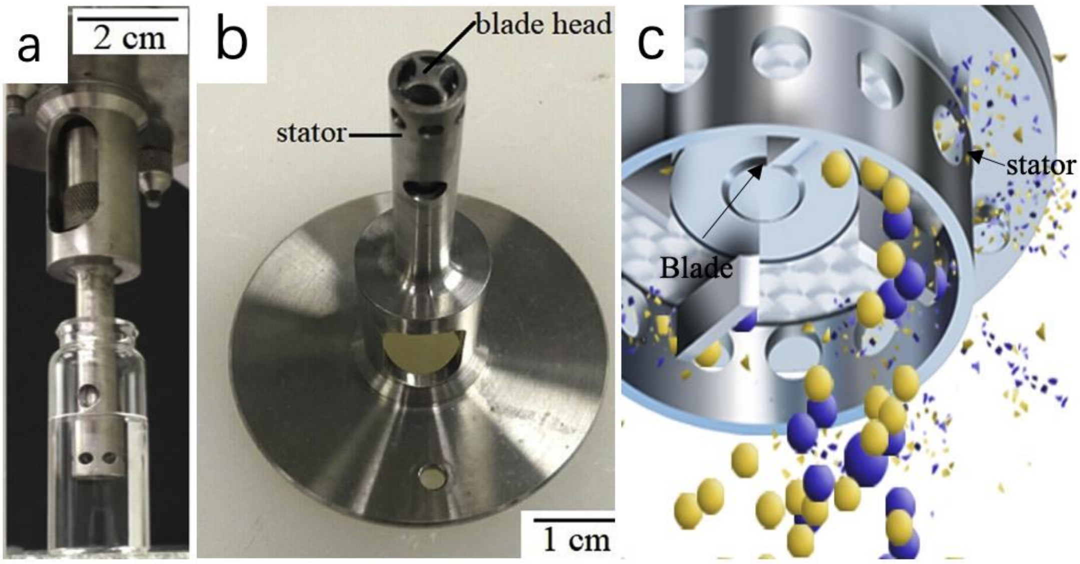

Figure 2.18 (a) high shear mixing set-up, (b) details of high shear mixer work head and (c) particle breakdown at the work head [6].

Although the high shear mixing shows great potential to achieve a homogeneous particle suspension plating bath, only one research has applied it to composite coating fabrication. Zhou, Wang and Walsh [6] compared the effects of high shear mixing and magnetic stirring as particle dispersion method towards Ni-MoS_2 coating. Cross-sectional SEM images reveal that Ni-MoS_2 composite coating using particle dispersion via magnetic stirring shows extensive porosities throughout the coating structure, with some cavities of over 50 μm (**Figure 2.19 a**). On the contrary, Ni-MoS_2 composite coating using particle dispersion via high-shear mixing exhibits a compact coating structure **Figure 2.19 (b)**. Non-lubricated roller-on-plate tests have been conducted to evaluate the tribological performance of Ni-MoS_2 coatings prepared via different particle dispersion methods. Results show that Ni-MoS_2 coating prepared with high-shear mixing exhibited lower friction coefficient and better wear resistance (CoF = 0.08, wear track depth = 12 μm) than those of Ni-MoS_2 coating prepared with magnetic stirring (CoF = 0.16, wear track depth = 80 μm). Authors attribute the enhanced self-lubrication and wear resistance to a compact and uniform coating structure which provides firm support for the MoS_2 particles to allow an effective shear to take place. Moreover, the smooth surface of Ni-MoS_2 coating prepared via high shear mixing can promote complete tribofilm formation during sliding contact motion, which reduces direct contact between the coating and bearing steel, hence the reduction in friction and wear depth.

In recent years, the use of high shear mixing to achieve uniform particle dispersion has extended beyond laboratory-scale applications. The scaling up of high shear mixing processes has proven effective across various industries. Successful examples include the preparation of battery electrode slurries for energy storage applications, the creation of stable emulsions in lotions in the pharmaceutical industry, and the dispersion of pigments in the paint sector. However, the commercialisation of scaled-up high shear mixers still faces two major challenges: (1) high energy consumption and (2) rapid degradation of the mixing components.

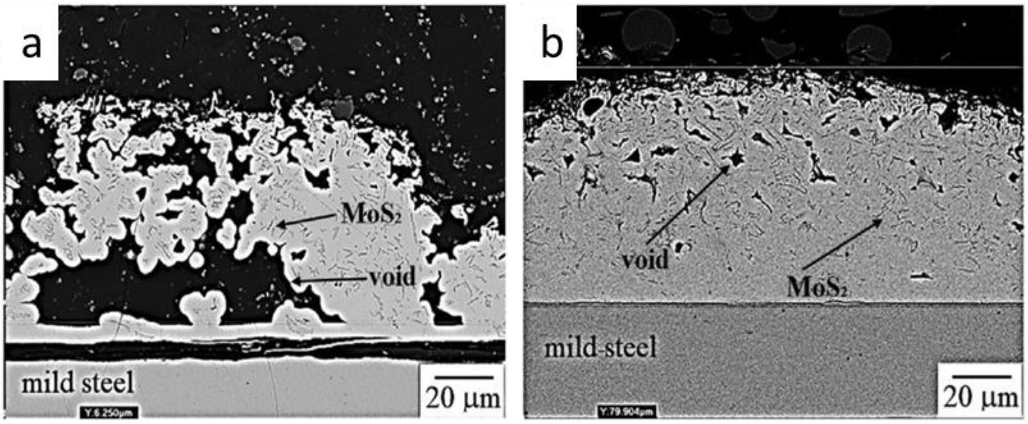

Figure 2.19 Cross-sectional images of (a) Ni-MoS2 coating from a bath in which particle dispersion is achieved by magnetic stirring, (b) Ni-MoS2 coating via particle dispersion from high shear mixing [6].

2.4.3.3 Ball milling treatment

It is well known that the top layer of metals or alloys could be refined by means of surface mechanical attrition treatments such as shot peening [142], grinding [143] or milling[144]. Whether the same effect could be brought to electroplating by mechanical attrition has attracted attention from both academia and industry. In 1972, Eisner and his co-workers [145] first combined mechanical attrition with conventional electroplating to achieve ultra-high-speed metal plating. In their research, two different methods of introducing mechanical attrition have been proposed. The first method was driving a plate to rub against the cathode during electroplating. However, this could lead to excessive work hardening and made the final coating brittle. The second method introduced mechanical attrition by ball milling in a vibrating tub. The result showed that a dense Ni coating could be obtained even at a high deposition rate of 25 μm per minute. Therefore, ball milling is deemed as an appropriate mechanical attrition technique that has been further applied in later studies.

A number of pure metal/ alloy coatings (e.g. Ni, Cu, Cr, Ni-P) and composite coatings (e.g. Ni-P-SiC, Ni-P-multiwalled carbon nanotubes) have been successfully deposited with the assistance of ball milling [146-155]. Although the core of this technique remains the same, which is using mechanical disturbance to make ceramic or glass balls abrade on the sample surface, the equipment setup varied for each study. **Figure 2.20** summarises the types of equipment setup utilized in ball milling assisted electroplating techniques from the literature. For the single-sided plating or small samples plating, horizontal and vertical vibration-induced ball milling is commonly used (**Figure 2.20 a**). In this setup, the plating bath is placed on the top of a vibrator which provides a sinusoidal vibration in either horizontal or vertical direction. When the plating bath is vibrated, glass/ceramic balls can roll horizontally or bump vertically on the sample surface, providing mechanical attrition to the coatings simultaneously during the plating process. Vibrating amplitude and frequency are two main parameters determining the properties of final coatings [146, 148]. However, drawbacks of this setup include fluctuation in thickness, difficult to scale-up and non-uniform coating quality [152]. On the other hand, stirring induced ball milling (**Figure 2.20 b**) and rolling drum induced ball milling (**Figure 2.20 c**) can perform double-sided plating and thick sample plating. However, these two settings are limited to electroless plating [155]. For the cylinder-shaped sample, rotating cylinder electrode induced ball milling (**Figure 2.20 d**) is employed to refine coating surface.

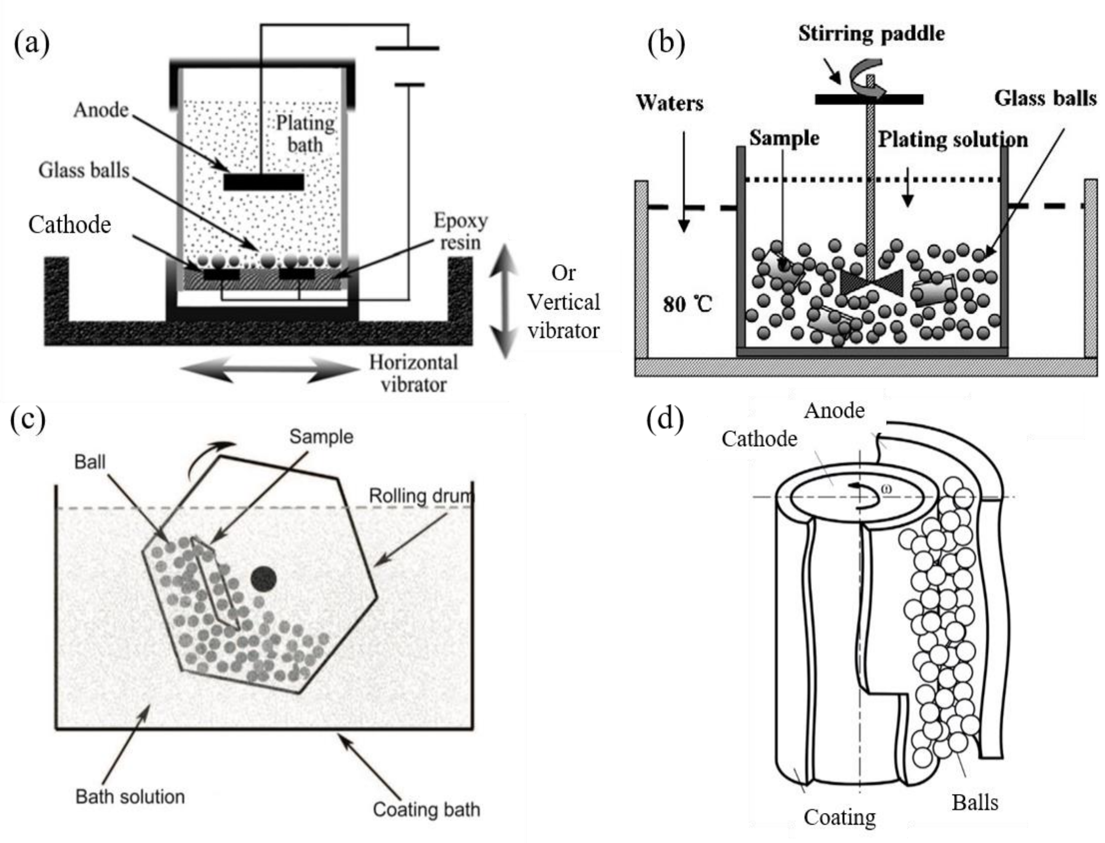

Figure 2.20 Ball milling assisted electroplating setup (a) Milling induced by a horizontal or vertical vibrator, (b) Milling induced by solution stirring, (c) Milling induced by a rolling drum, (d) Milling induced by rotating cylinder cathode [147, 149, 152, 155].

In the last two decades, many research groups have studied the effect that ball milling during the electro- or electroless- plating process may have on the characteristics of the resulting coatings. **Table 2.6** below summarises some findings from numerous studies. Ni and its alloys are the main metal materials used for investigation. Compared with conventional electroplating, ball milling assisted Ni, Ni-P, and Cu coatings exhibited less porosity and more compact structures even at much higher current density (above limiting current) [146-148, 151-153]. As a result of coating densification, properties such as hardness, tensile strength, and corrosion resistance enhanced to a large extent. In addition, Zhu et al. [149] also claimed that with ball milling, the residual stress in electrodeposited hard chromium evolved from tensile to compressive (between 1000 to 1600 MPa), which would be beneficial to resist crack formation and increase microhardness. To get a better understanding of the ball milling mechanism in electroplating, authors proposed two models of electrocrystallisation. In the following paragraph, descriptions of these two models will be presented.

Table 2.6 Coatings prepared with the assistance of ball milling

Coating type	Substrate	Deposition technique	Ball milling parameters	Effect of ball milling on final coatings	Ref
Pure Ni	Carbon steel	Direct current plating	- Ball milling induced by a horizontal vibrator; - Glass ball (d = 1, 5, 7 mm); - Vibration frequency from 3.0 to 5.0 Hz;	- Ni coating deposited under the ball milling has a smooth surface, refined grains and pore-free structure. - Ball milling allowed high deposition rate even at high current density (above limiting current). - Compared with the process without ball milling, Ni coating deposited with ball milling exhibits a higher hardness value and better corrosion resistance	[146]
Pure Ni	Carbon steel	Direct current plating	- Ball milling induced by a horizontal vibrator; - Glass ball (d = 1 and 5 mm); - Vibration frequency from 0 to 6.0 Hz;	- With ball milling, the coating became smooth and pore-free. - Electrodeposited Ni grains were refined by ball milling, leading to improvement in the hardness, tensile strength and corrosion resistance. -Increasing vibration frequency resulted in higher hardness and corrosion resistance due to grain refinement, compressive stress, and coating structure densification.	[147]
Pure Cu	Carbon steel	Direct current plating	- Ball milling induced by a vertical vibrator; - Glass ball (d = 1, 3, 5, 7 mm);	- Ball milling led to a compact and pore-free Cu coating. - With high current density (40 and 50 A/dm^2), ball milling changes the Cu coatings from a loose, dendritic	[148]

Coating type	Substrate	Deposition technique	Ball milling parameters	Effect of ball milling on final coatings	Ref
			- Vibration frequency from 3.0 to 5.0 Hz;	structure with many gaps to a compact structure with a lower level of porosity.	
Hard Cr	A cylindrical 300M steel	Pulse current plating	- Rotating cylinder cathode; - Ceramic ball (d = 1mm); - Rotation speed from 140 to 320 rpm	- With ball milling, a crack-free coating was achieved, with a smooth and mirror-like surface. - Ball milling led to lower current efficiency (14-17%) compared with no ball milling process (18-20%) - Ball milling resulted in compressive residual stress of 1446 MPa in the circumferential direction and 1343 MPa in the axial direction. -Hardness value decreased with increasing level of ball milling (higher rotation speed).	[149]
Ni-P	Magnesium alloy	Electroless plating	- Ball milling induced by a continuous stirring solution; - Alumina ball (d = 1-1.5 mm);	- Ball milling resulted in Ni-P coating with smooth morphology, compact structure, and pore-free surface. - The phase of the deposited Ni-P transformed from amorphous to crystallized with the assistance of ball milling. -Ball milling could form an alloy layer at the interface between coating and substrate. - Ball milling improved adhesion, hardness and corrosion resistance of Ni-P coating.	[150]

Coating type	Substrate	Deposition technique	Ball milling parameters	Effect of ball milling on final coatings	Ref
				- Ball milling avoided surface cracking as a result of the heat treatment of Ni-P deposits.	
Ni-P	Carbon steel	Direct current plating	- Ball milling induced by a horizontal vibrator; - Glass ball, diameters (*d*) of 1, 5 and 7 mm (many balls of *d* = 1 mm with a total weight of 12 g, ten balls of *d* = 5 mm and five balls of *d* = 7 mm). - Vibration frequency of 4.5 Hz	- Ni-P coatings assisted by ball milling were smoother in surface, thinner in thickness, harder in hardness, more positive in corrosion potential, and greater in polarisation resistance compared with the Ni-P coatings deposited without ball milling. - Ball milling mad the Ni-P deposits crystallized in-situ during the plating process, thereby avoiding crystallization-induced cracking after heat treatment. - Ball milling made the fast electrodeposition of Ni-P at high current density.	[151]
Ni-P	Magnesium alloy	Electroless plating	- Ball milling carried out in a rolling drum; - Ceramic balls but size not given;	- Ni-P coating deposited by ball milling had a crystallized Ni-P solid solution structure. - Compared with conventional electroless plating, Ni-P coating prepared with ball milling had finer grains, better corrosion resistance and higher hardness. - Costing thickness was reduced by ball milling. - After heat treatment, cracks appeared seriously in the conventional electroless plated Ni-P coating after same heat treatment could be eliminated by ball milling.	[152]

Coating type	Substrate	Deposition technique	Ball milling parameters	Effect of ball milling on final coatings	Ref
Ni-P	Magnesium alloy	Direct current plating	- Ball milling induced by a horizontal vibrator; - Glass ball (*d* = 1, 5 mm) - Vibration frequency of 3 Hz	- With ball milling, gaps and pores sharply reduced in size and number, and no cavities can be found. - The interface between coating and substrate evolved from clear to ambiguous with the assistance of ball milling, indicating a better adhesion - Mechanical attrition helped to remove oxides and hydroxides film on the substrate and expose the fresh substrate, eliminating the need for traditional pretreatment.	[153]
Ni-P-SiC	Carbon steel	Direct current plating	- Ball milling induced by a horizontal vibrator; -Glass ball (d = 1, 5, 7 mm); -vibration frequency of 4.5 Hz;	- Ni-P-SiC coating with ball milling exhibited higher particle content than conventional coating. - Under the assistance of ball milling, the adhesion between coating and substrate improved. - During heat treatment, cracks and defects produced in conventional coatings can be avoided by ball milling. - Ball milling combined with heat treatment improved both hardness and corrosion resistance to a large extent.	[154]
Ni-P-multiwalled carbon nanotubes	Carbon steel	Electroless plating	- Ball milling induced by a stirring bath; - Glass ball (d = 2 mm);	- Ball milling significantly promoted particle incorporation in Ni-P matrix. - Composite coating assisted by ball milling showed rougher surface than conventional coating.	[155]

Coating type	Substrate	Deposition technique	Ball milling parameters	Effect of ball milling on final coatings	Ref
			- Glass ball quantity in bath solution = 1600 g/L; - Before plating, multiwalled carbon nanotubes were treated by ball milling for particle dispersion;	- After heat treatment, Ni-P- multiwalled carbon nanotubes coating assisted by ball milling became porous, and the embedded CNTs turned blurred, which is likely caused by the oxidation of CNTs. - The hardness of ball milling assisted composite coating was only 12 % of that in the conventional coating after heat treatment. - Ball milling assisted composite coating showed a better anti-friction property (CoF = 0.15) than conventional coating (CoF = 0.66).	

The formation of the smooth and compact metal coating prepared by ball milling can be explained by the fundamentals of electroplating. The metal electroplating can be divided into four important steps, namely mass transport, interface reaction, nucleation and grain growth. Ning and He [148] developed a model to analyze the effect of ball milling based on the above steps. **Figure 2.21** schematically compares the structure of metal coating deposited under conventional conditions with that prepared under ball milling assistance. It can be noticed that the conventional electrodeposited metal develops a fine grain layer (or the grain nucleation zone) at the initial stage (**Figure 2.21 a**). However, as plating goes on, a large grain layer (or the grain growth zone) is formed, resulting in a rough and uneven coating surface (**Figure 2.21 b**). This phenomenon can be explained by the formation of a concentration gradient of metal ions in the boundary layer. Prior to electroplating, the solution composition in the bath solution is homogeneous, which means the metal ions concentration in the boundary layer is the same as that in the bulk solution. As a potential is applied to the plating system, a current is distributed homogeneously across the cathode surface, and metal ions are immediately reduced and nucleated to form a fine-grained coating zone. In the meantime, a concentration gradient of metal ions is established in the boundary layer due to the depletion of metal ions. As plating goes on, the metal grains proceed to grow. Since the shape and size of grains are irregular, the current distribution on the cathode surface is no longer uniform. Current density tends to be higher on larger grains, resulting in preferential grain growth of big grains and porous and rough coating surface [156].

On the other hand, as ball milling is applied to the electroplating process, the concentration gradient of metal ions in boundary layers is disturbed due to the rolling or bumping motion of glass balls. Therefore, the current distribution on the cathode surface keeps uniform, and the nucleation of grains processes at a high rate. Consequently, the condition for grains to grow speedup is hindered, resulting in a fine microstructure of the coating. Besides, the deposited metal can be further peened or cold-worked by the moving glass balls. Mechanically ball-rolling might in-situ mechanically polish the surface during the electroplating process. Any protruding summits were worn out by the mechanically ball-rolling, thereby yielding a dense and compact coating structure (**Figure 2.21 c and d**).

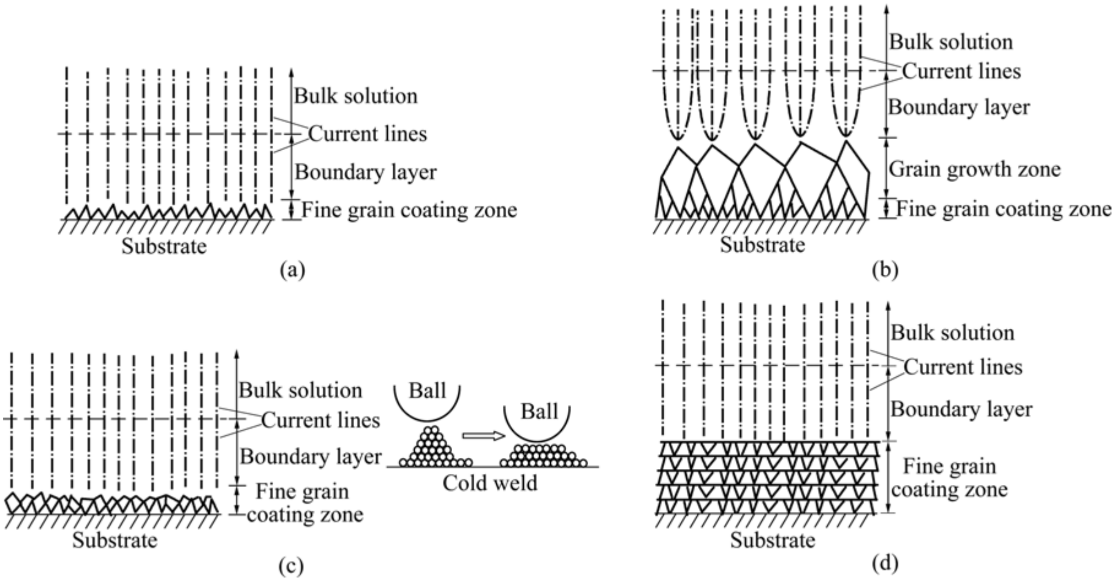

Figure 2.21 Model on the formation of electrodeposits: (a) Initial stage of conventional electroplating, (b) Grain growth stage of conventional electroplating, (c) Initial stage of ball milling assisted electroplating, (d) Grain growth stage of ball milling assisted el [148].

Zhu et al. [149] proposed another model which involves hydrogen disentanglement from lattice to explain the effects of ball milling on the complete elimination of cracks for hard chromium coating. It is widely believed that the electroplating of chromium is always accompanied by hydrogen evolution because the standard electrode potential of the hydrogen is more positive than chromium [157-160]. As the hydrogen atoms co-deposited with chromium are entangled in the crystal lattice, the residual tensile stress will rise considerably. As a result, the chromium deposit contains a network of cracks throughout the entire deposit, owing to a high residual tensile stress (**Figure 2.22 a-c**).

On the contrary, during electroplating with ball milling, the ceramic balls can mechanically polish the growing chromium deposits. As shown in **Figure 2.22 d**, the ceramic balls polish the electrodeposited chromium and apply pressure to the lattice. When the balls roll over the region containing entangled hydrogen, the hydrogen atoms escape as hydrogen gas, and their positions could be occupied by chromium atoms under the squeezing and pressing of the beads (**Figure 2.22 e and f**). Therefore, the cracks induced by hydrogen entanglement disappear completely, and a smooth and compact chromium coating is obtained.

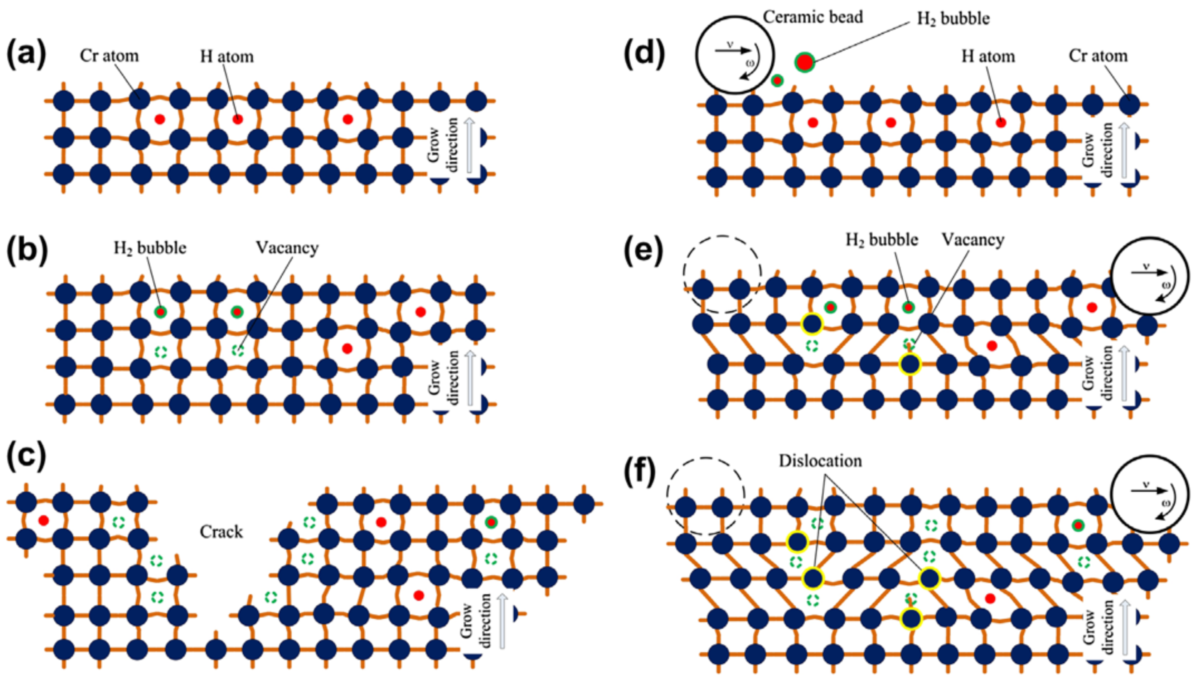

Figure 2.22 Model of electrocrystallisation process of cracked chromium under conventional electroplating (a-c) and crack-free chromium electrodeposited with the assistance of ball milling [149].

Besides the electroplating of pure metals, ball milling has also proven to be beneficial in Ni-P alloy plating and composite plating. The research group at the University of Science and Technology Beijing carried out a series of studies of Ni-P alloy coatings and Ni-P-particles composite coatings under ball milling assistance [150-152, 154, 155]. They reported that ball milling assisted Ni-P coating exhibited a smoother surface (with “cauliflower-like” cluster size below 200 nm) than conventional Ni-P coating (cluster size of 5-20 μm). Additionally, small pores could be observed in the conventional Ni-P coating under high magnification, whereas no pores were formed on the surface of Ni-P coating prepared with the assistance of ball milling (**Figure 2.23 a and b**). As is known, heat treatment is a common method to increase the hardness of Ni-P deposits by the forming Ni_3P phase for precipitation strengthening [161-164]. However, after heat treatment at 400 ℃ for 1 h, cracks were observed on the conventional Ni-P coating (**Figure 2.23 c**). On the other hand, Ni-P coating prepared with ball milling assistance remained unchanged after heat treatment (**Figure 2.23 d**). This beneficial effect of ball milling can be attributed to the phase transformation of Ni-P deposits and be verified by the XRD pattern shown in **Figure 2.23 (e)**. During heat treatment, the amorphous phase in conventional Ni-P coating could be transformed into crystallized Ni and Ni_3P phases. Since the crystallized phase has a higher density than the amorphous phase, a tensile stress field might be generated due to the volume shrinkage and the mechanical constraint of the substrate. As a consequence, cracks are formed in the Ni-P coatings during heat treatment. In contrast, Ni-P coating prepared with ball milling has already exhibited a crystalline phase of Ni. Therefore, the heat treatment has a little effect on its surface morphology. Furthermore, the E_{corr} of ball milling assisted Ni-P coating is higher than that of conventional Ni-P coating (**Figure 2.23 f**), indicating that ball milling enhances the corrosion resistance. This enhancement can be explained by the compact and crack-free coating structure, which avoids corrosive liquid from reaching the substrate.

Although ball milling has been proven as an effective method to refine coating surface and enhance coating property, very few studies have applied ball milling into composite electroplating. The researches available in the literature are electroplated Ni-P-SiC coating and electroless plated Ni-P-multiwalled carbon nanotubes coating [154, 155]. Both studies reveal that ball milling could promote particle incorporation. However, surface morphology for each coating varies a lot. For Ni-P-SiC coating, ball milling improved coating/substrate adhesion and reduced the number of pores and cracks. Conversely, ball milling led to a rougher surface compared with conventional electroless plating. The different surface morphologies might be explained by different plating techniques applied and different properties of embedded particles (e.g. conductivity).

In summary, ball milling in electroplating or electroless plating can bring numerous benefits to the final coatings. However, there are still some aspects of ball milling, which requires further exploration. Firstly, the parameters such as glass ball diameters and filling volume in the electrolyte, vibrating frequency, etc., should also be optimized to improve the coating performance further. Secondly, comprehensive modelling of ball milling should be developed to quantify the effects. Lastly, whether this method can be applied to densify self-lubricating composite coating such as Ni-MoS_2 or Ni-WS_2 is worthwhile to be investigated.

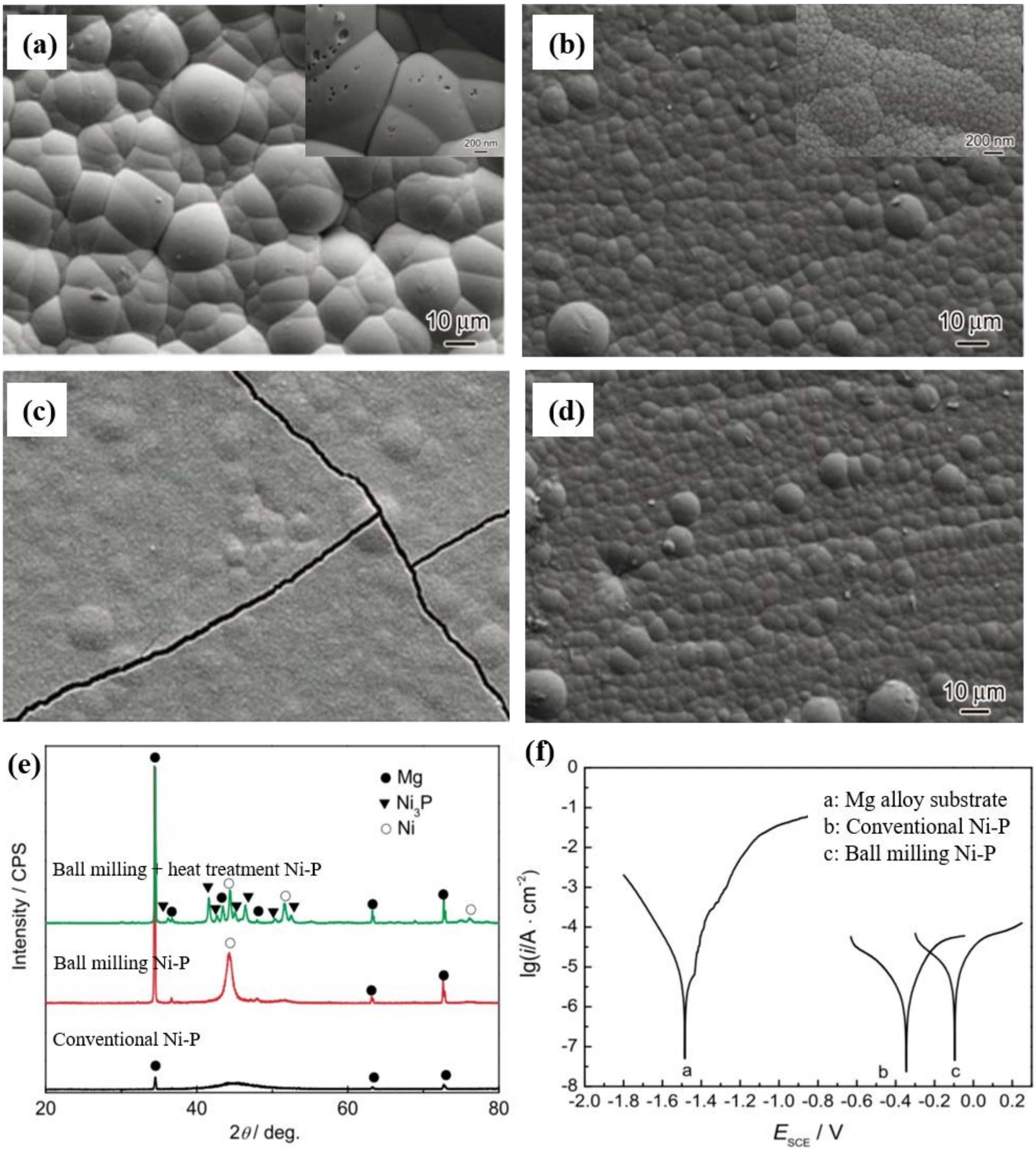

Figure 2.23 SEM images of surface morphology (a) conventional Ni-P coating, (b) Ni-P coating prepared with the assistance of ball milling, (c) conventional Ni-P coating after heat treatment, (d) Ni-P coating with ball milling after heat treatment; (e) XRD pattern and (d) polarization curves [152]

2.4.4 Additives and surfactant

As mentioned, particle agglomeration may easily occur in the electrolyte bath due to high surface free energy. The high ionic strength of electrolyte could further aggravate the agglomeration phenomenon. As a consequence, the final composite coating would exhibit inhomogeneous composition and rough surface, which results in poor mechanical properties. Until now, there are two major ways attempting to alleviate the above problem. The first is the physical method which includes particle dispersion and bath agitation discussed in Section 2.4.3. The second is adding additives or surfactants into a bath solution which can be classified as a chemical method. In this section, the second method of using surfactants of additives will be reviewed. But before that, it is necessary to give a brief introduction of surfactants.

Surfactants (also known as surface-active agents) are amphipathic molecules that consist of a polar or ionic hydrophilic head and a non-polar hydrophobic tail. In the bath solution containing suspended particles, the hydrophobic tail preferentially adsorbs on the particles, whereas the hydrophilic head sticks out towards the bulk solution. Such an arrangement of surfactant adsorption reduces the surface energy of particles, thereby avoiding particle agglomeration. Furthermore, based on the nature of the hydrophilic part, surfactants can be classified into non-ionic, cationic and anionic types. In the latter two types, either positive or negative charge can be imparted to the particle, which will induce electrostatic repulsion between particles and further promote particle dispersion. From literature, cationic and anionic surfactants have been most frequently used in the plating solution. However, a few studies also claimed that a combination of cationic and anionic surfactant is beneficial to develop high-quality composite coatings with smooth surface morphologies and dense structures. In the following sub-sections, different surfactant usage will be reviewed based on their categories.

2.4.4.1 Cationic surfactant

Cationic surfactants have been extensively used to assist particle dispersion in both electro- and electroless plating solution. By far, the most frequently added surfactants include cetyltrimethylammonium bromide (CTAB) [165-172], Benzyl ammonium salts (BAS) [173], and Hexadecylpyridinium bromide (HPB) [174, 175]. In composite electroplating, the dispersion particles can be influenced by the particle surface charge. The adsorption of cationic surfactants can shift the surface charge to more positive values. As shown in **Figure 2.24 (a)**, in a composite electroplating bath, particles are surrounded by a layer of liquid (fixed layer), and the boundary of this layer is the slipping plane. The potential difference between the slipping plane and the bulk solution called zeta potential (ζ) is measured to quantify the change of surface charge induced by surfactants. Particle dispersibility can be evaluated by the magnitude of zeta potential. In general, particles with an absolute value of the zeta potential below 8 mV are unstable and prone to agglomerate. In contrast, particles with an absolute value higher than 30 mV are well-dispersed [176]. Figure **2.24 (b)** illustrates the particle co-deposition process with the assistance of cationic surfactant. When the cationic surfactant is adsorbed on the particle surface, zeta potential will shift to a more positive value due to the formation of a positive charge around the individual particles (**Figure 2.24 c**). This shift of zeta potential value can produce a stable dispersion via electrostatic repulsion and promote the migration of particle towards cathode under an electric field.

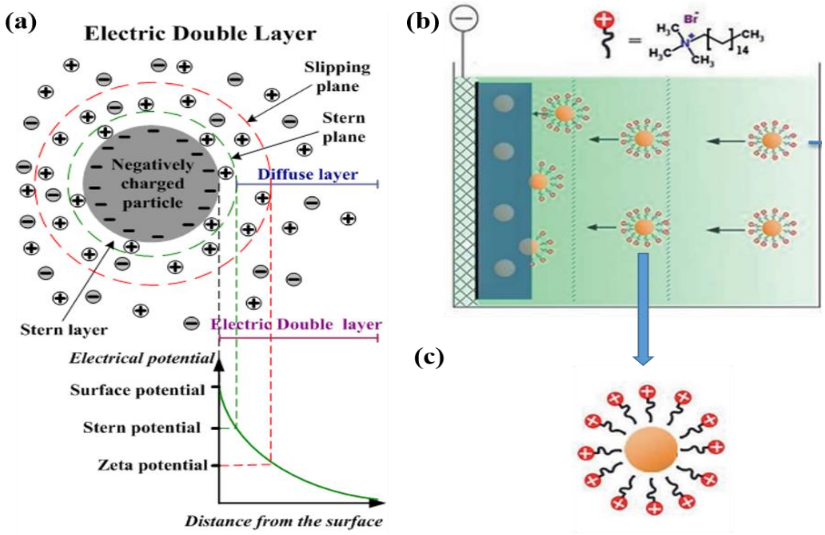

Figure 2.24 (a) Surface charge condition of suspended particles in the plating bath solution, (b) schematic illustration of particle co-deposition with the assistance of cationic surfactant, and (c) cationic surfactant adsorption on particle surface [177, 178]

In the last two decades, the effect of cationic surfactant has been investigated by many studies (**Table 2.7**). Nickel is the main metal matrix used, and the most commonly employed particles include SiC, TiO_2, Al_2O_3 etc.

It is widely believed that the addition of cationic surfactant promotes particle dispersion, avoids particle agglomeration and enhances particle co-deposition rate. The co-deposition behaviour of 250 nm SiC particles into the Ni matrix with the assistance of CTAB has been investigated by Ger [165]. In Ger's study, CTAB addition (0.028-0.084 mol/L) decreased particle size distribution from 1600-2300 nm (without surfactant) to 100-300 nm and increased SiC co-deposition content up to 11.5 vol%. Similar findings have also been reported by Kilic et al. [167] and Guo et al. [168]. As shown in **Figure 2.25**, both Zeta potential and embedded content exhibited a similar increasing trend with the addition of CTAB (**Figure 2.25 a and b**). Cross-sectional images also revealed that CTAB could increase the content of homogeneously distributed SiC in the Ni matrix (**Figure 2.25 c and d**) [167].

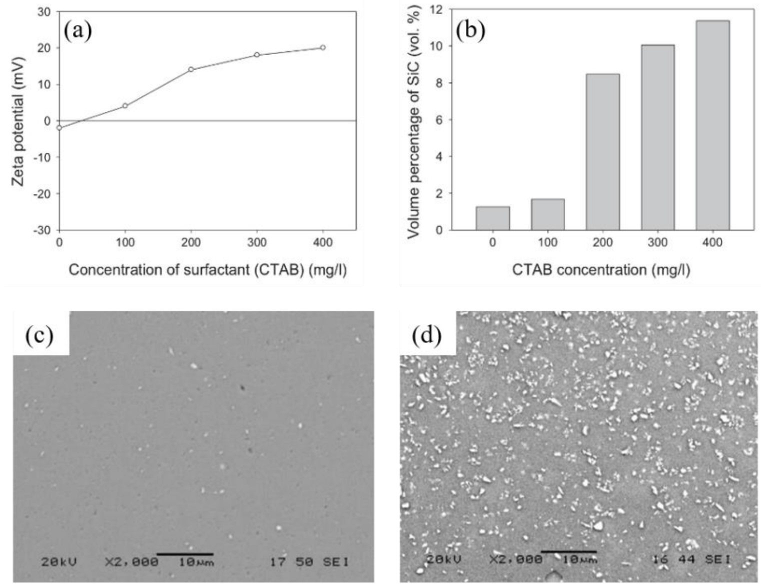

Figure 2.25 Effect of CTAB concentration on (a) particle zeta potential in plating solution and (b) particle content in final coatings; Cross-sectional images of Ni-SiC coatings deposited prepared with CTAB concentration of (c) 0 mg/L and (d) 400 mg/L [167]

In contrast to the above, cationic surfactant addition in plating solution has also been found to decrease the particle co-deposition in the metal matrix. The research carried out by Mohajeri, Dolati and Rezagholibeiki [169] found that particle content in electrodeposited Ni-WC coating decreased from 4.2 vol% to 0.05 vol% with the addition of CTAB (0.001 to 0.01 g/L). The contradictory finding was attributed to the low amount of surfactant used, which cannot supply enough surface charge on the particle surface for electrostatic repulsion. This was further confirmed by zeta potentials measured in the range of -10 to 10 mV. As stated previously, particles are unstable and tend to form large agglomerates when the absolute value of zeta potential is lower than 8 mV. According to the trajectory model proposed by Fransaer, Celis and Roos [41], the co-deposition of large agglomerates (size >1 μm) are difficult since the removal force (hydrodynamic forces and shear flow) in the agitated plating bath is greater than the adhesion force between particles and cathode. Therefore, a sufficient concentration of cationic surfactant is necessary to achieve homogeneous particle dispersion and a high particle co-deposition rate. However, excessive cationic surfactant addition may inhibit particle incorporation. Ning et al. [172] investigated the effect of CTAB on the Cu-TiO_2 coating prepared with a jet electroplating technique. In their research, the maximum TiO_2 content in the composite was 11.45 wt% at an optimum concentration of 0.03 g/L CTAB. Further increase in CTAB concentration slightly decreased TiO_2 co-deposition rate. This phenomenon could be explained as follows. When the CTAB concentration exceeds the optimum value, partial of them could be adsorbed on the cathode surface. This adsorption would create a large repulsive force between particles and cathode, thereby reducing the deposition rate of TiO_2.

From the above review, it can be concluded that the addition of cationic surfactant promotes particle dispersion, avoids particle agglomeration by forming a layer of positive charge around suspended particles in the plating solution. The particle content would be increased due to the enhanced electrophoretic migration under the electric field. However, the concentration of cationic surfactant should be carefully controlled. Too high or too low concentration will lead to either decrease in particle content or severe particle agglomeration.

Besides particle dispersion and particle co-deposition rate, cationic surfactant addition can also influence mechanical properties, tribological performance, and electrochemical properties of final composite coatings. Ger [165] observed that the microhardness of electrodeposited Ni-SiC coating increased from 375 Hv at 0.5 g/L CTAB to 550 Hv at 1.5 g/L CTAB. Similar hardness enhancement was also observed by Hou et al. [166] and Kilic et al. [167]. In general, increased hardness can be explained in three aspects. Firstly, the hardness of electrodeposited Ni-SiC coating is highly correlated to the content of embedded particles since SiC belongs to hard ceramic particles. By increasing CTAB concentration, composite coating with higher SiC content could be realized. Secondly, the increased amount of co-deposited SiC in the Ni matrix can restrain the growth of the Ni grains and reduce the distance between particles within the metal matrix, leading to grain refinement and dispersion hardening of final coatings. Lastly, the enhanced hardness might be a result of the hardened metal matrix. According to a parallel study conducted by Hou et al. [166], the addition of CTAB in Ni sulfamate bath significantly increased the hardness of pure nickel deposit. The mechanism for this hardening effect is not yet understood.

Opposite to the above research findings, Guo et al. [168] reported that CTAB addition could deteriorate both mechanical and electrochemical properties of Ni-CNTs coating. The microhardness value of Ni-CNTs coating prepared with 0.6 g/L CTAB was 40 Hv, which was much lower than Ni-CNTs coating without surfactant (160 Hv). The decrease in microhardness could be explained by the poor combination of CNTs with the Ni matrix. CTAB addition in the plating bath developed a layer of positive charge on the suspended CNTs particle surfaces, which may impair the combination of CNTs with Ni coating and decrease the strengthening effect. This poor combination was also testified by the adhesion test. For Ni-CNTs coating prepared with CTAB, cracking happened after the first bending cycle. Moreover, polarisation measurement showed that the corrosion potential of Ni-CNTs coating prepared with CTAB (-0.82 V) was more negative than the coating without surfactant (-0.41 V), indicating poor corrosion resistance. The decreased boundary adhesion between carbon nanotubes and nickel matrix by the cationic surfactant CTAB should be responsible for the poor electrochemical behaviours since the electrochemical activity at loose and defective boundaries is higher.

Besides CTAB, Wang [173] reported that the addition of another type of cationic surfactant BAS could reduce the conductivity of MoS_2 particles in Ni Watts plating solution. Therefore, more Ni^{2+} ions could deposit homogeneously over a wider area rather than on preferred conductive positions. The homogeneous deposition resulted in a smoother co-deposition layer with lower porosity. Although the researcher did not conduct coating characterization such as microhardness measurement and tribological test, it can be expected that Ni-MoS_2 coating prepared with BAS could exhibit higher hardness, better tribological performance and lower corrosion rate.

Table 2.7 Effect of cationic surfactant on the composite coatings

Coating type	Deposition technique	Particle size & concentration	Surfactant type & concentration	Particle dispersion stability	Incorporated particle	Effect of surfactant towards final composite coating	Ref
Ni-SiC	Direct current plating	250 nm; 0-20 g/L;	Cationic; Cetyltrimethyl ammonium bromide (CTAB); 0-1.5 g/L;	Agglomerate size measured by a dynamic light scattering method; SiC particle size in the Ni bath (1.6-2.3 μm) was greater than in DI water (200-300 nm) due to high ionic strength.	Increased with increasing ratio of added surfactant to SiC concentration; Up to 11.5 vol%;	- CTAB addition resulted in a higher percentage of uniformly distributed SiC particles. - Ni-SiC coating exhibited higher hardness with an increasing ratio of added surfactant to SiC concentration; - The adsorption of CTAB on the SiC particle surface increased the adhesion force to the cathode, which allowed larger particles to be embedded.	[165]
Ni-SiC	Direct current plating	0.1-1.0 μm; 20 g/L;	Cationic; Cetyltrimethyl ammonium bromide (CTAB); 0-0.4 g/L;	Measured by Zeta potential; Increased with CTAB concentration;	Increased with CTAB concentration; Up to 11.5 vol%;	- Introducing CTAB into bath solution not only increased SiC content in the composite coating but also led to a non-agglomerated particle dispersion;	[167]

Coating type	Deposition technique	Particle size & concentration	Surfactant type & concentration	Particle dispersion stability	Incorporated particle	Effect of surfactant towards final composite coating	Ref
				From -3.0 to 20.0 mV;		- Increasing CTAB concentration resulted in the lattice distortion of the Ni matrix; - The hardness and wear resistance of Ni-SiC coating was enhanced with increasing CTAB addition up to 0.3 g/L in the electrolyte, but a further increase in CTAB concentration deteriorated both properties.	
Ni-carbon nanotubes	Direct current plating	Size not given; 0.1-0.3 g/L;	Cationic; Cetyltrimethyl ammonium bromide (CTAB); 0.6 g/L;	N/A;	4.75-10.84 wt%;	- CTAB increased particle content in the Ni-CNTs coating. - Ni-CNTs coating with CTAB became rough and loose. - CTAB decreased the grain size of the deposited coating. - The addition of CTAB resulted in low coating hardness and poor coating/substrate adhesion.	[168]

Coating type	Deposition technique	Particle size & concentration	Surfactant type & concentration	Particle dispersion stability	Incorporated particle	Effect of surfactant towards final composite coating	Ref
						- CTAB deteriorated the corrosion resistance of Ni-CNTs coatings.	
Ni-WC	Direct current plating	50 nm; 10-40 g/L;	Cationic; Cetyltrimethyl ammonium bromide (CTAB); 0.002 to 0.2 g/L	Measured by Zeta potential; Increased with CTAB concentration; From -10 to 26 mV;	Decreased from 4.2 % to 0.05 % in the range of 0.001 to 0.01 g/L CTAB;	- Particle content in the coating decreased with increasing CTAB (0.001 to 0.01 g/L). - The size of the "nodular shape" Ni-WC on the coating surface decreased with the addition of CTAB.	[169]
Ni-P-carbon nanotubes	Electroless plating	Diameter: 40-60 nm; Length: 5-15 μm; 0-0.05 g/L	Cationic; Hexadecyl trimethylammonium Bromide (CTAB); 0.075 g/L;	Measured by UV-vis; Absorbance peak at 400 nm wavelength; Maximum absorbance at the 0.075 g/L CTAB to 25 mg/L CNT ratio;	N/A;	- The addition of CTAB promoted particle dispersion in the electroless bath, and the optimum dispersion was achieved at the 0.075 g/L CTAB to 25 mg/L CNT ratio; - Agglomerates and bundles of CNTs could be observed on the	[170]

Coating type	Deposition technique	Particle size & concentration	Surfactant type & concentration	Particle dispersion stability	Incorporated particle	Effect of surfactant towards final composite coating	Ref
						coating surface even at the optimum surfactant ratio.	
Ni-P-nanodiamond	Electroless plating	4-5 nm; 0.1 g/L	Cationic; Cetyltrimethyl ammonium bromide (CTAB); 0-0.004 g/L	N/A;	N/A;	- Surface morphology was rough, and some cracks can be observed when CTAB was added into the bath solution. - An abrupt composition change was found at the interface of the substrate and coating due to high cathodic reactivity of CTAB. Therefore, poor adhesion was noticed. - The addition of CTAB in bath solution deteriorated wear resistance of coating due to the crack formation.	[171]
Cu-TiO_2	Jet electroplating	120 nm; 50 g/L;	Cationic;	Measured by Zeta potential;	Up to 11.5 wt% at 0.03 g/L CTAB;	- CTAB addition led to an increase of TiO_2 content in the composite coating up till the	[172]

Coating type	Deposition technique	Particle size & concentration	Surfactant type & concentration	Particle dispersion stability	Incorporated particle	Effect of surfactant towards final composite coating	Ref
	(modified DC plating);		Cetyltrimethyl ammonium bromide (CTAB); 0.01-0.05 g/L;	Increased with CTAB concentration; From -6.5 to 8.9 mV;		concentration of 0.03 g/L after which particle content decreased; - Cu-TiO_2 deposited with CTAB became homogeneous; - With optimum CTAB concentration (0.03 g/L), both hardness and wear resistance were enhanced obviously.	
Ni-MoS_2	Direct current plating	4.5 µm; 5-50 g/L	Cationic; Benzyl ammonium salts (BAS); 0.1 g per g/L MoS_2;	Measured by Zeta potential; Increased with increasing surfactant concentration; -35 to 30 mv	20.0-35.0 vol%;	- The adsorption of BAS reduced the conductivity of MoS_2. A smooth co-deposition layer with low porosity was obtained. - The improvement by surfactant was limited. Pores were still observable from cross-section views.	[173]

2.4.4.2 Anionic surfactant

Anionic surfactants are the most widely used class of surfactants in industrial applications due to their relatively low cost of manufacture. They are practically used in almost every type of detergent [179, 180]. In the past few decades, many researchers applied anionic surfactants as effective particle dispersive agents in composite electroplating. Different from cationic surfactants discussed previously, the hydrophilic groups of anionic surfactants possess a negative surface charge. Therefore, particles adsorbed by anionic surfactants could form a negative surface charge in plating solutions. Although the particles with negative surface charge might be excluded by cathode in the electroplating system, electrostatic repulsion between particles induced by the adsorption of anionic surfactants can effectively avoid particle agglomeration. The well-dispersed particles can approach the cathode surface by bath agitation and be incorporated into the coating. According to the research conducted by Mohajeri, Dolati and Rezagholibeiki [169], the adsorption mechanism of negatively charged particles can be explained by the second stage of the Guglielmi model [39]. In an electroplating bath, the negatively charged particles can be surrounded by a layer of metal ions due to the electrostatic attraction. When these particles approach the cathode surface, they can be embedded into deposit by the reduction reaction of the metal ion layer. So far, the most extensively used anionic surfactant in composite electroplating is sodium dodecyl sulphate (SDS) [168-172, 181-185]. **Table 2.8** summarises the usage of SDS in direct current plating, electroless plating and pulse current plating.

The concentration of anionic surfactant SDS in the plating solution should be maintained at an optimum level to achieve stable particle dispersion and high content of particle embedment. Either too low or too high SDS addition could result in particle agglomeration or deterioration of plating bath, thereby hindering particle co-deposition. Kartal et al. [182] investigated the effect of SDS addition towards pulse current plated Ni-WC coating. They observed that the zeta potential of suspended particles in the plating solution constantly decreased from -10 mV to -30 mV with increasing SDS concentration (0-0.2 g/L). In addition, WC content in the composite coating increased to 24.2 wt% up to the optimum SDS concentration of 0.1 g/L. However, a further increase in SDS concentration led to a sharp decrease in the incorporated particle content. The increasing trend of particle incorporation in the range of 0 to 0.1 g/L SDS could be explained by the more negative zeta potential value, indicating a sufficient repulsive electrostatic force between individual particles to avoid agglomeration. However, when SDS concentration increased beyond optimum value, extra molecules could play an electrolyte role and increase the plating bath's ionic strength, which would decrease electrostatic repulsion and increase the amount of agglomerated particles. In another study carried out by Zarebidaki and Allahkaram [170], particle dispersibility in the electroless Ni-P-CNTs plating bath was evaluated using the UV-vis spectroscopy method. It has been found that particle dispersibility improved with increasing SDS concentration up to an optimum value of 0.025 g/L. Above this value, particle dispersibility deteriorated, and authors attributed this to the micelle formation of surfactants. At high concentrations, surfactant molecules form micelles in solution. In other words, at high concentration of surfactants, portions of surfactants extend into the liquid phase and interact with each other. This interaction causes flocculation and decreases the dispersion of nanotubes at high surfactant concentration.

Apart from particle dispersibility and the amount of incorporated particle, surface morphologies of composite coatings are also highly related to the addition of anionic surfactants. Guo et al. [168] and Yasin et al. [181] reported SDS addition could lead to a coarse surface with bulge morphologies. In these two studies, particles used for co-deposition are carbon nanotubes and graphene, which all belong to conductive particles. As mentioned in Section 2.4.1, the co-deposition of conductive particles is prone to form a rough and porous coating structure. In solution with SDS, negative functional groups might be adsorbed on the conductive particle surfaces, promoting the metal ions reduction on these particles and aggravating the bulged deposition. In contrast, Abdoli and Rouhaghdam [171] observed that electroless Ni-P-diamond coatings prepared with high SDS concentration (3 or 4 mg/L) exhibited smoother surface morphologies than the ones modified with CTAB or low concentration of SDS (0.4 mg/L). A similar result was also observed by Jiang et al. [185]. They reported that the addition of 0.1 g/L SDS could develop a smooth and homogeneous surface morphology with a dense and compact coating structure.

It is well known that the incorporation of second phase particles into electrodeposited coating could result in an enhancement in mechanical properties (i.e., hardness and adhesion strength), tribological performance, and corrosion resistance. The addition of anionic surfactant during the plating process can further improve these properties [168, 171, 172, 181-183]. Guo et al. [168] reported that the hardness of Ni-CNTs coating increased form 160 Hv to 280 Hv when 0.6 g/L SDS was added into the plating bath. Yasin et al. [181] claimed that the addition of SDS could enhance hardness, adhesion strength and corrosion resistance of Ni-graphene coating. (**Figure 2.26**). Both research groups stated that the adhesion strength between embedded particles and metal matrix plays an important role in the strengthening effect. At high SDS concentration, the negative surface charge formed on the particle surfaces could attract more Ni^{2+} ions and develop a good combination between Ni deposition layer and particles. This improved combination may reduce voids and defects of composite coatings, thereby achieving better electrochemical properties.

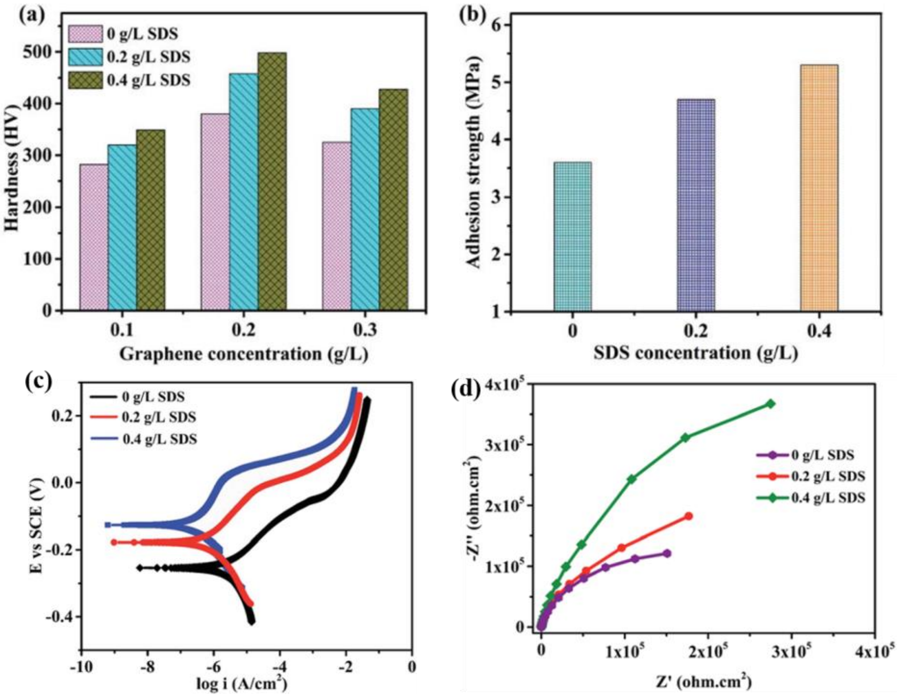

Figure 2.26 Effect of SDS on the (a) microhardness, (b) adhesion strength, (c) polarisation curves in 3.5 % NaCl solution and (d) impedance of Ni-graphene coatings (graphene concentration is 0.2 g/L except (a)) [181].

However, a few researchers also claimed that excessive SDS concentration could deteriorate coating properties [182-184]. For example, the hardness and wear resistance of Ni-WC coating increased with increasing SDS concentration up to 0.1g/L. Further SDS addition led to a decrease in both properties. In another study of pulse current Cr-WC coating, the author attributed the phenomenon of decreased wear resistance to the embrittlement of coating when excessive SDS was added into the plating bath [182]. Therefore, it can be concluded that the concentration of SDS addition should be carefully controlled to achieve the best performance of the composite coating.

Table 2.8 Effect of anionic surfactants on the composite coatings

Coating type	Deposition technique	Particle size & concentration	Surfactant type & concentration	Particle dispersion stability	Incorporated particle	Effect of surfactant towards final composite coating	Ref
Ni-carbon nanotubes	Direct current plating	Size not given; 0.1-0.3 g/L	Anionic; Sodium dodecyl sulphate (SDS); 0.6 g/L;	N/A;	4.58-4.91 wt%;	- SDS decreased the co-deposited CNTs content slightly. - Coatings deposited with SDS became more homogeneous and smoother than coatings without surfactant. - SDS decreased the grain size of deposited coatings. - Ni-CNTs coatings deposited with SDS showed higher hardness and better coating/substrate adhesion than coatings without surfactant. - The addition of SDS slightly increased the corrosion resistance of the coating.	[168]
Ni-WC	Direct current plating	50 nm; 10-40 g/L;	Anionic;	Measured by zeta potential;	Increased and reached a peak of 10 %	- Particle content in the coating increased first, then decreased	[169]

Coating type	Deposition technique	Particle size & concentration	Surfactant type & concentration	Particle dispersion stability	Incorporated particle	Effect of surfactant towards final composite coating	Ref
			Sodium dodecyl sulphate (SDS); 0.002 to 0.2 g/L	Decreased with increasing SDS concentration; From -25 to -30 mV;	at 0.005 g/L SDS, then decreased with further SDS addition.	with increasing SDS concentration (0.001 to 0.01 g/L). - The addition of SDS enhanced the microhardness and corrosion resistance of the final coating.	
Ni-P-carbon nanotubes	Electroless plating	Diameter: 40-60 nm; Length: 5-15 µm; 0-0.05 g/L	Anionic; Sodium dodecyl sulphate (SDS); 2.0 g/L;	Measured by UV-vis; Absorbance peak at 400 nm wavelength; Maximum absorbance at the 2 g/L SDS to 25 mg/L CNT ratio;	N/A;	- With the addition of SDS, the co-deposited CNTs were distributed evenly in the Ni-P matrix, and no agglomeration was observed. - Optimum ratio of SDS to CNTs resulted in uniform particle dispersion in the final coating, which yielded the highest hardness.	[170]
Ni-P-nanodiamond	Electroless plating	4-5 nm; 0.1 g/L;	Anionic; Sodium dodecyl sulphate (SDS);	N/A;	6.5 vol% at optimum SDS concentration	- Particle content in the coating increased with increasing SDS concentration;	[171]

Coating type	Deposition technique	Particle size & concentration	Surfactant type & concentration	Particle dispersion stability	Incorporated particle	Effect of surfactant towards final composite coating	Ref
			0-0.004 g/L			- Surface morphology evolved from rough to smooth with increasing SDS concentration; - Ni-P-diamond deposited with high SDS concentration (3 or 4 mg/L) showed the highest hardness and wear resistance, as well as the lowest friction coefficient.	
Cu-TiO_2	Jet electroplating (modified DC plating);	120 nm; 50 g/L;	Anionic; Sodium dodecyl sulphate (SDS); 0.05-0.15 g/L;	Measured by Zeta potential; Decreased with SDS concentration; From -6.5 to -15.6 mV;	Up to 8.9 wt% at 0.05 g/L SDS;	- SDS addition led to an increase of TiO2 content in the composite coating up till the concentration of 0.05 g/L after which particle content decreased; - Cu-TiO2 deposited with SDS became homogeneous; - With optimum SDS concentration (0.05 g/L), both hardness and wear resistance was enhanced obviously.	[172]

Coating type	Deposition technique	Particle size & concentration	Surfactant type & concentration	Particle dispersion stability	Incorporated particle	Effect of surfactant towards final composite coating	Ref
Ni-graphene	Direct current plating	Size not given; 0.1-0.3 g/L;	Anionic; Sodium dodecyl sulphate (SDS); 0-0.4 g/L;	N/A	7.0-24.0 wt%	- Particle content in Ni-graphene coating increased with increasing SDS concentration. - The addition of SDS increased the roughness of Ni-graphene coating to a large extent. - SDS reduced grain size and changed preferred orientation of Ni-graphene coating. - The microhardness, adhesion and corrosion resistance of the Ni-graphene coating are found to increase with the increasing concentration of SDS.	[181]
Ni-WC	Pulse current plating	< 1 µm; 20 g/L;	Anionic; Sodium dodecyl sulphate (SDS); 0-0.2 g/L;	Measured by Zeta potential; Decreased with increasing SDS concentration;	15.0 – 24.2 wt%	- Particle content in Ni-WC coating reached a peak at 0.1 g/L SDS. - A dense Ni-WC coating was obtained with an SDS concentration of 0.1 g/L	[182]

Coating type	Deposition technique	Particle size & concentration	Surfactant type & concentration	Particle dispersion stability	Incorporated particle	Effect of surfactant towards final composite coating	Ref
				From -10 to -30 mV		- SDS of 0.1 g/L concentration led to the smallest grain size. - The addition of SDS increased hardness and enhanced tribological performance of Ni-WC coating.	
Cr-WC	Pulse current plating	70 nm; 10 g/L;	Anionic; Sodium dodecyl sulphate (SDS); 0-2.0 g/L;	N/A;	0.5-2.0 wt%	- WC content in the coating increased with increasing SDS concentration up to 1.0 g/L. But WC content remained constant with a further increase of SDS concentration. - Cr-WC coating became smoother and denser with the fewer particle agglomerates when SDS was added into the bath solution. - The hardness of coating increased with increasing SDS concentration.	[183]

Coating type	Deposition technique	Particle size & concentration	Surfactant type & concentration	Particle dispersion stability	Incorporated particle	Effect of surfactant towards final composite coating	Ref
						- Appropriate amount of SDS enhanced wear resistance of Cr-WC coating (0.2-1.0 g/L), but excessive SDS (2 g/L) embrittled Cr-WC coating.	
Ni-Al_2O_3	Direct current plating	Nano-sized; 10 g/L	Anionic; Sodium dodecyl sulphate (SDS); 0.05-0.3 g/L	N/A;	Increased and reached a peak at 0.125 g/L; Quantity not given;	- Particle content increased with increasing SDS concentration up to 0.125 g/L. However, further SDS increase led to micelle formation and a decrease in particle incorporation. - Increasing SDS concentration up to an optimum value (0.125 g/L) resulted in more uniform particle distribution, higher hardness and better corrosion resistance.	[184]
Ni-Al_2O_3	Direct current plating	150 nm; 10 g/L;	Anionic;	Measured by particle size distribution and sedimentation test;	Al: 8.6 wt%;	- The addition of SDS resulted in higher Al_2O_3 content compared to coating without surfactant.	[185]

Coating type	Deposition technique	Particle size & concentration	Surfactant type & concentration	Particle dispersion stability	Incorporated particle	Effect of surfactant towards final composite coating	Ref
			Sodium dodecyl sulphate (SDS); 0.1 g/L;	Particle size in bath solution was larger than raw material, indicating particle agglomeration; Al_2O_3 particle settled quickly as long as the stirring stopped, indicating poor particle dispersion.		- Ni-Al2O3 coating deposited with SDS showed a smooth and homogeneous surface morphology with a dense and compact coating structure. No pores could be observed.	

2.4.4.3 Combination of cationic and anionic surfactant

In the previous two sections, the effects of cationic and anionic surfactants on composite coatings have been reviewed. Both types of surfactants have their merits and drawbacks (**Table 2.9**). Instead of using a single type of surfactant in the composite plating process, numerous studies also found that combined cationic and anionic surfactants could enhance both particle incorporation and compactness of the composite coatings [174, 175, 185, 186]. However, the mechanism of combined surfactants addition has not been clearly explained in the literature. Therefore, in this section, it is necessary to review combined surfactants and explore their potential applications in composite electroplating.

Table 2.9 Merits and drawbacks of cationic and anionic surfactants

Surfactant type	Merits	Drawbacks
Cationic	* Avoid particle agglomeration; * Enhance particle co-deposition rate;	* Poor particle/ metal matrix bonding; * Excessive amount embrittle coating;
Anionic	* Smooth and dense coating in most cases; * Strong particle/ metal matrix bonding;	* Low particle content due to repulsion; * Micelle formation and increased ionic strength at excessive surfactant addition;

Table 2.10 lists a few studies with combined cationic and anionic surfactants in composite electroplating. Generally, compared with coatings deposited from the bath with single surfactant addition, combined surfactants led to smoother surface morphologies and denser coating structures. As a result, properties such as hardness, wear-resistance and corrosion resistance could be enhanced. The following paragraphs will provide detailed reviews of two typical studies in which the effect of combined SDS and HPB on Ni-Al_2O_3 coating has been investigated.

Chen et al. [174] studied surface morphology, hardness and wear resistance of Ni-Al_2O_3 coatings prepared from bath solutions containing various HPB concentration and fixed addition of 0.1 g/L SDS. They observed that the amount of co-deposited Al_2O_3 particles increased from 8.3 vol% with no HPB addition to 14.7 vol% with 0.3 g/L HPB addition. The increment of particle embedment can be ascribed to positive charge developed around individual particles, as indicated by increasing zeta potential. However, the hardness and wear resistance enhanced with increasing HPB concentration up to an optimum value of 0.15 g/L, beyond which a decreasing trend was observed in both properties. By conducting a parallel study of HPB effects on pure Ni coatings, the deteriorated hardness and wear resistance were observed by the Ni matrix embrittlement at excessive HPB concentration. In a later study, the effect of combined surfactants towards Ni-Al_2O_3 coating was further investigated by Jiang et al. [185]. The macro- and micro- surface morphologies, along with EDS results, are illustrated in **Figure 2.27**. Similar to the research carried out by Chen et al. [174], Jiang et al. also revealed that SDS addition alone helped to form a smooth and dense surface morphology but less particle incorporation compared with Ni-Al_2O_3 coating deposited without surfactant (**Figure 2.27 a and b**), while HPB addition alone deteriorated the coating quality with obvious exfoliation (**Figure 2.27 c**). Homogeneous particle distribution of high Al_2O_3 content could only be realized by combined addition of SDS and HPB (**Figure 2.27 d**).

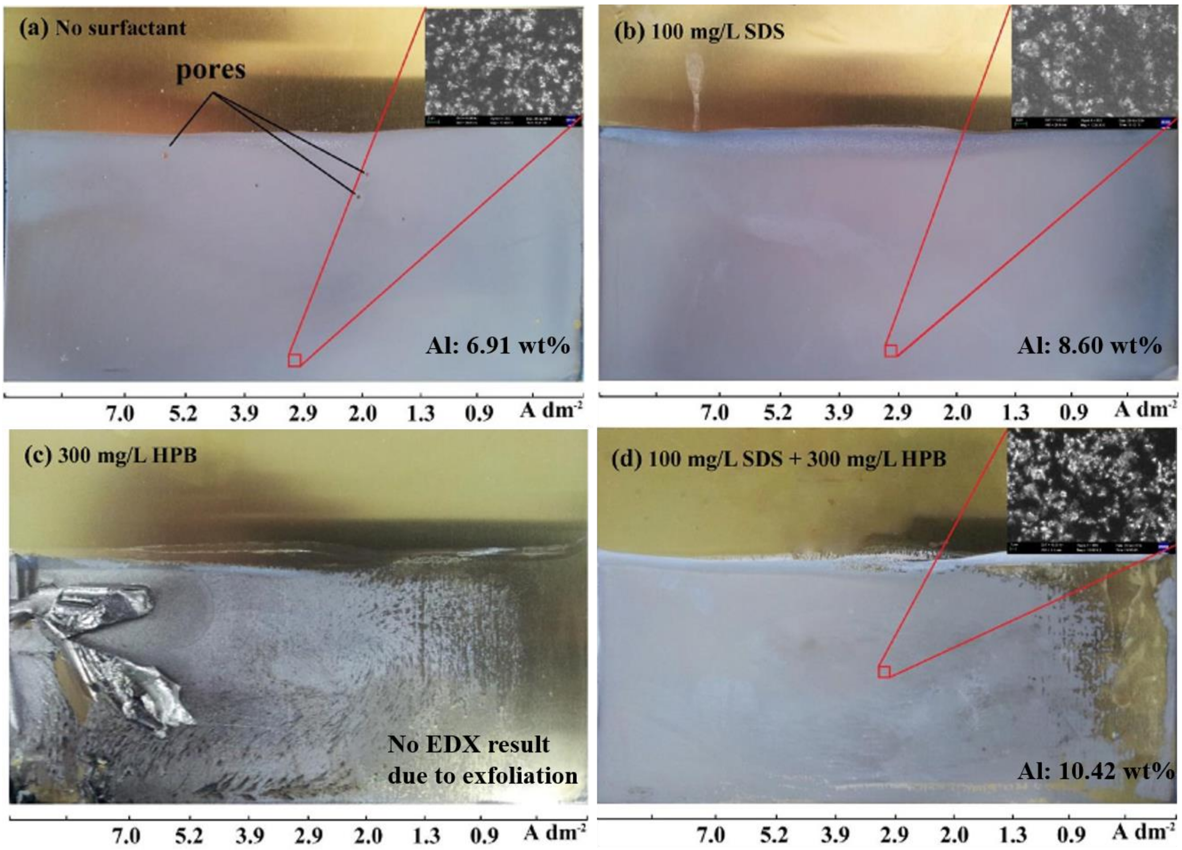

Figure 2.27 Marco- and micro- surface morphologies of electroplated Ni-Al2O3 coatings prepared from Hull Cell: (a) no surfactant, (b) 100 mg/L SDS only, (c) 300 mg/L HPB only and (d) 100 mg/L SDS + 300 mg/L HPB, EDS results shown at the corner [185].

To understand the adsorption mechanism of combined HPB and SDS, Jiang et al. [185] also carried out zeta potential measurement in both static water-diluted Watts bath and dynamic (or stirring) Watts bath. In the static bath, zeta potential increased with increasing HPB addition (**Figure 2.28 a**), which agrees with Chen et al.'s findings [174]. However, in the dynamic bath, zeta potential values fluctuated within -0.8 mV to 0.8 mV at various HPB concentrations (**Figure 2.28 b**). Moreover, particle migrations under the electric field were slow and moving directions were random (**Figure 2.28 c and d**). Therefore, the authors proposed that the directional electrophoresis migration of particles across the bath was limited due to the high ionic concentration in the bath environment. The high particle content with smooth and dense features of Ni-Al_2O_3 coatings was explained by the enhanced affinity between Al_2O_3 containing bath solution and the cathode (or growing metal). As shown in **Figure 2.28 (e)**, surfactant addition effectively reduced the contact angle on both the Cu substrate and Ni coating. The low contact angle indicates low surface tension at the solid/liquid interface, which favours particles/ metal matrix combination and gas escapement during electrodeposition. As a result, better wettability due to surfactant addition greatly improved the coating quality with a smooth and dense feature.

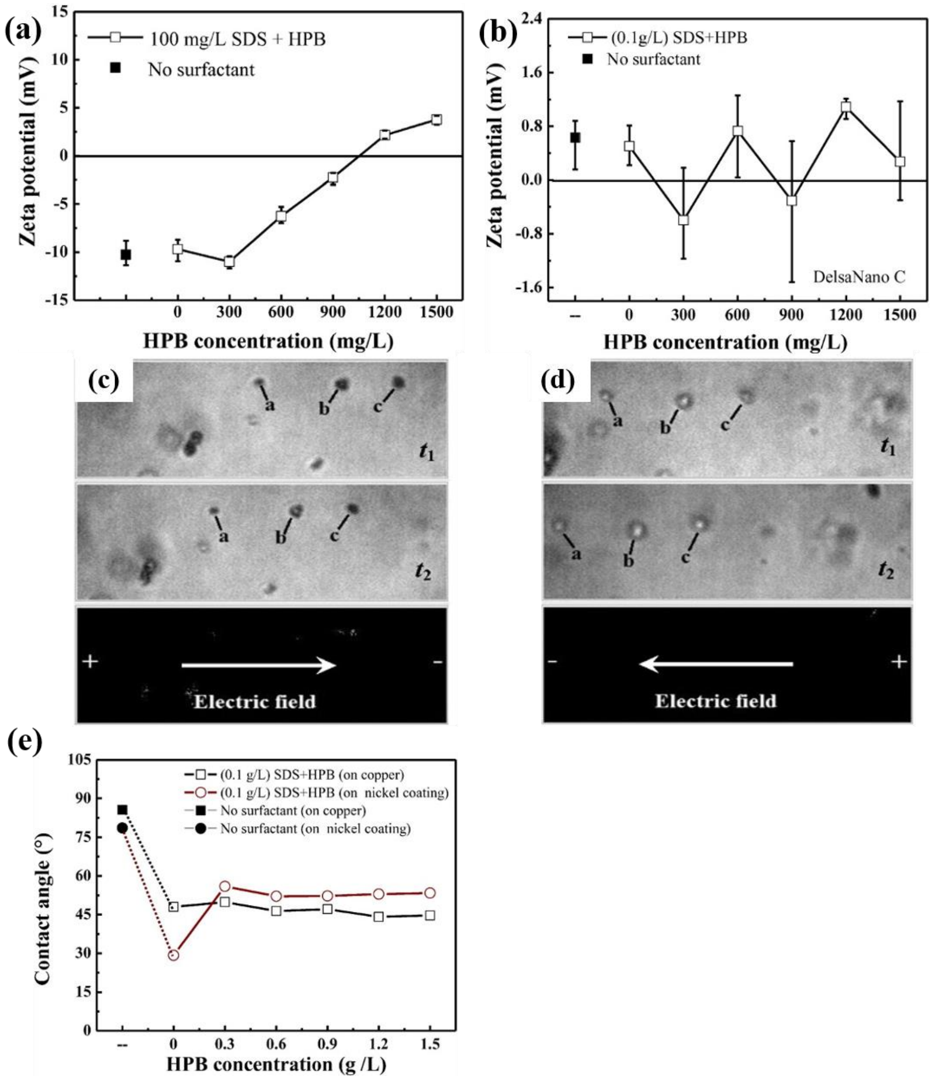

Figure 2.28 Zeta potential of Al_2O_3 measured in (a) static water-diluted Watts bath, (b) dynamic undiluted Watts bath; (c) and (d) are random particle movement under electric field; (e) is contact angle of Al_2O_3 containing Watt's bath on Cu substrate and Ni coating with SDS and/or HPB addition, respectively [185].

Table 2.10 Effect of combined surfactants on the composite coatings

Coating type	Deposition technique	Particle size & concentration	Surfactant type & concentration	Particle dispersion stability	Incorporated particle	Effect of surfactant towards final composite coating	Ref
Ni-Al_2O_3	Direct current plating	0.8 µm; 20 g/L;	Cationic; Hexadecylpyridinium bromide (HPB); 0-0.3 g/L; + Anionic; Sodium dodecyl sulphate (SDS); 0.1 g/L;	Measured by Zeta potential; Increased with increasing HPB concentration; From -4.9 to 20.0 mV.	Increased with HPB concentration; Up to 14.7 wt%;	- The combination of HPB and SDS improved the amount of co-deposited particle, reduced particle agglomeration and achieved uniform particle distribution in Ni matrix; - Appropriate HPB concentration (0.15 g/L) plus fixed SDS concentration (0.1 g/L) led to enhanced hardness and wear resistance of Ni-Al_2O_3 coating; - Excessive HPB concentration resulted in brittle Ni matrix, thereby deteriorating composite coating quality.	[174]
Ni-TiO_2	Direct current plating	30 nm; 0-15 g/L;	Cationic; Hexadecylpyridinium bromide (HPB);	N/A;	Increased with HPB concentration;	- Particle content increased with increasing HPB concentration;	[175]

Coating type	Deposition technique	Particle size & concentration	Surfactant type & concentration	Particle dispersion stability	Incorporated particle	Effect of surfactant towards final composite coating	Ref
			0-0.3 g/L; + Anionic; Sodium dodecyl sulphate (SDS); 0.2 g/L;		Up to 7.3 wt%;	- Surface roughness increased slightly with increasing HPB concentration; - The addition of HPB altered the crystal orientation of Ni-TiO_2 coating. Thus, the coatings exhibited various hardness. - Ni-TiO_2 coating deposited with 0.3 g/L HPB plus 0.2 g/L SDS showed maximum hardness and best wear resistance due to combined effect of altered crystal orientation and increased TiO_2 amount.	
Ni-Al_2O_3	Direct current plating	150 nm; 10 g/L;	Cationic; Hexadecylpyridinium bromide (HPB);	Measure by Zeta potential in water-diluted Watts bath	Al: 10.42 wt% at 0.3 g/L HTAB;	- The addition of combined surfactant resulted in “soft” agglomerates which could be	[185]

Coating type	Deposition technique	Particle size & concentration	Surfactant type & concentration	Particle dispersion stability	Incorporated particle	Effect of surfactant towards final composite coating	Ref
			0-1.5 g/L; + Anionic; Sodium dodecyl sulphate (SDS); 0.1 g/L;	and original Watts bath respectively; In a water-diluted Watts bath, Zeta potential increased from -12 to 4 mV with increasing HPB concentration In the original bath, Zeta potential fluctuated with HPB due to high ionic concentration;		dispersed easily when the bath agitation was re-applied; - The combination of SDS and HPB led to higher particle content compared with single surfactant usage; - Ni-Al_2O_3 coating prepared with combined surfactant sowed dense structure. However, coating quality largely depended on current density;	
Ni-Zircon	Direct current plating	0.13 µm; 50 g/L;	Cationic; Cetyltrimethyl ammonium bromide (CTAB);	N/A;	5.3 wt%;	- The addition of SLS avoided the formation of pits; - CTAB addition was very effective in increasing the amount	[186]

Coating type	Deposition technique	Particle size & concentration	Surfactant type & concentration	Particle dispersion stability	Incorporated particle	Effect of surfactant towards final composite coating	Ref
			0.18 g/L; + Anionic; Sodium lauryl sulphate (SLS); 2 g/L;			of Zircon particles in the Ni matrix; - The nodular features were reduced, and surface morphology became smooth in coating prepared from the solution containing CTAB. - CTAB reduced particle agglomeration and promoted uniform particle distribution in the Ni matrix; - Ni-Zircon coating prepared with CTAB showed enhanced hardness and corrosion resistance than plain Ni-Zircon coating.	

2.4.4.4 Saccharin addition in electroplating

In electroplating, saccharin has long been used as an organic additive to improve brightness, reduce internal stress, and refine the grain structure. Hassani, Raeissi and Golozar [187] studied the effect of saccharin on the electrodeposited Ni-Co coatings. They found that the addition of saccharin (1 g/L) could inhibit the pyramidal growth of Ni-Co deposit, and thus, a smooth and compact surface could be obtained. Similar findings have also been reported by Ma et al. [188]. In their research, the synergetic effects of two types of additives, namely saccharin and 2-butin-1,4-diol (BD), on Ni-Co alloy coatings were investigated. As shown in **Figure 2.29**, Ni-Co coating exhibited lens-shaped clusters at a low additive concentration (0.1 g/L saccharin and 0.1 g/L BD), but as the additive concentration increased (2 g/L saccharin and 0.5 g/L BD), the surface became smooth and dense. Moreover, the authors also reported that the increasing additive concentration led to a substantial decrease in the grain size from 190 nm to 11 nm. In another study of nickel electrodeposition [189], the decrease of grain size could be observed when saccharin concentration increased from 0 to 3 g/L. However, a further increase in saccharin concentration had no significant effect on grain size.

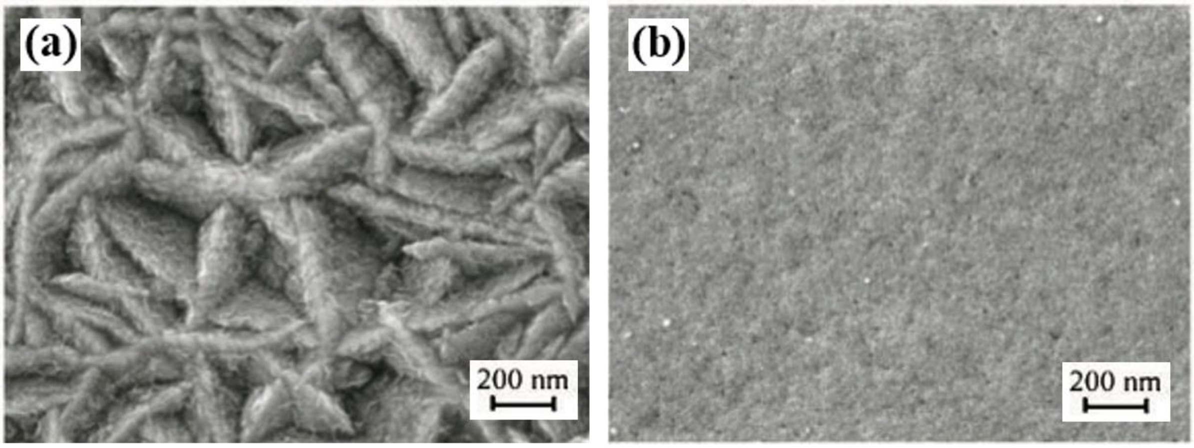

Figure 2.29 Secondary electron images of Ni-Co coatings containing (a) 0.1 g/L saccharin and 0.1 g/L BD and (b) 2 g/L saccharin and 0.5 g/L BD [188].

Numerous mechanisms have been proposed regarding the influence of saccharin on the grain size of electroplated coatings. The detailed discussion of these mechanisms has been summarised in an early review article by Franklin [190]. In brief, the important role of saccharin as a grain refiner is its effect on (i) blocking the active surface on the cathode by the formation of complex compounds, which increases the nucleation rate and decreases the surface diffusion of metal ions and hence inhibits the crystalline growth [191]. (ii) hydrogen evolution and/or adsorption [192], and (iii) change in cathodic overpotential [193]. To quantify the relationship between saccharin concentration and grain size of deposits, Rashidi and Amadeh [189] developed a mathematical model based on the surface blocking mechanism. For a given constant current density, the average grain size of coating deposited with known saccharin concentration can be calculated by the following equation.

$$d = k_s(1 + kC_S^m)^n \qquad 2.12$$

Where d is the average grain size; k_s, k, m and n are constant parameters derived experimentally by curve fitting; C_S is the saccharin concentration in the electroplating bath. From **Figure 2.30**, it can be noted that the experimental data are in good agreement with the theoretical model.

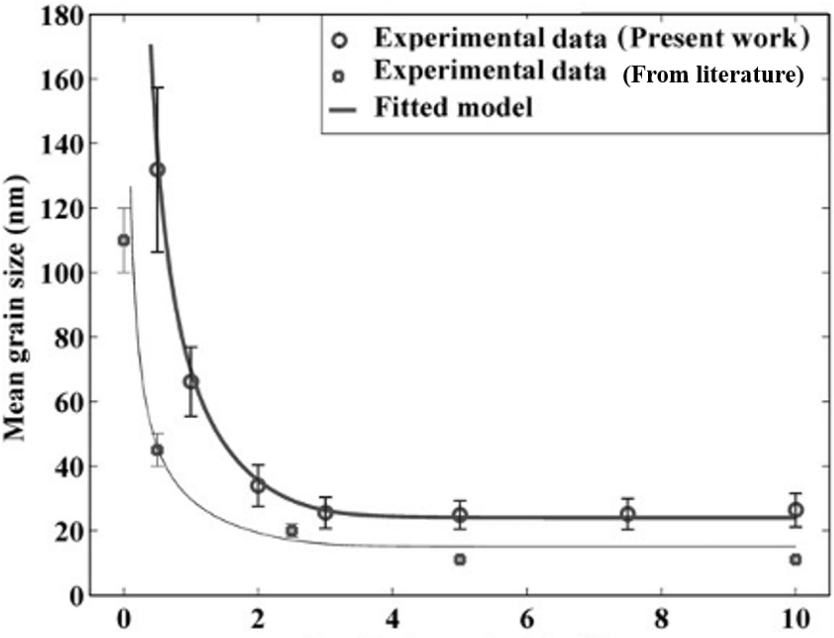

Figure 2.30 Comparison of experimental data and theoretical model for the variation of grain size of nickel deposits as a function of saccharin concentration [189].

2.4.5 Particle modification

Particles used for co-deposition have also been considered as an important parameter, which would significantly influence both appearance and properties of composite coatings. Many researchers focused their investigation on the impact of particle concentration and particle size. However, very few of them considered the electrical conductivity of particles. In early research, Stankovic and Gojo [194] systematically studied electrodeposited composite coatings of copper with insulating (SiC and Al_2O_3), semi-conductive (MoS_2) and conductive (graphite) particles. They found that that composite coating with insulating particles displayed smooth surface morphologies and compact structures. On the contrary, composite coatings with semi-conductive and conductive particles exhibited sponge-like structures, irregular surfaces, and high roughness (**Table 2.11**). Similar coating structures could also be observed in the co-deposition of other conductive particles such as WS_2 [13-15, 57], carbon nanotubes (CNTs) [195, 196] and WC [197, 198]. Therefore, it can be inferred that the co-deposition of semi-conductive and conductive particles are likely to form a sponge-like and porous structure. Undoubtedly, these composite coatings would suffer from a short lifespan, as they are prone to wear during service.

Since the origin of porous structures of such coatings is ascribed to the semi-conductive and conductive nature of the embedded particles, reduction of conductivity through particle modification would be a feasible method to densify coatings. From literature, particle modification can be achieved in two ways. One is pre-treatment of particles, i.e., coating semi-conductive or conductive particles with insulating materials. The other is a mixture of different particles for co-deposition. In the following sections, a detailed review of these two methods will be given.

Table 2.11 Comparison of electrodeposited composite coatings with insulating, semi-conductive and conductive particles [194]

Types of particle	**Conductivity**	**Appearance**	**Structure**	**Roughness, Ra (μm)**
SiC	Insulating	Smooth	Compact	0.55-0.63
α-Al_2O3	Insulating	Smooth	Compact	0.44-0.98
MoS_2	Semi-conductive	Cauliflower-like	Sponge-like	1.43-4.4
Graphite	Conductive	Rough and powdery	Sponge-like	6.5-15.5

2.4.5.1 Pre-treatment of particles

The pre-treatment process can alter particle conductivity through chemical reactions such as polymerisation and hydrolysis. After pre-treatment, particles that are originally semi-conductive or conductive could be coated with a dielectric material layer. Therefore, during composite electroplating, metal ions can only be deposited on the substrate rather than on the particle surfaces, avoiding the dendritic growth. A series of studies [199-201] summarized in **Table 2.12** have proved that the pre-treatment of MoS_2 particles helped to form a compact and dense composite coating. Two types of dielectric materials, namely polystyrene ($(C_8H_8)_n$) and Al_2O_3 [200], have been successfully coated on the surface of MoS_2 during pre-treatment. The MoS_2 particles coated with polystyrene (PS/MoS_2) were obtained by polymerization [199]. The reaction can be described as following. The as-received MoS_2 particles (40 g) were dispersed into ethanol solution (100 ml) and then mixed with 300 mL water. After that, 0.2 g of polyvinylpyrrolidone (($(C_6H_9NO)_n$), 0.6 g of azobisisobutyronitrile ($C_8H_{12}N_4$), and 20 ml of monomer styrene (C_8H_8) were added at room temperature with stirring. The mixture was heated to 65 ℃ for polymerization in a water bath, and the final modified MoS_2 particles are collected by centrifugation. On the other hand, the MoS_2 particles coated with Al_2O_3 (Al_2O_3/MoS_2) were achieved through a hydrolysis reaction of aluminium nitrate nonahydrate ($Al(NO_3)_3{\cdot}9H_2O$) [200]. SEM images of surface morphology and cross-section revealed that Ni-PS/MoS_2 and Ni-Al_2O_3/MoS_2 coatings were smoother and denser than Ni-MoS_2 coating. Additionally, the results of particle content in **Table 2.12** show that pre-treated MoS_2 particles could be more easily co-deposited than pristine MoS_2. Researchers attributed this phenomenon to the high electrical conductivity of MoS_2. During electroplating, the incorporated MoS_2 cause a stronger electric field at the particle adsorption sites. Therefore, Ni^{2+} ions preferentially deposit on the MoS_2, forming protrusions on the cathode surface. At the same time, MoS_2 particles in bulk solution adsorb more easily on protrusion ends than cathode surface, resulting in loosely dendritic growth of Ni-MoS_2 coating. The loosely adsorbed MoS_2 particles would be removed by ultrasonic irradiation during the coating cleaning process, leading to a low volume percentage of MoS_2 in the coating. On the other hand, the pre-treated MoS_2 particles can avoid dendritic growth due to reduced conductivity. Particles embedded securely in the compact coating would not be influenced during ultrasonic cleaning. Accordingly, a higher particle content is observed in Ni-PS/MoS_2 and Ni-Al_2O_3/MoS_2 coatings.

Apart from structure densification and high particle co-deposition rate, particle pre-treatment also enhances the mechanical and tribological properties of composite coatings. Under the same electroplating condition, Ni-Al_2O_3/MoS_2 coating exhibited higher hardness and better wear resistance than Ni-MoS_2 coating (**Table 2.12**). The improvement in hardness can be explained in two aspects. The first is the more obvious particle dispersion effect, as Ni-Al_2O_3/MoS_2 coating has higher particle content and denser coating structure than Ni-MoS_2 coating. The second is the hard nature of Al_2O_3. Al_2O_3 coated MoS_2 particles possess higher hardness than pristine MoS_2 particles. Incorporating harder particles would increase the hardness of final composite coatings. The reduced wear loss of Ni-Al_2O_3/MoS_2 coating was attributed to the dense and compact coating structure, which provides firm support for the sliding contact. Oppositely, the dendritic Ni-MoS_2 coating is prone to be crushed and sheared off, resulting in higher wear loss. The increased hardness may also explain the enhanced wear resistance of Ni-Al_2O_3/MoS_2 coating. According to Archard law [202, 203], the wear rate is inversely proportional to the hardness. The pre-treatment of MoS_2 leads to higher hardness and, therefore, better wear resistance. For Ni-PS/MoS_2 coating, although the wear test has not been conducted, a significant increase in hardness can be observed. Huang et al. [201] further studied the microhardness and tribological behaviour of electrodeposited Ni-Al_2O_3/MoS_2 coating with various Al_2O_3 content (5 wt% to 50 wt%) coated on the MoS_2 particles. With the increase of Al_2O_3 content, the composite coating becomes more compact and uniform, exhibiting higher hardness value and better wear resistance. However, the friction coefficient increased with higher Al_2O_3 wt%.

Table 2.12 Comparison between composite coatings with and without particle pre-treatment [199-201]

Coating type	Particle concentration (g/L)	Particle content (vol%)	Hardness (Hv)	CoF	Wear loss (mg)
Ni-MoS_2	0-30	2.8-6.0	283-510	0.18-0.37	9.7-14.1
Ni-Al_2O_3/MoS_2	0-30	3.9-12.0	300-575	0.21-0.40	9.0-11.1
Ni-PS/MoS_2	0-30	3.0-11.0	370-660	N/A	N/A

Although the pre-treatment of MoS_2 particles help to form a compact and dense coating structure, it has the following disadvantages [199-201]:

1. Time-consuming. The polymerization process to synthesize PS/MoS_2 takes up to 12 h.
2. The reaction process is complicated. Either hydrolysis or polymerization requires steps including heating, filtering, rinsing and drying.
3. Difficult to control the composition of treated particles. Low Al_2O_3 content would result in a porous coating structure due to insufficient insulation of MoS_2 particles. High Al_2O_3 content would deteriorate the anti-friction property.
4. Pollution and contamination. Particle pre-treatment requires a series of chemical reactions. Effluent discharge is harmful to the environment.

2.4.5.2 Mixed particle co-deposition

Although it is possible to densify metal-conductive (or semi-conductive) coatings via particle pre-treatment, the complicated and time-consuming reaction process makes this method less attractive for bulk production and industrial application. Alternatively, introducing hybrid inclusions (mixing conductive/semi-conductive particles with non-conductive particles) into the metal matrix seems to be a facile and versatile method to develop compact coatings. As mentioned in Section 2.4.5, the deposition pattern of metal ions on the conductive (or semi-conductive) particles and the insulating particles is different. The conductive (or semi-conductive) particles can induce dendritic growth of deposit due to the enhanced electric field. Oppositely, the insulating particles are gradually buried by the metal deposited on the substrate, forming smooth and dense composite coating structures. When both conductive and insulating particles are added to the electroplating bath, it can be expected that the partial area of the cathode surface could be occupied by insulating particles. Therefore, the dendritic growth induced by the adsorption of conductive particles could be partially avoided. Wang et al. [204] developed Ni-Al_2O_3-MoS_2 coatings by adding the different concentration of MoS_2 particles (0.5 g/L to 2.0 g/L) into Ni-Al_2O_3 (Al_2O_3 concentration is 10 g/L) coating system. They found that the coating structures are primarily dependent on MoS_2 concentration. As shown in **Figure 2.31**, Ni-Al_2O_3-MoS_2 coating exhibited dense and compact structure when the MoS_2 concentration in the electrolyte bath was 0.5 g/L, 1.0 g/L and 2.0 g/L (**Figure 2.31 A, B and D**). However, when 1.5 g/L MoS_2 was added into the electroplating bath, the coating was rough and porous (**Figure 2.31 C**). **Table 2.13** summarises the properties of Ni-Al_2O_3-MoS_2 coating,

$Ni-Al_2O_3$ coating and $Ni-MoS_2$ coating from literature. It can be noted that $Ni-Al_2O_3-MoS_2$ coating demonstrated a combination of the advantages of Al_2O_3 particles in high hardness and MoS_2 particles in low friction.

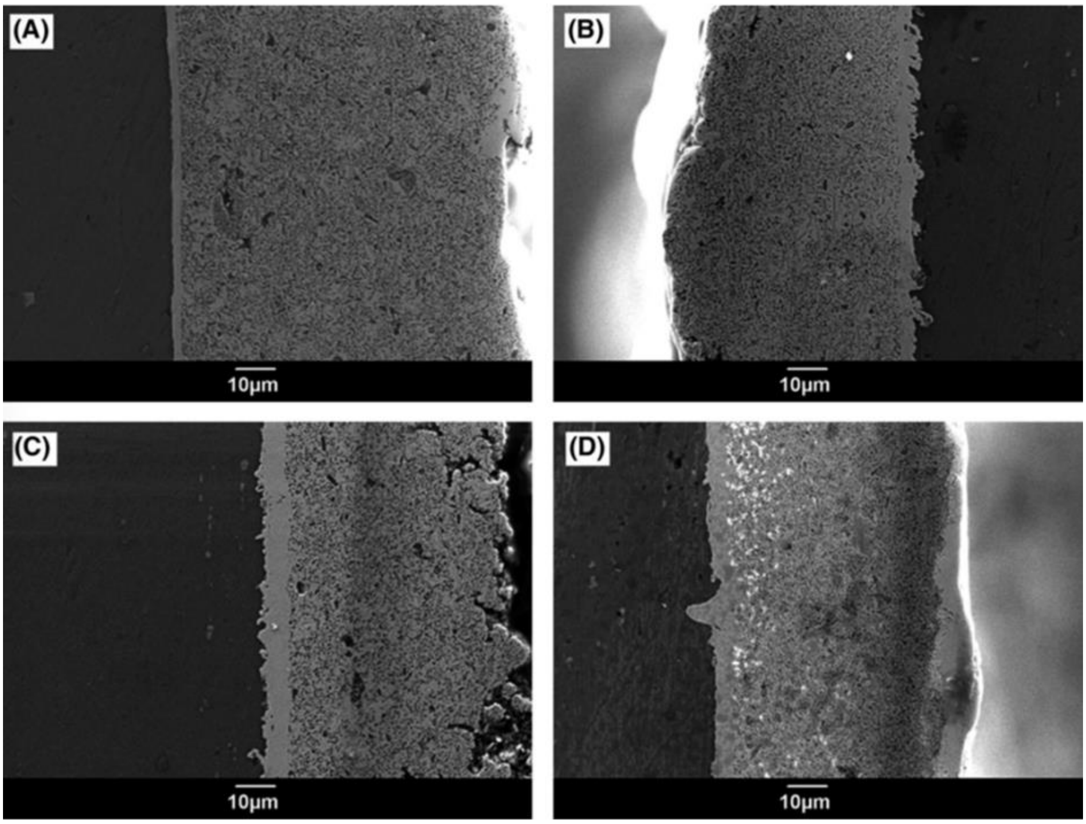

Figure 2.31 Cross-section morphologies of $Ni-Al_2O_3-MoS_2$ coatings prepared from electrolyte bath with Al_2O_3 concentration of 10 g/L and MoS_2 concentration of (A) 0.5 g/L, (B) 1.0 g/L, (C) 1.5 g/L and (D) 2.0 g/L [204].

Table 2.13 Comparison between $Ni-Al_2O_3$ coating, $Ni-MoS_2$ coating and $Ni-Al_2O_3-MoS_2$ coating [7] [204]

Coating type	MoS_2 concentration (g/L)	Al_2O_3 concentration (g/L)	Mo content (wt%)	Microhardness (Hv)	CoF	Wear rate (10^{-3} kg/m)
$Ni-Al_2O_3$	0	10	0	600	0.55	1.63
$Ni-MoS_2$	1	0	6.02	150	0.38	N/A
$Ni-Al_2O_3-MoS_2$	1	10	9.66	525	0.05	0.62

In the past two decades, similar studies on mixed particles co-deposition have been extensively conducted (**Table 2.14**). Fazel et al. [205] reported that the addition of solid lubricant particles (i.e. MoS_2 and graphite) into Ni-SiC coatings could enhance the stability of tribological performance at elevated temperature (300 ℃). However, the high MoS_2 concentration (12 g/L) in the electroplating bath could induce dendritic growth of composite coating. Consequently, Ni-SiC-MoS_2 coating exhibited porous structures. Many other researchers also showed that the combination of PTFE particles with hard ceramic particles (i.e. SiC and Al_2O_3) could develop composite coatings with self-lubricating and wear-resistant properties[206-208]. Chen et al. [206] developed Ni-P-Al2O_3-PTFE composite coatings by electroless deposition. In order to determine the optimum particle combination, an orthogonal test using 25 samples with different Al_2O_3 and PTFE concentration in the plating bath was conducted. It was found that the combination of 3g/L Al_2O_3 particles and 10 ml/L PTFE emulsion resulted in the best tribological performance, with a friction coefficient of 0.11 and a wear loss of 1.6 mg. Tang et al. [207] also observed that the electrodeposited Ni-PTFE-Al_2O_3 composite with both low friction and low wear loss could only be achieved when the PTFE/Al_2O_3 ratio was 3:1. Therefore, it can be concluded that the final properties of hybrid composite coatings are dependent on the particle ratio.

Compared with particle pre-treatment, the method of particle mixture has the advantages of easy operation, timesaving and less pollution. However, there are two challenges for mixed particle co-deposition. Firstly, the ratio of mixed particles should be carefully controlled. Wang et al. [204], Chen et al. [206] and Tang et al. [207] all reported that the desired combination of coating properties (self-lubrication and wear resistance) could only be achieved with a specific ratio. Secondly, no theoretical models have yet been proposed for mixed particle co-deposition. Therefore, empirical laboratory trails remain essential.

Table 2.14 Summary of composite coatings with co-deposition of mixed particles

Coating type	Deposition technique	Particle one (size and concentration)	Particle two (size and concentration)	Particle content in the coating	Friction coefficient	Ref
Ni-SiC-MoS_2	Direct current plating	MoS_2 (< 10 µm; 12 g/L)	SiC (< 10 µm; 12 g/L)	Not given	0.45-0.55	[205]
Ni-SiC-graphite	Direct current plating	Graphite (< 10 µm; 12 g/L)	SiC (< 10 µm; 12 g/L)	Graphite: 11 vol%; SiC: 18 vol%;	0.36-0.43	[205]
Ni-P-Al_2O_3-PTFE	Electroless plating	60 % PTFE emulsion (< 500 nm, 5-15 ml/L)	Al_2O_3 (20-50 nm, 1-5 g/L)	With optimum combination; Element Al: 0.85 wt%; Element F: 1.19 wt%;	0.17	[206]
Ni-Al_2O_3-PTFE	Direct current plating	PTFE (5 µm; 12 g/L)	Al_2O_3 (200 nm; 2-8 g/L)	PTFE: 24.2-26.6 wt%; Al_2O_3: 8.1-13.8 wt%;	0.20-0.40	[207]
Ni-P-SiC-PTFE	Electroless plating	PTFE dispersion (size is not given; 6-8 ml/L)	SiC (4.5 µm; 8-10 g)	Not given	0.52	[208]

2.5 Summary

TMD materials (i.e. MoS_2 and WS_2 particles) are also promising candidates to fabricate self-lubricating and superhydrophbic surfaces due to their unique lamellar structure and low surface energy (65-120 mJ/cm^2). In the past decade, the electro-co-deposition of TMD particles with metal for self-lubricating and superhydrophobic functions have been extensively studied in academia. However, very few successful cases of such coatings have been reported for real engineering applications. The inherent disadvantages of rough surfaces, porous coating structures, poor abrasion resistance and lack of precisely morphology control have limited the commercial promotion for both applications. Therefore, this work aims to overcome the aforementioned disadvantages and promote the industrial applications of such coatings. Through a detailed literature review, previous efforts on how to address these challenges have been summarised, which inspired the research directions of this work stated as follows.

(1) A major challenge for self-lubricating application is the rough coating surface and porous coating structure. From the literature review, the origins of porous coating structure were attributed to (i) hydrogen evolution, (ii) particle agglomeration and (iii) disturbance of electric field due to co-deposition of conductive particles. To develop a coating with smooth surface and dense structure, previous attempts from literature include achieving uniform particle dispersion, applying suitable additives or surfactants, and adding second phase particle to create hybrid composite coating. In this work, the aforementioned methods are combined together to optimise the electrodepostion parameters for densifying coating structure. Specifically, the combination of TMD particles with different type and size of ceramic particles (SiC and TiO_2) were thoroughly studied their combining effect towards surface morphology, coating structure and tribological performance were investigated.

(2) On the other hand, due to the low surface energy of MoS_2 and WS_2 particles, the electro-co-deposition of such particles also shows potential for superhydrophobic applications. However, MoS_2 and WS_2 are soft solid lubricant materials. The co-deposition of these particles may result in weak mechanical robustness of composite coatings. Ni-WS_2 coating quickly lost superhydrophobicity within 125 cm under the pressure of 2.83 kPa in the linear abrasion test [13]. To address this issue, adding a third phase hard ceramic particle into the metal-TMD system to develop hybrid composite coatings is feasible. Although the method of mixing different particles has been reported in electrodeposited

metal-TMD coatings for self-lubricating applications [17, 18], no study has explored hybrid composite coatings for superhydrophobic applications. Therefore, in this work SiC and TiO2 particles were separately added to Ni-MoS_2 and Ni-WS_2 coating system to develop robust superhydrophobic coatings. The corrosion properties and abrasion resistance of electrodeposited hybrid composite coatings have also been evaluated. Considering the enhancement induced by hard ceramic particles, the newly designed hybrid composite coatings shows great potential for practical superhydrophobic applications in industry.

3 Experimental methodology

3.1 Coating sample preparation

Composite coatings were electrodeposited on mild steel substrates by direct current. In general, the electroplating process can be divided into three main steps, namely substrate pre-treatment, plating bath solution preparation and composite coating electrodeposition. In the following subsections, detailed descriptions of each step will be provided. Additionally, the cross-section preparation method and coating thickness measurement will be included.

3.1.1 Substrate pre-treatment

AISI 1020 steel plates were chosen as substrates for electroplating. AISI 1020 steel is a type of low-carbon steel with a carbon content of 0.17 to 0.23 % [209]. It can be used in a variety of industrial applications, including axles, camshafts and cold-headed bolts. However, low carbon steel is susceptible to corrosion. Therefore, in the process of application, metal finishing is usually required. One way of metal finishing is by electroplating. As mentioned in Section 2.1, coating thickness is dependent on the shape of the cathode (substrate). To achieve uniform coating thickness, a parallel plate cathode with a dimension of 80 mm × 20 mm × 3 mm was used in this research. Before electrodeposition, the as-received steel plates were firstly wet ground by 120, 800, 1200 grits abrasive papers (Struers, waterproof SiC papers). After that, substrates were activated by immersing into a 10% hydrochloric acid for 30 s and rinsed with distilled water. The purpose of substrate pre-treatment was to remove oxides and contaminants to ensure smooth and uniform substrate surfaces for electrodeposition. The surface roughness of the substrate after pre-treatment is about 20 nm.

3.1.2 Preparation of plating bath solution

The classic nickel Watts solution was selected for electroplating as it is the most commercialised bath with the advantages of low maintenance costs and high reliability [210]. The chemical composition of the bath solution includes nickel sulphate, nickel chloride and boric acid (details shown in **Table 3.1**). In addition, two types of additives were added to the basic plating bath. One was surfactant, which helps to disperse particles in a plating solution, and the other was saccharin, which can refine electrodeposited grains, relieve internal stress, and increase coating brightness and hardness. According to the previous work conducted by the research group at the University of Southampton [211], the optimum saccharin concentration was determined to be 1.5 g/L. However, the usage of surfactant in composite electroplating is more complicated (discussed in Section 2.3.4). Thus, in this research, the surfactant concentration will be investigated as an important parameter affecting final composite coatings.

After electrolyte solution preparation, particles (either single or combined) were added to form a composite electroplating bath. In order to achieve particle dispersion homogeneously and avoid agglomeration, electrolyte with added particles were premixed using a Silverson L4RT high shear mixer at 8000 rpm for 1 hour (parameters determined by the Zhou et al.'s research [6]).

Table 3.1 Composition of basic nickel Watts bath solution

Chemicals	Manufacturer	Purity	Concentration (g/L)
Nickel sulphate hexahydrate ($NiSO_4 \cdot 6H_2O$)	Sigma-Aldrich	> 99.0%	250
Nickel chloride hexahydrate ($NiCl_2 \cdot 6H_2O$)	Sigma-Aldrich	> 98.0%	45
Boric acid (H_3BO_3)	Sigma-Aldrich	> 99.5%	40

3.1.3 Composite coating electrodeposition

Composite coatings were electroplated by direct current provided by Aim-TTi Bench Power Supply. **Figure 3.1** shows the electrodeposition setup. Nickel (Goodman Alloys Ltd) and mild steel (AISI 1020 after pre-treatment) with the same dimensions (80 mm × 20 mm × 3 mm) were used as anode and cathode, respectively. The electrodes were sealed with polyester tape (Cole-Parmer, UK), leaving an exposed area of 30 mm × 20 mm for plating. During electrodeposition, the current density was maintained at 4 A/dm^2, and the vertical, parallel electrodes were 25 mm apart in an 80 ml cylindrical beaker at a constant temperature of 40 ℃.

The solution bath was stirred by a PTFE-coated steel magnetic stirrer. The stirring speed was set to 600 rpm. The deposition time for each sample was either 30 minutes or 60 minutes.

After completion of electrodeposition, the coated samples were rinsed with distilled water to remove loose particles and then dried using a hair dryer. The coated samples were then transferred to a vacuum oven to remove liquid from the asperities and grooves of coatings.

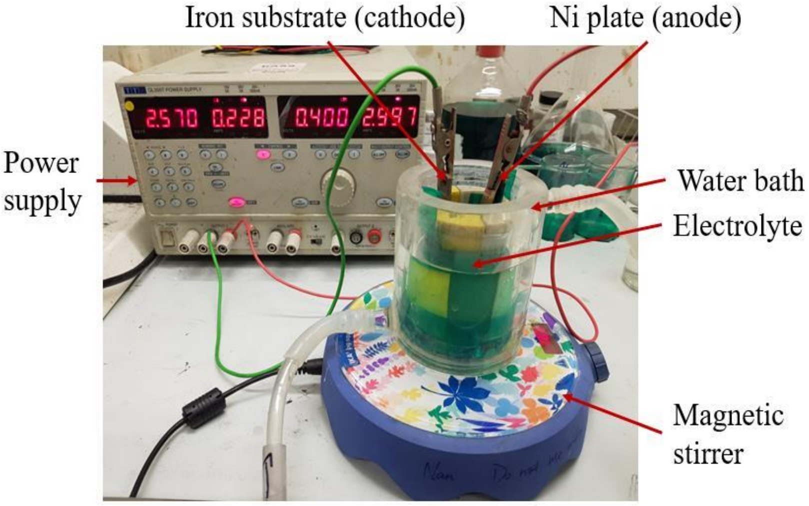

Figure 3.1 Electrodeposition setup

The experimental details of the electrodeposition of composite coatings are shown in **Table 3.2**. The process parameters used in this research were optimized in previous studies. The high shear mixing speed and time were determined based on the work of Zhou et al [6]. Electroplating parameters, including current density, bath agitation, pH, and deposition time, were selected from the optimized values reported in the work of Zhao et al [198]. The particle concentration in the electroplating solution was 10 g/L. The reason to choose a particle concentration of 10 g/L was based on studies conducted by Zhao et al. [13] and He et al. [14]. Both studies revealed that composite coatings deposited with 10 g/L of WS_2 exhibited lotus-like hierarchical structures and a relatively high particle incorporation rate (around 4.8 wt%), thus showing superhydrophobicity.

Table 3.2 Composition of composite electroplating bath and process parameters of electrodeposition

Composite electroplating bath	
Basic nickel Watts solution	80 ml
Surfactant, CTAB	0.1-0.5 g/L
Saccharin	1.5 g/L
Particle	In following Table 3.4 and Table 3.5
Process parameters	
Particle dispersion	High shear mixing (8000 rpm, 1 h)
pH	3-4
Current density	4 A/dm^2
Deposition time	30 min or 1 h
Bath agitation by magnetic stirring	600 rpm

In this research, MoS_2 and WS_2 particles with different sizes were respectively co-deposited into Ni matrix to form nickel single-particle composite coatings. Nickel hybrid composite coatings were developed by mixing SiC or TiO_2 particles with MoS_2 or WS_2 particles for co-deposition. According to previous studies [212, 213], the size of co-deposited particles can significantly affect the morphology and structure of the final coatings. Therefore, both nano- and micron-sized particles were co-deposited with a nickel matrix. TiO_2 and SiC ceramic particles were selected for their excellent mechanical properties, which enhance the wear resistance of the resulting hybrid composite coatings. **Table 3.3** shows the basic information of the particles used in this research. Particle size and type The sample designations for each nickel single-particle composite coating and nickel hybrid composite coating are provided in **Table 3.4** and **Table 3.5**, respectively.

Table 3.3 Basic information of particles used in this research

Particle	**Supplier**	**Purity**	**Particle size**
MoS_2, type one	Shanghai ST-Nano Science & Technology Co. Ltd	99.9 %	300 nm
MoS_2, type two	Shanghai ST-Nano Science & Technology Co. Ltd	99.9 %	1-2 µm
WS_2, type one	Changsha Huajing Powdery Material Technological Co. Ltd	99.9 %	80 nm
WS_2, type two	Shanghai ST-Nano Science & Technology Co. Ltd	99.9 %	200 nm
SiC, type one	Nanjing Emperor Nano Material Co. Ltd	99.9 %	40 nm
SiC, type two	Shanghai ST-Nano Science & Technology Co. Ltd	99.9 %	8.5 µm
TiO_2	Polysciences, Inc.	99.9 %	21 nm

Table 3.4 Nickel single-particle composite coatings fabricated by different particle size and deposition time (basic electrolyte solution 80 ml, T = 40℃, magnetic stirring at 600 rpm, CTAB: 0.1 g/L)

Sample	MoS_2 (g/L) (1.2 µm)	MoS_2 (g/L) (4.8 µm)	WS_2 (g/L) (275 nm)	WS_2 (g/L) (1.1 µm)	Deposition time
M1	10	–	–	–	30 min
M2	10	–	–	–	60 min
M3	–	10	–	–	30 min
M4	–	10	–	–	60 min
W1	–	–	10	–	30 min
W2	–	–	10	–	60 min
W3	–	–	–	10	30 min
W4	–	–	–	10	60 min

Table 3.5 Nickel hybrid composite coatings fabricated by different particle combination (basic electrolyte solution 80 ml, T = 40℃, magnetic stirring at 600 rpm, deposition time = 60 min, CTAB: 0.1 g/L)

Sample	Particle 1 (Concentration: 5g/L)	Particle 2 (Concentration: 5g/L)
Ni-MoS_2-WS_2	MoS_2 (1.2 µm)	WS_2 (1.1 µm)
Ni-SiC (40 nm)-MoS_2	MoS_2 (1.2 µm)	SiC (40 nm)
Ni-SiC (8.5 µm)-MoS_2	MoS_2 (1.2 µm)	SiC (8.5 µm)
Ni-SiC (40 nm)-WS_2	WS_2 (1.1 µm)	SiC (40 nm)
Ni-SiC (8.5 µm)-WS_2	WS_2 (1.1 µm)	SiC (8.5 µm)

Sample	Particle 1 (Concentration: 5g/L)	Particle 2 (Concentration: 5g/L)
Ni-TiO_2-MoS_2	MoS_2 (1.2 µm)	TiO_2 (21 nm)
Ni-TiO_2-WS_2	WS_2 (1.1 µm)	TiO_2 (21 nm)

3.1.4 Cross-section preparation and coating thickness measurement

Samples for SEM cross-section view imaging were prepared by two methods: cryogenic fracturing and metallography (i.e. cutting, mounting, grinding and polishing). Each cross-sectional method is described in detail below.

In the cryogenic fracturing method, the coating sample was first immersed in liquid nitrogen for 5 min. Then, the coating was delaminated and bent away from the substrate by using a scalpel. The delaminated coating was bent and snapped into two pieces using tweezers. The fractured surface was subsequently observed in SEM. Cryogenic fracturing has the advantage of preserving the original structure of the coating. However, a flat coating cross-section cannot be achieved, which increases the difficulty of observation.

In the conventional metallography method, the coating sample was first cut by a precision saw (Mecatome T210) with a blade rotation speed of 2000 rpm and a feed rate of 0.1 mm/s. The sample was covered by lab tissue paper during the cutting process to protect the coating. Then, the cut sample with cross-section was hot mounted in conductive by Opal 410 automatic hot mounting machine. To get a smooth cross-section ready for SEM observation, the mounted sample was ground by 120, 800, and 1200 grits abrasive paper and then polished by 6 µm and 1 µm diamond paste. After grinding and polishing, the cross-section sample was cleaned with acetone in an ultrasonic bath for 5 min to remove contamination. The conventional metallography method has been extensively used in this research. However, it should be noted that the grinding and polishing process could elongate soft MoS_2 particles in the composite coating, which deforms the cross-sectional view.

The coating thickness was directly measured from the cross-section prepared by the metallography method. According to the research carried out by Long and his coworkers [214], cross-section prepared by metallography can provide accurate coating thickness measurement. However, cryogenic fracturing was found to be ineffective in coating thickness measurement since the fracture surface might not be perpendicular to the substrate. Specifically, for each coating sample, thickness measurement was performed 5 times on a secondary electron image (magnification of 100 times), and the average value was recorded as the coating thickness.

3.2 Characterization of the fabricated composite coatings

A series of techniques and testing methods were applied (listed in **Table 3.6**) to characterise the fabricated composite coatings. In the following subsections, the operation conditions of these techniques will be specified.

Table 3.6 Summary of characterization techniques

Techniques	Principle	Information obtained
SEM and EDS	Secondary electrons; emission of characteristic X-rays from the interaction of the electron beam.	Surface morphology, elemental distribution across the surface, quantitative elemental analysis.
Alicona	Optical microscopy, 3D modelling of surface morphology.	Surface 3D profile, surface roughness value.
Water contact angle	Measurement of the angle between the water droplet and coating surface.	Surface wettability.
Water immersion test	Monitoring surface condition after immersing samples into DI water.	The durability of water-repellent properties.
Electrochemical test	Potentiodynamic polarisation and electrochemical impedance spectroscopy	Quantified corrosion properties and mechanism of corrosion.
Linear abrasion test	Reciprocating sliding motion of superhydrophobic surfaces against grinding paper	Quantified abrasion resistance of superhydrophobic surfaces.
Microhardness test	Vickers hardness indenter.	Microhardness value
Reciprocating wear test	Reciprocating sliding of steel ball against coating surfaces.	Coefficient of friction, wear rate.

3.2.1 Scanning electron microscopy and energy dispersive X-ray spectroscopy

A JOEL JSM 6500F/7200F SEM was employed to observe surface morphologies and cross-sections of composite coatings. The applied voltage was set to 15 kV, and the working distance was set to 10 mm. In this report, secondary electron SEM images were used to analyse the surface morphologies, cross-sections and wear tracks of coatings. The elemental composition was studied by an energy dispersive X-ray spectroscopy (Oxford Instruments INCA 300 EDS attached to SEM). For each coating sample, the EDS analysis was performed three times on an area of 1200 μm × 850 μm at the central part of the sample surface, and the quantitative elemental composition results were recorded by taking the average.

3.2.2 Alicona G4 InfiniteFocus

Alicona G4 InfiniteFocus was used to analyse the surface profiles of composite coatings. The Alicona G4 InfiniteFocus is a metrological tool that uses 'Focus-Variation' to measure surface roughness. 'Focus-Variation' combines the small depth of focus of an optical system with vertical scanning to provide topographical information from the variation of focus. The main component of the system is precision optics containing various lens systems that can be equipped with different objectives, allowing measurements with different resolution. The working principle of Alicona G4 Infinite focus can be described as following. Firstly, with a beam splitter, the light emitted from the white light source is inserted into the optical path of the system and focused on the sample through the objective. Once the light hits the specimen, it can be either reflected equally strong into every direction (in the case of diffuse reflection) or scattered mainly into one specific direction (in the case of specular deflection). Secondly, the rays emerging from the specimen can be bundled in the optics and collected by a light-sensitive sensor behind the beam splitting mirror. However, due to the depth of the optics is very small, only small regions of the sample can be sharply imaged. To perform a complete inspection of the surface with full depth of field, the precision optics should move vertically along the optical axis and continuously capture data from the surface. Lastly, the acquired data can be converted into 3D topographical information via mathematical algorithms. In this research, surface roughness and wear depth were measured by Alicona. Sample images were captured with object lens magnification of 5 times.

The roughness of the profile was measured by using the "Profile Roughness Measurement" module (**Figure 3.2**). The specific methods are as follows.

1. Set the upper and lower limit along the optical axis (Z-axis) to allow a complete scan of the surface with full depth of field.
2. Move the precision optics vertically along the optical axis to continuously capture data from the surface.
3. Select the “Profile Roughness Measurement” module from the menu bar.
4. Measurement is conducted on a 2D-optical image of a loaded dataset.
5. Specify the evaluation length to extract the desired profile. The evaluation length should comply with the Recommended Cut-off (ISO 4288-1996) (see Appendix A).
6. Parameters such as average roughness (Ra), root mean square roughness (Rq) and mean peak to valley height (Rz) on the selected profile line can be obtained.

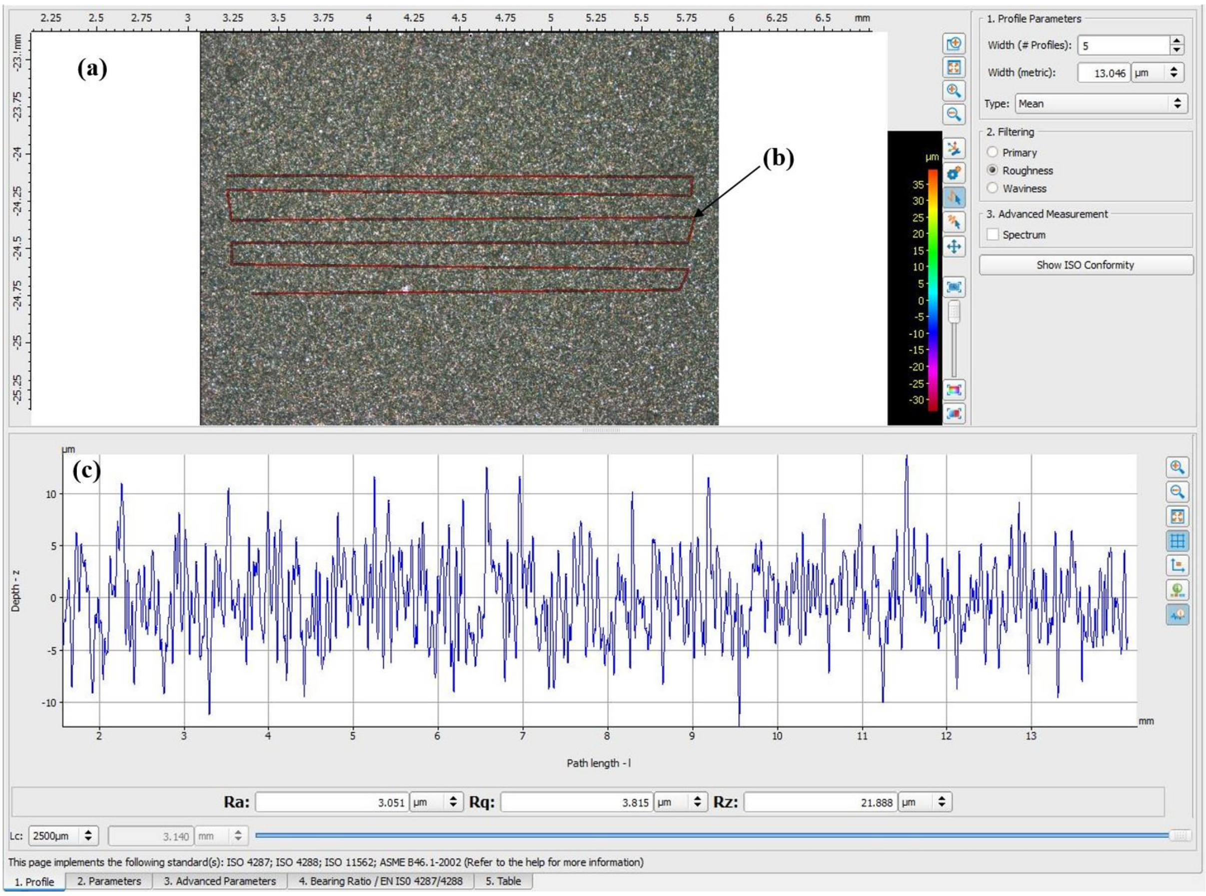

1. Profile Parameters
Width (# Profiles): 5
Width (metric): 13.046 µm
Type: Mean

2. Filtering
○ Primary
● Roughness
○ Waviness

3. Advanced Measurement
☐ Spectrum

Ra: 3.051 µm Rq: 3.815 µm Rz: 21.888 µm
Lc: 2500µm 3.140 mm

This page implements the following standard(s): ISO 4287; ISO 4288; ISO 11562; ASME B46.1-2002 (Refer to the help for more information)

Figure 3.2 Profile Roughness Measurement. (a) 2D-optical image of a loaded dataset; (b) extracted profile line, the evaluation length should be 15 mm for Ra values between 2 and 10 µm (c) extracted roughness profile.

The wear track on the coating surface was analysed by the ‘Profile Form Measurement’ module. The measurement range was controlled to capture all the data on the worn surface. The start and end positions were located on the unworn surfaces at the two edges of the wear track. After the measurement, the profile of the dataset can be extracted from the 2D-optical image (**Figure 3.3 a**). **Figure 3.3 (b)** is the extracted profile from coating surfaces. The wear depth was measured by the ‘Height Step’ function. The regions that define the reference level was selected first. Afterwards, the regions which define the measure level was selected. The obtained result of this distance measurement was the wear depth. In the current stage of research, the wear depth was determined by only one measurement in the middle of the wear track. However, since the rig produces a sinusoidal velocity profile, the condition may vary along the wear track. Therefore, only one measurement could not represent all the conditions along the wear track. The measurement were carried out at three locations and the average value was recorded as wear depth.

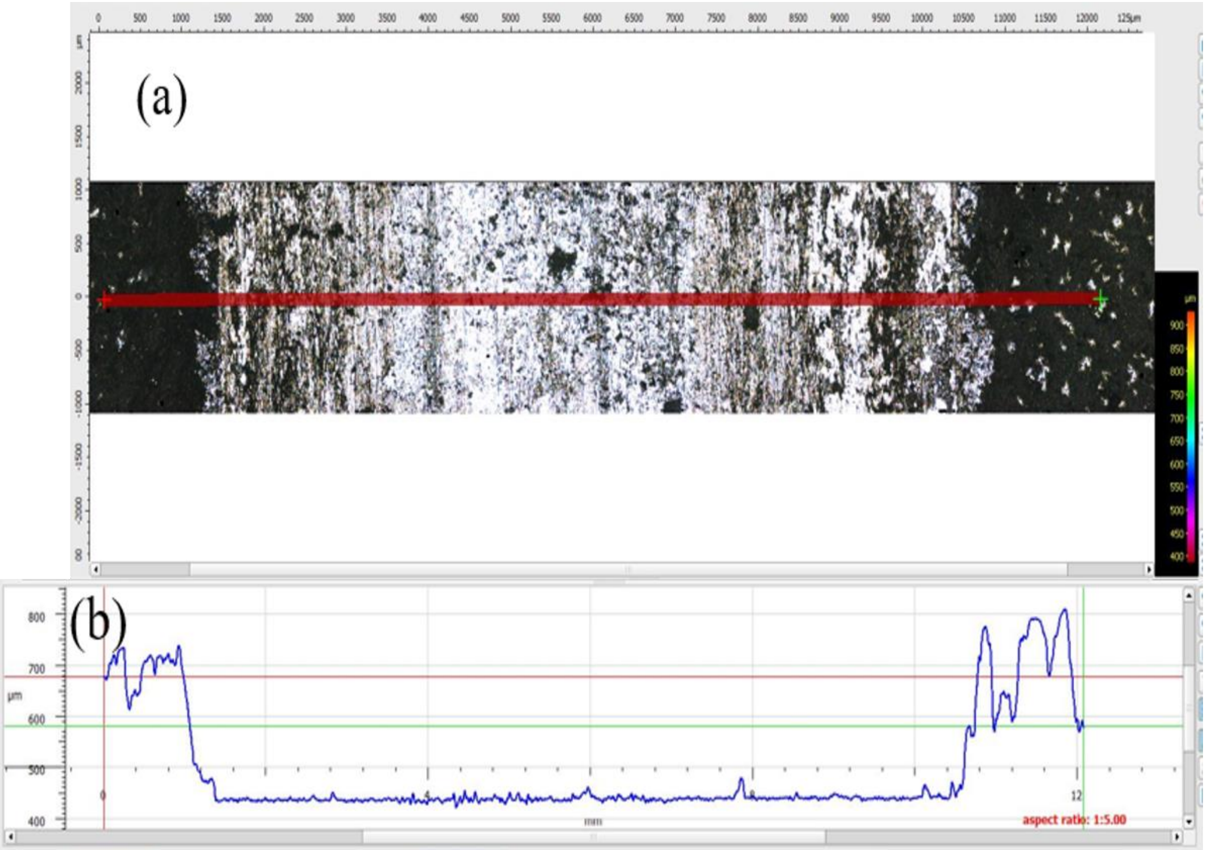

Figure 3.3 Profile Form Measurement. (a) 2D-optical image for profile extraction; (b) preview of the extracted profile; (c) Height Step measurement.

3.2.3 Surface wettability measurement

Kruss DSA 100 was used to test the wettability of coating surfaces by measuring the contact angle of a water droplet resting on the surface. During the wettability measurement, water droplet (8 microliters) was dropped onto the coating surface using a syringe. Images that shows the interaction between the water droplet and the coated surfaces were recorded by a built-in camera. To analyse the captured images, a software called imageJ was employed. By fitting the water droplet shape with a circle, the water contact angle can be obtained (**Figure 3.4**). In this research, five readings were taken for each coating, and the contact angle was determined by the average taken.

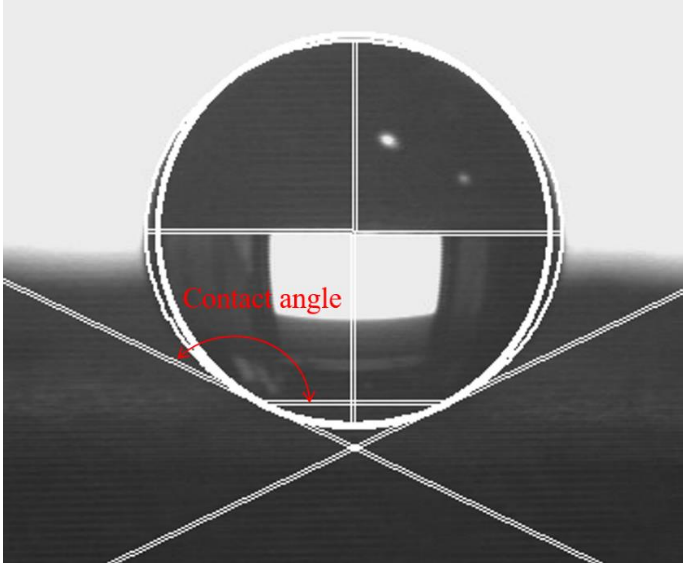

Figure 3.4 Water contact angle measurement by the fitting method

3.2.4 Water immersion test

The durability of the water-repellent property of superhydrophobic coating was determined by a simple water immersion test. Composite coatings showing superhydrophobic properties were immersed in deionized water. Before the water immersion test, the composite coating exhibited a dark colour in the air (**Figure 3.5 a**). When the composite coating was immersed in water, a layer of air bubbles was formed on superhydrophobic coating surface (**Figure 3.5 b**). This phenomenon has also been reported by Zhou et al. [113]. In their work, this shining layer was defined as an “air cushion”, which consisted of captured air in the gap between hierarchical structures on the coating surface. However, with the increase of immersing time, the “air cushion” gradually decreases and eventually disappears, resulting in the loss of surface superhydrophbicity. This phenomenon is attributed to the transition of wetting model from Cassie-Baxter's model to Wenzel's model (**Figure 3.5 c**). Murakami, Jinnai and Takahara ascribed this transition to the loss of energy barrier induced by external fluid pressure [215]. In this work, the coating sample was taken out of the water every 10 mins to check surface wettability during immersion test. The surface wettability was visually inspected by placing water droplets on the coating surface. If the water droplet can form a spherical shape and roll off easily, the coating is considered to maintain the hydrophobic state. By recording the time that each coating can maintain the hydrophobic state, the durability of water-repellent properties can be roughly estimated and compared.

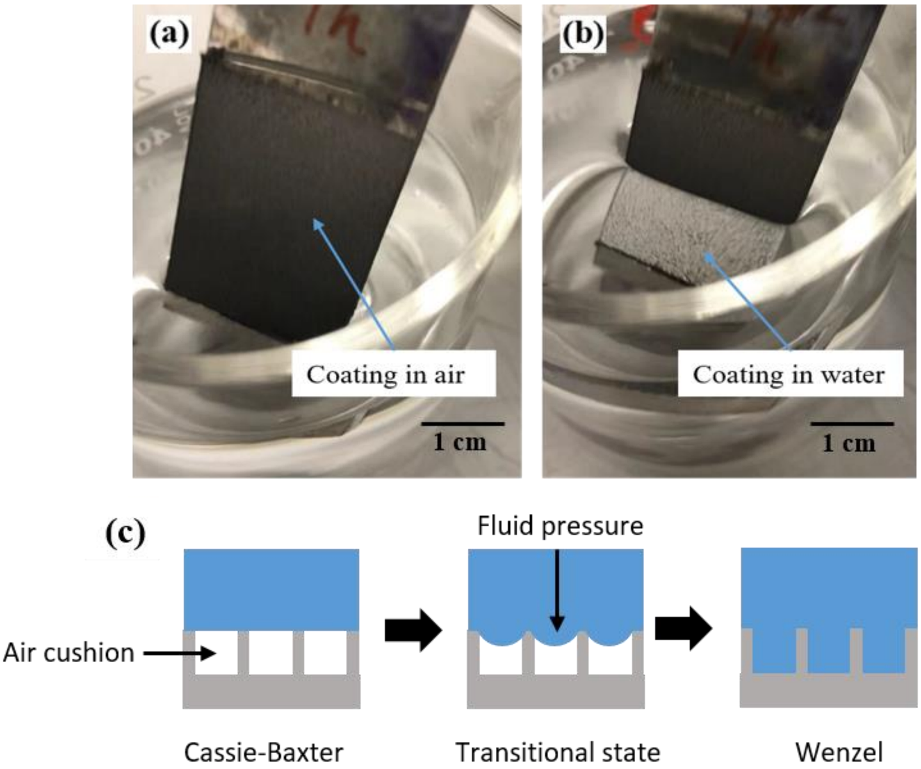

Figure 3.5 Water immersion test of coating seen in optical photographs. (a) Before the water immersion test, the coating sample is exposed to the air; (b) the coating sample is partially immersed into the water; (c) schematic of wetting model transition

3.2.5 Electrochemical test

The electrochemical tests, including potentiodynamic polarisation and electrochemical impedance spectroscopy (EIS) were performed on an electrochemical workstation (Autolab PGSTAT302N) to evaluate the corrosion resistance of the fabricated coating. All tests were performed in 3.5 wt% NaCl solution with a conventional three-electrode system shown in **Figure 3.6**. The electrochemical test setup consists of a silver/ silver chloride (Ag/AgCl) as reference electrode, a platinum electrode as the counter electrode, and the coating sample with an exposed area of 1 cm^2 as the working electrode. The potentiodynamic polarisation curve was obtained from ± 250 mV vs open circuit potential (OCP) at a scan rate of 5 mV/s. The corrosion potential and corrosion current density were obtained by the Tafel extrapolation method.

EIS measurement was conducted in the frequency range from 10^5 to 10^{-2} Hz under the amplitude of the sinusoidal signal of 10 mV. The obtained impedance data was further fitted by a plugin of NOVA software to get an equivalent circuit.

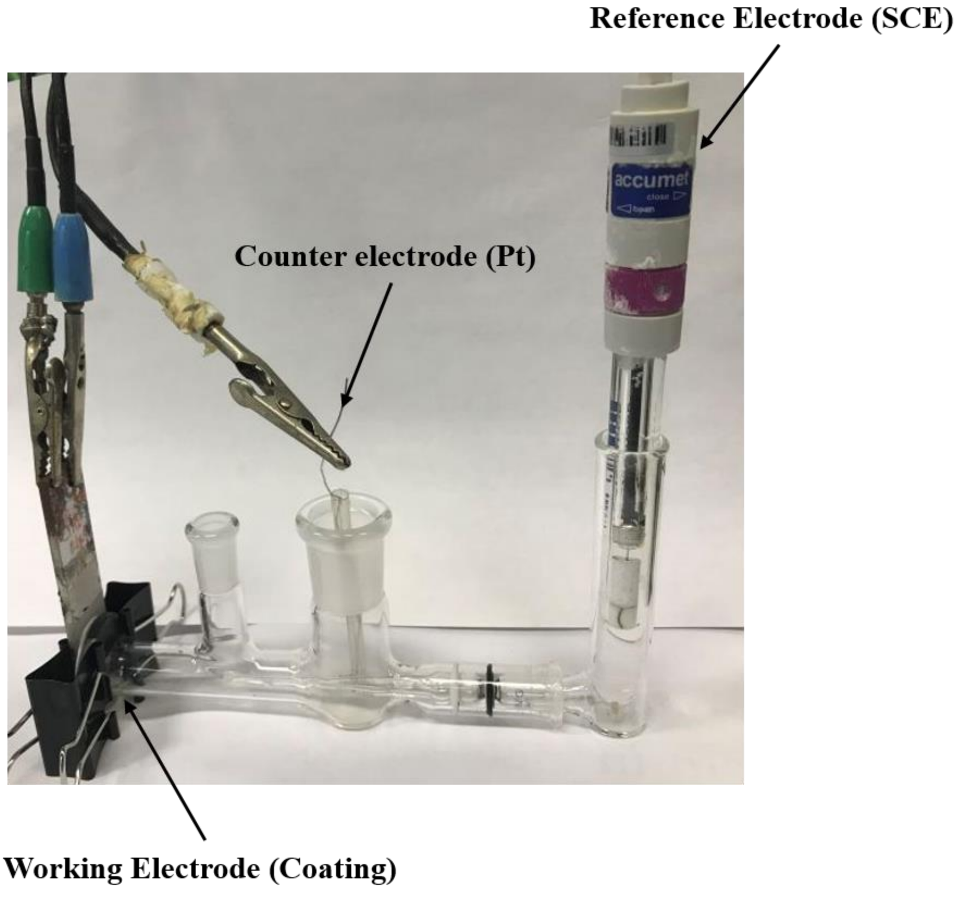

Figure 3.6 Electrochemical test setup

3.2.6 Linear abrasion test

The abrasion resistance of the superhydrophobic coating was evaluated by a linear abrasion test [85, 113, 216-220]. The as-deposited coating was faced down to an 800-grit SiC sandpaper, and then a 100 g weight with 1 cm diameter was placed on the back of the coating sample. Considering the weight of coating sample (36 g), the contact pressure was calculated to be 2.2 kPa. The superhydrophobic coating sample, facing to sandpaper, was moved along the ruler for 10 cm as one cycle. The WCA and SA were measured every five cycles until the superhydrophobicity was lost (WCA < 150° and SA > 10°).

3.2.7 Microhardness test

The microhardness of the composite coating was measured by a Matsuzawa Seiki MHT-1 Vickers microhardness tester equipped with a diamond indenter. The indenter is in pyramid shape and has an angle of 136° between opposite faces. All microhardness indentations were conducted on the cross-sections of composite coatings. The cross-sectional surfaces were prepared by the metallography method in Section 3.1.4. The applied load (*F*) and dwell time were set to 100 g and 15 s. Once the test was completed, an integrated optical microscope was used to measure the lengths of the two diagonals of the diamond-shaped impression left by the diamond indenter. The average diagonal length in millimetre (*d*) was recorded and the microhardness value (*Hv*) was calculated by the equation below.

$$Hv = \frac{2F \sin\frac{136°}{2}}{d^2} \quad \text{……………………….………….3.1}$$

Where *F* is in *kgf* and *d* is in millimetres.

For each sample, five measurements were carried and the average value was recorded as the microhardness of the composite coating.

3.2.8 Reciprocating wear test

The tribological performance of composite coatings was investigated by a reciprocating cylinder-on-flat TE-77 tribometer (**Figure 3.7**) at a temperature of 23 ℃ - 25 ℃ and a humidity of about 40 %. An AISI-52100 stainless steel bearing cylinder roller (diameter of 6 mm, length of 10 mm) supplied by Bearing Warehouse Ltd was used as the counterbody. According to the datasheet given by the supplier, the roughness of the roller is less than 0.16 μm, and the hardness is 700 HV. Before the test, the counterpart cylinder and holder were cleaned with Isopropanol to remove dirt and grease. A separate new cylinder was employed for each test to avoid cross-contamination. The parameters of the test were set as the following: an applied load of 20 N, a sliding frequency of 1 Hz, sliding stroke of 2.69 mm, a testing time of 1000 s. The reciprocating wear test parameters were the same as the previous research of Ni-MoS_2 coating [6]. Coatings with porous structures are prone to damage under high contact pressure. Therefore, using the cylinder as a counterpart could avoid coating damage since the line contact (cylinder on the plate) pressure is lower than that of point contact (ball on the plate). Hertzian contact pressure was calculated to be 0.15 GPa, with the details of the calculation provided in Appendix A. The properties of pure nickel coatings were utilised for the Hertzian contact calculation.

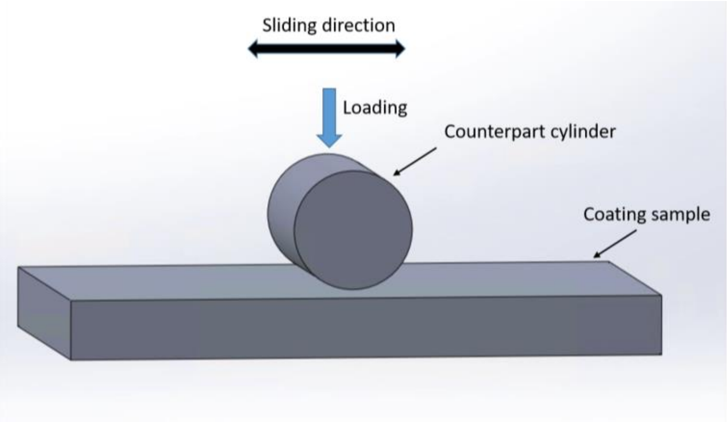

Figure 3.7 Schematic illustration of TE-77 line contact friction test

3.2.9 Error and uncertainty of measurement

The error and uncertainty of measurement for each test were estimated from the standard deviation and are shown as error bars in figures present in the next chapters. The standard deviation was calculated by the following equation.

$$\sigma = \sqrt{\frac{1}{N}\sum_{i}^{N}(x_i - \mu)^2} \quad \ldots\ldots \; 3.2$$

Where σ is the standard deviation, N is the number of obtained values, x_i is the individual measured value, and μ is the mean of all values.

4 Superhydrophobic composite coatings

4.1 Introduction

From the literature review, transition metal dichalcogenides (TMD) such as MoS_2 and WS_2 particles with very low surface free energies are ideal candidates for the preparation of superhydrophobic surfaces. So far, many studies have successfully developed superhydrophobic composite coatings by adding these particles into conventional plating baths. However, due to the conductive or semi-conductive nature of these particles, these electrodeposited superhydrophobic coatings suffer from non-compact and porous structures, which limits their long-term durability in practical engineering applications.

Additionally, MoS_2 and WS_2 are soft solid lubricant materials. The co-deposition of these particles may result in weak mechanical robustness of composite coatings. Consequently, during real applications, the delicate surface structure could easily be damaged even with a slight fingernail scratch, therefore shortening their service life. According to Zhao et al. [13], Ni-WS_2 coating quickly lost superhydrophobicity within 125 cm under the pressure of 2.83 kPa in the linear abrasion test.

The research in this chapter aims to develop a robust superhydrophobic coating with improved abrasion resistance. Based on the review in Section 2.4, the addition of another type of particle (with different conductivity) into the existing composite coating system (e.g. Ni-WS_2) might be an effective method to enhance the abrasion resistance. Specifically, this chapter can be divided into two main parts. The first part investigated nickel single-particle composite coating (Ni-MoS_2 and Ni-WS_2). The effect of particle size and deposition time on surface morphology, surface roughness and surface wettability were studied. After that, the optimum process parameters (particle size and coating time) were used for the electrodeposition of nickel hybrid composite coatings in the second part. Different particle combinations were used to prepare nickel hybrid composite coatings, and their effects on final coating properties were investigated.

4.2 Results and analysis

4.2.1 Nickel single-particle composite coatings

This section investigated nickel single-particle composite coatings. MoS_2 and WS_2 particles with different sizes were respectively co-deposited into the Ni matrix via electrodeposition. Process parameters, including deposition time and particle size, were controlled to investigate their influences on surface morphology, surface topography and surface wettability.

The secondary electron SEM images of as-received MoS_2 and WS_2 particles are shown in **Figure 4.1** and **Figure 4.2**, respectively. For each type of MoS_2 and WS_2, particle size was measured on the SEM image using imageJ software, and the results are displayed in **Figure 4.1 (c and f)** and **Figure 4.2 (c and f)**. The number of particles selected for the particle size measurement was 100, and the mean size of each type of particle was obtained by taking the average of these measured values. From **Figure 4.1**, it can be observed that both type one (**Figure 4.1 a and b**) and type two (**Figure 4.1 d and e**) MoS_2 particles are randomly shaped and exhibit flake-like structures. The mean sizes of type one and type two MoS_2 particles were measured to be 1.2 μm and 4.8 μm, which are greater than the sizes reported by suppliers (**Table 3.3**). **Figure 4.2** shows that type one WS_2 particles are in angular shapes with a mean size of 275 nm (**Figure 4.2 a-c**), while type two WS_2 particles are in flake-like shapes with a mean size of 1.1 μm (**Figure 4.2 d-f**). The measured particle sizes of both types of WS_2 particles are also greater than the sizes reported by suppliers. The discrepancies between the measured particle sizes and reported sizes may be due to agglomeration caused by long-time storage (5 years since purchased) [221]. In the following sections, the measured particle sizes will be used as particle parameters. For the deposition of each nickel single-particle composite coating sample, sample designation and corresponding parameters can be found in **Table 3.4**.

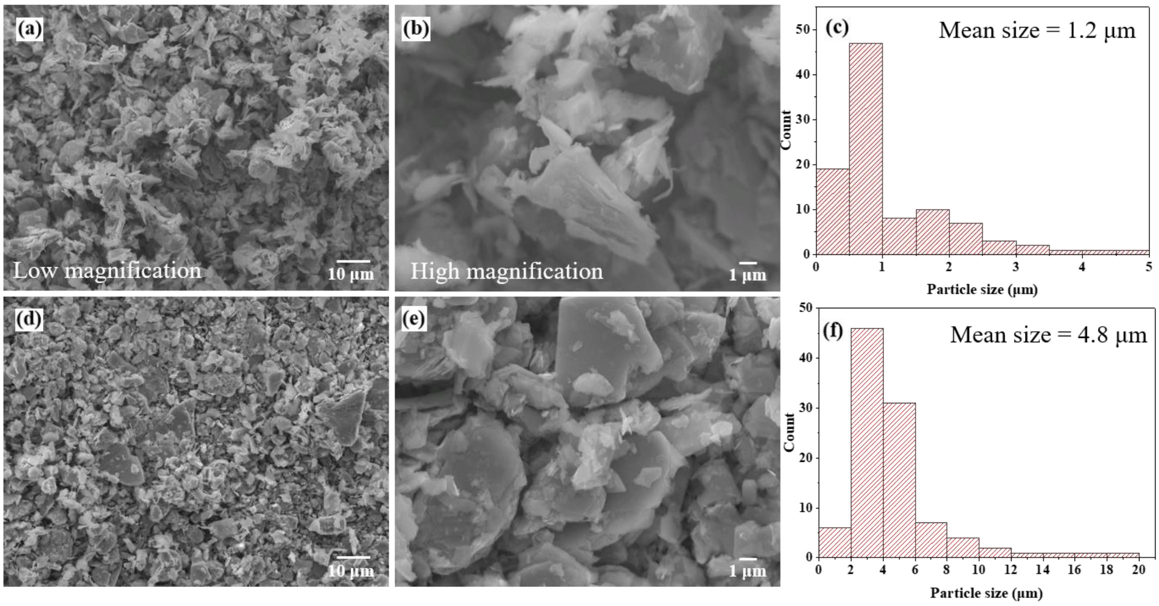

Figure 4.1 (a-b) Secondary electron SEM images of as-received type one MoS_2 particle at low and high magnifications respectively; (c) particle size distribution of type one MoS_2; (d-e) Secondary electron SEM images of as-received type two MoS_2 particles at low and high magnifications respectively; (f) particle size distribution of type two MoS_2.

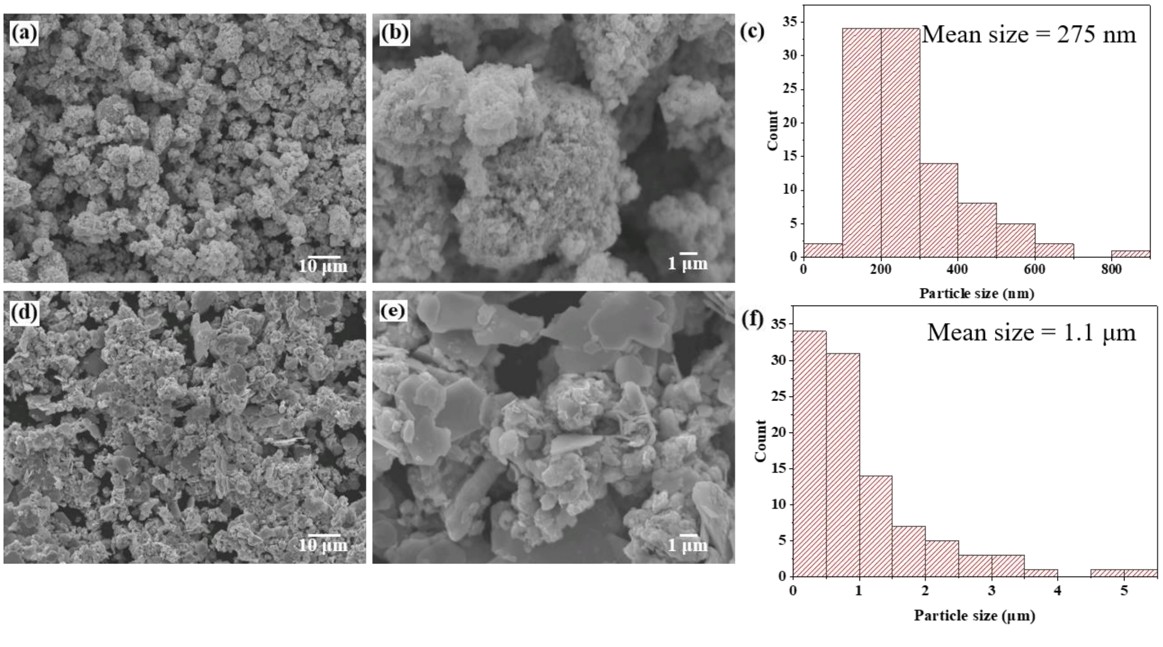

Figure 4.2 Secondary electron SEM images of as-received type one WS_2 particle at low and high magnifications respectively; (c) particle size distribution of type one WS_2; (d-e) Secondary electron SEM images of as-received type two WS_2 particles at low and high magnifications respectively; (f) particle size distribution of type two WS_2.

4.2.1.1 Morphology and compositional analysis

The SEM images of Ni-MoS_2 coatings are shown in **Figure 4.3**. Sample M1 (particle size: 1.2 μm, deposition time: 30 min) has a rough surface morphology (**Figure 4.3 a**). The high magnification SEM image reveals that M1 coating surface was porous and consisted of many loosely attached MoS_2 particles. (**Figure 4.3 b**). In **Figure 4.3 (e-f)**, a similar morphology can be on the sample M3 (particle size: 4.8 μm, deposition time: 30 min). As the deposition time increased from 30 min to 60 min, the surface morphology of Sample M4 (particle size: 4.8 μm, deposition time: 60 min) remained rough (**Figure 4.3 g-h**). However, Sample M2 (particle size: 1.2 μm, deposition time: 60 min) showed smooth surface morphology, and some holes with a diameter of about 110 μm were observed on the coating surface (**Figure 4.3 c**). According to the study conducted by Zhao et al. [13], the formation of holes might be caused by hydrogen evolution during electrodeposition.

Figure 4.4 shows the EDS results of nickel single-particle composite coatings. As shown in **Figure 4.4 (a)**, the EDS analysis was performed on an area of 1200 μm × 850 μm on the Sample M1 (particle size: 1.2 μm, deposition time 30 min). The EDS spectrum and quantitative analysis of Sample M1 are shown in **Figure 4.4 (b)** and **Figure 4.4 (c)**. For each sample, a single EDS analysis was conducted on the central area of the coating surface. This specific location was chosen to avoid the edge effect, which can result in non-uniform deposition due to the higher current density at the edges or corners of the substrate. It can be noted that the ratio of element molybdenum (8.77 at%) and element sulphur (19.86 at%) is 1:2.3, which is roughly consistent with the element ratio in MoS_2 (1:2). The MoS_2 particle content in the Sample M1 (29.4 wt%) was obtained by adding the weight percentage of element molybdenum (16.73 wt%) and element sulphur (12.65 wt%). The particle content of other nickel single-particle composite coating was obtained in the same way. **Figure 4.4 (d)** shows the EDS results of Ni-MoS_2 coatings. Both particle size and deposition time can affect the MoS_2 content in composite coatings. Smaller particles (1.2 μm) were easier to be co-deposited, and a longer deposition time (60 min) resulted in higher particle content in the coatings. For Ni-MoS_2 coatings, the highest particle content in the coating was 42.2 wt%, achieved by using a particle size of 1.2 μm and a deposition time of 60 min.

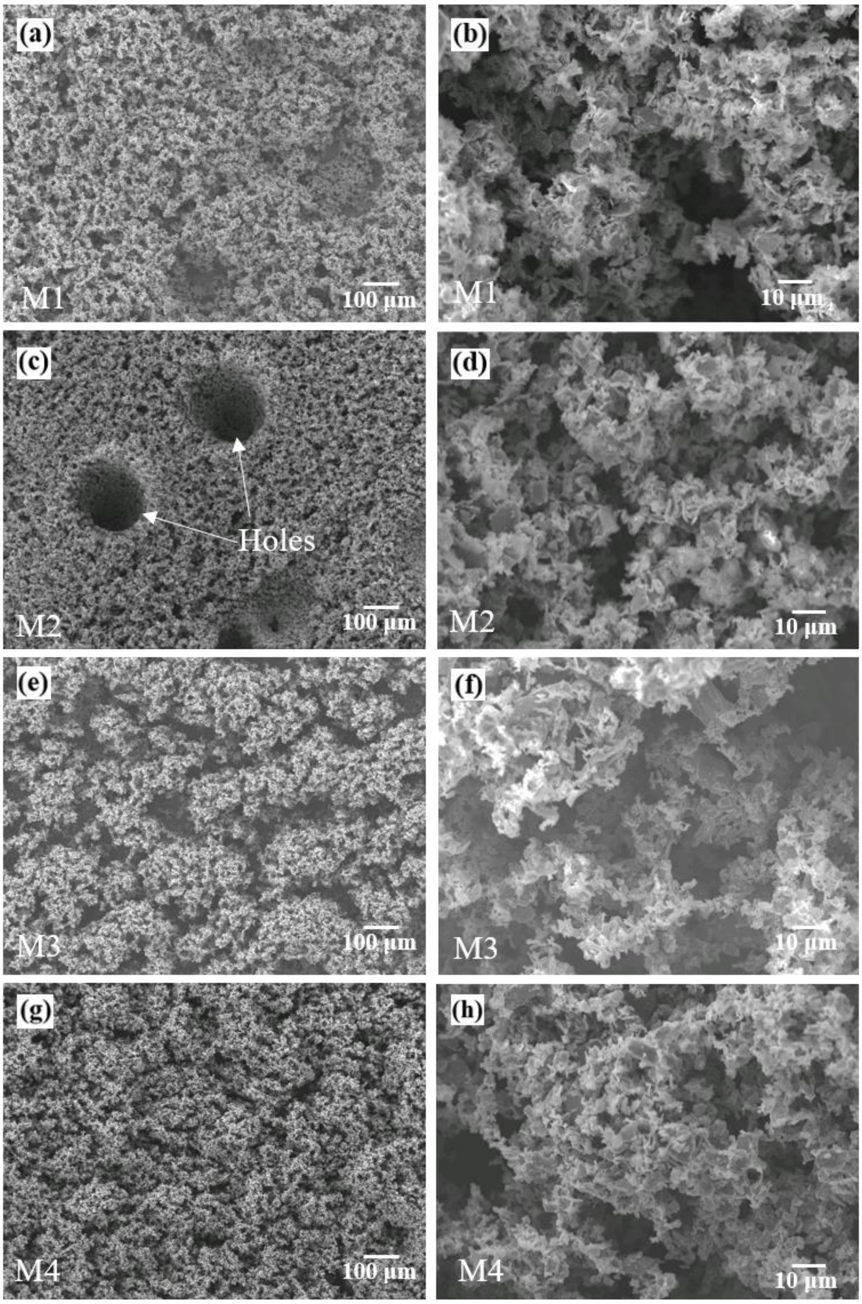

Figure 4.3 Secondary electron SEM images of Ni-MoS_2 coating samples deposited with different particle size and various deposition time (a-b) M1, 1.2 µm, 30 min at low and high magnifications respectively; (c-d) M2, 1.2 µm, 60 min at low and high magnifications respectively (e-f) M3, 4.8 µm, 30 min at low and high magnifications respectively; (g-h) M4, 4.8 µm, 60 min at low and high magnifications respectively.

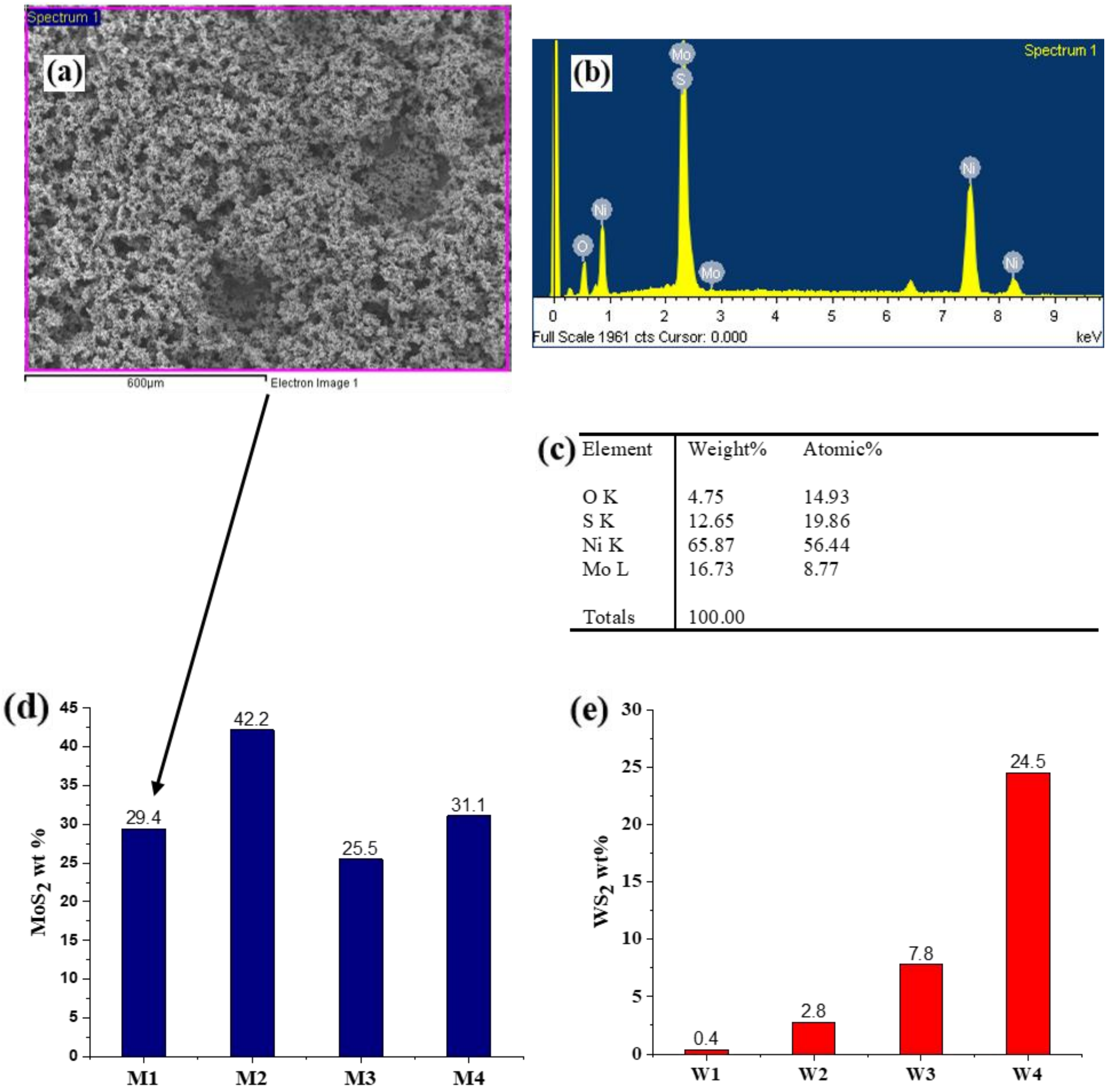

Element	Weight%	Atomic%
O K	4.75	14.93
S K	12.65	19.86
Ni K	65.87	56.44
Mo L	16.73	8.77
Totals	100.00	

Figure 4.4 (a) EDS analysis performed on Sample M1 coating surface; (b) EDS spectrum of the Sample M1; (c) EDS quantitative analysis of the Sample M1; (d) EDS results of Ni-MoS$_2$ coatings prepared with different particle size and deposition time; (e) EDS results of Ni-WS$_2$ coatings with different particle size and deposition time.

Ni-WS$_2$ coatings showed different surface morphologies with both the particle size and deposition time. For particle size of 275 nm, the Ni-WS$_2$ coating after 30 min exhibited a rough morphology containing many round nodular protrusions (**Figure 4.5 a**). These round nodular protrusions were determined as Ni. A high magnification image also showed that almost no WS$_2$ particles were co-deposited (**Figure 4.5 b**). As the deposition time increased to 60 min, the coating surface became porous. Very few WS$_2$ clusters were attached to the protruding surface, forming a "cauliflower-like" appearance (**Figure 4.5 c**). On the other hand, Ni-WS$_2$ coating with a larger particle size (1.1 µm) exhibited more "cauliflower-like" patterns (**Figure**

4.5 e-h). Further increase in deposition time (30 min to 60 min), the “cauliflower-like” surface morphology changed from sparse in **Figure 4.5 (e)** to dense in **Figure 4.5 (g)**, which meant more WS_2 particles were attached to the coating surface. Under high magnification, Ni-WS_2 coatings also revealed non-compact surface structures **(Figure 4.5 b, d, f, h)**.

The EDS result in **Figure 4.4 (e)** shows the particle content in each Ni-WS_2 coating sample. For Ni-WS_2 deposited with smaller particle (275 nm), the particle content was only 0.4 wt% with a deposition time of 30 min. Although WS_2 particle content showed a slight increase with a longer deposition time (60 min), the incorporated WS_2 was still less than 3 wt%. On the other hand, the particle content detected in Ni-WS_2 coating deposited with larger particle (1.1 μm) increased from 7.8 wt% to 24.5 wt% as the deposition time increased from 30 min to 60 min. The EDS results revealed that the particle size is an important factor affecting the amount of co-deposited particles. In the discussion section, the effect of particle size will be further analysed.

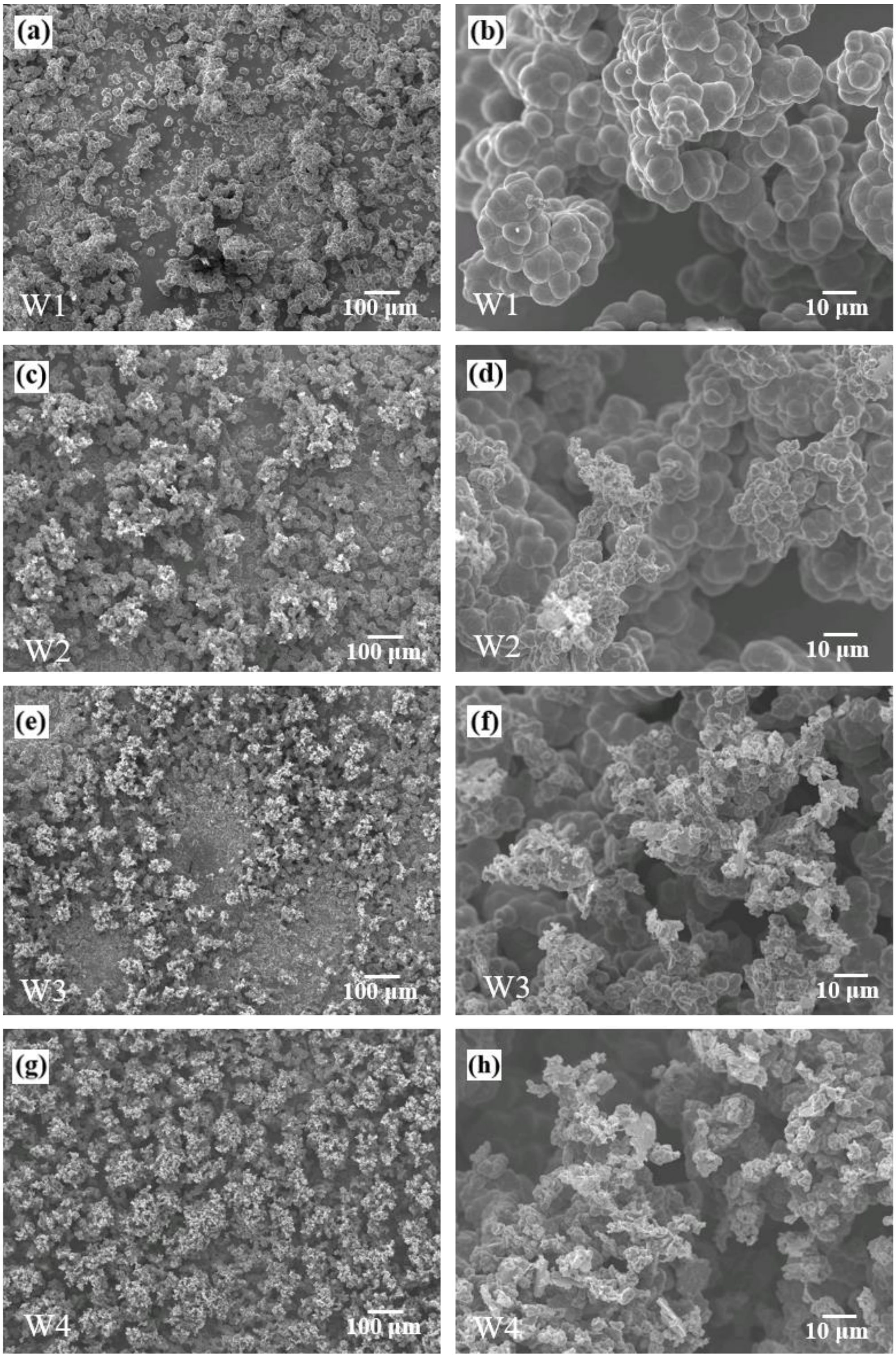

Figure 4.5 Secondary electron SEM images of Ni-WS$_2$ coating samples deposited with different particle size and various deposition time (a-b) W1, 275 nm, 30 min at low and high magnifications respectively; (c-d) W2, 275 nm, 60 min at low and high magnifications respectively (e-f) W3, 1.1 µm, 30 min at low and high magnifications respectively; (d) W4, 1.1 µm, 60 min at low and high magnifications respectively. Particle concentration for all coatings is 10 g/L.

The cross-section of Sample M2 was analysed to examine the coating structure. This cross-section was prepared using the cryogenic fracturing method described in Section 3.1.4. Only Sample M2 was selected as the representative sample for cross-sectional observation, as all nickel single-particle composite coatings exhibit similar coating structures. As shown in **Figure 4.6 (a)**, Sample M2 coating has a thickness of 180 μm and exhibits a sponge-like structure. Nodular growth of deposit was observed in the coating near the substrate, while numerous MoS_2 particles (confirmed by EDS) were loosely attached to the outermost layer of coating. The EDS analysis was performed on the cross-section of Sample M2. Ten EDS spectrums were analysed from the coating/substrate interface to the coating surface (**Figure 4.6 b**). Each spectrum has an area of 300 μm × 18 μm. **Figure 4.6 (c)** shows the EDS results obtained in each spectrum. It can be noted that nickel content is greater than 90 wt% from spectrum 1 to spectrum 5. The high nickel content indicates that the nodular shaped deposit observed in the first 90 μm layer of coating mainly consists of nickel. From spectrum 6 to spectrum 10, it can be observed that the element sulphur (2.4 wt% to 12.7 wt%) and element molybdenum (2.5% to 18.6 wt%) gradually increase, which indicates that more MoS_2 particles were embedded into the coating with the progression of electroplating.

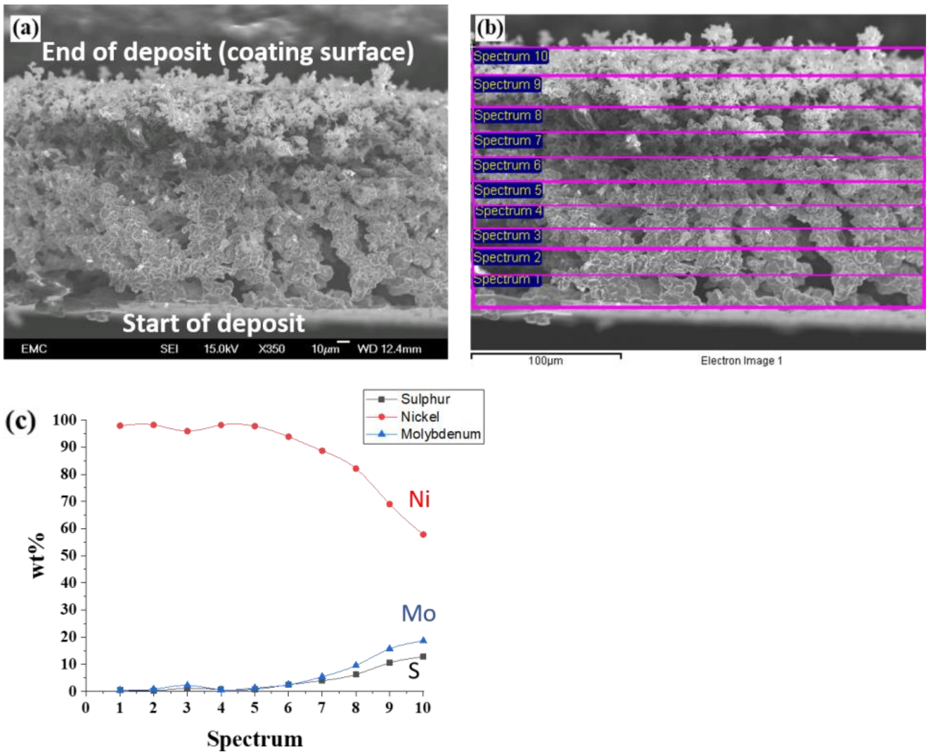

Figure 4.6 (a) Secondary electron SEM image of the cross-section of Sample M2 coating (particle size: 1.2 μm, deposition time: 60 min); (b) EDS analysis performed on the cross-section; (c) EDS quantitative result of each spectrum on the cross-section.

4.2.1.2 Surface topography and superhydrophobicity

3D model images of Ni-MoS_2 and Ni-WS_2 coatings are shown in **Figure 4.7** and **Figure 4.8**, respectively. The roughness of Ni-MoS_2 coatings prepared with 30 min deposition time (Sample M1 and Sample M3) was about 30 μm (**Figure 4.7 a and c**). The increase in deposition time (60 min) led to smoother surfaces with lower average roughness values (**Figure 4.7 b and d**). This finding is consistent with the SEM images and EDS results in the previous section. As the deposition time increased, more MoS_2 particles were co-deposited, which resulted in higher MoS_2 contents in the coating. For Ni-WS_2 coating, the roughness increased with increasing deposition time. EDS analysis (**Figure 4.4 e**) shows that very few WS_2 particles (< 10 wt%) were co-deposited with a short electrodeposition time (30 min). Since the dendritic growth of deposit only occurred at particle-adsorbed positions, the low content of WS_2 particles may not lead to very rough coating surfaces (**Figure 4.8 a and c**). However, as the deposition time increased to 60 min, more WS_2 particles were adsorbed on the coating surface, which promoted the dendritic growth and resulted in high surface roughness (**Figure 4.8 b and d**).

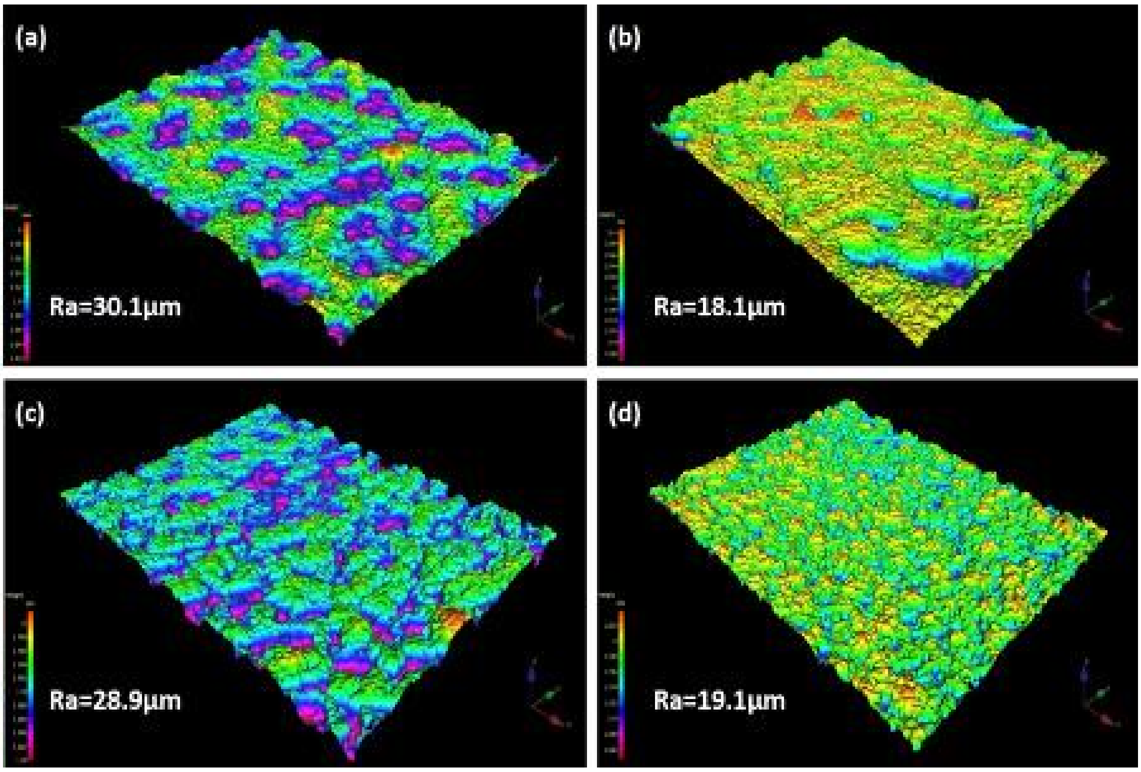

Figure 4.7 3D model of Ni-MoS_2 coatings with particle size and deposition time of (a): M1, 1.2 μm, 30 min; (b): M2, 1.2 μm, 60 min; (c): M3, 4.8 μm, 30 min; (d) M4, 4.8 μm, 60 min.

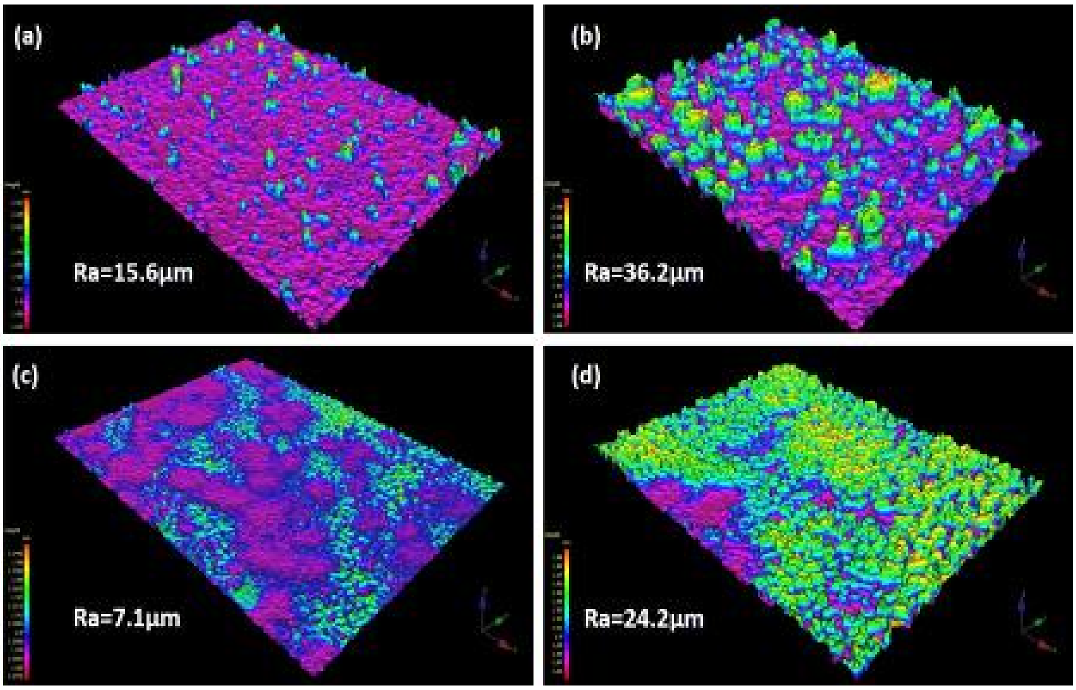

Figure 4.8 3D model of Ni-WS_2 coatings with particle size and deposition time of (a): W1, 275 nm, 30 min; (b): W2, 275 nm, 60 min; (c): W3, 1.1 μm, 30 min; (d) W4, 1.1 μm, 60 min.

Before measuring the water contact angles, Ni-MoS_2 and Ni-WS_2 coatings were exposed to the ambient environment for one week to allow for the gradual evaporation of residual solution from the electroplating process. Previous studies also reported a wettability transition from hydrophilicity to superhydrophobicity following one week of air exposure[95, 96, 100]. This transition was attributed to the adsorption of low surface energy airborne hydrocarbons [85].

Table 4.1 summarises the contact angle values of different coatings and their corresponding plating parameters and surface roughness. The relationship between surface roughness and water contact angle is illustrated in **Figure 4.9**. It can be noted that increasing roughness resulted in higher water contact angles, which was in agreement with He et al. [15] 's work. In addition, superhydrophobicity (contact angle >150º) was achieved by Ni-MoS_2 coating with 30 min deposition time and Ni-WS_2 coating with 60 min deposition time. For nickel single-particle coatings, the highest contact angle was achieved by Ni-WS_2 coating with 1.1 μm particle size and 60 min deposition time (158.8 ± 2.5º). This value is very consistent with previous research, which showed a superhydrophobic Ni-WS_2 coating had a contact angle of 158.3° [13].

Pure Ni coating has a contact angle of 77.6º and is intrinsically hydrophilic. According to Wenzel's model [73], increasing surface roughness should decrease contact angles. However, the results in **Table 4.1** indicate that the water contact angle is higher when placed on a rougher surface. The contradictory finding can be explained by Cassie-Baxter's model [75]. The rough surfaces of both Ni-MoS_2 and Ni-WS_2 coatings allow air to be entrapped between surface protrusions, thereby preventing the penetration of water droplets.

Table 4.1 Summary of nickel single-particle composite coatings

Sample	Deposition time and particle size	Average roughness, Ra (µm)	Water contact angle (degree)
M1	30 min; 1.2 µm	30.1	147.0 ± 3.1
M2	60 min; 1.2 µm	18.1	143.7 ± 4.5
M3	30 min; 4.8 µm	28.9	155.5 ± 1.9
M4	60 min; 4.8 µm	19.1	145.3 ± 3.6
W1	30 min; 275 nm	15.6	116.3 ± 15.9
W2	60 min; 275 nm	36.2	153.5 ± 8.3
W3	30 min; 1.1 µm	7.1	144.5 ± 2.5
W4	60 min; 1.1 µm	24.2	158.8 ± 2.5

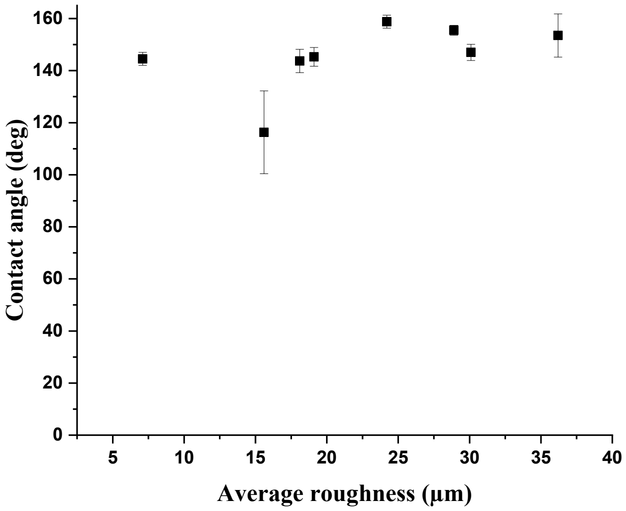

Figure 4.9 Water contact angle as a function of surface roughness for nickel single-particle composite coatings

4.2.2 Nickel hybrid composite coatings

Although using the appropriate parameters (particle size and deposition time) can develop superhydrophobic nickel single-particle coatings, porous coating structures were observed for all coating samples. In order to improve the compactness of nickel composite coatings, more than one type of particles was co-deposited into the nickel matrix. The idea of combining different particles was inspired by a previous study, which showed Ni-MoS_2-Al_2O_3 coatings having a dense structure [201]. In this research, two types of particles (SiC and TiO_2) were added into Ni-MoS_2 and Ni-WS_2 coating systems. The sample designations and particle combinations of nickel hybrid composite coatings can be found in **Table 3.5**. The effects of different particle combinations on surface morphology, coating topography and surface wettability were investigated. In addition, to evaluate the compactness of nickel hybrid composite coatings, the cross-sectional view of each coating was investigated.

4.2.2.1 Surface morphologies and cross-sections of nickel hybrid composite coating

Figure 4.10 shows the surface morphology and cross-section of Ni-MoS_2-WS_2 coating. Ni-MoS_2-WS_2 exhibited a rough surface morphology (**Figure 4.10 a**). The high-magnification SEM image reveals that many particles are bonded to the surface, forming the top layer of the Ni-MoS_2-WS_2 coating. (**Figure 4.10 b**). The SEM images of the cross-section of Ni-MoS_2-WS_2 coating with low and high magnification are shown in **Figure 4.10 (c) and (d)**. The thickness of Ni-MoS_2-WS_2 coating was measured to be 126.8 µm. It can be noted that Ni-MoS_2-WS_2 coating consists of two layers (shown in **Figure 4.10 c**). The first layer is relatively dense and has a thickness of 80 µm. Small cracks at the interface between coating and substrate could be observed. These cracks might be formed during the preparation of cross-section (**Figure 4.10 c**). The second layer is porous and consists of bonded particles. The dark grey lumps observed in the coating (**Figure 4.10 d**) might be the embedded particles, which needs to be verified by EDS analysis in future work.

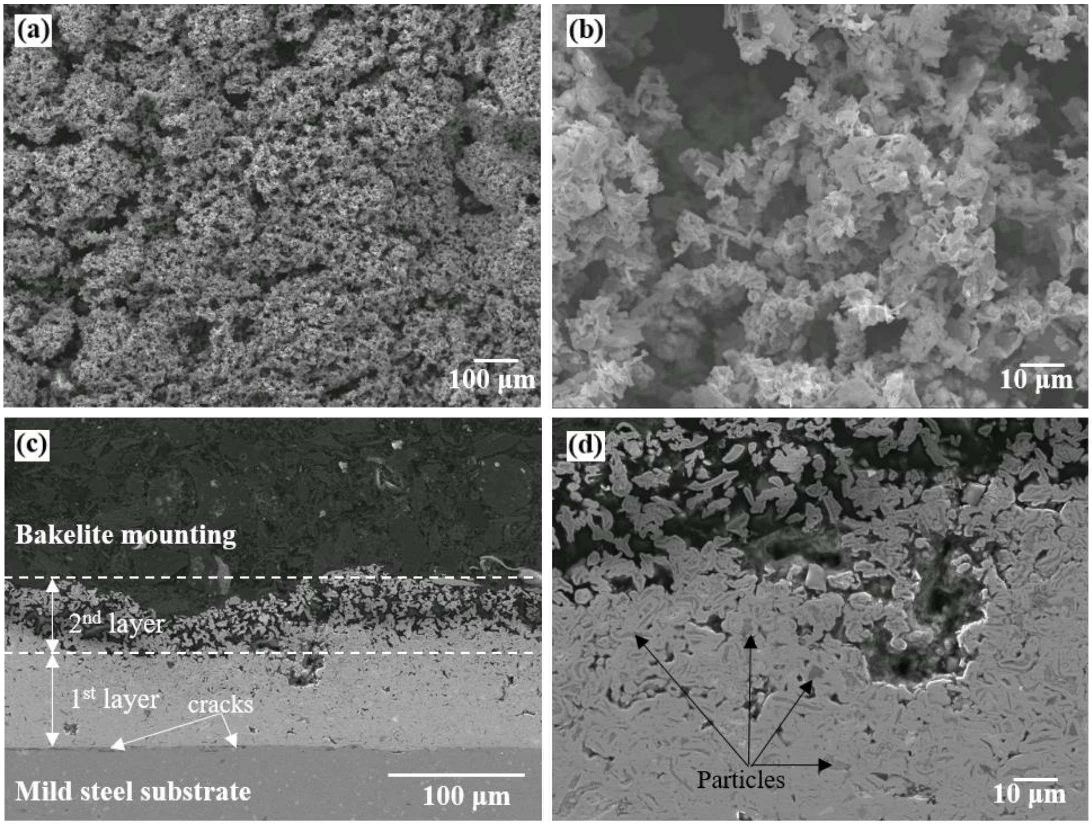

Figure 4.10 Secondary electron SEM images of surface morphology of Ni-MoS_2-WS_2 coating with (a) low magnification and (b) high magnification; Cross-sectional view of Ni-MoS_2-WS_2 with (c) low magnification and (d) high magnification.

SEM images of nickel hybrid composite coatings containing SiC particles are displayed in **Figure 4.11**. It can be noted that composite coatings containing the same size of SiC particles exhibit similar surface morphologies. The coating surfaces of Ni-SiC (40 nm)-MoS_2 and Ni-SiC (40 nm)-WS_2 are relatively smoother compared to other hybrid composite coatings and are composed of numerous closely packed small nodules. (**Figure 4.11 a and e**). Ni-SiC (8.5 µm)-MoS_2 and Ni-SiC (8.5 µm)-WS_2 show rough surfaces with sparsely distributed large nodules (**Figure 4.11 c and g**). The high magnification SEM images of each coating are shown as well. For the nickel hybrid composite coatings containing 40 nm SiC, the nodular growth of the deposit can be identified. Moreover, only a few particles are attached to the coating surface (**Figure 4.11 b and f**). In contrast, numerous embedded particles can be observed on the composite coating surfaces when 8.5 µm SiC particles are used for co-deposition (**Figure 4.11 d and h**). EDS results of each nickel hybrid composite coatings are shown in **Table 4.2**. It can be noted that the SiC contents in Ni-SiC (40 nm)-MoS_2 and Ni-SiC (40 nm)-WS_2 coatings are lower than that in Ni-SiC (8.5 µm)-MoS_2 and Ni-SiC (8.5 µm)-WS_2 coatings, which indicates that the co-deposition of nano-sized SiC particles are more difficult than micron-sized SiC particles. Similar findings have also been reported in the study conducted by Garcia, Fransaer and Celis [222]. Moreover, EDS results also reveal that the content of both MoS_2 and WS_2 particles in hybrid composite coatings can be affected by the other co-deposited particles. The MoS_2 and WS_2 contents are 23.1 wt% and 6.1 wt% when the other type of co-deposited particle is 8.5 μm SiC. However, the content of MoS_2 and WS_2 dropped to 2.0 wt% and 1.7 wt% when 40 μm SiC was co-deposited. This finding has not yet been reported by other research, and the underlying mechanism is not well understood. In future work, the deposition mechanism of hybrid composite coatings will be investigated.

The cross-sections of Ni-SiC-MoS_2 and Ni-SiC-WS_2 coatings are shown in **Figure 4.12**. By comparison, it can be noticed that the coating structures are largely dependent on the size of SiC particles used for co-deposition. For hybrid composite coatings deposited with 40 nm SiC addition, the coating structures are dense, and no obvious voids can be observed (**Figure 4.12 a and c**). However, the top layers of coatings are relatively rough. In addition, very few particles are embedded within the nickel matrix, which is in agreement with the EDS results. On the other hand, hybrid composite coatings deposited with 8.5 μm SiC particles have a greater thickness and more embedded particles. However, small voids and dendritic growth of coating can be observed from the cross-sections of Ni-SiC (8.5 μm)-MoS_2 and Ni-SiC (8.5 μm)-WS_2, respectively (**Figure 4.12 b and d**).

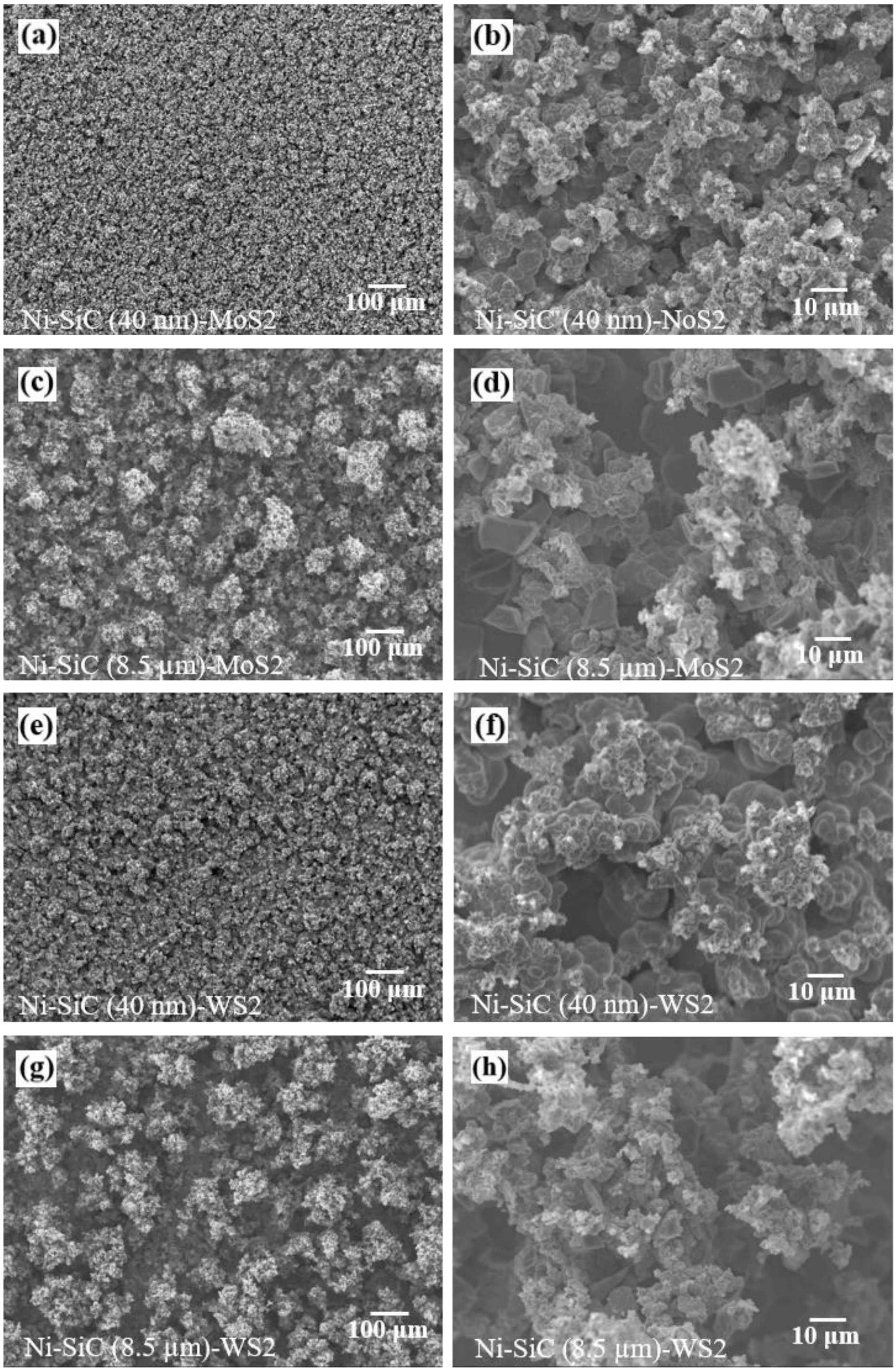

Figure 4.11 Secondary electron SEM images of surface morphologies of (a-b) Ni-SiC (40 nm)-MoS_2 coating at low and high magnifications respectively; (c-d) Ni-SiC (8.5 μm)-MoS_2 coating at low and high magnifications respectively; (e-f) Ni-SiC (40 nm)-WS_2 coating at low and high magnifications respectively; (g-h) Ni-SiC (8.5 μm)-MoS_2 coating at low and high magnifications respectively.

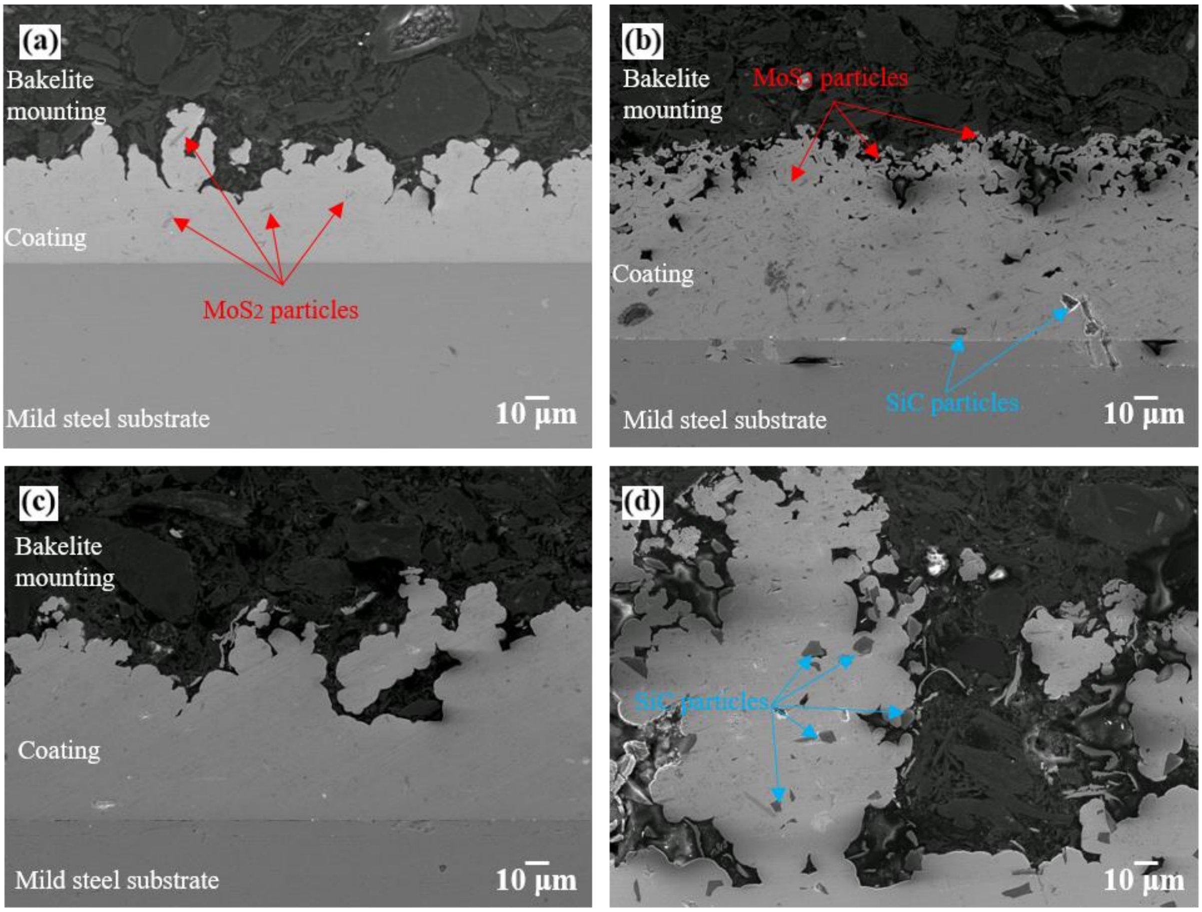

Figure 4.12 Secondary electron SEM images of cross-sectional views of (a) Ni-SiC (40 nm)-MoS_2; (b) Ni-SiC (8.5 µm)-MoS_2; (c) Ni-SiC (40 nm)-WS_2; (d) Ni-SiC (8.5 µm)-WS_2.

Table 4.2 EDS results of Ni-SiC-MoS_2 and Ni-SiC-WS_2 coatings

Sample	MoS_2 (wt%)	WS_2 (wt%)	SiC (wt%)
Ni-SiC (40 nm)-MoS_2	2.0	N/A	3.9
Ni-SiC (8.5 µm)-MoS_2	23.1	N/A	12.5
Ni-SiC (40 nm)-WS_2	N/A	1.7	3.9
Ni-SiC (8.5 µm)-WS_2	N/A	6.1	23.0

Surface morphologies and cross-sections of hybrid composite coatings containing TiO_2 particles are shown in **Figure 4.13**. It can be seen that Ni-TiO_2-MoS_2 coating and Ni-TiO_2-WS_2 coating have completely different surface morphologies and coating structures. Ni-TiO_2-MoS_2 coating exhibits a rough surface (**Figure 4.13 a**). The cross-sectional view shows that the Ni-TiO_2-MoS_2 coating is sponge-like and full of pores (**Figure 4.13 c**). In contrast, the structure of Ni-TiO_2-WS_2 coating is relatively dense (**Figure 4.13 f**), and the coating surface is composed of numerous nodules (**Figure 4.13 d**). The high magnification SEM image exhibits that a great amount of particles are loosely attached to the surface of Ni-TiO_2-MoS_2 coatings (**Figure 4.13 b**). In contrast, the SEM image of Ni-TiO_2-WS_2 coating under high magnification shows nodular growth of nickel deposit with very few particles attached (**Figure 4.13 e**). EDS results in **Table 4.3** also confirm that the particle content in Ni-TiO_2-MoS_2 coating is higher than that in Ni-TiO_2-WS_2 coating.

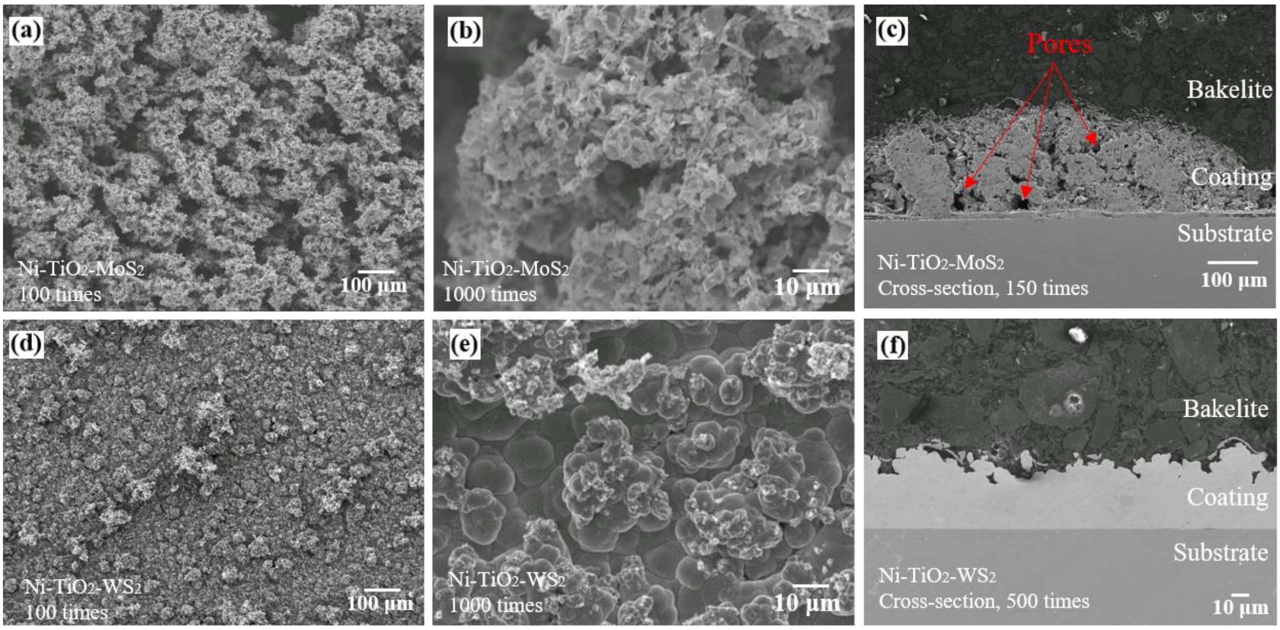

Figure 4.13 Secondary electron SEM images of (a-b) surface morphologies of Ni-TiO_2-MoS_2 at low and high magnifications respectively; (c) Cross-section of Ni-TiO_2-MoS_2 with a low magnification; (d-e) surface morphologies of Ni-TiO_2-WS_2 at low and high magnifications respectively; (f) cross-section of Ni-TiO_2-WS_2 with a high magnification.

Table 4.3 EDS results of Ni-TiO_2-MoS_2 and Ni-TiO_2-WS_2 coating

Sample	MoS_2 (wt%)	WS_2 (wt%)	TiO_2 (wt%)
Ni-TiO_2-MoS_2	38.6	N/A	7.5
Ni-TiO_2-WS_2	N/A	1.7	2.5

4.2.2.2 Surface wettability of nickel hybrid composite coatings

The water contact angle on each nickel hybrid composite coating was tested. All nickel hybrid composite coatings achieved superhydrophobicity after one week of exposure to ambient air, as indicated by the water contact angle measurements summarised in **Table 4.4**. Initially, freshly prepared coatings exhibited superhydrophilicity, with water droplets spreading quickly across the surfaces. A wettability transition phenomenon was observed during air exposure, as the water contact angle gradually increased over time. This finding suggests that a wettability transition occurred during a week exposure under ambient conditions, leading to the development of superhydrophobic properties.

Superhydrophobicity was achieved in nickel hybrid composite coatings with remarkably low MoS_2 or WS_2 content, as low as 1.7 wt% for both Ni-SiC (40 nm)-WS_2 and Ni-TiO_2-WS_2 coatings. This contrasts with previous studies by Zhao et al. [13] and He et al. [14], where the minimum particle content required for superhydrophobicity in Ni-P-WS_2 and Ni-WS_2 coatings was reported to be 3.6 wt% and 4.0 wt%, respectively. SEM images reveal that the Ni-SiC (40 nm)-MoS_2, Ni-SiC (40 nm)-WS_2, and Ni-TiO_2-WS_2 coatings exhibit hierarchical nodular surface structures, which is one of factors attributing to superhydrophobicity. Additionally, a wettability transition from hydrophilicity to superhydrophobicity was observed after one week of exposure. This suggests that the surface energy of these three coatings decreased during ambient exposure, possibly due to the adsorption of low-surface-energy airborne hydrocarbons [100].

Table 4.4 Surface topography and wettability of each nickel hybrid composite coating

Sample	Coating morphology and structure	Surface roughness (µm)	Water contact angle	Super hydrophobicity
Ni-MoS_2-WS_2	Rough and porous	20.0 ± 2.5	161.7 ± 3.0	Yes
Ni-SiC (40 nm)-MoS_2	Nodular structure but dense	3.2 ± 0.2	157.6 ± 2.0	Yes
Ni-SiC (8.5 µm)-MoS_2	Rough surface with few voids	24.3 ± 3.1	155.5 ± 3.9	Yes
Ni-SiC (40 nm)-WS_2	Nodular structure but dense	6.3 ± 1.0	158.6 ± 2.9	Yes

Sample	Coating morphology and structure	Surface roughness (µm)	Water contact angle	Super hydrophobicity
Ni-SiC (8.5 µm)-WS$_2$	"Dendrite-like" coating structure	31.8 ± 4.9	166.2 ± 1.6	Yes
Ni-TiO$_2$-MoS$_2$	Rough and porous	28.6 ± 3.6	159.2 ± 0.9	Yes
Ni-TiO$_2$-WS$_2$	Rough surface but dense structure	9.5 ± 1.2	155.6 ± 2.6	Yes

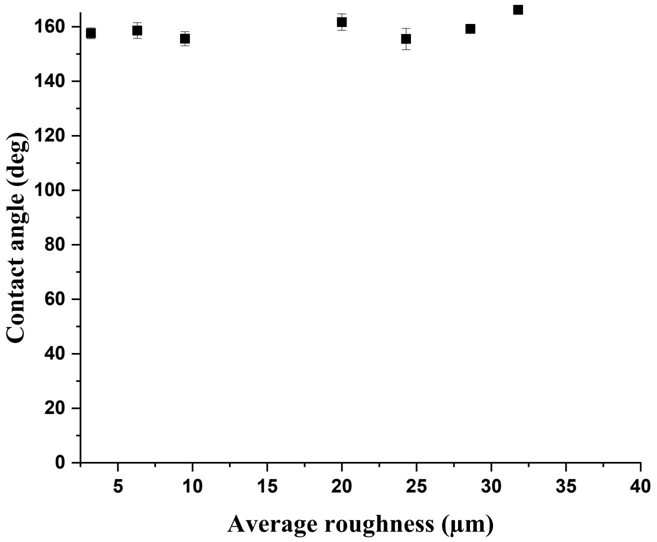

Figure 4.14 Water contact angle as a function of surface roughness for nickel hybrid composite coatings

4.2.3 The durability of hydrophobicity under water immersion

A water immersion test was conducted to evaluate the durability of the hydrophobicity of the deposited coatings. This test was performed exclusively on samples exhibiting superhydrophobicity, namely M3, W2, W4, Ni-MoS$_2$-WS$_2$, Ni-SiC (40 nm)-MoS$_2$, Ni-SiC (8.5 µm)-MoS$_2$, Ni-SiC (40 nm)-WS$_2$, Ni-SiC (8.5 µm)-WS$_2$, Ni-TiO$_2$-MoS$_2$ and Ni-TiO$_2$-WS$_2$. Other samples were not included in this test because, although they are hydrophobic, their water repellence properties are inferior to those of superhydrophobic coatings. Trials also demonstrated that these surfaces became completely wet shortly after immersion in water. The water immersion test results are shown in **Table 4.5**. It can be noted that most coating samples lost hydrophobic properties within one hour of the water immersion test. Ni-TiO$_2$-MoS$_2$ is the only sample demonstrating excellent durability. The coating maintained its hydrophobicity after being immersed in water for two days, which is significantly longer than the duration reported in a previous study on electrodeposited superhydrophobic Cu-MoS_2 coatings. In that study, the Cu-MoS_2 coating lost its hydrophobicity within 30 minutes [16]. The air layer observed on the coating surface (mentioned in Section 3.2.4) did not fade away in the water immersion test. The excellent durability might be attributed to the microporous and nanoporous structures (**Figure 4.13 c**) in which air can be entrapped. Water immersion test has been performed on Ni-TiO_2-MoS_2 coating sample three times, and the results showed good repeatability.

Table 4.5 Results of water immersion test

Sample	Time to maintain hydrophobic after being immersed in DI water
M3	20 – 30 min
W2	< 10 min
W4	< 10 min
Ni-MoS_2-WS_2	60 min
Ni-SiC (40 nm)-MoS_2	20 – 30 min
Ni-SiC (8.5 µm)-MoS_2	< 10 min
Ni-SiC (40 nm)-WS_2	< 10 min
Ni-SiC (8.5 µm)-WS_2	20 – 30 min
Ni-TiO_2-MoS_2	2 days
Ni-TiO_2-WS_2	10 – 20 min

4.2.4 Corrosion protection of the coatings

The potentiodynamic polarization tests were conducted to evaluate the corrosion improvement achieved by the superhydrophobic coating. Three samples were selected for the test: steel substrate, pure nickel coating, and Ni-SiC (8.5 µm)-WS_2. The steel substrate was chosen as a reference sample to assess the improvement that can be achieved by applying only the nickel coating and the superhydrophobic coating. Ni-SiC (8.5 µm)-WS_2 was selected as the representative of the superhydrophobic coating because it exhibits the highest water contact angle of 166.2 ± 1.6°. The potentiodynamic polarization test was conducted on each sample once, and the results are presented in **Figure 4.15**. The corrosion potential (E_{corr}) and corrosion current density (I_{corr}) were derived from the linear part of the polarisation curves through the Tafel extrapolation method. The polarisation resistance (R_p) was calculated by the Stern-Geary equation [223] shown below:

$$R_P = \frac{\beta_a \times \beta_c}{2.303 \times (\beta_a + |\beta_c|)} \dots\dots\dots\dots\dots\dots 4.1$$

where βa and βc are the anodic and cathodic Tafel slopes ($\Delta E/\Delta logi$) obtained from the linear region of potentiodynamic polarisation curves.

The corrosion rates of the substrate and coatings were determined by Equation 4.2 [224]:

$$Corrosion\ rate\ (\mu m\ per\ year) = \frac{i_{corr} \times a \times t}{\rho \times n \times F} \dots\dots\dots\dots\dots\dots 4.2$$

where i_{corr} is the corrosion current density (A/cm^2), a is the atomic mass (g/mol), t is time in seconds, ρ is the density of samples, n is the number of electrons transferred per molecule or atom of samples. F is the Faraday constant (96485 coulomb/mol). The important electrochemical parameters, including corrosion potential, corrosion current, polarisation resistance and corrosion rate, are summarised in Table 4.6.

By comparing the data in **Table 4.6**, it can be noted that the steel substrate has the most negative corrosion potential (E_{corr} = -0.69 V vs Ag/AgCl), suggesting that the steel substrate is susceptible to corrosion. With a layer of electrodeposited pure Ni, the corrosion potential shifted positively to -0.24 V vs Ag/AgCl, indicating that pure Ni coating provided corrosion protection for steel substrate. The corrosion potential of superhydrophobic Ni-SiC (8.5 µm)-WS_2 coating is the most positive (E_{corr} = -0.14 V vs Ag/Cl). From the perspective of thermodynamics, the Ni-SiC (8.5 µm)-WS_2 has the lowest tendency to corrode. In view of the kinetics of corrosion, the corrosion current density of Ni-SiC (8.5 µm)-WS_2 coating (I_{corr} = 4.29 × 10^{-7} A/cm^2) is much lower than that of steel substrate (I_{corr} = 1.48 × 10^{-5} A/cm^2) and pure Ni coating (I_{corr} = 4.36 × 10^{-6} A/cm^2). The corrosion inhibition efficiency (η) of the superhydrophobic Ni-WS_2-µSiC coating can be evaluated by [225].

$$\eta = \frac{|I_{corr\ steel\ substrate} - I_{corr\ coating}|}{I_{corr\ steel}} \times 100\% \dots\dots\dots\dots\dots\dots 4.3$$

Where I is the corrosion current density. η of Ni-SiC (8.5 µm)-WS_2 coating was calculated to be 97.1%, confirming its good corrosion protection. Moreover, the Ni-WS_2-µSiC coating has corrosion rate of 4.62 µm/year which is about 3700 times slower than the steel substrate (172 µm/year).

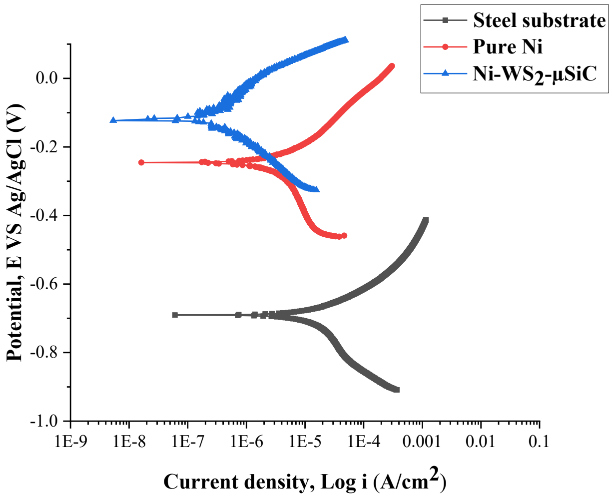

Figure 4.15 Potentiodynamic polarisation curves of the steel substrate, pure Ni coating, and Ni-SiC (8.5 µm)-WS_2 coatings.

Table 4.6 Derived results from the potentiodynamic polarisation test.

Sample	E_{corr} (V)	I_{corr} (A/cm^2)	Polarization resistance ($\Omega \cdot cm^2$)	Corrosion rate (µm/year)
Steel substrate	-0.69	1.48×10^{-5}	1904.76	172
Pure Ni	-0.24	4.36×10^{-6}	9811.55	0.47
Ni-SiC (8.5 µm)-WS_2	-0.14	4.29×10^{-7}	65401.05	0.046

The EIS test was conducted to further investigate the corrosion behaviour of the coating during the exposure to 3.5 wt% NaCl solution at room temperature. The same three samples, namely steel substrate, pure nickel coating and Ni-SiC (8.5 µm)-WS_2 were tested to evaluate the corrosion improvement and understand the corrosion mechanism. **Figure 4.16** shows both the Nyquist plots and Bode plots. The Nyquist plots of the steel substrate, pure Ni coating and superhydrophobic Ni-SiC(8.5 µm)-WS_2 coating exhibit three different capacitive loops (**Figure 4.16 a and b**). The corrosion resistance can be roughly estimated by the diameter of these capacitive loops. Therefore, it can be inferred that the corrosion resistance of the superhydrophobic Ni-SiC (8.5 µm)-WS_2 coating is better than that of steel substrate and pure Ni coating since the capacitive loop of Ni-SiC (8.5 µm)-WS_2 has the largest diameter. This finding is more obvious in Bode – impedance modulus (|Z|) vs log frequency plots (**Figure 4.16 c**). At the low frequency of 0.01 Hz, the |Z| value of Ni-WS_2-µSiC coating is about 15 times greater than that of pure Ni coating, 65 times compared with steel substrate.

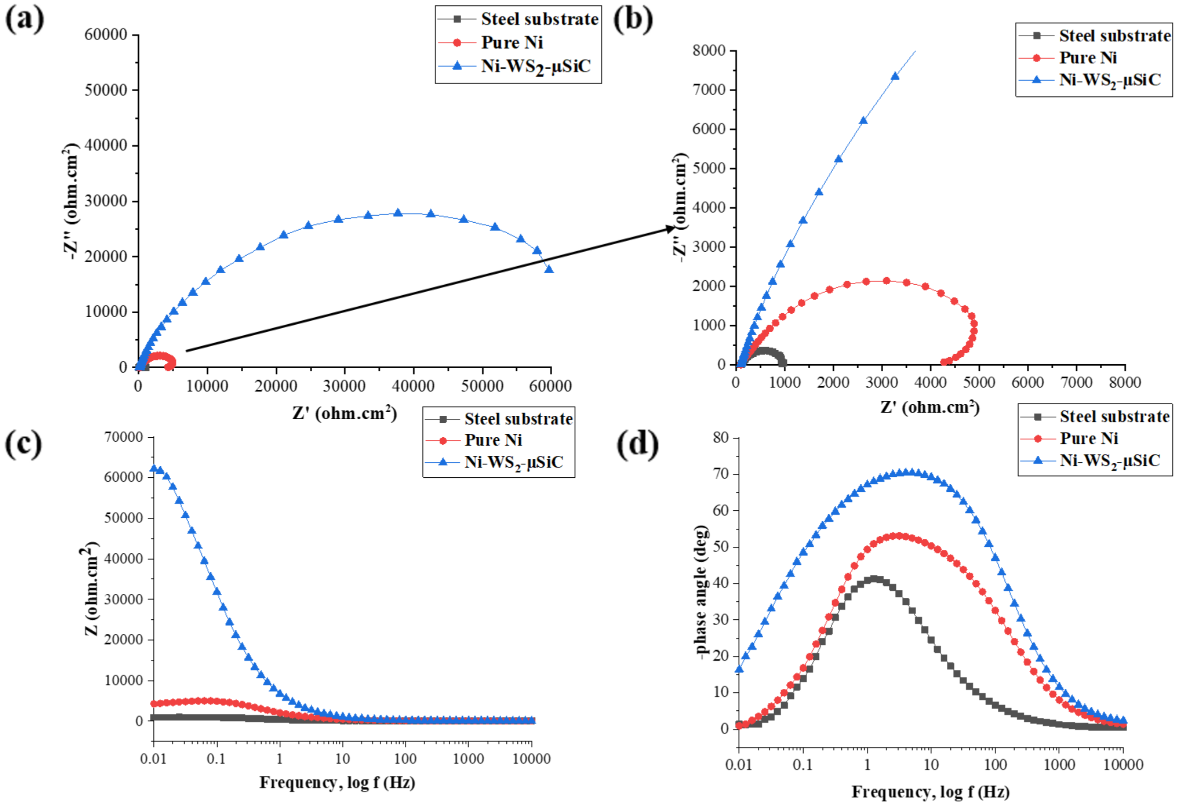

Figure 4.16 EIS results of the steel substrate, pure Ni and Ni-SiC (8.5 µm)-WS_2 coating in 3.5 wt% NaCl solution; (a) Overall Nyquist plots; (b) enlarged Nyquist plot; (c) and (d) are bode plots.

4.2.5 Abrasion resistance of the coatings

Lack of abrasion resistance is one of the most urgent challenges for the practical application of superhydrophobic surfaces. The abrasive resistance of superhydrophobic Ni-WS_2 and Ni-SiC (8.5 μm)-WS_2 coatings were studied by a linear abrasion test. Variations of water contact angles and sliding angles as a function of abrasion distance are shown in **Figure 4.17**. For Ni-WS_2 coating, the WCA decreased gradually during the test. After 600 cm of abrasion distance, the WCA still maintained above 150°. However, the sliding angle reached 10° at the abrasion distance of 450 cm and increased afterwards. Therefore, Ni-WS_2 coating lost superhydrophobicity at an abrasion distance of 450 cm. On the other hand, Ni-SiC (8.5 μm)-WS_2 coating maintained superhydrophobicity (WCA > 150° and SA < 10°) even after a 2000 cm abrasion distance, indicating good abrasive resistance.

To understand the loss of superhydrophobicity of Ni-WS_2 and Ni-SiC (8.5 μm)-WS_2 coatings, the surface morphologies of coatings after the linear abrasion test were investigated and shown in **Figure 4.18**. After 600 cm abrasion distance, the protrusions on the Ni-WS_2 coating have been totally flattened (**Figure 4.18 a**). Under high magnification, obvious abrasive wear scars can be seen on the coating surface (**Figure 4.18 b**). This observation indicated that the hierarchical coating structures are fragile and susceptible to wear damage. Therefore, in real applications, Ni-WS_2 coating cannot provide long-term superhydophobicity due to the lack of abrasive resistance. On the other hand, the protrusions on the Ni-SiC (8.5 μm)-WS_2 coating could still be identified after 2250 cm abrasion distance (**Figure 4.18 c**). Under high magnification in **Figure 4.18 (d)**, only the top areas of protrusions were observed to be flattened. Moreover, some protrusions remained undamaged even the Ni-SiC (8.5 μm)-WS_2 coating lost superhydrophobicity after the abrasion test. The comparison of two worn surfaces confirmed that Ni-SiC (8.5 μm)-WS_2 coating is more abrasive resistant than Ni-WS_2 coating.

According to Archard law [202], the wear performance is largely dependent on the hardness of the coating. To explain the different abrasion resistance of Ni-WS_2 and Ni-SiC (8.5 μm)-WS_2 coatings, the microhardness test was conducted. From **Figure 4.19**, it is worth noting that the hardness of Ni-SiC (8.5 μm)-WS_2 coating is more than 3 times higher than that of Ni-WS_2 coating. The difference in hardness can be explained by the nature co-deposited particles. As is known, WS_2 belongs to soft lubricant particles while SiC belongs to hard ceramic particles. From EDS results, it can be noted that WS_2 content in Ni-SiC (8.5 μm)-WS_2 coating (6.0 wt%) is much lower than Ni-WS_2 coating (18.1 wt%). In addition, a large quantity of SiC particle (13.9 wt%) can be detected in Ni-SiC (8.5 μm)-WS_2 coating. Therefore, Ni-SiC (8.5 μm)-WS_2

with higher content of hard ceramic particles and lower content of soft lubricant particles can be expected to have higher hardness. The hardness results are consistent with Archard law. Ni-SiC (8.5 μm)-WS_2 with higher hardness is more resistant to wear damage.

Apart from coating hardness, the abrasion resistance of electrodeposited coatings is also determined by the residual strain introduced during electroplating processes. The residual strain can be either tensile or compressive. Compressive residual strain is generally advantageous, as it enhances the hardness and toughness of the coating, thereby improving its ability to resist wear and deformation. In contrast, tensile residual strain can lead to microcracks and delamination, which compromises abrasion resistance. To further enhance the abrasion resistance of electrodeposited superhydrophobic coatings, investigating the residual strain in composite coatings is a worthwhile direction for future research.

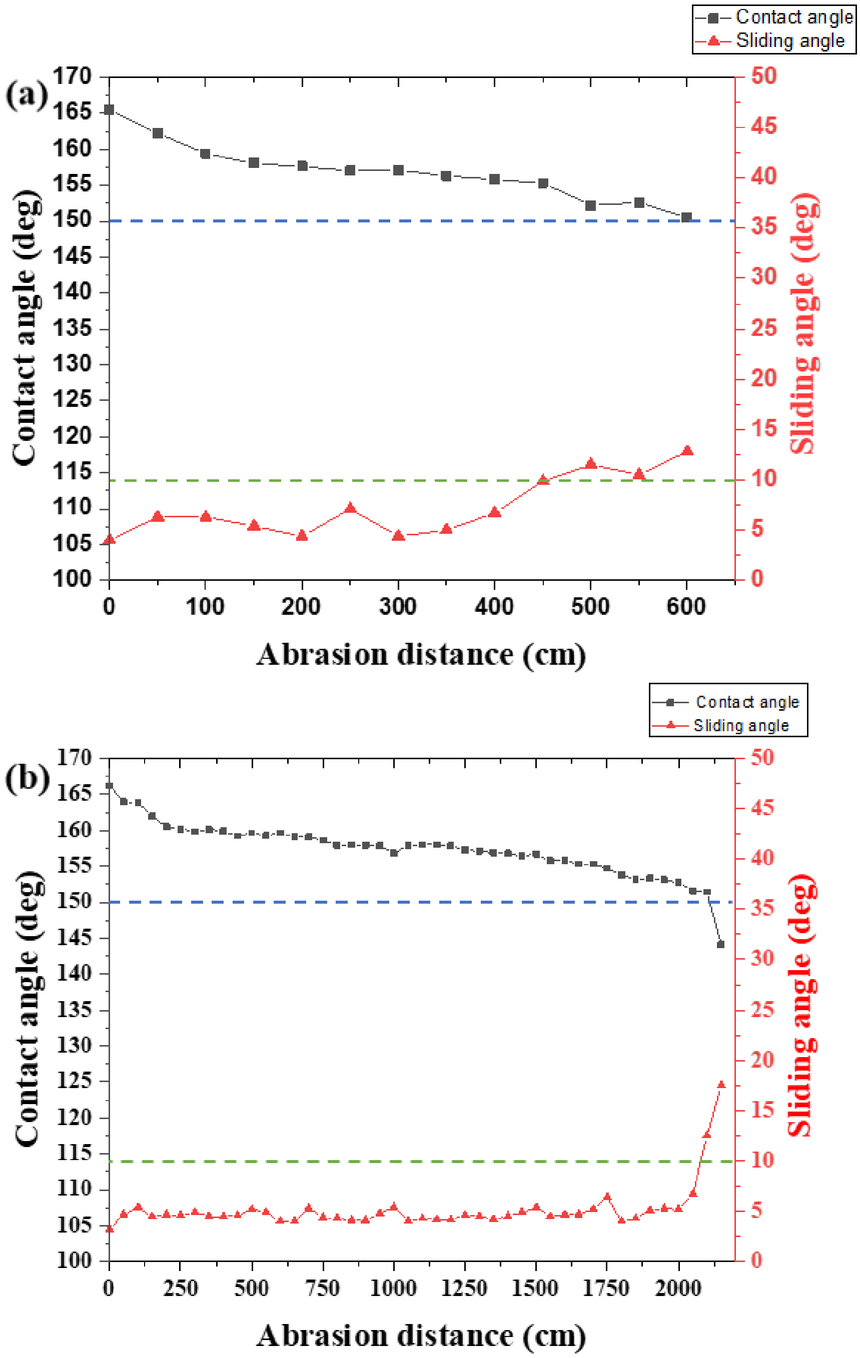

Figure 4.17 Water contact angles and sliding angles as a function of abrasion distance; (a) Ni-WS_2 coating; (b) Ni-SiC (8.5 μm)-WS_2 coating.

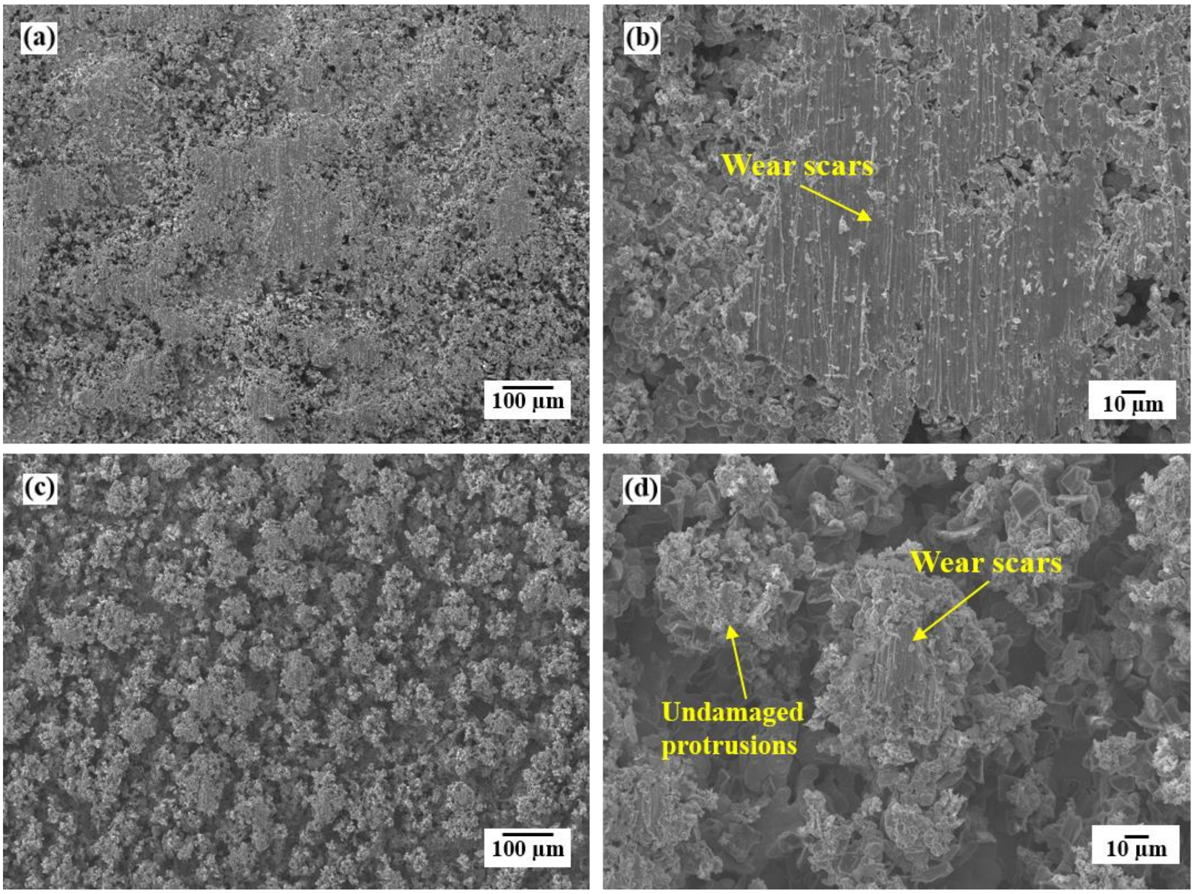

Figure 4.18 Surface morphologies after linear abrasion test. (a) Ni-WS_2 coating and (b) corresponding high magnification; (c) Ni-SiC (8.5 µm)-WS_2 coating and (d) corresponding high magnification.

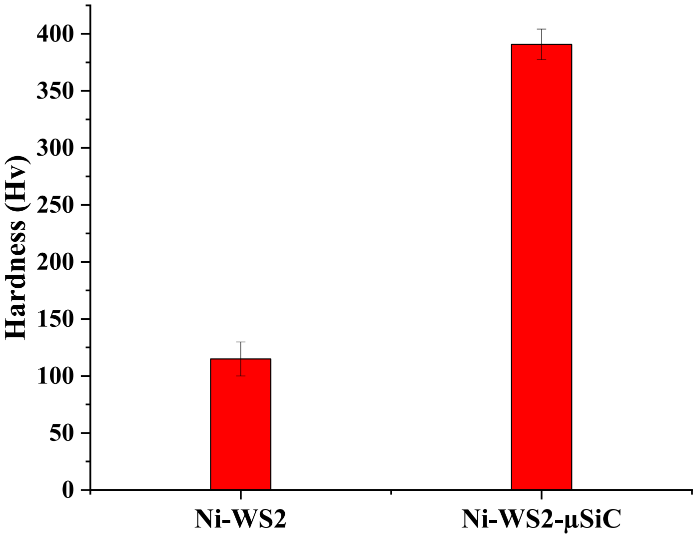

Figure 4.19 Microhardness of Ni-WS_2 and Ni-SiC (8.5 µm)-WS_2 coatings.

4.3 Discussion

4.3.1 Effect of particle size on composite coatings

As indicated in **Figure 4.3**, **Figure 4.4** and **Figure 4.5**, the particle size is a key factor influencing both surface morphology and particle incorporation rate. Either too large (4.8 µm MoS_2) or too small particles (275 nm WS_2) will result in low particle contents in the coating. A similar phenomenon has also been observed in nickel hybrid composite coatings. The compositional analysis of Ni-SiC (40 nm)-MoS_2, Ni-SiC (40 nm)-WS_2 showed that nano-sized SiC (40 nm) are difficult to be co-deposited than micron-sized SiC (8.5 µm). These findings are in agreement with the results of many previous studies [222, 226-228]. Kim and Yoo [227] reported that co-deposited SiC content in the Ni matrix increased as the particle size increased up to 14.0 µm. However, a further increase in particle size resulted in a decrease in SiC content. This phenomenon can be explained as follows. With the increasing particle size, the nickel ions and surfactants adsorbed on particles will increase. Accordingly, the electrophoretic motion of particles could be enhanced, and more particles could be transferred to the cathode surface for co-deposition. However, when the particle size is beyond the optimum value, particles have a tendency to settle down, which leads to a decrease in the co-deposition amount.

In another study of Ni-SiC coating [226], the iso-electric point for micron-sized SiC and nano-sized SiC particles were measured to be 3.0 and 7.0, respectively, indicating that micron-sized SiC particles were more negative than nano-sized SiC particles in the Zeta potential. This finding further confirmed that positive ions could be easily adsorbed on the micron-sized particles. During the electro-codeposition process, the adsorbed positive ions on the particle surface will form a layer of ionic cloud with a positive charge. With the assistance of the electric field, the positively charged particles will be attracted and transferred to the cathode surface. This motion is called electrophoresis. Since the amount of adsorbed positive ions on nanosized SiC particles is lower than that on micron-sized SiC particles, nano-sized SiC particles possess a lower charge. As a result, their mobility in the electric field is reduced. This reduced mobility limits the effective transport of nano-sized SiC particles to the cathode surface, thereby decreasing the co-deposition rate. According to the Stokes model [226], assuming the shape of suspended particles are in a spherical shape, the electrophoretic velocity (V_E) in an electric field can be calculated by the following equation:

$$V_E = \mu_E E = \frac{q}{6\pi\eta r} E \quad \ldots\ldots\ldots\ldots\ldots\ldots\ldots\ldots 4.4$$

Where μ_E represents the electrophoretic mobility, E is the strength of the electric field, q is the charge of the particle, r is the radius of a particle, η is the viscosity of the suspension. From Stokes model, the electrophoretic velocity of particles is proportional to surface charge (q) and inverse to the particle size, which is not evident to predict the electrophoretic velocity with the micron-sized particles or nano-sized particles. The low deposition rate with nano-sized particles may require new data and theory to elucidate the mechanism of nucleation and growth. The above discussion indicates that the particle dispersion and electrophoretic motion are two important factors influencing particle behaviour in the electroplating bath. Further work on particle motion is needed to understand which mechanism is dominant. The electrophoretic motion can be evaluated by measuring zeta potential, and a simple sedimentation test can estimate the particle dispersion.

The current research found that the co-deposition of nano-sized particles also contributed to dense coating structures of nickel hybrid composite coatings. Coating sample Ni-SiC (40 nm)-MoS_2, Ni-SiC (40 nm)-WS_2 and Ni-TiO_2-WS_2 with the embedment of nano-sized SiC (40 nm) and TiO_2 (21 nm) particles all exhibited dense and compact cross-sections with almost no voids observed. This can be considered as a huge structure improvement compared with nickel single-particle composite coatings (i.e. Ni-MoS_2 and Ni-WS_2). On the other hand, although the particle combination of self-lubricating particles (MoS_2 or WS_2) with nano-sized particles (40 nm SiC or 21 nm TiO_2) helped to densify the coating structure, the adsorbed MoS_2 or WS_2 particles adsorbed on the coating surface could still result in nodular growth of nickel deposit on the top layer of hybrid composite coatings. Therefore, closely packed nodules were observed in **Figure 4.12 (a and c)** and **Figure 4.13 (f)**. However, one thing that remains unknown is that the combination of TiO_2 and MoS_2 particles resulted in a very porous coating structure, which is quite different from the observation of Ni-TiO_2-WS_2 coating.

4.3.2 Effect of surface morphology on coating superhydrophobicity

Roughness and surface free energy are two important parameters determining surface wettability. The water contact angle increased with increasing surface roughness for nickel single-particle coatings (Ni-MoS_2 and Ni-WS_2). Superhydrophobicity was achieved on M3 (Ra = 28.9 µm), W2 (Ra = 36.2 µm) and W4 (Ra = 24.2 µm) coatings with high surface roughness value. This is consistent with the results of He et al. [14], which indicates that a higher water contact angle can be achieved on the rougher Ni-P-WS_2 coating surface. Such wetting state belongs to the Cassie Baxter model. The rough coating surface showing hierarchical protrusion structure allows a great deal of air entrapped, which resist water penetration and surface wetting. In later research carried out by Zhou et al. [113], a shining "air cushion" was observed on the rough surface of Ni-WC-WS_2 coating when the coating sample was immersed into water, which further confirmed that the air entrapment is the main reason for maintaining superhydrophobic state. A similar "air cushion" was also found in the current research when composite coatings were immersed in DI water for the durability study (**Figure 4.20**).

However, as shown in **Figure 4.14**, superhydrophobicity was also observed on Ni-SiC (40 nm)-MoS_2 and Ni-SiC (40 nm)-WS_2 coatings with relatively smooth surfaces (Ra < 5 μm). SEM images in **Figure 4.11** reveal closely packed nodule structures on coating surfaces. It can be expected that the closely nodular coating structures might have a similar ability of air entrapment. Further investigations will be required in future work to get a better understanding of the superhydrophobicity mechanism of nickel hybrid composite coatings.

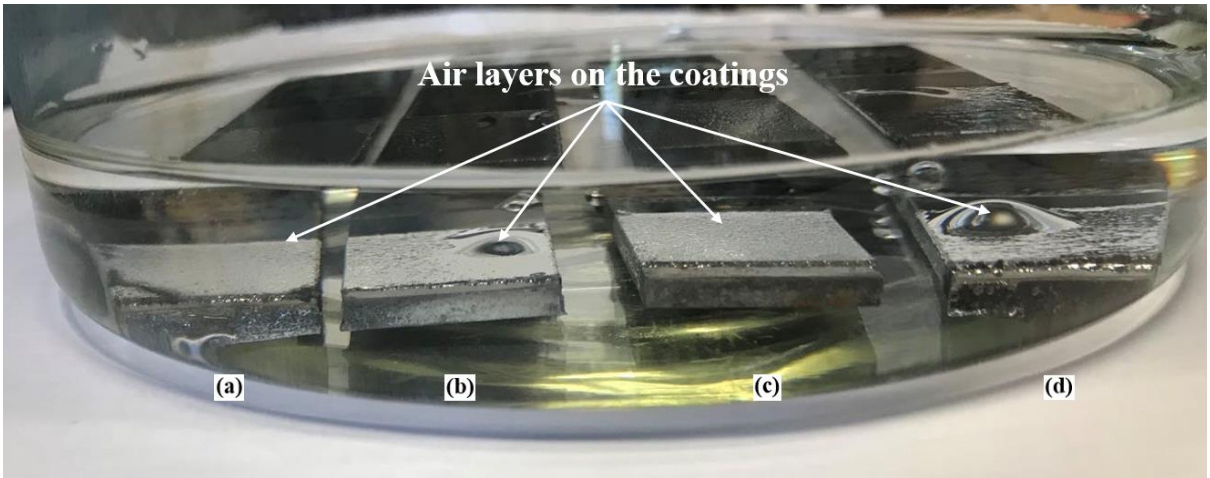

Figure 4.20 Air layers formed on the nickel single-particle composite coatings, (a) M1; (b) M3; (c) W2; (d) W4.

4.3.3 Corrosion mechanism of superhydrophobic coatings

To elucidate the corrosion mechanism of superhydrophobic coatings, two different equivalent circuits were constructed to fit the experimental EIS data by the Nova software (**Figure 4.21 a and b**). Besides, simple schematics in **Figure 4.21 (c) and (d)** are employed to better understand the corrosion processes of different samples. **Figure 4.21 (a)** illustrates the equivalent circuit of steel substrate and pure Ni coating [96, 218, 224]. In this fitting circuit, R_s represents the solution resistance. R_{ct} stands for the charge transfer resistance. *Cdl* is the capacitor to model the electrical double layer at the interface of corrosive solution and electrode. **Figure 4.21 (c)** shows the corresponding schematic of the corrosion process in 3.5 wt% NaCl solution. Compared with steel substrate and pure Ni coating, the corrosion mechanism of superhydrophobic Ni-SiC (8.5 μm)-WS_2 coating is more complicated. According to Souto et al. [229], a metal covered with an undamaged coating can be modelled by a resistor and the coating capacitance in series, reflected by a vertical line in the Nyquist plot. However, in our case, the Nyquist plot of the superhydrophobic Ni-SiC (8.5 μm)-WS_2 coating is a depressed semi-circle, which means that the 3.5 wt% NaCl solution penetrated into the coating and formed a new liquid/metal interface under the coating, the corrosion phenomenon occurred at this new interface. Therefore, the corrosion behaviour at the new interface was modelled as a double-layer capacitance in parallel with a kinetically controlled charge-transfer reaction, as shown in **Figure 4.21 (b)**. This mechanism has also been schematically presented in **Figure 4.21 (d)**, where a small amount of corrosive solution passed through the “coating + air layer” barrier and induced reaction at the interface. In **Figure 4.21 (b)**, R_c represents the coating resistance, and *CPE* is the constant phase element. In a real electrochemical system, $CPE_{coating}$ is employed to replace the ideal coating capacitance. According to the literature [224], the impedance of *CPE* can be calculated by the following equation,

$$Z_{CPE} = \frac{1}{Y_0(j\omega)^{\alpha}} \qquad \text{4.5}$$

Where in this Equation 4.5, Y_0 is the general admittance function, ω is the angular frequency, j is the imaginary number ($j = \sqrt{-1}$), and α is an experimental exponent of the *CPE*. The value of α is in the range of 0 to 1.

The fitted values of each equivalent circuit element are summarised in **Table 4.7**. R_{ct}, which represents the charge transfer resistance between the steel substrate and corrosive solution, is the most significant parameter reflecting the corrosion resistance of the sample. From **Table**

4.7, it can be noted that the value of R_{ct} increased significantly after electroplating. In particular, the R_{ct} of the superhydrophobic Ni-SiC (8.5 μm)-WS_2 is 50158 $\Omega\cdot cm^2$, 97.7 times and 18.3 times higher than that of the steel substrate and the pure Ni coating. This finding is in agreement with the results of potentiodynamic polarisation, and further verifies that superhydrophobic Ni-WS_2-μSiC coating can provide excellent corrosion protection for the substrate.

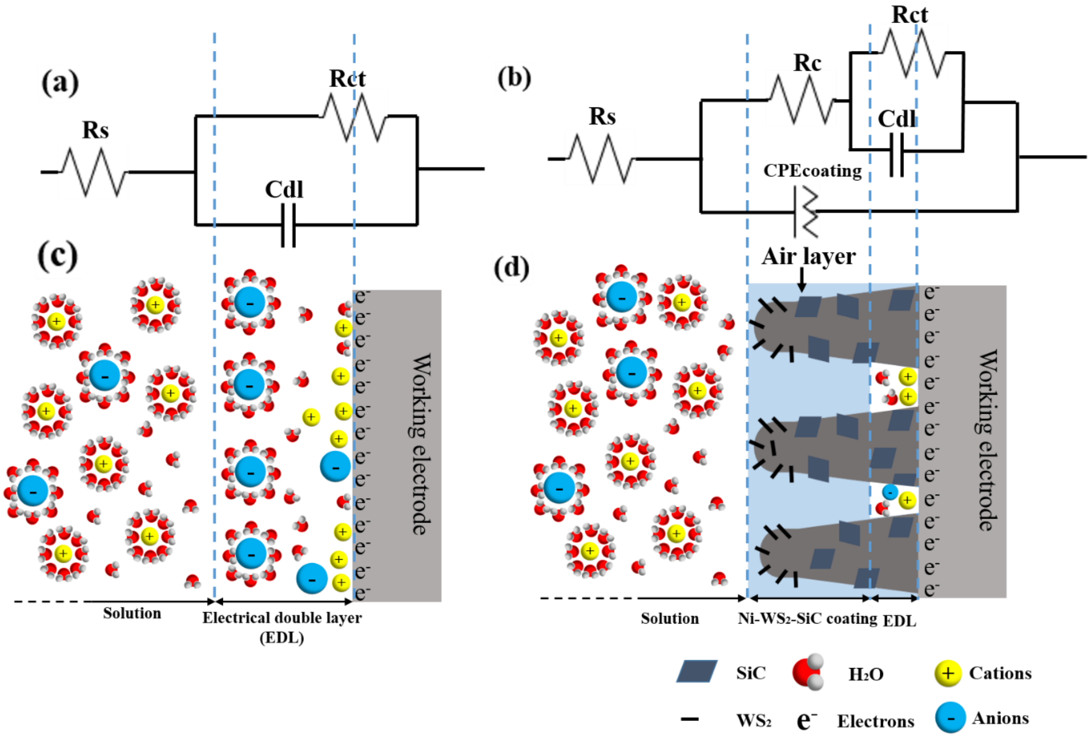

Figure 4.21 Equivalent circuit of (a) steel substrate and pure Ni and (b) superhydrophobic Ni-SiC (8.5 μm)-WS_2 coating; (c) and (d) are the corresponding schematics of corrosion processes.

Table 4.7 Calculated values of equivalent circuit elements

Sample	Rs ($\Omega\cdot cm^2$)	Rc ($\Omega\cdot cm^2$)	$CPE_{coating}$ ($F\cdot cm^{-2}\cdot s^{\alpha-1}$)	$\alpha_{coating}$	Cdl ($F\cdot cm^{-2}$)	Rct ($\Omega\cdot cm^2$)
Steel substrate	69.5	N/A	N/A	N/A	5.7×10^{-4}	513.3
Pure Ni	67.6	N/A	N/A	N/A	7.6×10^{-5}	2735.3
Ni-SiC (8.5 μm)-WS_2	63.9	5.15	4.7×10^{-5}	0.7	7.5×10^{-6}	50158.0

4.4 Summary of test results

1. Nickel single-particle composite coatings with superhydrophobic properties have been successfully developed by direct current electrodeposition. Surface roughness measurement and cross-section analysis reveal that nickel single-particle composite coatings (Ni-MoS2) exhibited rough surfaces and porous structures.

2. The coating structures became dense when particle combinations of (1) 40 nm SiC and 1.2 µm MoS2, (2) 40 nm SiC and 1.1 µm WS2, (3) 21 nm TiO2 and 1.1 µm WS2 were co-deposited into Ni matrix. These coatings also showed relatively smooth surface morphologies with closely packed nodule structures.

3. Ni-TiO2-MoS2 exhibited excellent durability during the water immersion test. The coating surface maintained hydrophobic after being immersed in water for two days. The excellent durability was attributed to the microporous/nanoporous structures in which air could be entrapped. Therefore, a continuous and tightly adhered air layer was formed on the coating surface, preventing direct contact between the coating and surrounding water.

4. Particle size plays an important role in determining surface morphologies and embedded particle content of composite coatings. Either too small or too large particle size will lead to a low particle co-deposition rate. For nickel hybrid composite coatings, the addition of nano-sized particles is beneficial. The incorporation of nano-sized SiC particles reduced the content of co-deposited MoS2 or WS2 particles, thereby alleviating the dendritic growth of coatings and promoting the formation of compact coating structures.

5. The electrochemical tests confirmed the excellent anti-corrosion performance of superhydrophobic Ni-SiC (8.5 µm)-WS2 coating in 3.5 wt% NaCl solution. The air layer formed on the hierarchical structure of Ni-SiC (8.5 µm)-WS2 coating reduced the penetration of corrosive solution and provided a corrosion barrier for the substrate.

6. Compared with Ni-WS2 coating, the addition of SiC particles enhanced about 4-5 times the abrasion resistance of the coating. The Ni-SiC (8.5 μm)-WS2 coating could maintain superhydrophobicity even after a 2000 cm abrasion distance, indicating that such coating has promising potential for robust industrial applications.

5 Self-lubricating composite coatings

5.1 Introduction

The co-deposition of solid lubricants such as MoS_2 and WS_2 particles into a metal matrix to form self-lubricating coatings have been researched for decades. However, the porous and non-compact coating structures induced by the dendritic growth of composite deposits have become the major challenge inhibiting long-term durability. Although the literature survey shows that using pulse current or ultrasonic bath agitation might densify the coating structures, these methods require either expensive equipment or very careful control. Therefore, it is necessary to develop a facile and low-cost method to deposit a self-lubricating coating with a dense structure.

The research in this chapter is divided into three sections. The first section is the electrodeposition of Ni-MoS_2 coatings. The effect of particle concentration on surface morphology, coating structure, and tribological performance was investigated. The second section studied the effect of cationic surfactant CTAB on Ni-MoS_2, Ni-WS_2 and Ni-MoS_2-WS_2 coatings. The last section is to evaluate the tribological properties of nickel hybrid composite coatings.

Particle content and coating structure are two primary factors influencing the tribological performance of the self-lubricating coating. The findings in chapter 4 indicate that, under the same electrodeposition condition, the co-deposition of 1.2 μm MoS_2 particles could lead to higher particle content and lower roughness of Ni-MoS_2 coating compared with 4.8 μm MoS_2 particles (**Figure 4.4** and **Figure 4.7**). Therefore, 1.2 μm MoS_2 particle was selected for Ni-MoS_2 coating deposition. In addition, the effect of surfactant was studied by adding different concentrations of CTAB into the electroplating bath. In previous of Ni-SiC coating [167], the addition of CTAB up to 0.3 g/L promoted the co-deposition rate of SiC particles. However, the excessive CTAB concentration (0.4 g/L) could result in embrittlement of metal matrix and therefore deteriorate tribological performance. Therefore, in this research, CTAB concentration in the electroplating bath was 0.1 g/L, 0.2 g/L and 0.5 g/L. Moreover, previous chapter demonstrated nickel hybrid composite coating samples Ni-SiC-MoS_2, Ni-SiC-WS_2, and Ni-TiO_2-WS_2 have smooth coating surfaces and dense coating structures (**Figure 4.12** and **Figure 4.13**). Robust tribological performance can be expected on these coatings. Therefore, the tribological tests on these hybrid composite coatings were investigated.

5.2 Results and analysis

5.2.1 Effect of particle concentration on Ni-MoS_2 coating

Surface morphologies of pure Ni coating and Ni-MoS_2 coatings deposited from electroplating baths containing different MoS_2 concentrations are displayed in **Figure 5.1**. Both pure Ni and Ni-MoS_2 coatings were prepared using nickel Watts bath in **Table 3.1** with addition of 0.1 g/L CTAB. The deposition time was 60 min. The pure Ni coating presents a flat and smooth surface (**Figure 5.1 a**). In contrast, Ni-MoS_2 coating deposited from electroplating bath containing 1 g/L MoS_2 particles shows a very rough surface. The nodular protrusions with many MoS_2 particles attached are randomly located on the coating surface (**Figure 5.1 b**). The formation of such nodular structures is due to the conductive nature of MoS_2 particles, which promotes the dendritic growth of deposits. In addition, due to the low particle concentration (1 g/L), very few sites can be occupied for dendritic growth. Therefore, the distribution of these protrusions is sparse. With the increase of MoS_2 concentration (2 g/L), the size of the nodular protrusion increased (**Figure 5.1 c**). When the particle concentration increased to 5 g/L, nodular protrusions almost covered the whole coating surface, leaving very narrow gaps uncovered (**Figure 5.1 d**). With further increase of particle concentration (10 g/L), Ni-MoS_2 coating shows refined surface morphology (**Figure 5.1 e**). However, many pores appeared on the surface. A similar phenomenon has also been reported by Zhao et al. [13]. The pore formation might be caused by intensive hydrogen evolution. The high MoS_2 concentration in the bath led to a decrease in bath conductivity. Thereby, the cell voltage of the bath would increase. A high cell voltage indicated a high negative overpotential at the cathode, which could result in intensive hydrogen evolution to block the electrodeposition. Subsequently, the uncoated area formed pores on the coating surface. Further increase of MoS_2 concentration (20 g/L) led to coarse surface morphology (**Figure 5.1 f**). Excessive particle concentration could cause severe particle agglomeration in the electrolyte. Therefore, during the electrodeposition process, MoS_2 particles might form large aggregates and settle to the bottom of the bath.

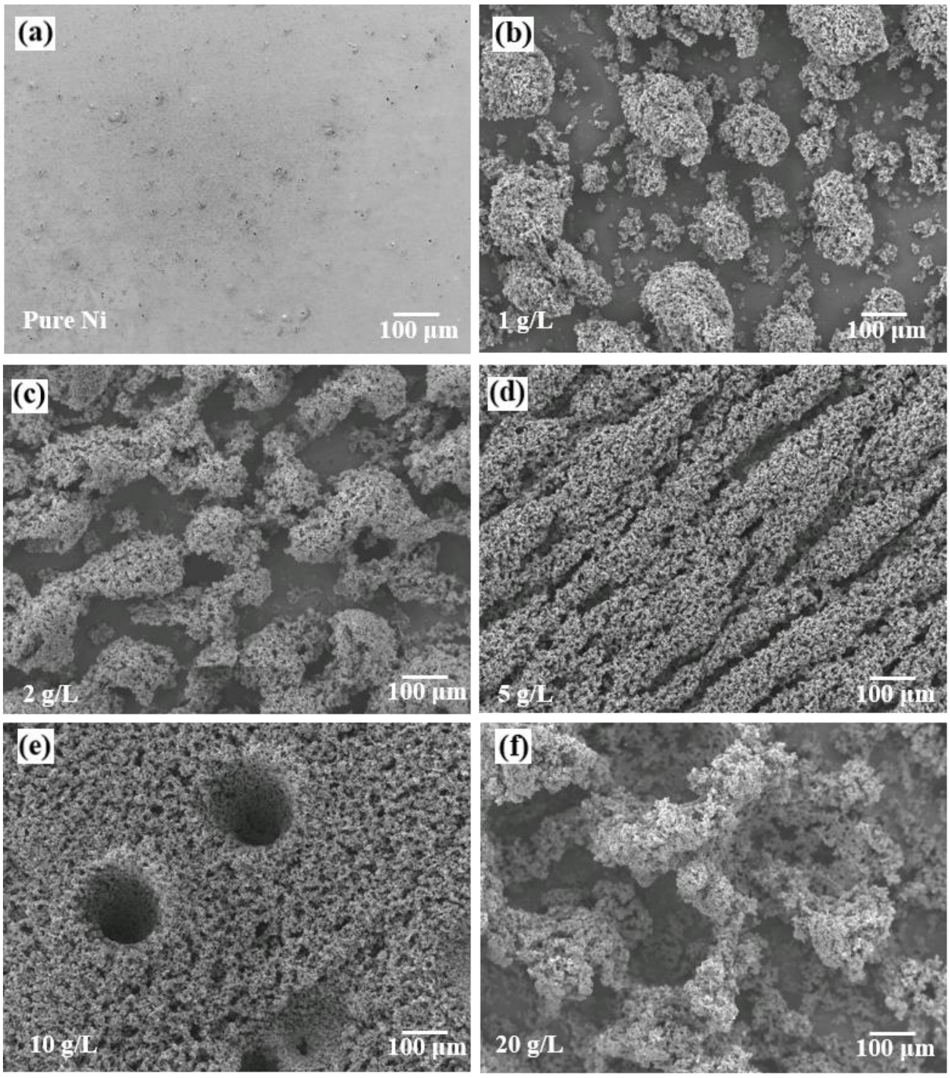

Figure 5.1 Secondary electron SEM images of surface morphologies of (a) pure Ni coating; (b-f) Ni-MoS_2 coatings deposited from electrolytes with a particle concentration of 1, 2, 5, 10, 20 g/L. Deposition time of 60 min and CTAB concentration of 0.1 g/L.

As shown in **Figure 5.2**, the surface topographies of coatings can be reflected by Alicona 3D surface reconstruction. Pure Ni coating presents a uniform contrast, suggesting a flat surface. On the contrary, Ni-MoS_2 coating deposited with 1 g/L particle concentration shows a rough surface with large peaks and troughs. With the increase of particle concentration, surface morphologies of Ni-MoS_2 coatings became smoother. When the particle concentration increased to 10 g/L, green/yellow contrast colours were homogeneously distributed across the coating surface, showing improved smoothness. Additionally, Alicona 3D view also reveals holes (purple dents), which is in agreement with the observation in the SEM image. However, with a further increase of the MoS_2 concentration to 20 g/L, the purple/green contrast colours represent large size of protrusions, indicating high surface roughness.

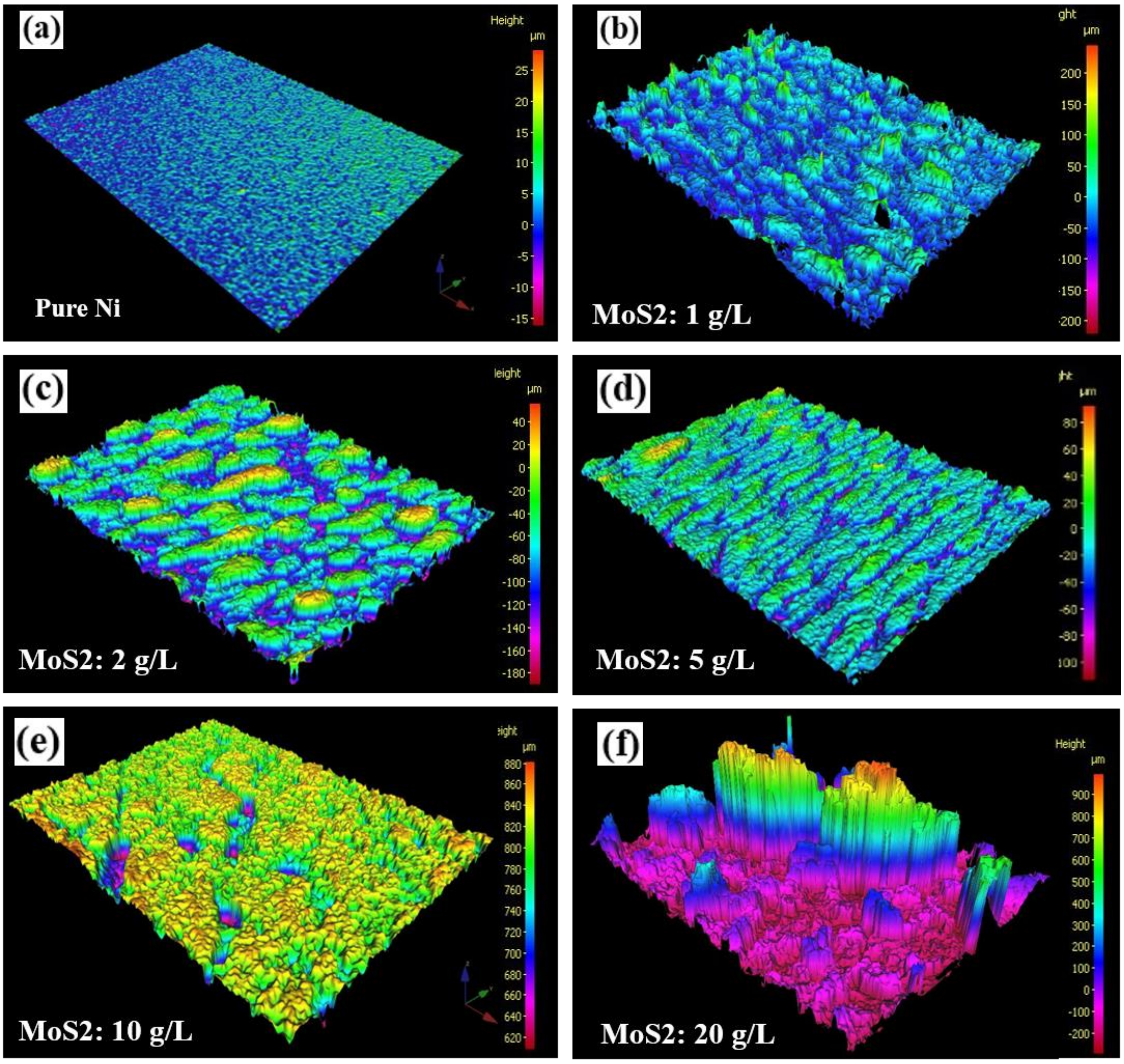

Figure 5.2 3D surface topographies of (a) pure Ni coating; (b-f) Ni-MoS_2 coatings deposited from electrolytes with particle concentration of 1, 2, 5, 10, 20 g/L.

EDS results of Ni-MoS_2 coating prepared from different particle concentration is shown in **Figure 5.3 (a)**. The incorporated MoS_2 content in the coatings shows a linear increase with increasing particle concentration up to 5 g/L in the electroplating bath. The maximum MoS2 content was around 42.5 wt% which was realized at particle concentration between 5 to 10 g/L. However, a further increase in MoS_2 concentration (20 g/L) led to a dramatic decrease in particle incorporation. This phenomenon has also been reported in many other composite electroplating systems such as Ni-P-MoS_2 [4], Ni-WS_2 [13], Ni-P-WS_2 [14] and Ni-WC[198]. The possible cause of reduced particle content at high particle concentration might be particle agglomeration. The agglomerated particles could settle down in the electroplating bath. **Figure 5.3 (b)** shows the average roughness values of Ni-MoS_2 coating prepared with different particle concentration. It can be observed that average roughness values decreased from 36.8 µm at 1 g/L to 18.1 µm at 10 g/L. Further increase of particle concentration to 20 g/L resulted in a significant increase in roughness value.

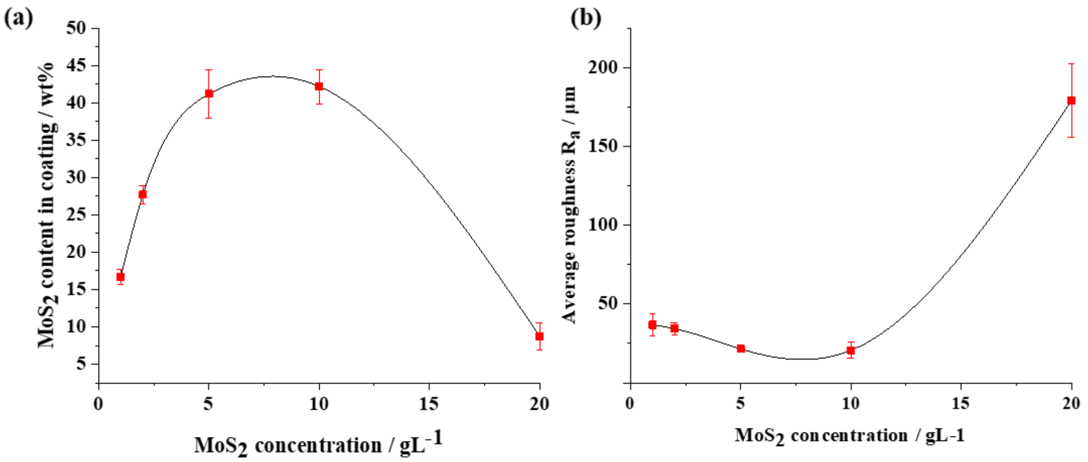

Figure 5.3 EDS measured MoS_2 content in the composite coating as a function of particle concentration in the electrolyte; (b) the average roughness value of coating as a function of particle concentration in the electroplating bath.

Figure 5.4 shows the cross-sectional SEM images of Ni-MoS_2 coatings. Pure Ni coating exhibits a dense and compact coating structure **(Figure 5.4 a)**. However, the cross-sectional view of Ni-MoS_2 deposited with 1 g/L particle concentration shows two distinct parts from the coating/substrate interface to the coating surface (**Figure 5.4 b**). The first part is a thin layer with a thickness of about 18.7 µm deposited on the substrate. Almost no particles were observed in this layer. The second part consists of dendritic protrusions. The average height of these protrusions is 149.3 ± 10.3 µm, as measured from secondary electron SEM images using ImageJ software. These protrusions are discretely distributed on the first thin layer. Although the gaps between protrusions gradually narrowed as the MoS_2 concentration increased up to 10 g/L **(Figure 5.4 c-e)**, obvious pores can still be observed. When MoS_2 concentration increased to 20 g/L, the uniformity of Ni-MoS_2 coating became poor. Some areas of the substrate surface were not covered by the coating. A possible explanation for the low coverage of Ni-MoS_2 coating is that the porous and fragile coating was crushed and wiped off during cross-section preparation.

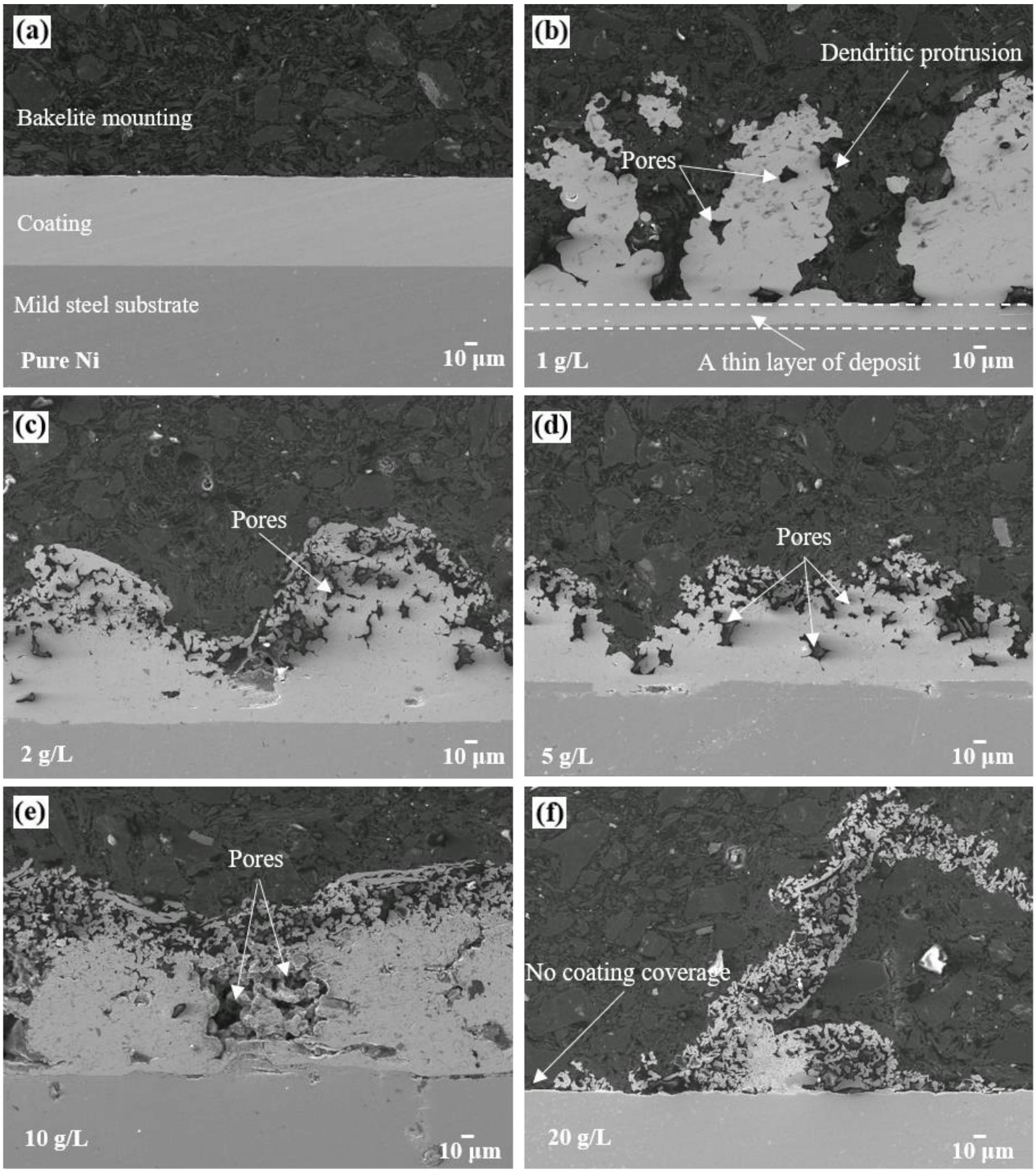

Figure 5.4 Secondary electron SEM images of cross-sectional views of (a) pure Ni coating, (b-f) Ni-MoS_2 coatings deposited from electrolytes with a particle concentration of 1, 2, 5, 10, 20 g/L.

Figure 5.5 (a) shows coating thickness measured from the cross section of pure Ni coating and Ni-MoS_2 coatings deposited with different MoS2 concentration. Pure Ni coating exhibits consistent thickness with value of 72.3 µm. With the addition of 1 g/L MoS_2 particles, the coating thickness increased by 132.4%. The coating thickness decreased to 86.8 µm when the MoS_2 concentration was increased to 5 g/L. However, a further increase in MoS_2 concentration to 20 g/L resulted in a thickness of 203 µm. Moreover, the thickness values exhibited significant variation between measurements, as indicated by the large deviation. This finding is consistent with the aforementioned cross section observation in **Figure 5.4**.

Figure 5.5 (b) is the hardness of pure Ni coating and Ni-MoS_2 coatings deposited with different MoS_2 concentration. Compared with pure Ni coating, all Ni-MoS_2 coatings exhibit lower hardness. In addition, with the increase of MoS_2 concentration, the hardness of Ni-MoS_2 coating dropped gradually from 280.8 Hv (at 1 g/L) to 246.5 Hv (at 5 g/L). A further increase in MoS_2 concentration (10 g/L) led to a dramatic decrease in hardness. It might suggest that the low hardness of Ni-MoS_2 coating was caused by non-compact microstructure containing the high porosity shown in **Figure 5.4 (b-e)**. The indentation marks on coating cross-sections were investigated to understand the decrease in hardness. As shown in **Figure 5.6**, the indentation marks on cross-sections of Ni-MoS_2 coatings deposited with 1 g/L, 2 g/L and 5 g/L particle concentration are in clear diamond shapes. However, the indentation mark on the cross-section of Ni-MoS_2 coating prepared with 10 g/L MoS_2 was not clear, and many cracks were observed. It can be speculated that the porous coating structure of Ni-MoS_2 (10 /L) observed in **Figure 5.4 (e)** could not withstand loading from the indenter and tended to be crushed during the hardness test. Therefore, a dramatic decrease in hardness could be observed when the MoS_2 concentration in the electroplating bath was 10 g/L. As the corners of the indentation mark are not clearly defined, the hardness value of the Ni-MoS_2 coating prepared with 10 g/L MoS_2 can only be roughly estimated based on the diagonals of the indentation mark.

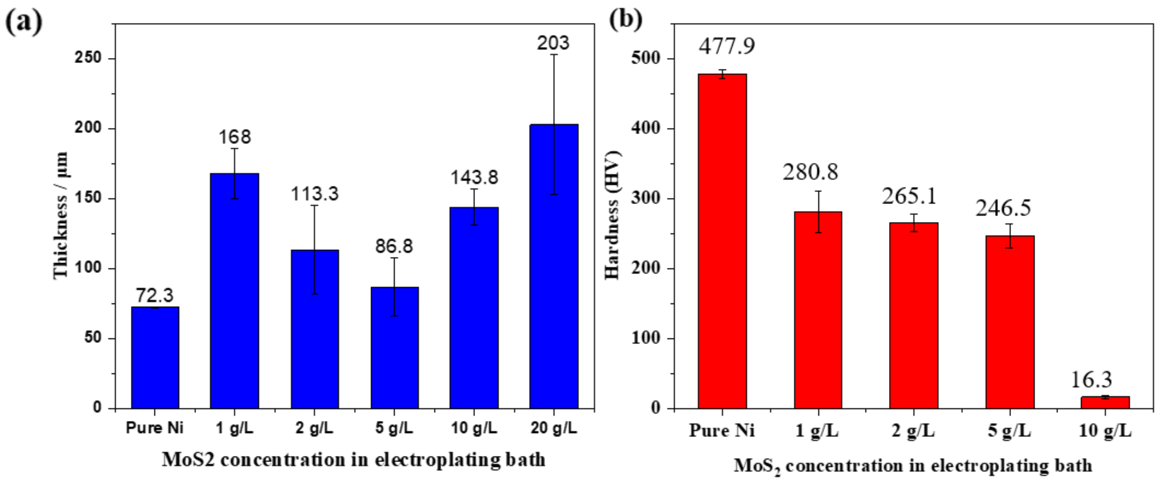

Figure 5.5 (a) Thickness value of pure Ni coating and Ni-MoS_2 coating deposited from electroplating bath containing different particle concentration; (b) Vickers hardness of Ni-MoS_2 coating deposited from electroplating bath containing different particle concentration.

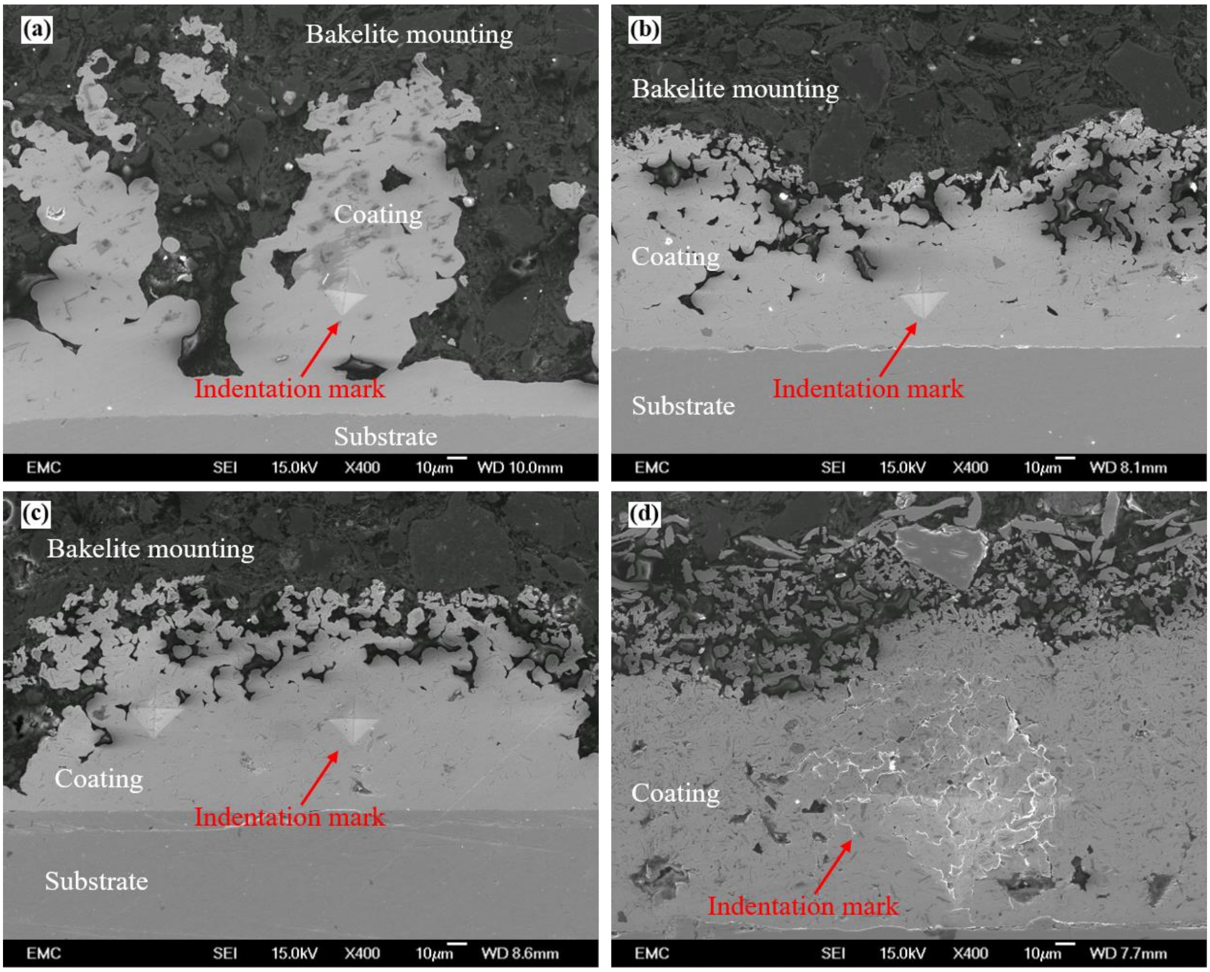

Figure 5.6 Secondary electron SEM images of indentation marks on cross-section of Ni-MoS_2 coatings deposited from electroplating bath containing (a) 1 g/L, (b) 2 g/L, (c) 5 g/L and (d) 10 g/L particle concentration.

The friction coefficients versus time produced by the pure Ni and Ni-MoS_2 coatings sliding against the counterpart cylinders are shown in **Figure 5.7**. For pure Ni coating, the friction coefficient increased to 0.65 during the initial 250 s. Then, the friction coefficient fluctuated but still maintained at a relatively stable level (0.55-0.62) within test time from 250 to 700 s. Afterwards, severe fluctuations were observed. The friction test was stopped after 900 s since severe damage was observed on the pure Ni coating surface. The coating in the contact area was broken into pieces and exfoliated from the substrate, indicating coating failure. In contrast, all the Ni-MoS_2 coatings maintained a low friction coefficient throughout the friction test. Especially for Ni-MoS_2 coating deposited with 1 g/L, 2 g/L and 5 g/L particle concentration, their friction coefficients maintained below 0.05 throughout the entire test. Ni-MoS_2 coatings deposited with 10 g/L and 20 g/L particle concentration showed a bit higher friction coefficient

(0.10-0.12) throughout the test. It is noticeable that both Ni-MoS_2 (10 g/L) and Ni-MoS_2 (20 g/L) coatings show a run-in period with a friction coefficient up to 0.22 at the initial stage of the friction test. The run-in period might be caused by the porous coating structure, which could be crushed at the beginning of the friction test. After the run-in period, tribofilms could be formed between Ni-MoS_2 coatings and counterpart cylinders, providing stable low friction throughout the test. The formation of tribofilm can be verified by wear track analysis in **Figure 5.11** and EDS analysis in **Figure 5.12**.

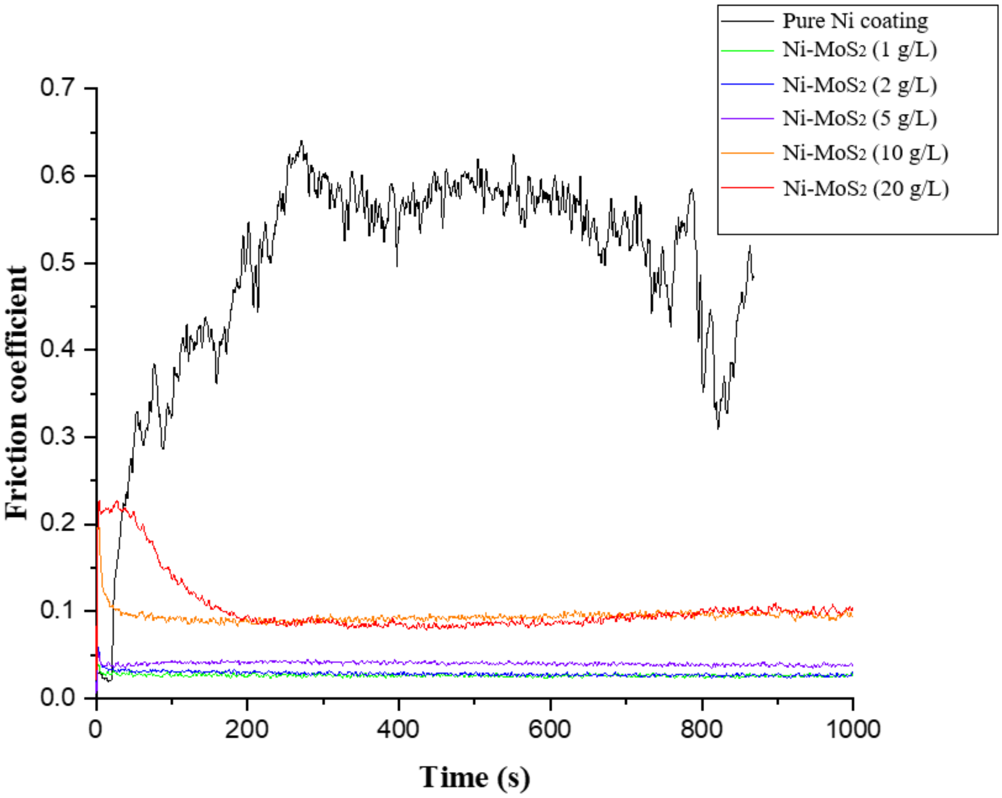

Figure 5.7 Friction coefficient of pure Ni and Ni-MoS_2 coatings.

The wear rates of Ni-MoS_2 coatings were estimated by wear depth obtained from Alicona 3D surface reconstruction (**Figure 5.8**). Details of wear depth measurement is described in Section 3.2.2. It can be noted that the wear tracks of Ni-MoS_2 coatings deposited from high particle concentration bath (10 g/L and 20 g/L) are more obvious and deeper compared with Ni-MoS_2 coatings deposited from low particle concentration bath (1 g/L, 2 g/L and 5 g/L). However, the wear loss in this study does not necessarily reflect the removal of coating material. During the reciprocating wear test, Ni-MoS_2 coatings with porous structures were crushed under the load of the counterpart cylinder. As a result, the flat surface observed on the wear track could be attributed to the compaction of the porous Ni-MoS_2 coatings.

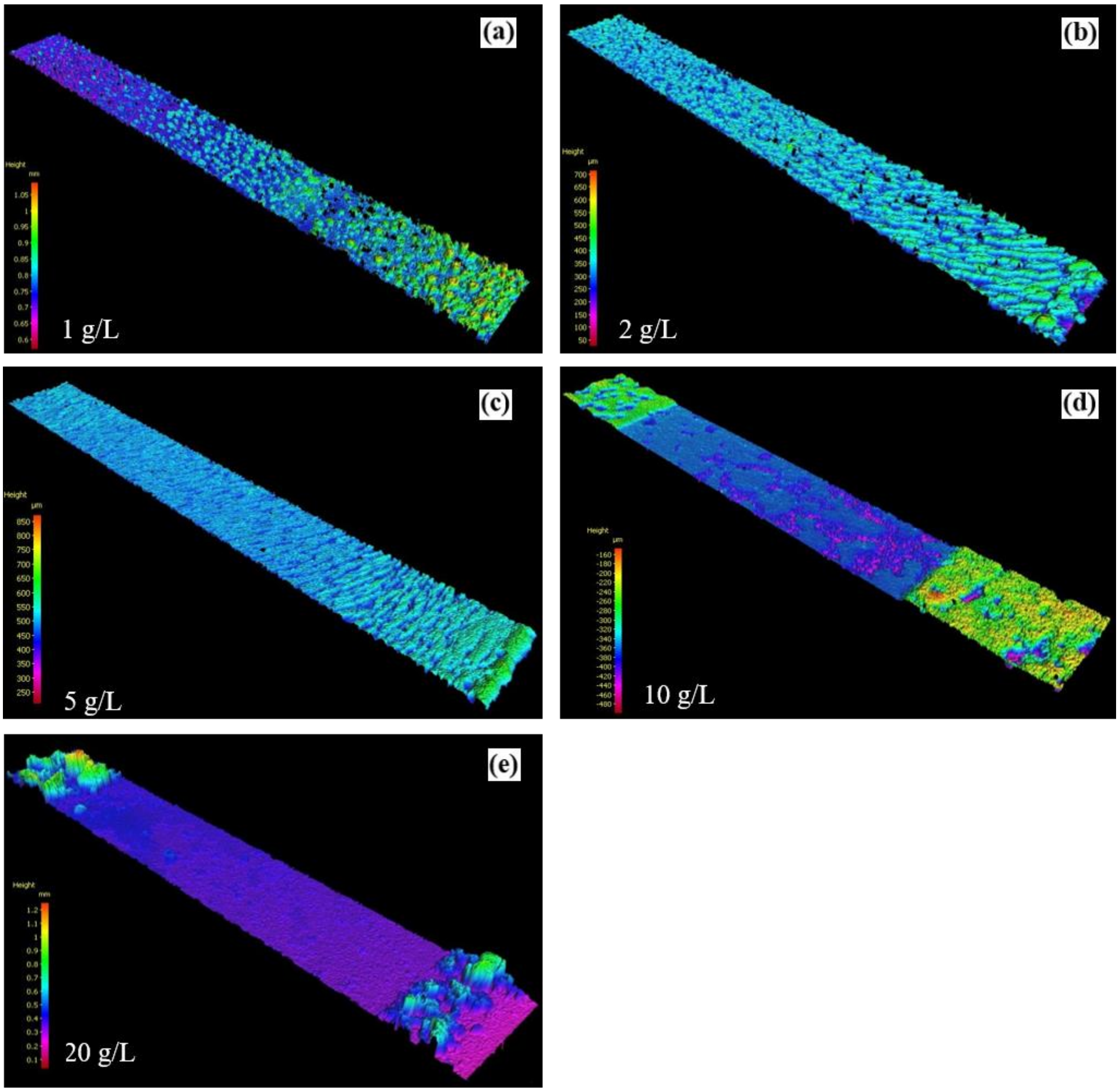

Figure 5.8 Alicona 3D surface reconstruction of worn surfaces of Ni-MoS_2 coatings prepared from electrolyteS containing MoS_2 concentration of 1, 2, 5, 10, 20 g/L.

As shown in **Figure 5.9**, wear depth increases with increasing concentration of MoS_2 particles in the electroplating bath. This finding is consistent with hardness results. The hardness of Ni-MoS_2 coating deposited with 1 g/L, 2 g/L, and 5 g/L particle concentration is ten times greater than that of Ni-MoS_2 deposited with 10 g/L and 20 g/L particle concentration. Therefore, during friction test, Ni-MoS_2 coatings deposited from a low particle concentration bath can withstand high loading rather than be crushed by counterpart cylinders. Moreover, Ni-MoS_2 coating deposited from electroplating bath containing 20 g/L particles shows the highest roughness and the most severe dendritic protrusions, which can be easily worn during the friction test. Therefore, Ni-MoS_2 coating deposited form particle concentration of 20 g/L shows the deepest wear track.

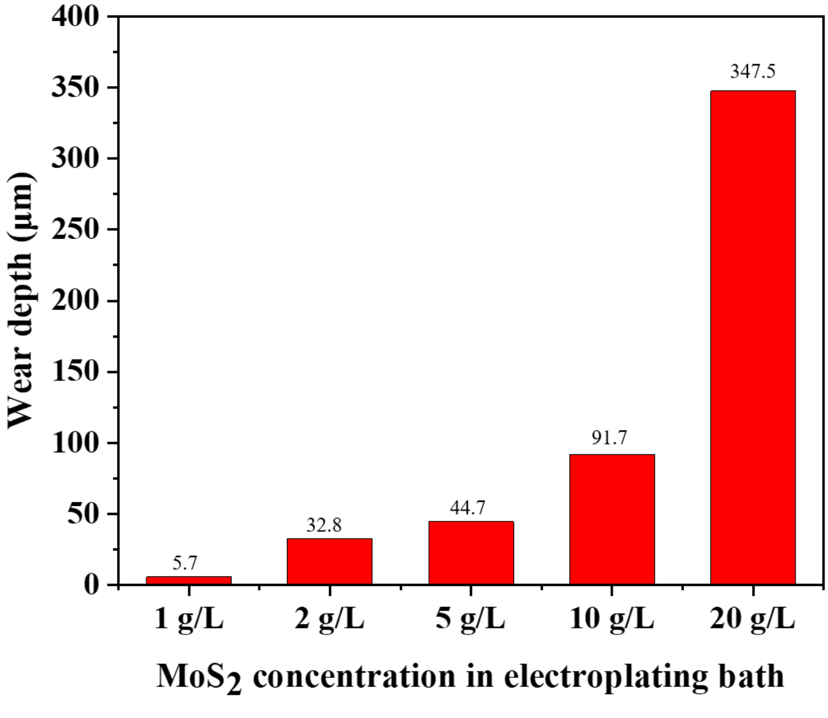

Figure 5.9 Wear depth of Ni-MoS_2 coatings deposited from electrolytes containing MoS_2 concentration of 1, 2, 5, 10, 20 g/L.

After 1000 s friction test, wear tracks of pure Ni coating investigated by SEM and displayed in **Figure 5.10**. Deep grooves along the sliding direction can be observed on the wear track of pure Ni coating. In addition, cracks can also be identified on the worn surface, suggesting that pure Ni coating lost integrity under the sliding contact motion. What's more, EDS results obtained from both worn and unworn pure Ni coating surface are illustrated in **Table 5.1**. By comparison, two important findings can be extracted. Firstly, the oxygen content detected on the worn surface is 13.4 wt%, which is much higher than that of unworn surface (1.1 wt%). The high oxygen content on the wear track indicates that the pure Ni coating experienced severe oxidative wear during the reciprocating wear test. The oxide layer was formed due to the high frictional forces and heat generation on the contact surface. Secondly, the detection of the iron element (0.7 wt%) indicates that the pure Ni coating surface was worn during the reciprocating wear test, allowing the steel substrate signal to be detected by EDS analysis.

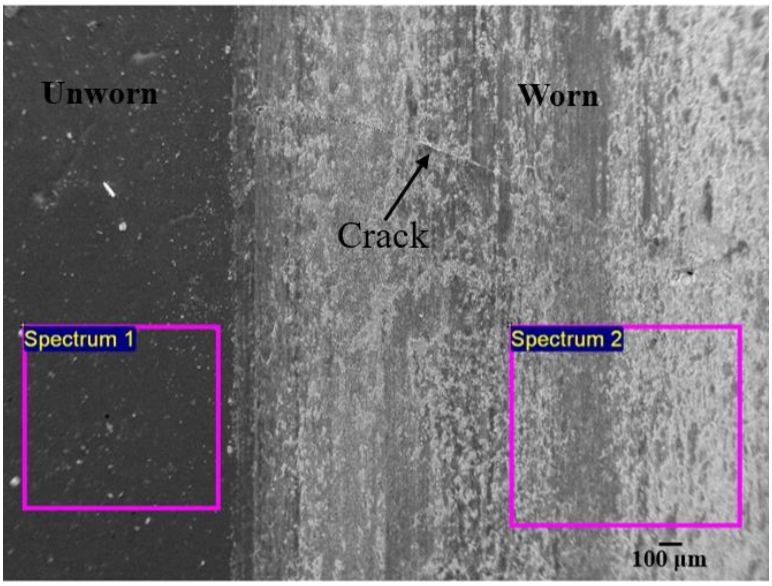

Figure 5.10 Secondary electron SEM image of pure Ni coating surface after friction test.

Table 5.1 EDS compositional analysis on pure Ni coating after friction test

	O (wt%)	Ni (wt%)	Fe (wt%)
Spectrum 1	1.14	98.86	N/A
Spectrum 2	13.35	85.95	0.69

Wear tracks on Ni-MoS_2 coatings are shown in **Figure 5.11 (b-f)**. After 1000 s of friction test, Ni-MoS_2 deposited from electroplating bath containing 1 g/L particle shows the least wear damage. Compared with the original coating surface morphology **(Figure 5.1 b)**, the nodular protrusions on the worn surface almost remain intact. Only top areas of protrusions have been flattened. The dark patches observed on the flattened areas were analysed by EDS (**Figure 5.12**). The results in **Figure 5.13 (d)** shows that the dark patches are rich in element molybdenum (10.8 wt%) and sulphur (9.7 wt%). Therefore, during the friction test, these dark patches (also called tribofilm) can provide low friction on the coating/counterpart contact zone. Many previous studies have also reported similar dark patches on wear tracks [4, 6, 14]. The dark patch formation was attributed to the accumulation and compaction of MoS_2 rich wear debris. During the friction test, the generated wear debris had a tendency to be accumulated and compacted on the porous surfaces due to the high contact pressure (Hertzian line contact pressure of 0.15 GPa) [230]. As a result, the highly porous microstructures on the top of dendritic protrusions were flattened to form dense and smooth surfaces (dark patches). **Figure 5.11 (b-d)** show that with the increasing amount of MoS_2, the area of dark patches on the wear tracks became larger. However, when particle concentration increased to 10 g/L or 20 g/L, wear track exhibits a different surface morphology. For Ni-MoS_2 (10 g/L), dark patches cover a major area of wear track, which means the structures on the coating surface have been totally flattened (**Figure 5.12 e**). Similarly, on the wear track of Ni-MoS_2 (20 g/L), a large area of dark patch can also be found (**Figure 5.12 f**). Besides, lots of wear debris were found on the wear track, which might be caused by the fracture of dendritic protrusions. Due to the porous coating structure of Ni-MoS_2 coating (20 g/L), the debris cannot form a compact tribofilm on the coating/counterpart contact region.

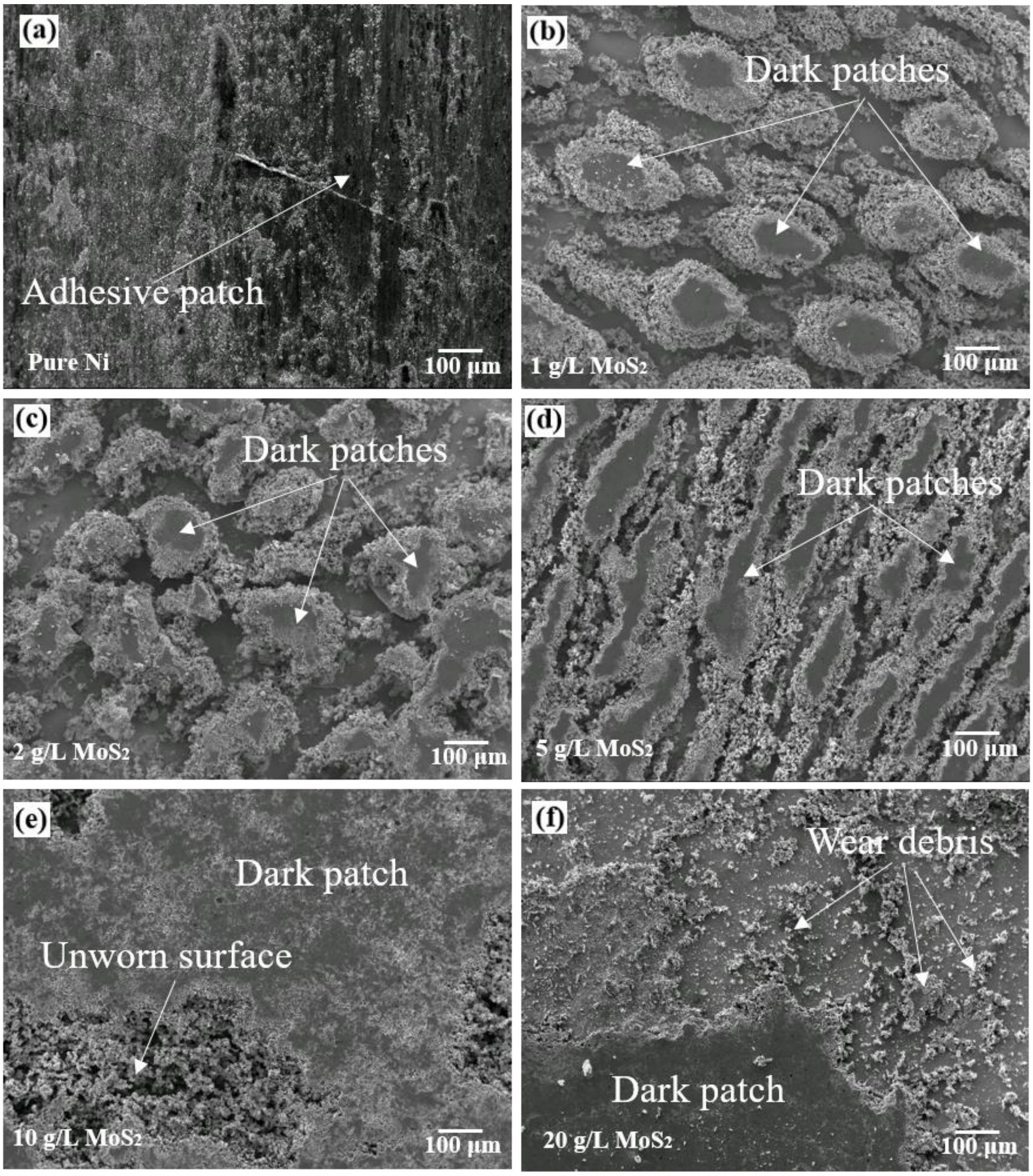

Figure 5.11 Secondary electron SEM images of wear tracks on (a) pure Ni coating and (b-f) Ni-MoS_2 coatings deposited from electrolytes containing MoS_2 concentration of 1, 2, 5, 10, 20 g/L.

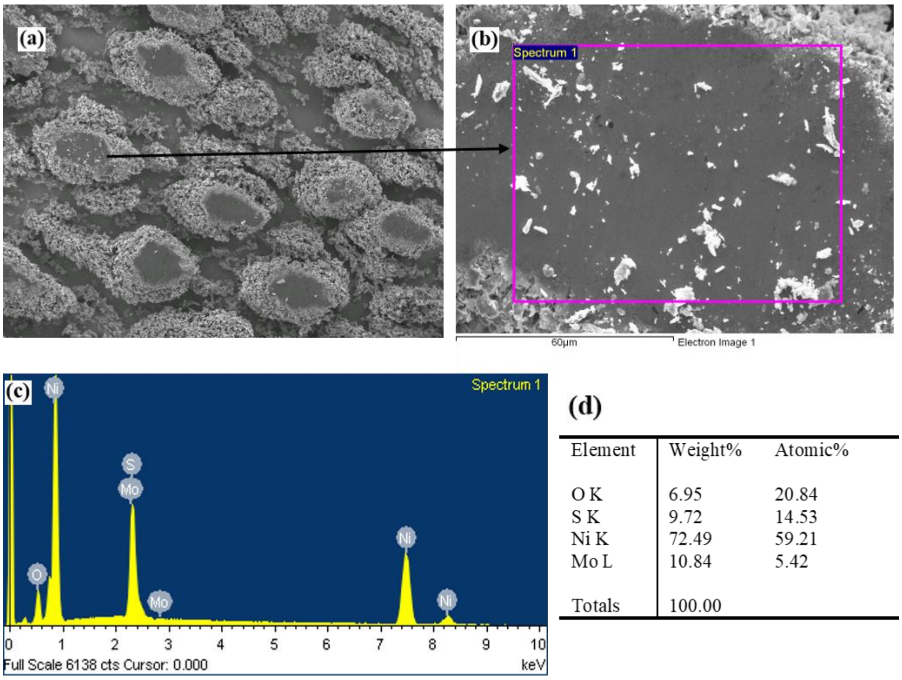

Element	Weight%	Atomic%
O K	6.95	20.84
S K	9.72	14.53
Ni K	72.49	59.21
Mo L	10.84	5.42
Totals	100.00	

Figure 5.12 (a) Secondary electron SEM image of wear track of Ni-MoS_2 coating deposited with 1 g/L MoS_2; (b) EDS analysis on the tribofilm; (c) EDS spectrum; (d): Quantitative EDS results.

The wear tracks of the counterpart cylinders and their corresponding EDS results are illustrated in **Figure 5.13** and **Table 5.2**, respectively. The counterpart cylinder sliding against pure Ni coating exhibits rough wear scars surrounded by widely spread pieces of debris (**Figure 5.13 a**). EDS results also reveal that the worn surface (against pure Ni coating) contain very high oxygen and nickel content (8.2 wt% and 19.1 wt%, respectively), indicating severe oxidation and coating damage occurred during the friction test. On the other hand, wear tracks of counterpart cylinders tested against Ni-MoS_2 coatings consist of a continuous dark patch (tribofilm) surrounded by lots of wear debris (**Figure 5.13 b-f**). Compositional analysis on the wear tracks (**Table 5.2**) suggests that MoS_2 particles can be released from composite coatings during friction test and then transferred onto the counterpart cylinders to form a tribofilm layer acting as lubrication. Lower oxygen content compared with counterpart cylinder sliding against pure Ni also verifies reduced oxidation caused by frictional heat. Moreover, it is noteworthy that wear tracks of cylinder tested against Ni-MoS_2 (10 g/L and 20 g/L) coatings are wider than others. This can be explained by the low coating hardness, making the counterpart cylinder plough deeply into the coating surface. The lower value of element Mo and S on wear track of cylinder against Ni-MoS_2 (10 g/L) could be explained by the inhomogeneous distribution of tribofilm on the cylinder.

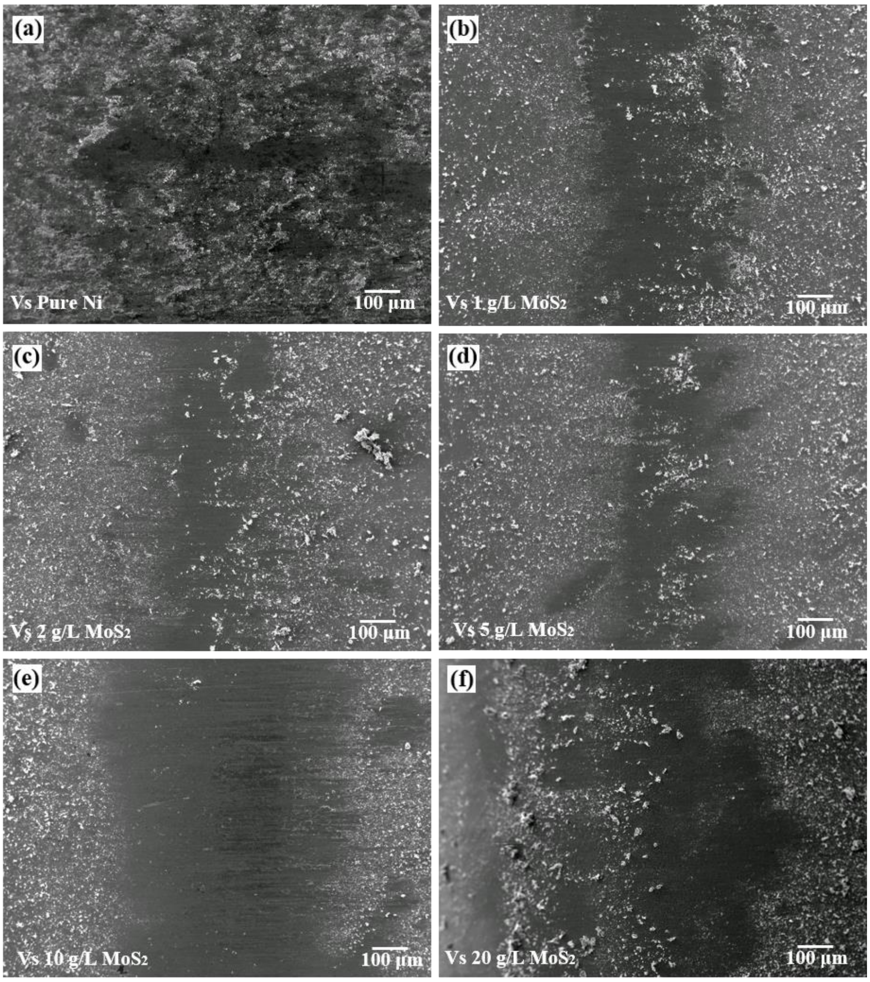

Figure 5.13 Secondary electron SEM images of wear tracks on counterpart cylinders (a) sliding against pure Ni coating; (b-f) sliding against Ni-MoS_2 coatings deposited from electrolytes containing particle concentration of 1, 2, 5, 10, 20 g/L.

Table 5.2 EDS compositional analysis on the wear tracks of counterpart cylinders sliding against pure Ni coating and Ni-MoS_2 coatings deposited from electroplating bath containing different particle concentration.

Counterpart (particle content)	O (wt%)	Fe (wt%)	Cr (wt%)	Ni (wt%)	Mo (wt%)	S (wt%)
Vs pure Ni	8.17	71.20	1.18	19.09	N/A	N/A
Vs Ni-MoS_2 (1 g/L)	6.82	68.59	1.32	13.59	6.04	3.64
Vs Ni-MoS_2 (2 g/L)	4.62	79.70	1.63	8.64	3.51	1.89
Vs Ni-MoS_2 (5 g/L)	4.62	75.74	1.31	10.19	4.78	3.36
Vs Ni-MoS_2 (10 g/L)	6.90	73.29	1.42	10.09	5.68	2.62
Vs Ni-MoS_2 (20 g/L)	6.23	75.02	1.54	12.29	2.65	2.26

5.2.2 Effect of surfactant

This research aims to develop a Bifunctional composite coating with a dense structure. However, the findings in the previous section reveal that the co-deposition of MoS_2 particles leads to the dendritic growth of nickel deposit. Although increasing particle concentration (up to 10 g/L) in electrolyte helps to close the gaps between dendritic protrusions and smoothen surface morphologies, a high level of porosity can still be observed from coating cross-section. Moreover, the composite coating containing high MoS_2 content tends to be soft, which makes it unable to support loading from counterpart and easily be crushed under sliding contact motion. Consequently, Ni-MoS_2 coating exhibited high friction coefficient and wear rate in the friction test.

To improve the mechanical properties and tribological performance of Ni-MoS_2 coating, it is necessary to densify the coating structure. Previous research carried out by Wang [173] reported Ni-MoS_2 coating deposited from electroplating bath containing cationic surfactant BAS has better adhesion, lower porosity and denser structure than the coating without surfactant addition. According to Wang, the improvement of coating structure is attributed to the reduced particle conductivity achieved by BAS adsorption. However, in Wang's study, the densification of Ni-MoS2 coatings was studied only through SEM images of coating surface and cross-section. Further characterization (e.g. hardness test and tribological test) to evaluate the effects brought by coating densification has not been carried out. Therefore, in this research, the effect of cationic surfactant on the co-deposition of the conductive particle was investigated. Specifically, the cationic surfactant chosen for investigation was CTAB, one of the most frequently used surfactants in academia and industry. Composite coating systems of the investigation were Ni-MoS_2, Ni-WS_2 and Ni-MoS_2-WS_2 coatings. The particle concentration in the electrolyte was set as 10 g/L according to the findings in the previous section (refined coating surface morphology obtained with a concentration of 10 g/L).

The optical images of pure Ni coatings and Ni-MoS_2 coatings (10 g/L) prepared with and without surfactant are illustrated in **Figure 5.14**. Pure Ni coating deposited without CTAB addition shows many pits and pores distributed across the coating surface. In contrast, pure Ni coating deposited with 0.1 g/L CTAB addition shows a mirror-like surface. From previous study, the addition of CTAB reduces the surface tension of electroplating solution, which promotes the escape of generated hydrogen bubble and promote uniform growth of pure Ni deposit [231]. Similarly, the comparison of Ni-MoS_2 coatings also suggests that CTAB addition can improve the smoothness of the coating surface by inhibiting the MoS_2 particle agglomeration and dendritic growth of the Ni-MoS_2 deposit.

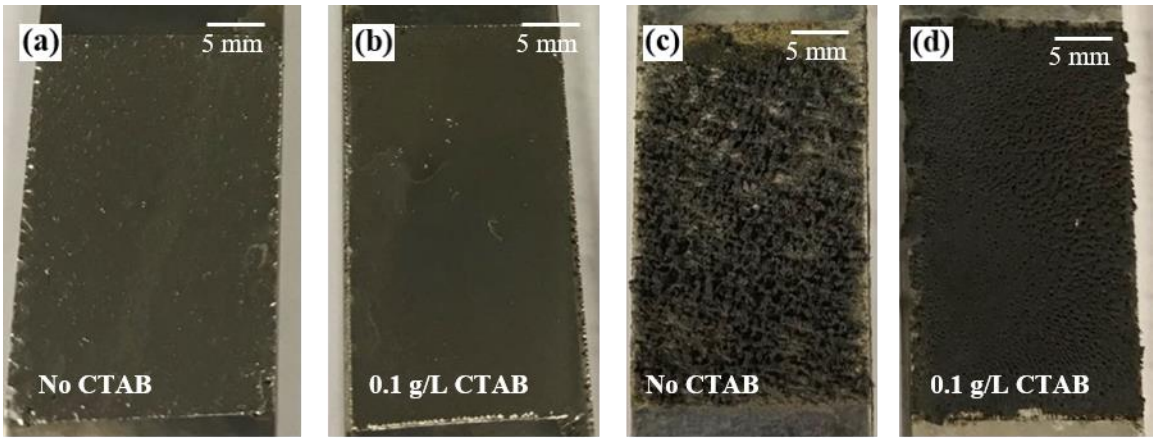

Figure 5.14 Surface appearances of coatings prepared from electrolytes with or without CTAB addition (a-b) pure Ni coatings; (c-d) Ni-MoS_2 coatings, particle concentration 10 g/L.

The surface morphology evolution of Ni-MoS_2, Ni-WS_2 and Ni-MoS_2-WS_2 coatings with increasing CTAB concentration from 0.1 g/L to 0.5 g/L is shown in **Figure 5.15**. It can be noted that the holes found on Ni-MoS_2 coating deposited with 0.1 g/L CTAB addition disappeared with increasing CTAB concentration (**Figure 5.15 a-c**). In addition, all Ni-MoS_2 coatings exhibit smooth and refined surface morphologies. On the contrary, the surfaces of all Ni-WS_2 coatings are relatively rough and coarse (**Figure 5.15 d-f**), which means that the variation of CTAB addition in the electroplating bath has little effect on the surface morphologies of Ni-WS_2 coatings. Different from Ni-MoS_2 and Ni-WS_2 coatings, the surface morphology of Ni-MoS_2-WS_2 coatings changed from rough to fine when the CTAB concentration increased from 0.1 g/L to 0.2 g/L (**Figure 5.15 g-h**). However, further increasing the CTAB concentration to 0.5 g/L will result in the formation of pits on the coating surface (**Figure 5.15 i**). The evolution of composite coating surface morphologies can also be verified by Alicona 3D surface reconstruction (**Figure 5.16**), which shows that increasing CTAB concentration can reduce the surface roughness of Ni-MoS_2 and Ni-MoS_2-WS_2 coatings but has little effect on Ni-WS_2 coating.

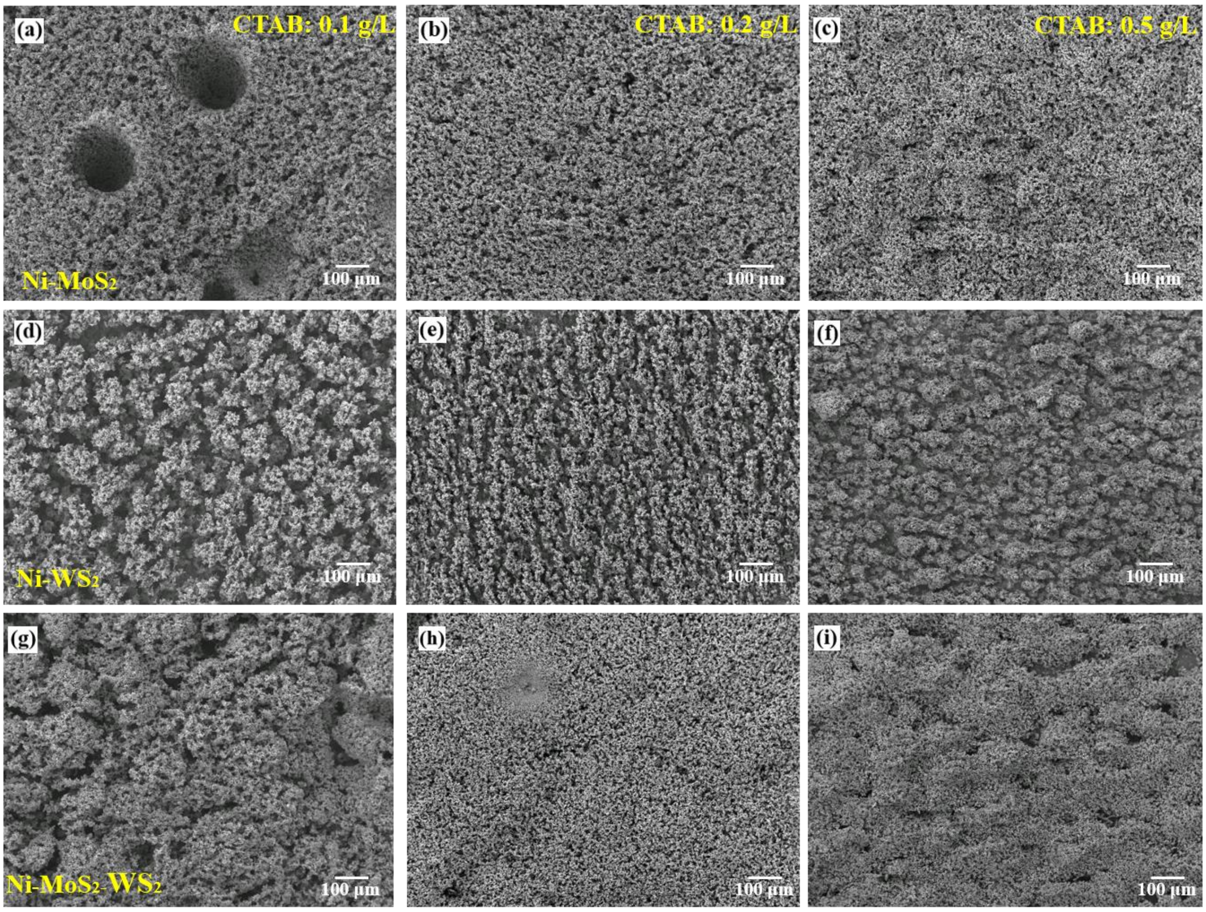

Figure 5.15 Secondary electron SEM images of (a-c): Ni-MoS_2 coatings; (d-f): Ni-WS_2 coatings; (g-i): Ni-MoS_2-WS_2 coatings prepared from electrolytes containing CTAB concentration of 0.1, 0.2 and 0.5 g/L. For Ni-MoS_2 coatings, particle size and concentration are 1.2 µm and 10 g/L; for Ni-WS_2 coatings, particle size and concentration are 1.1 µm and 10 g/L; for Ni-MoS_2-WS_2 coatings, particle addition is 1.2 µm (5 g/L) MoS_2 + 1.1 µm (5 g/L) WS_2.

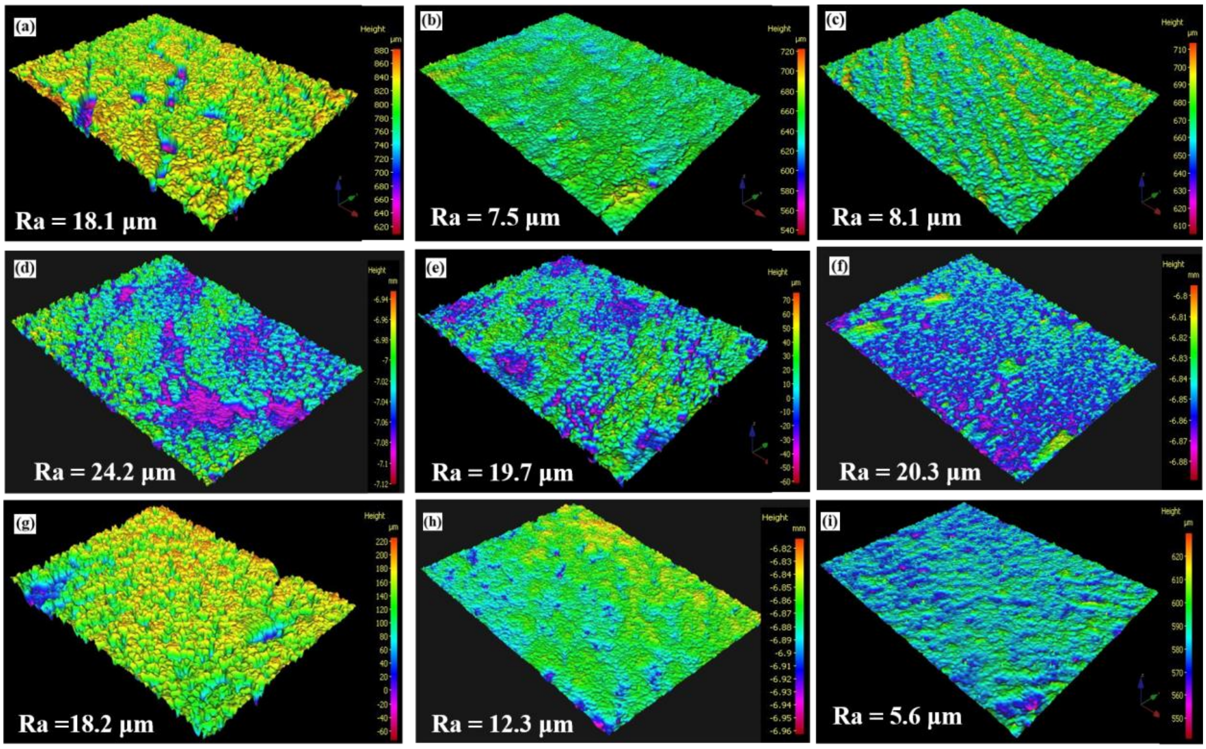

Figure 5.16 3D surface topographies of (a-c): Ni-MoS_2 coatings; (d-f): Ni-WS_2 coatings; (g-i): Ni-MoS_2-WS_2 coatings deposited from electrolytes containing CTAB concentration of 0.1, 0.2 and 0.5 g/L.

Figure 5.17 shows the change of particle content in the composite coatings as a function of CTAB concentration in the electrolyte. It can be seen that the particle content in the Ni-MoS_2 coatings was higher than that of the Ni-WS_2 coatings under the same CTAB concentration. In addition, with the increase of CTAB concentration, particle content in the Ni-MoS_2 coating became higher, while particle content in the Ni-WS_2 coating remained almost at the same level. On the other hand, both MoS_2 and WS_2 content in Ni-MoS_2-WS_2 coatings decreased when CTAB concentration increased from 0.1 g/L to 0.5 g/L.

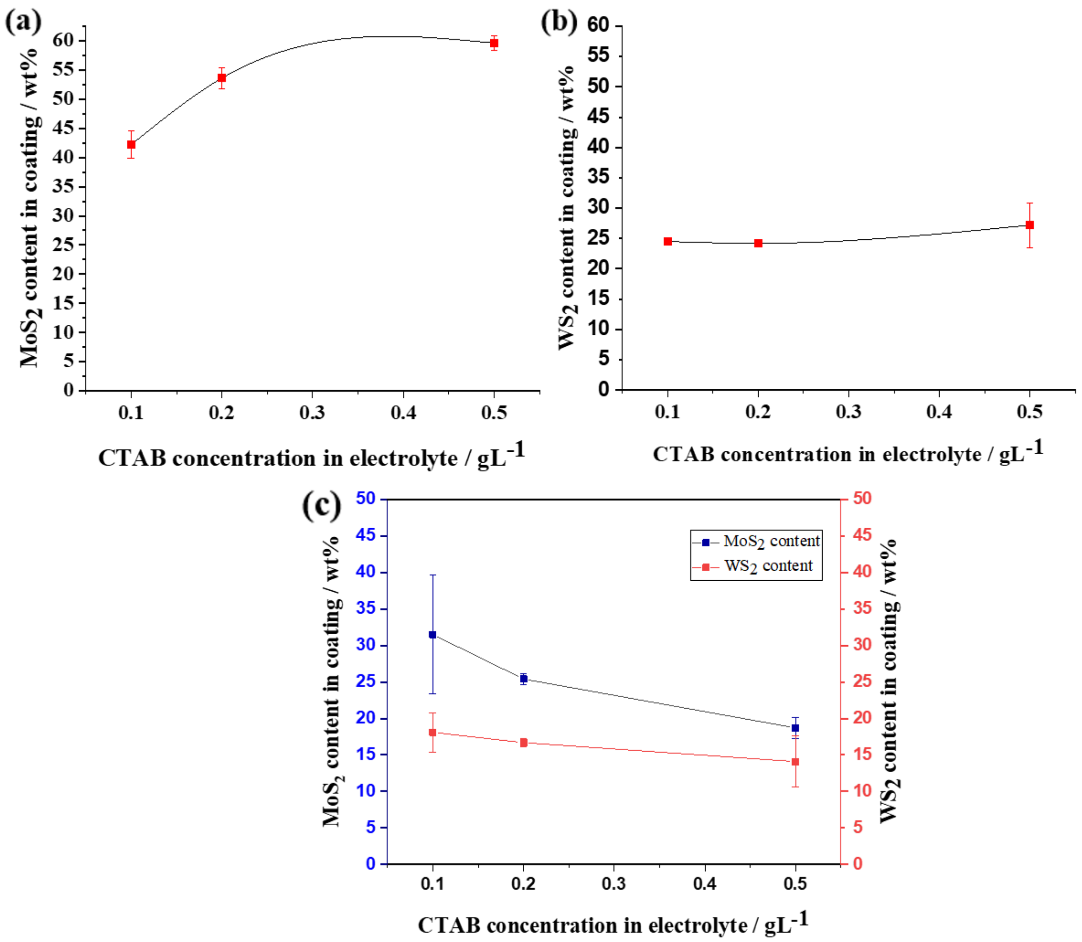

Figure 5.17 EDS measured particle content in (a) Ni-MoS_2 coatings; (b) Ni-WS_2 coatings; (c) Ni-MoS_2-WS_2 coatings deposited from electrolytes containing CTAB concentration of 0.1, 0.2, and 0.5 g/L.

SEM images of cross-sectional views of Ni-MoS_2 coatings deposited with different CTAB concentration are shown in **Figure 5.18**. With 0.1 g/L CTAB addition, Ni-MoS_2 coating presents a structure full of voids. The corresponding high magnification SEM image reveals that the coating is very porous and contains numerous MoS_2 particles. When CTAB concentration increased to 0.2 g/L, the coating structure became denser and smaller voids were observed. Moreover, under high magnification, the distribution of the MoS_2 particles in the Ni matrix is uniform. The coating structure was densified by further increasing CTAB concentration. Ni-MoS_2 coating deposited with 0.5 g/L CTAB showed the lowest level of voids. The cross-section also reveals that only nickel was deposited on the substrate in the first few micrometres of deposit growing. The amount of embedded MoS_2 particles gradually increased from the coating/substrate interface to the coating surface. This observation of MoS_2 particle distribution is consistent with the EDS analysis shown in **Figure 4.6 (c)**. At the initial stage of composite electroplating, Ni^{2+} ions near the cathode were reduced to form a nickel deposit. As electroplating time increased, MoS_2 particles were transported to the cathode surface through bath agitation and electrophoretic motion, eventually co-depositing with nickel. Therefore, a gradual increase of MoS_2 particle was observed from the cross-section of Ni-MoS_2 coatings.

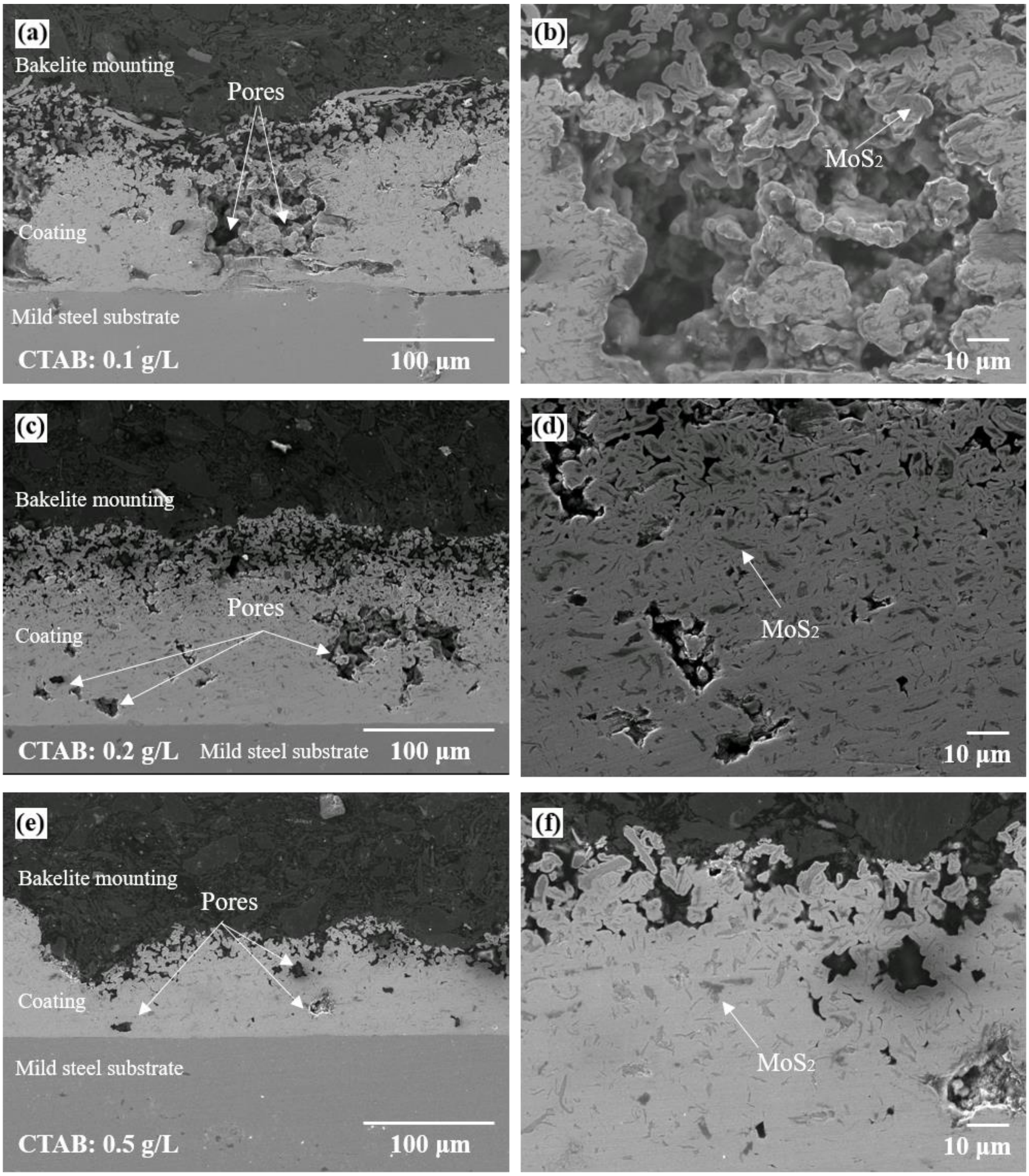

Figure 5.18 Secondary electron SEM images of cross-sectional views of Ni-MoS_2 coatings deposited from electrolytes containing CTAB concentration of (a-b): 0.1 g/L at low and high magnifications respectively; (c-d): 0.2 g/L at low and high magnifications respectively; (e-f): 0.5 g/L at low and high magnifications respectively.

The cross-sections of Ni-WS_2 coatings deposited with different CTAB concentration are shown in **Figure 5.19**. Ni-WS_2 coatings exhibit similar porous structures to that of Ni-MoS_2 coatings. However, the uniformity of Ni-WS_2 coating is much worse compared with Ni-MoS_2 coatings. As shown in **Figure 5.19 (a)**, the Ni-WS_2 coating deposited with 0.1 g/L CTAB shows a valley-shaped defect with only a thin layer of deposit covering the substrate. The high magnification SEM image shows that the outmost layer is porous (**Figure 5.19 b**). When CTAB concentration increased to 0.2 g/L, the uniformity of Ni-WS_2 coating improved (**Figure 5.19 c**), but the dendritic growth of deposit can be observed on the outmost layer of coating (**Figure 5.19 d**). As the CTAB concentration further increased to 0.5 g/L, obvious cracks could be found at the interface (**Figure 5.19 e**), indicating poor bonding between coating and substrate. Moreover, the high magnification SEM image in **Figure 5.19 (f)** shows that the dendritic growth of deposit on the top layer became more severe at a high concentration of CTAB (0.5 g/L).

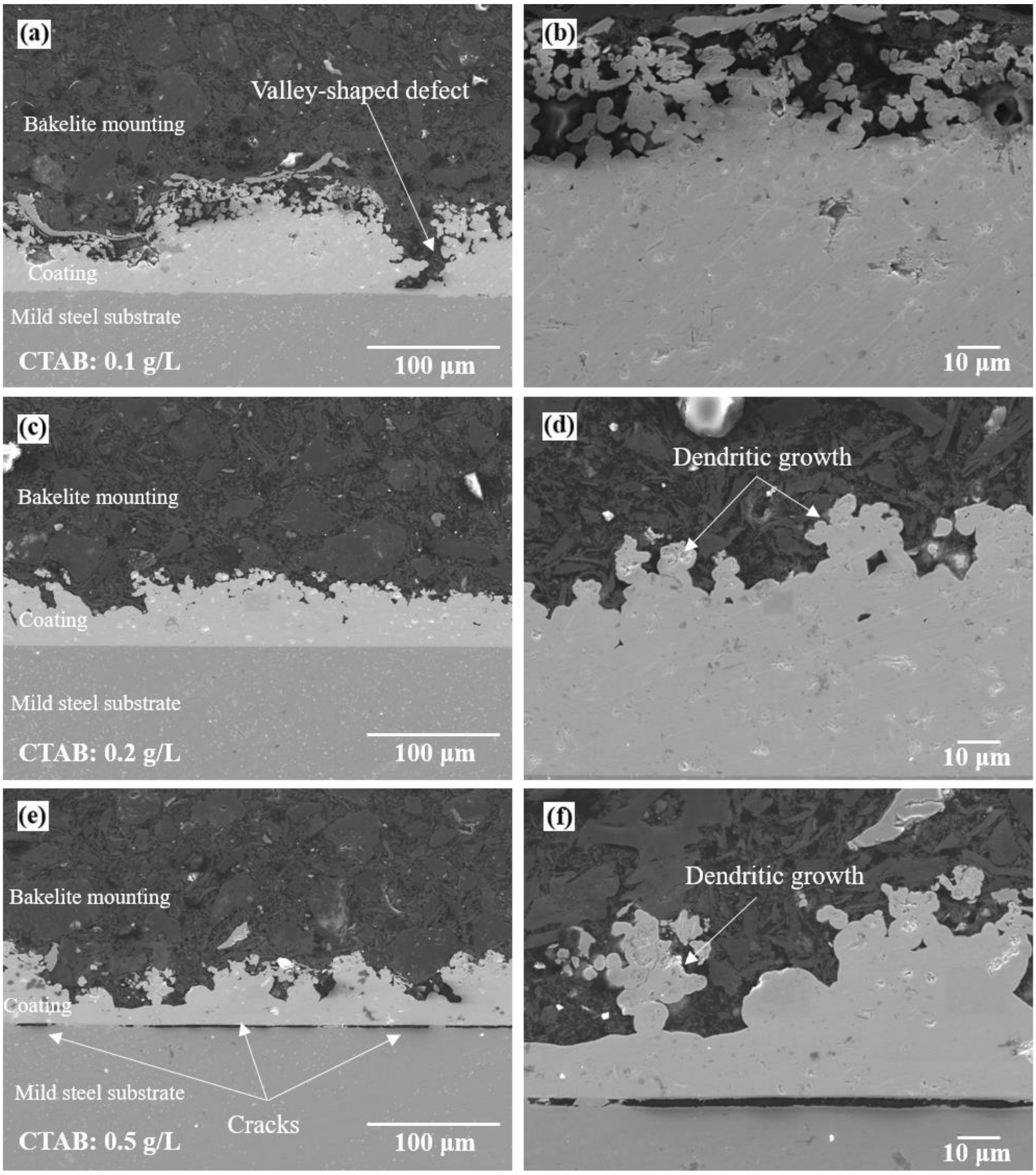

Figure 5.19 Secondary electron SEM images of cross-sectional views of Ni-WS_2 coatings deposited from electrolytes containing CTAB concentration of (a-b): 0.1 g/L at low and high magnifications respectively; (c-d): 0.2 g/L at low and high magnifications respectively; (e-f): 0.5 g/L at low and high magnifications respectively.

The cross-sectional views of all Ni-MoS_2-WS_2 coatings can be divided into two layers (**Figure 5.20**). The first layer close to the substrate is relatively dense. The second layer is porous and consists of loosely adsorbed particles surrounded by deposited nickel. The high magnification SEM cross-sectional images show that Ni-MoS_2-WS_2 coatings contain lots of particles within the Ni matrix.

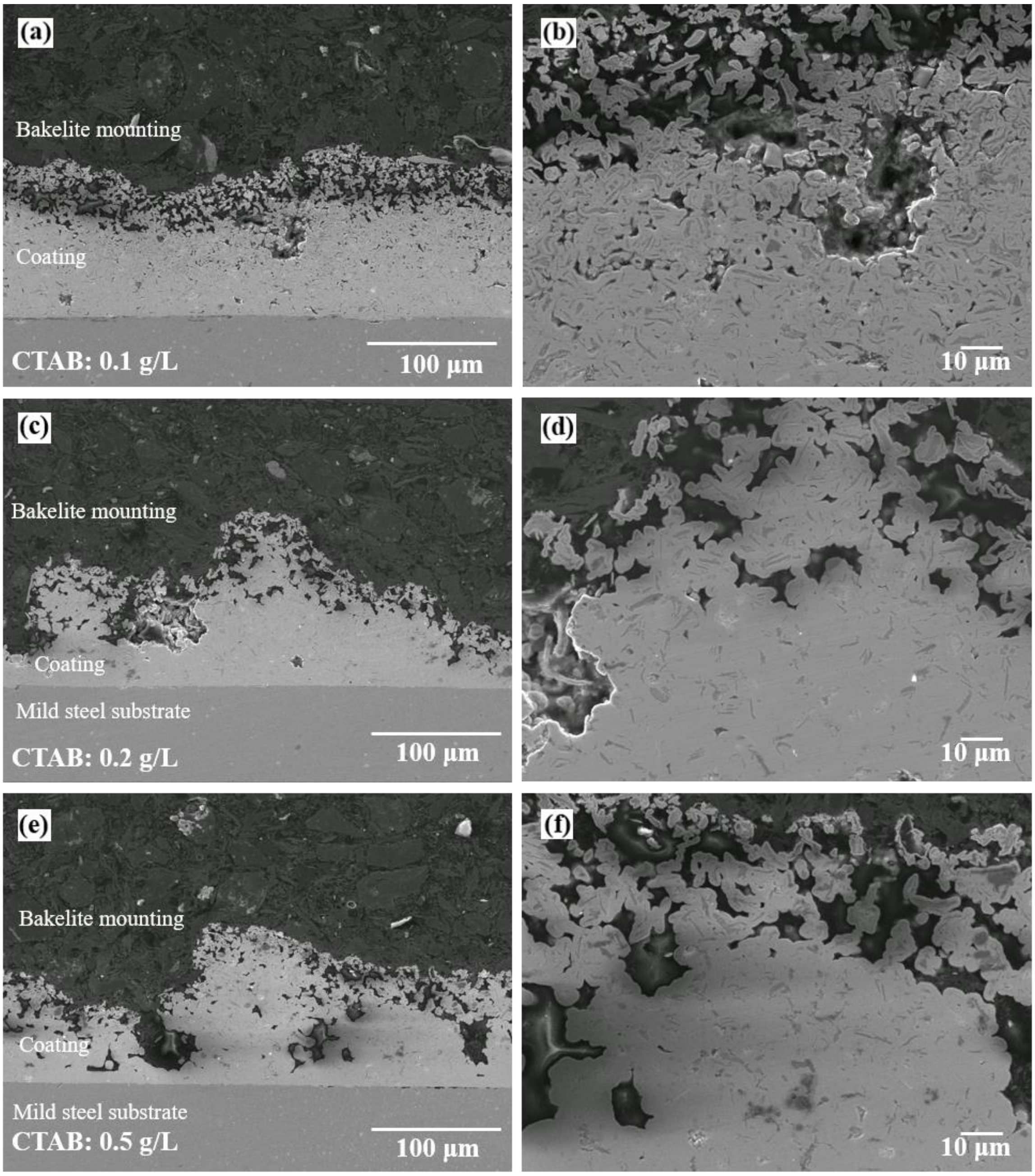

Figure 5.20 Secondary electron SEM images of cross-sectional views of Ni-MoS_2-WS_2 coatings deposited from electrolytes containing CTAB concentration of (a-b): 0.1 g/L at low and high magnifications respectively; (c-d): 0.2 g/L at low and high magnifications respectively; (e-f): 0.5 g/L at low and high magnifications respectively.

The thickness of Ni-MoS_2, Ni-WS_2 and Ni-MoS_2-WS_2 coatings deposited with different CTAB concentration are shown in **Figure 5.21**.Coating thickness values were measured from cross-sectional SEM images. For all three types of coatings, the lowest thickness values were observed with 0.5 g/L CTAB concentration. It can also be noted that the coating thickness of Ni-WS_2 and Ni-MoS_2-WS_2 decreased with increasing CTAB concentration. However, for Ni-MoS_2 coating, such decreasing trend was not observed. In addition, Ni-WS_2 coating thickness was much lower than Ni-MoS_2 and Ni-MoS_2-WS_2 coatings under all CTAB concentration. The low coating thickness of Ni-WS_2 coating can be attributed to the low co-deposited particle content, which decreased tendency of dendritic Ni-WS_2 deposit formation.

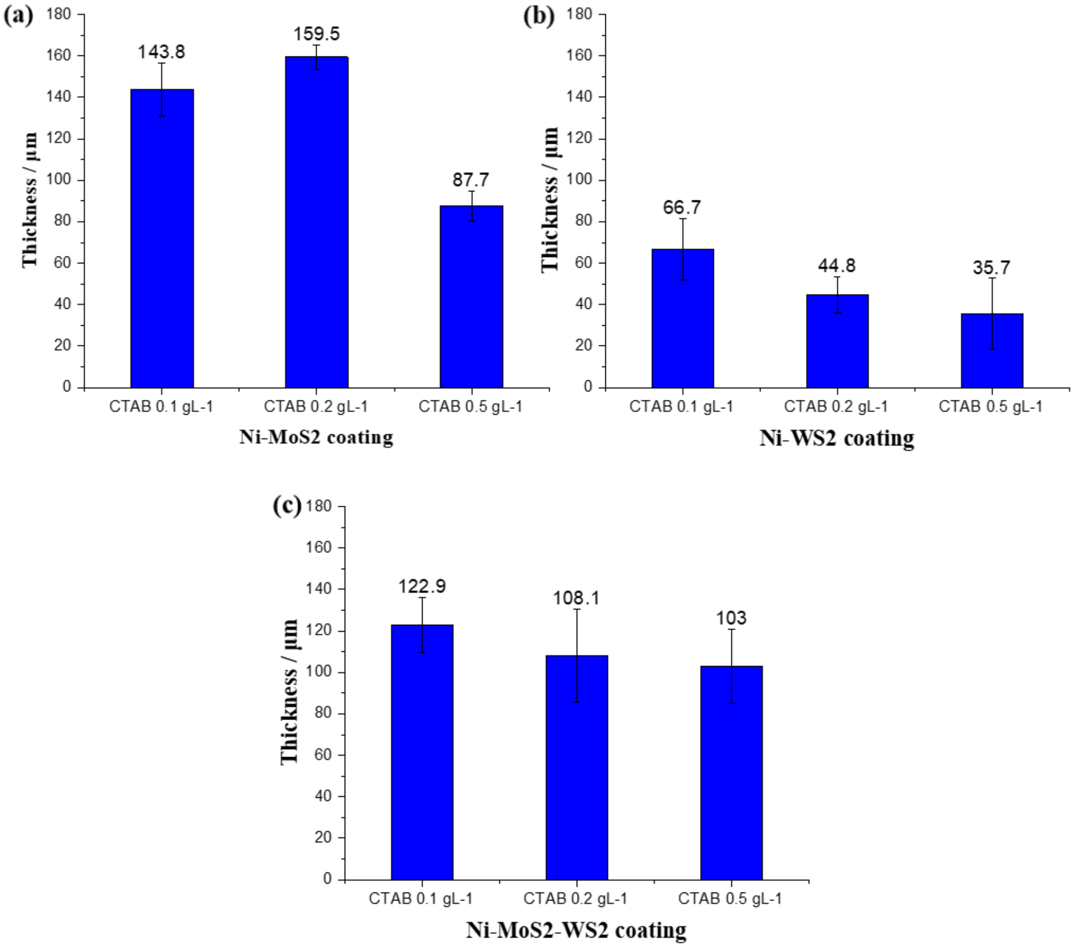

Figure 5.21 Coating thickness measurement of composite coatings deposited from electrolytes containing different CTAB concentration, (a) Ni-MoS_2 coatings; (b) Ni- WS_2 coatings; (c) Ni-MoS_2-WS_2 coatings.

The hardness measurement conducted on the cross-section of composite coatings is illustrated in **Figure 5.22**. It can be noted that the hardness of Ni-MoS_2 and Ni-MoS_2-WS_2 coatings increased with increasing CTAB concentration.. This increase can be attributed to the lower embedded particle content observed on the cross-sectional views of coatings. However, the hardness of the Ni-WS_2 coating did not show a tendency to increase with higher CTAB concentration because the cross-sectional views of Ni-WS_2 coatings do not vary a lot from one another. Moreover, under the same level of CTAB addition, the hardness of Ni-WS_2 coating is greater than that of Ni-MoS_2 and Ni-MoS_2-WS_2 coatings. The greater hardness can be explained by the denser coating structures of Ni-WS_2 compared with the other two types of composite coatings. The indentation marks observed in the cross-sections of most samples are clearly defined (similar to **Figures 5.6 a–c**), except for Ni-MoS_2 and Ni-MoS_2-WS_2 deposited with 0.1 g/L CTAB, which exhibit unclear indentation corners (similar to **Figure 5.6 d**).

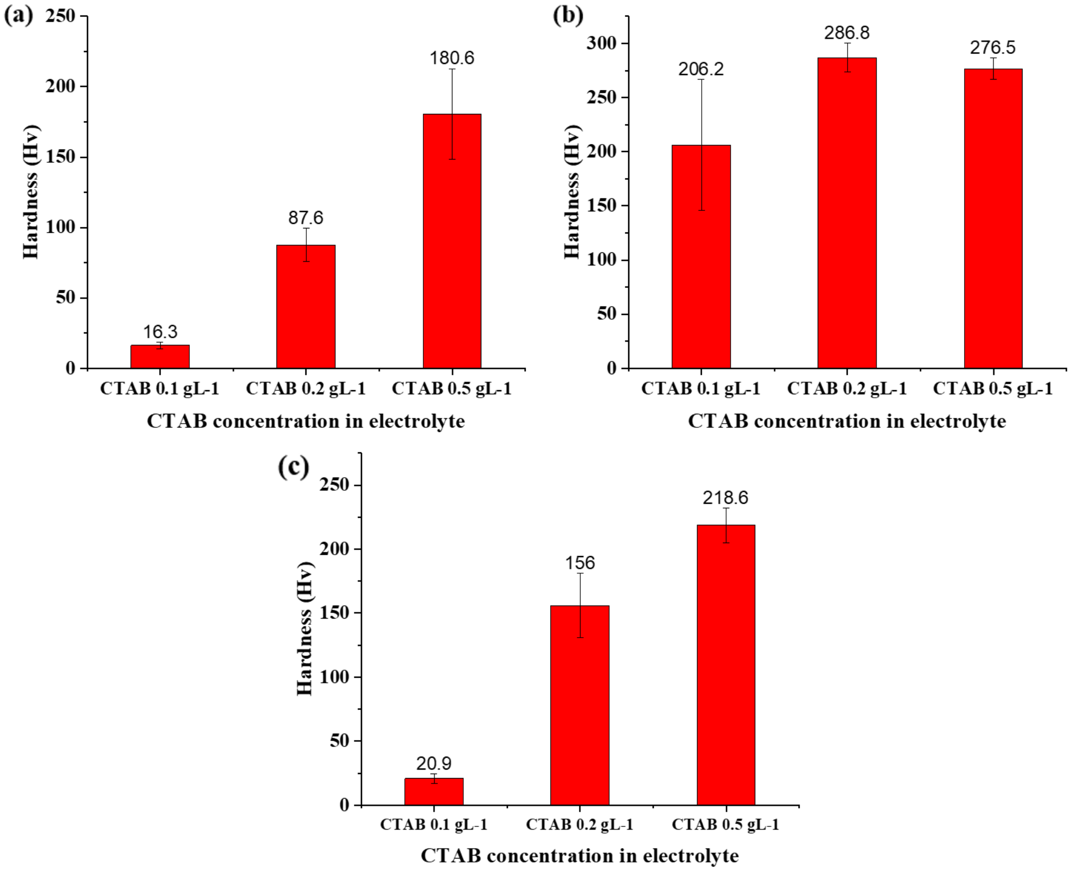

Figure 5.22 Hardness measurement of composite coatings deposited from electrolytes containing different CTAB concentration, (a) Ni-MoS_2 coatings; (b) Ni-WS_2 coatings; (c) Ni-MoS_2-WS_2 coatings.

The friction coefficient as a function of friction test time for composite coatings deposited with different CTAB concentration is illustrated in **Figure 5.23**. For both Ni-MoS_2 and Ni-MoS_2-WS_2 coatings, the lowest friction coefficients were 0.07 and 0.08, respectively, which were all achieved by adding 0.5 g/L CTAB concentration. It is worth noting that Ni-MoS_2 and Ni-MoS_2-WS_2 coatings had the shortest run-in period when CTAB concentration in electrolyte bath was 0.5 g/L. In addition, within the run-in period, the friction coefficient of Ni-MoS2 coating deposited with 0.1 g/L CTAB increased sharply up to 0.2 and then dropped. With the increase of CTAB concentration, the highest friction coefficient within the run-in period dropped to 0.09 at 0.5 g/L CTAB. A similar decreasing trend of friction coefficient within the run-in period can also be observed in Ni-MoS_2-WS_2 coating system. Unlike Ni-MoS_2 and Ni-MoS_2-WS_2 coatings, even though the CTAB concentration increased from 0.1 g/L to 0.5 g/L, the friction coefficient of all Ni-WS2 coatings remained at a low level of about 0.06. The different tribological performance of composite coatings can be explained as follows. For Ni-MoS_2 and Ni-MoS_2-WS_2 coatings, the surface morphologies changed from coarse to smooth with increasing CTAB concentration. During the "run-in" period, tribofilms are more readily formed on smoother coating surfaces. Therefore, Ni-MoS_2 and Ni-MoS_2-WS_2 coatings deposited with 0.5 g/L CTAB are easy to enter a stable and low friction state throughout the friction test. On the other hand, the hardness of Ni-MoS_2 and Ni-MoS_2-WS_2 coatings increased with increasing CTAB concentration. Composite coating with higher hardness can provide firm support for the solid lubricant particles to allow an effective shear to take place so that a low friction tribofilm may readily develop. This explained the low friction coefficient of Ni-MoS_2 and Ni-MoS_2-WS_2 coatings when 0.5 g/L CTAB was added into the electroplating bath. However, for Ni-WS_2 coating, both the surface morphologies and the hardness remained almost unchanged at various CTAB concentration. Therefore, the tribological properties of Ni-WS_2 coatings are similar.

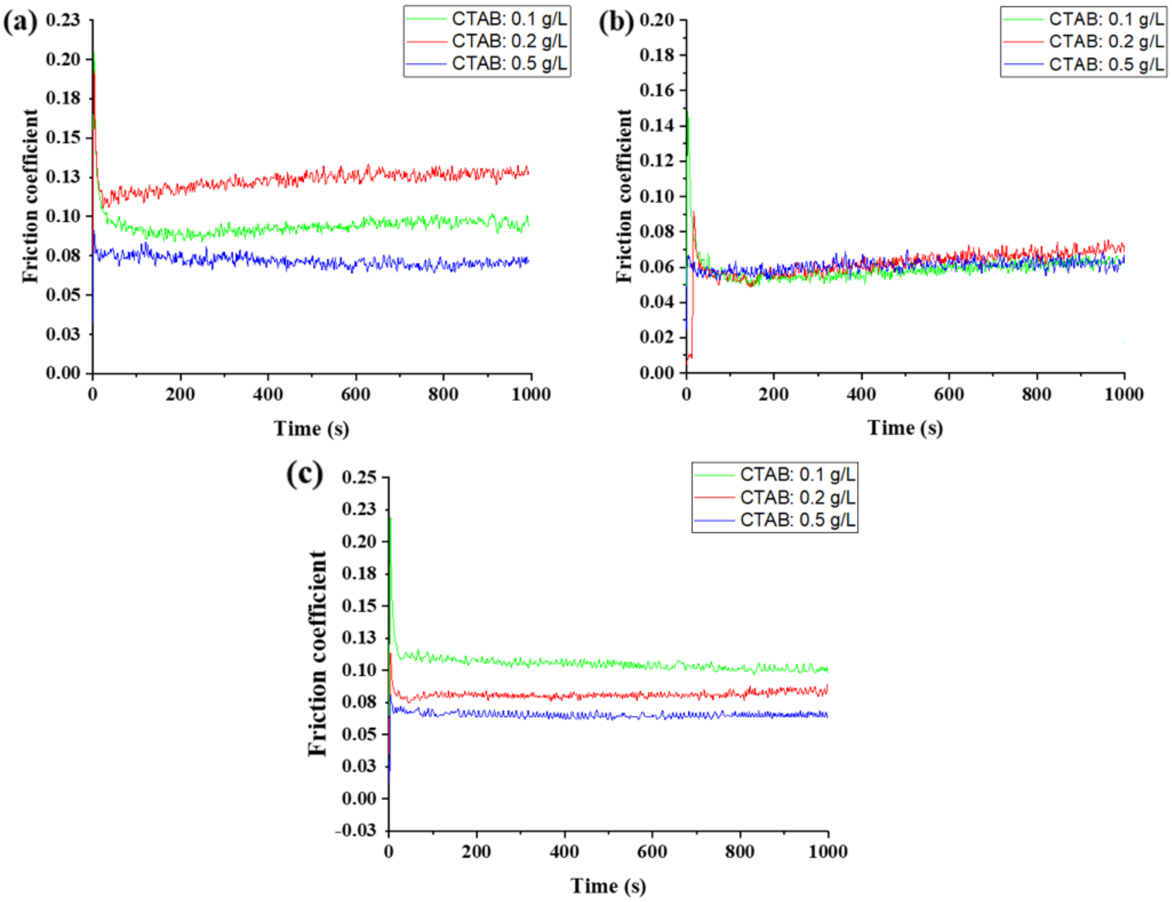

Figure 5.23 Friction coefficient as a function of time for composite coatings deposited with different CTAB concentration (as indicated in each image), (a) Ni-MoS_2 coatings; (b) Ni-WS_2 coatings; (c) Ni-MoS_2-WS_2 coatings.

SEM images of wear tracks on Ni-MoS_2 coatings and the corresponding counterpart cylinders are shown in **Figure 5.24**. A large area of dark patch was observed on the worn surface of Ni-MoS_2 coating deposited with 0.1 g/L CTAB (**Figure 5.24 a**). The corresponding SEM image of the wear track on the counterpart cylinder shows a continuous dark patch surrounded by lots of wear debris (**Figure 5.24 b**). EDS analysis revealed that the dark patch on the counterpart cylinder contains element nickel (10.1 wt%), molybdenum (5.7 wt%), and sulphur (2.7 wt%), indicating the transfer of tribofilm from the coating to the counterpart cylinder. As the CTAB concentration increased to 0.2 g/L, the dark patch area on the worn coating surface (**Figure 5.24 c**) and counterpart cylinder (**Figure 5.24 d**) decreased. With a further increase in CTAB concentration (0.5 g/L), the dark patch on the worn coating surface became discontinuous (**Figure 5.24 e**). The wear track on the counterpart cylinder was also found to become narrower (**Figure 5.24 f**). Compared with the original surface morphologies (**Figure 5.15 a-c**), the microstructures on Ni-MoS_2 coatings were flattened to form dark patches during the friction test.

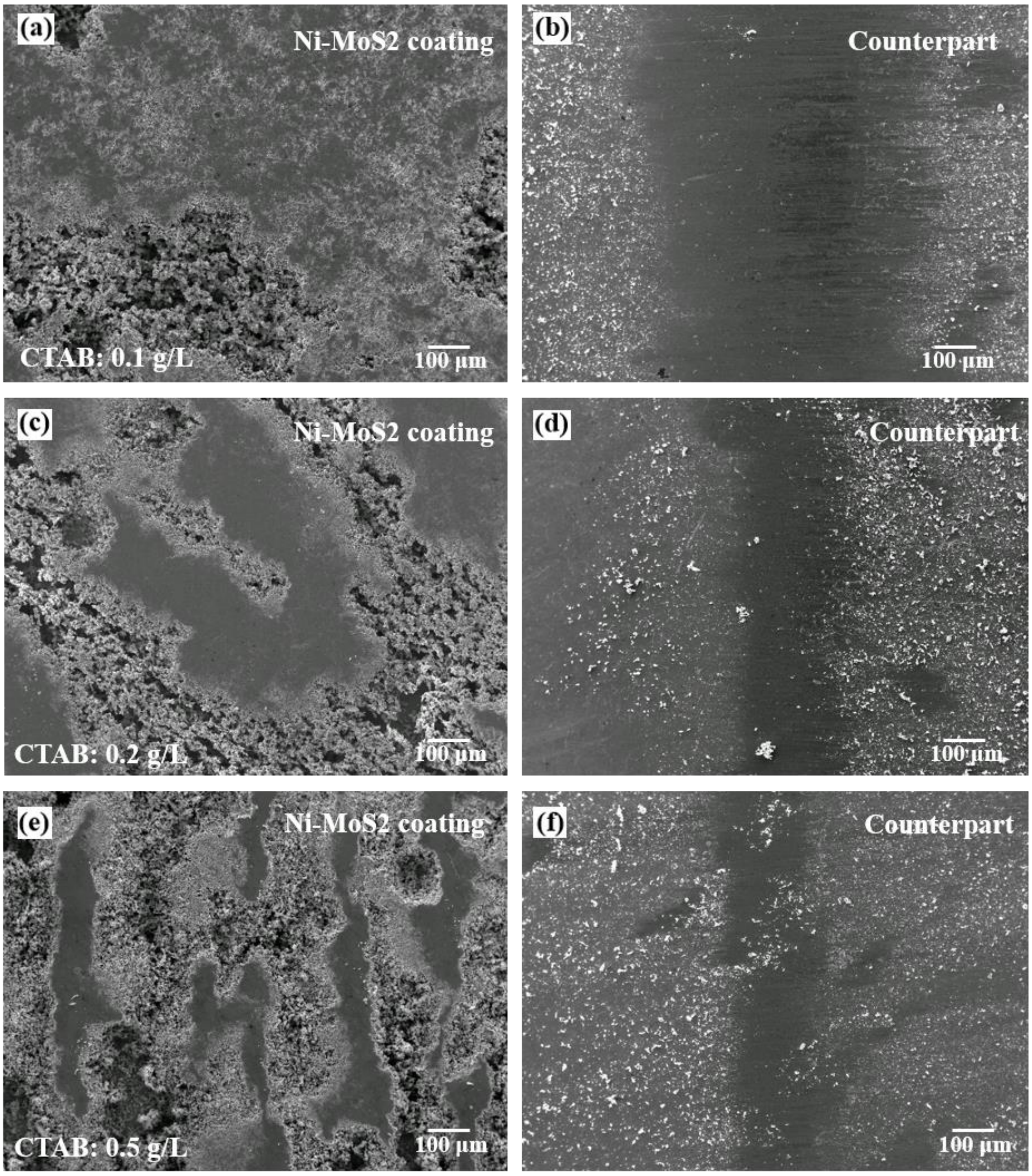

Figure 5.24 Secondary electron SEM images of wear tracks on Ni-MoS_2 coatings and their corresponding counterpart cylinders after 1000 s friction test, (a-b) CTAB addition of 0.1 g/L; (c-d) CTAB addition of 0.2 g/L; (e-f) CTAB addition of 0.5 g/L.

Figure 5.25 shows the wear tracks on Ni-WS$_2$ coatings and corresponding counterpart cylinders. Ni-WS$_2$ coatings deposited with 0.1 g/L CTAB shows discontinuous dark patches on the worn surfaces (**Figure 5.25 a**). Lots of debris was observed on the wear tracks of the corresponding counterpart cylinder (**Figure 5.25 b**). As the CTAB concentration increased to 0.2 g/L, the size of dark patches on the worn coating surface became smaller (**Figure 5.25 c**), and the wear track on the counterpart cylinder was much narrower (**Figure 5.25 d**). When CTAB concentration increased to 0.5 g/L, the morphologies of worn coating (**Figure 5.25 e**) and counterpart cylinder (**Figure 5.25 f**) were similar to that deposited with 0.1 g/L CTAB.

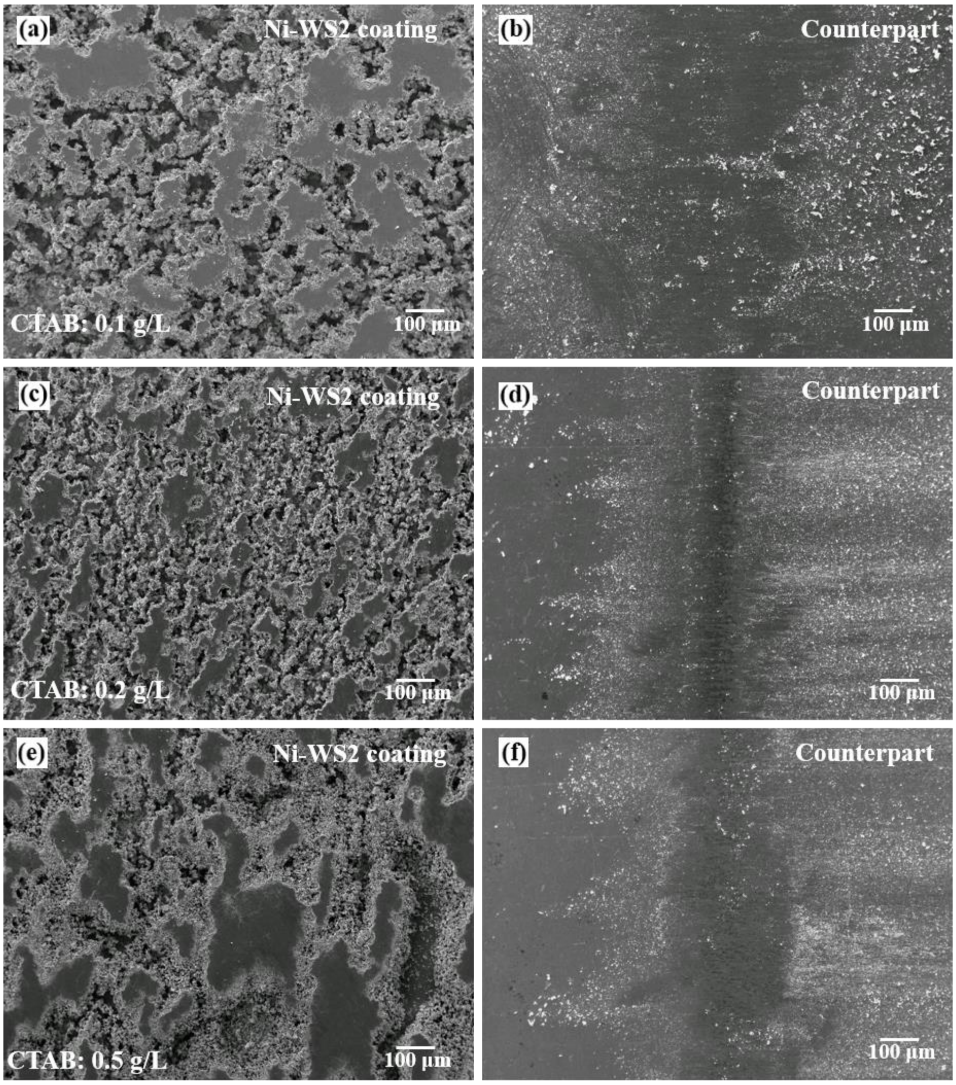

Figure 5.25 Secondary electron SEM images of wear tracks on Ni-WS$_2$ coatings and their corresponding counterpart cylinders after 1000 s friction test, (a-b) CTAB addition of 0.1 g/L; (c-d) CTAB addition of 0.2 g/L; (e-f) CTAB addition of 0.5 g/L.

The evolution of wear tracks on Ni-MoS_2-WS_2 coating with increasing CTAB concentration (**Figure 5.26**) is similar to Ni-MoS_2 coating. The dark patch area on the worn surface decreased as the CTAB concentration in the electroplating bath increased from 0.1 g/L to 0.5 g/L. The width of the wear track on the corresponding counterpart cylinder also decreased from about 450 µm at 0.1 g/L CTAB (**Figure 5.26 b**) to 150 µm at 0.5 g/L (**Figure 5.26 f**). The decrease of wear track depth on the counterpart cylinder might be related to the hardness of Ni-MoS_2-WS_2 coatings. Ni-MoS_2-WS_2 coating deposited with 0.1 g/L CTAB shows a low hardness (20.9 Hv). During the friction test, it could not withstand loading from the counterpart cylinder and tended to be crushed. In other words, the counterpart cylinder could plough deeply into the coating surface, resulting in a wide wear track. Oppositely, Ni-MoS_2-WS_2 coating deposited with 0.5 g/L CTAB shows higher hardness (218.6 Hv), which avoided the deep ploughing of the counterpart cylinder. Therefore, the wear track depth on the counterpart cylinder became narrow.

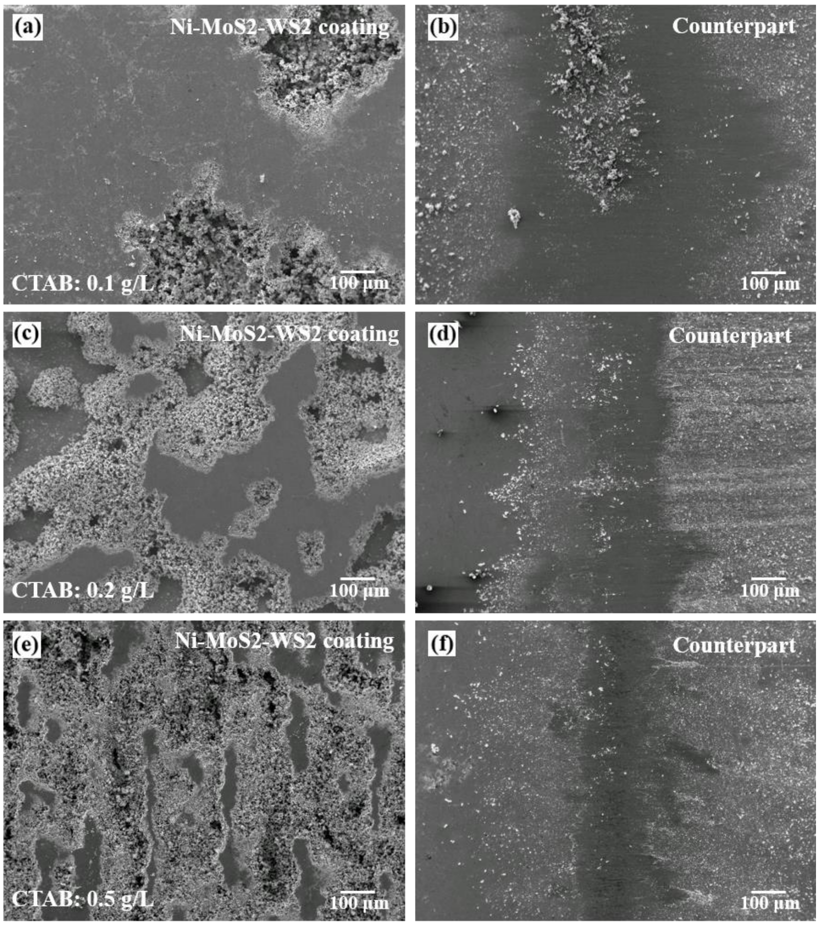

Figure 5.26 Secondary electron SEM images of wear tracks on Ni-MoS_2-WS_2 coatings and their corresponding counterpart cylinders after 1000 s friction test, (a-b) CTAB addition of 0.1 g/L; (c-d) CTAB addition of 0.2 g/L; (e-f) CTAB addition of 0.5 g/L.

Figure 5.27 shows the wear depth of composite coatings deposited with different CTAB concentration. With the increase of CTAB concentration, the wear depth of Ni-MoS_2 coating decreased from 91.7 μm to 25.5 μm. A similar decreasing trend in wear depth can also be found in the case of Ni-MoS_2-WS_2 coating. The high value of wear depth at low CTAB concentration (0.1 g/L) can be attributed to the compaction of coating structure during the wear test. As shown in optical images (**Figure 5.14**), the porous coating structure of Ni-MoS_2 coatings deposited without CTAB surfactant could easily be compacted during the sliding of counterpart cylinder, resulting in a high value of wear depth. With the addition of CTAB, Ni-MoS_2 coating exhibits a more uniform structure, which reduces surface roughness and improves wear resistance under sliding condition. However, the increase of CTAB in the electroplating bath of Ni-WS_2 coatings brought little effect on surface morphology, coating structure and hardness. Therefore, wear depth detected after 1000 s of friction test for all Ni-WS_2 coating maintained at a similar level (about 15 μm).

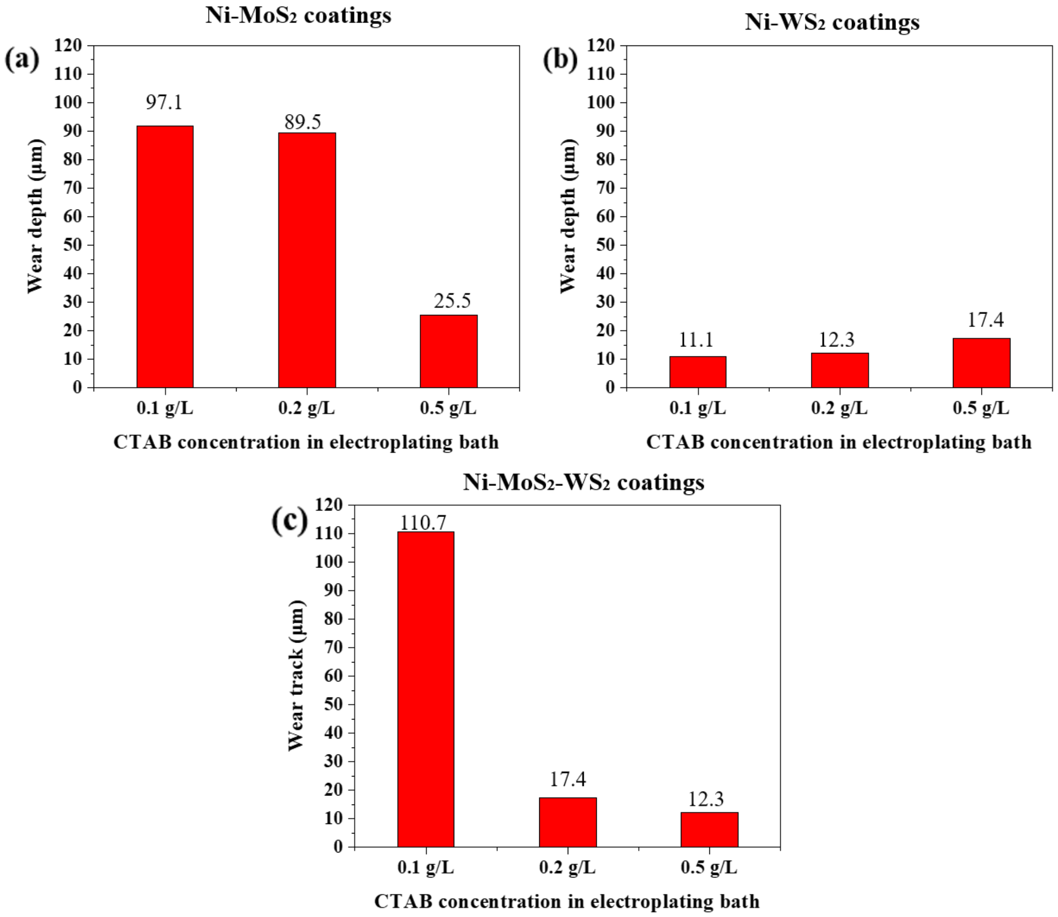

Figure 5.27 Wear depth measured on the composite coatings deposited with different CTAB concentration after 1000 s friction test, (a) Ni-MoS_2 coatings; (b) Ni-WS_2 coatings; (c) Ni-MoS_2-WS_2 coatings.

EDS results of wear tracks on Ni-MoS_2, Ni-WS_2 and Ni-MoS_2-WS_2 coatings and their corresponding counterparts are shown in **Table 5.3** and **Table 5.4** respectively. The phenomenon of tribofilm transferred from coatings to counterparts have been observed in all cases. However, in all cases, the compositional difference between wear tracks on each type of coating and its corresponding counterpart is not obvious. Therefore, it can be speculated that the amount of co-deposited particles is not the key factor determining tribological performance. Instead, the increase in coating hardness and decrease in surface roughness induced by increasing CTAB concentration contribute to the improved self-lubricating and wear resistant properties.

Table 5.3 EDS compositional analysis on wear track of Ni-MoS_2, Ni-WS_2 and Ni-MoS_2-WS_2 coatings deposited with different CTAB concentration after friction test

Sample (CTAB concentration)	O (wt%)	Ni (wt%)	Mo (wt%)	W (wt%)	S (wt%)
Ni-MoS_2 (0.1 g/L)	3.8	59.1	19.9	N/A	16.8
Ni-MoS_2 (0.2 g/L)	3.4	69.1	14.3	N/A	12.2
Ni-MoS_2 (0.5 g/L)	3.2	55.2	20.1	N/A	15.3
Ni-WS_2 (0.1 g/L)	2.5	77.8	N/A	15.1	3.58
Ni-WS_2 (0.2 g/L)	2.7	66.7	N/A	20.9	4.6
Ni-WS_2 (0.5 g/L)	2.4	55.8	N/A	27.6	6.3
Ni-MoS_2-WS_2 (0.1 g/L)	4.3	61.8	10.1	12.1	11.0
Ni-MoS_2-WS_2 (0.2 g/L)	5.5	54.0	10.6	10.7	11.5
Ni-MoS_2-WS_2 (0.5 g/L)	6.9	59.1	10.8	10.1	12.4

Table 5.4 EDS compositional analysis on counterpart cylinder against Ni-MoS_2, Ni-WS_2 and Ni-MoS_2-WS_2 coatings deposited with different CTAB concentration after friction test

Counterpart (CTAB concentration)	O (wt%)	Fe (wt%)	Ni (wt%)	Mo (wt%)	W (wt%)	S (wt%)
Vs Ni-MoS_2 (0.1 g/L)	6.9	73.3	10.1	5.7	N/A	2.6
Vs Ni-MoS_2 (0.2 g/L)	4.1	82.3	6.6	2.6	N/A	2.0
Vs Ni-MoS_2 (0.5 g/L)	6.3	71.8	12.1	5.7	N/A	2.7
Vs Ni-WS_2 (0.1 g/L)	4.4	76.1	7.2	N/A	9.6	1.3
Vs Ni-WS_2 (0.2 g/L)	6.0	71.7	10.4	N/A	8.7	1.5
Vs Ni-WS_2 (0.5 g/L)	5.8	68.7	11.1	N/A	11.4	1.7
Vs Ni-MoS_2-WS_2 (0.1 g/L)	5.9	65.7	14.5	3.0	6.9	2.7
Vs Ni-MoS_2-WS_2 (0.2 g/L)	7.1	47.7	21.6	6.8	9.9	6.0
Vs Ni-MoS_2-WS_2 (0.5 g/L)	4.8	80.0	7.7	1.6	2.9	1.3

5.2.3 Tribological performance of nickel hybrid composite coatings

The tribological properties of nickel hybrid composite coatings mentioned in Section 4.3.2 will be investigated in this part. It is expected that composite coatings with dense and compact structures will exhibit excellent tribological performance. In the previous section, the friction and wear performance of Ni-MoS_2-WS_2 coatings have already been studied. Therefore, in this section, the tribological performance of nickel hybrid composite coatings containing SiC or TiO_2 particles will be tested. The hybrid composite coatings studied in this section were deposited from electroplating bath with CTAB concentration of 0.1 g/L and saccharin concentration of 1.5 g/L. The deposition time to prepare these hybrid composite coatings were 60 min.

The friction coefficients versus time produced by the Ni-SiC-MoS_2 and Ni-SiC-WS_2 coatings are shown in **Figure 5.28**. During the 1000 s friction test, the friction coefficient of Ni-SiC (40 nm)-MoS_2 coating gradually increased from 0.25 to 0.37, while Ni-SiC (8.5 μm)-MoS_2 maintained a relatively stable friction coefficient of 0.30. The lower and more stable friction coefficient of Ni-SiC (8.5 μm)-MoS_2 might be explained by the high content of solid lubricant in the coating. As shown in **Table 4.2** of EDS results of Ni-SiC-MoS_2 and Ni-SiC-WS_2 coatings, the MoS_2 content in Ni-SiC (8.5 μm)-MoS_2 coating is 23.1 wt%, which is ten times higher than that in Ni-SiC (8.5 μm)-MoS_2 coating (2.0 wt%). A sufficient MoS_2 content could ensure the formation of a complete tribofilm between coating and counterpart, reducing the friction coefficient during sliding contact motion.

On the other hand, the friction coefficient of Ni-SiC (40 nm)-WS_2 coating experienced fluctuation between 0.5 to 0.6 during the first 400 s of friction test, indicating poor self-lubrication property. For Ni-SiC (8.5 μm)-WS_2 coating, the friction coefficient was low at the initial stage of the test (100 s to 200 s). Afterwards, a continuous increase from 0.2 to 0.5 was observed. The variation of friction coefficient suggests that Ni-SiC (8.5 μm)-WS_2 coating possessed self-lubrication initially but gradually lost function during the test.

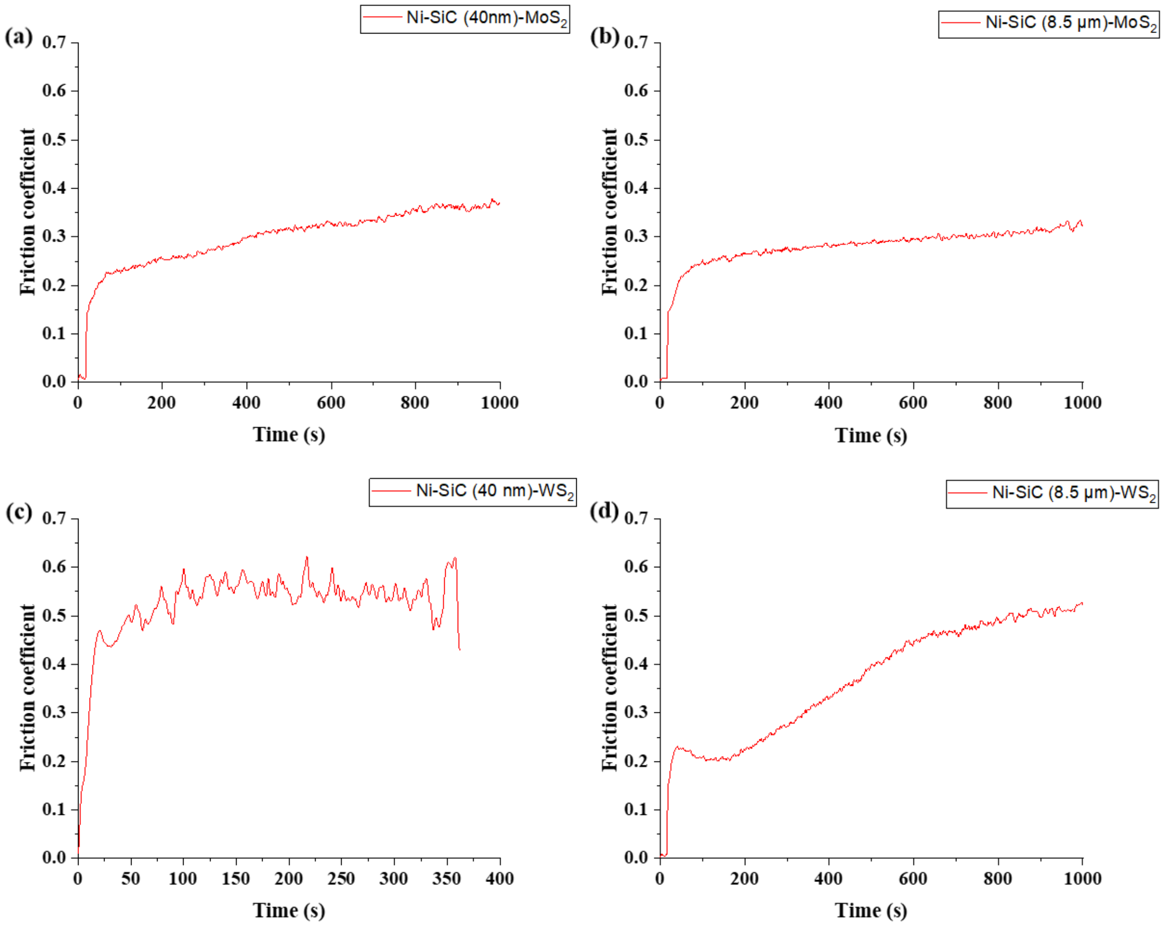

Figure 5.28 Friction coefficient as a function of time for (a) Ni-SiC (40 nm)-MoS_2 coating; (b) Ni-SiC (8.5 µm)-MoS_2 coating; (c) Ni-SiC (40 nm)-WS_2 coating; (d) Ni-SiC (8.5 µm)-WS_2 coating.

The worn surfaces of Ni-SiC-MoS_2 and Ni-SiC-WS_2 coatings after the friction test were compared with the original surfaces before the friction test (**Figure 5.29**). For Ni-SiC (40 nm)-MoS_2 coating, the closely packed nodules observed on the coating surface (**Figure 5.29 a**) have been flattened after the friction test. Abrasive grooves along the sliding direction can also be found on the worn surface (**Figure 5.29 b**), indicating that the Ni-SiC (40 nm)-MoS_2 coating experienced abrasive wear during the friction test. A similar phenomenon of surface structure flattening has also been observed on the worn surface of Ni-SiC (8.5 µm)-MoS_2 coating. Unlike the worn surface of Ni-SiC (40 nm)-MoS_2 coating, which shows abrasive grooves, a dark patch (tribofilm) was formed on the Ni-SiC (8.5 µm)-MoS_2 coating (**Figure 5.29 d**). The formation of this dark patch might explain the relatively low and stable friction coefficient (CoF = 0.3). The worn surface of Ni-SiC (40 nm)-WS_2 coating is shown in **Figure 5.29 (f)**. It can be seen observed that the nodular structures shown on the original coating surface (**Figure 5.29 e**) were crushed into fragments after the friction test. In addition, abrasive grooves and debris can be found on the worn surface. **Figure 5.29 (h)** shows the worn surface of Ni-SiC (8.5 µm)-WS_2 coating. Microcracks and grooves can be found on the worn surface. Moreover, compared with the original surface morphology before the friction test (**Figure 5.28 g**), it can be noted that the microstructure on the original Ni-SiC (8.5 µm)-WS_2 coating surface was fractured into numerous debris. The presence of a large amount of debris on the wear track could induce adverse abrasive wear, which might explain the continuous increase in friction coefficient.

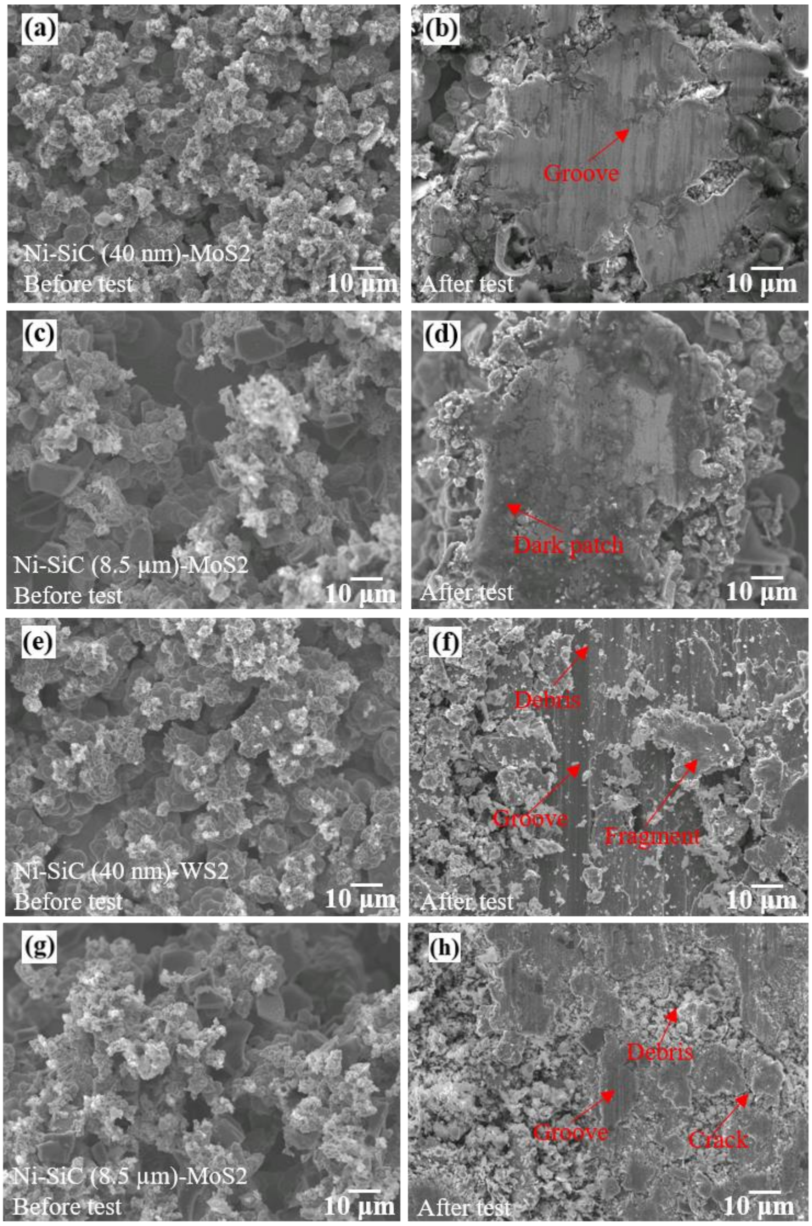

Figure 5.29 Secondary electron SEM images of Ni-SiC-MoS_2 and Ni-SiC-WS_2 coatings before and after 1000 s friction test. (a-b) Ni-SiC (40 nm)-MoS_2; (c-d) Ni-SiC (8.5 µm)-MoS_2; (e-f) Ni-SiC (40 nm)-WS_2; (g-h) Ni-SiC (8.5 µm)-WS_2

The worn surfaces on counterpart cylinders are shown in **Figure 5.30**. Compared with wear tracks of counterpart cylinders sliding against Ni-SiC-MoS_2 coatings, the wear tracks of counterpart cylinders sliding against Ni-SiC-WS_2 coatings exhibit deep grooves. In addition, numerous debris transferred from the coating surface accumulates on the side of wear tracks, indicating the high wear rate of Ni-SiC-WS_2 coatings.

EDS results of Ni-SiC-MoS_2 and Ni-SiC-WS_2 coatings and their corresponding counterpart surfaces after friction test are shown in **Table 5.5** and **Table 5.6** respectively. The MoS_2 and WS_2 particles remained on Ni-SiC-MoS_2 and Ni-SiC-WS_2 coatings after friction test were much lower than the coatings before friction test. In addition, EDS results on the wear track of counterpart indicated that there was no transfer of tribofim from coating surface. The lack of complete tribofilm between coatings and counterparts explained the poor self-lubricating properties of Ni-SiC-MoS_2 and Ni-SiC-WS_2.

Table 5.5 EDS compositional analysis on wear track of Ni-SiC-MoS_2 and Ni-SiC-WS_2

Sample	O (wt%)	Ni (wt%)	Mo (wt%)	W (wt%)	S (wt%)	Si (wt%)
Ni-SiC (40 nm)-MoS_2	7.0	90.2	0.7	N/A	0.5	0.9
Ni-SiC (8.5 µm)-MoS_2	8.4	70.4	1.8	N/A	3.2	8.1
Ni-SiC (40 nm)-WS_2	2.2	95.4	N/A	1.1	0.3	0.5
Ni-SiC (8.5 µm)-WS_2	8.3	63.2	N/A	4.6	1.0	4.3

Table 5.6 EDS compositional analysis on the wear tracks of counterpart cylinders sliding against Ni-SiC-MoS_2 and Ni-SiC-WS_2

Sample	O (wt%)	Fe (wt%)	Ni (wt%)	Mo (wt%)	W (wt%)	S (wt%)	Si (wt%)
Vs Ni-SiC (40 nm)-MoS_2	2.3	89.0	6.3	N/A	N/A	N/A	0.4
Vs Ni-SiC (8.5 µm)-MoS_2	2.5	82.4	13.3	0.2	N/A	0.1	0.5
Vs Ni-SiC (40 nm)-WS_2	2.7	79.2	15.2	N/A	0.6	0.04	0.5
Vs Ni-SiC (8.5 µm)-WS_2	3.4	83.4	9.7	N/A	0.9	0.3	0.7

Table 5.7 summarises the mechanical and tribological test results of Ni-SiC-MoS_2 and Ni-SiC -WS_2 coatings. It can be noted that the hybrid coatings containing 40 nm SiC particles exhibit higher hardness and shallower wear tracks compared with those containing 8.5 μm SiC particles. Similar findings have also been reported in the research carried out by Garcia, Fransaer and Celis [222]. They reported a decrease in the particle size affects the hardness and wear resistance in a positive way. The composite coatings containing particles of different sizes may have different reinforcement mechanisms. For composite coatings containing nano-sized particles, the dominant strengthening is dispersion strengthening. The mechanism of dispersion strengthening can be explained as follows. In composite material, the moving dislocation cannot cut through particles in composite (**Figure 5.31 a**). Therefore, when the dislocation bypasses the particles, it will bow out between two particles. As the dislocation keeps moving, the bowed-out dislocation will become semi-circular in shape, and yielding will occur (**Figure 5.31 b**). After the yielding, the dislocation will leave Orowan loops around the particles (**Figure 5.31 c**). The formation of the Orowan loops can slow down the dislocation motion and therefore strengthening the composite material [232]. However, for composite coatings containing micron-sized particles, the reinforcement mechanism is particle strengthening, which is achieved because particles restrain matrix deformation by a mechanical constraint. In the current research, Ni-SiC (40 nm)-WS_2 coating contains nano-sized SiC particles (3.9 wt%). Therefore, dispersion strengthening can be expected. On the other hand, the co-deposited particles in Ni-SiC (8.5 μm)-MoS_2 coating are all micron-sized particles, which means the reinforcement mechanism is particle strengthening. According to Garcia, Fransaer and Celis [222], dispersion strengthening is more conducive than particle strengthening to achieve hard and wear-resistant composite coatings. Their findings are consistent with data in **Table 5.7**, which shows hybrid composite coatings containing nano-sized SiC exhibit higher hardness than those containing micron-sized SiC.

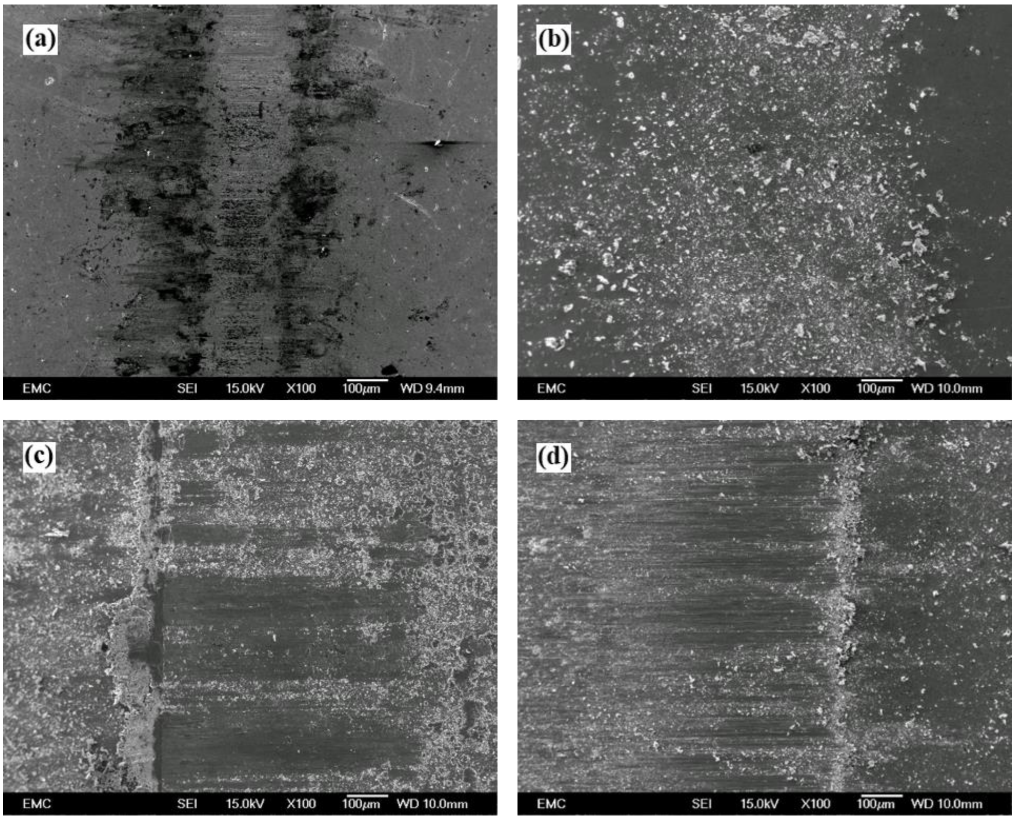

Figure 5.30 Secondary electron SEM images of wear tracks on counterpart cylinders sliding against (a) Ni-SiC (40 nm)-MoS_2 coating; (b) Ni-SiC (8.5 μm)-MoS_2 coating; (C) Ni-SiC (40 nm)-WS_2 coating; (d) Ni-SiC (8.5 μm)-WS_2 coating.

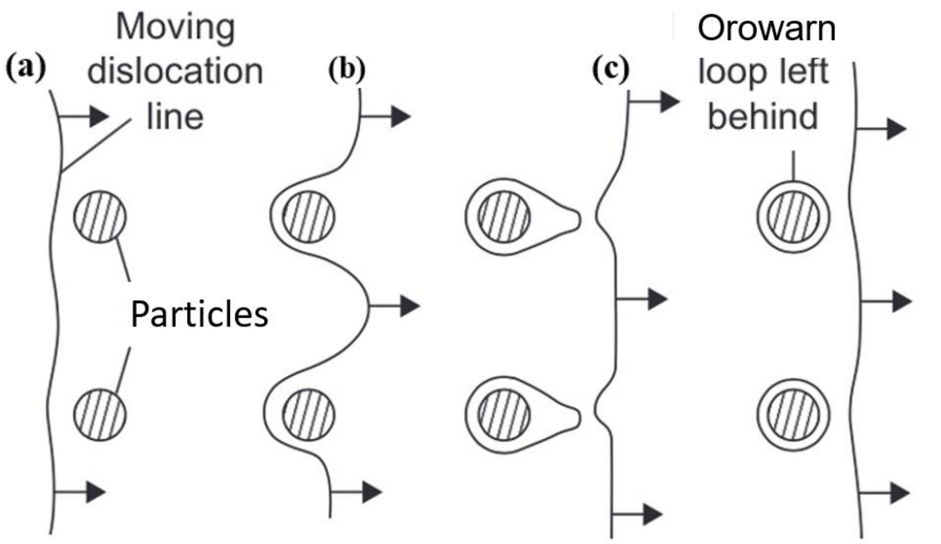

Figure 5.31 Schematics of dislocation bypassing particles in composite material (dispersion strengthening) [232].

Table 5.7 Mechanical and tribological properties of Ni-SiC-MoS_2 and Ni-SiC-WS_2 coatings

Sample	Hardness (Hv)	Friction coefficient	Wear depth (µm)
Ni-SiC (40 nm)-MoS_2	372.2 ± 9.9	0.37	7.7
Ni- SiC (8.5 µm)-MoS_2	321.4 ± 28.5	0.30	15.1
Ni- SiC (40 nm)-WS_2	392.9 ± 11.4	Fluctuation between 0.5 and 0.6	26.6
Ni-SiC (8.5 m)-WS_2	359.6 ± 26.3	0.50	27.3

Figure 5.32 shows the friction coefficient of Ni-TiO_2-MoS_2 and Ni-TiO_2-WS_2 coatings. For the Ni-TiO_2-MoS_2 coating, the friction coefficient was maintained at a stable level of 0.11 for up to 600 s in the friction test and then increased sharply to 0.45. After 900 s, the friction coefficient became quite unstable, indicating that Ni-TiO_2-MoS_2 coating lost self-lubricating function (**Figure 5.32 a**). On the other hand, the friction coefficient of Ni-TiO_2-WS_2 coating was high (0.50-0.55) and fluctuated severely during the entire friction test (**Figure 5.32 b**). The test was aborted after 500 s because coating failure was observed (coating was exfoliated afterwards).

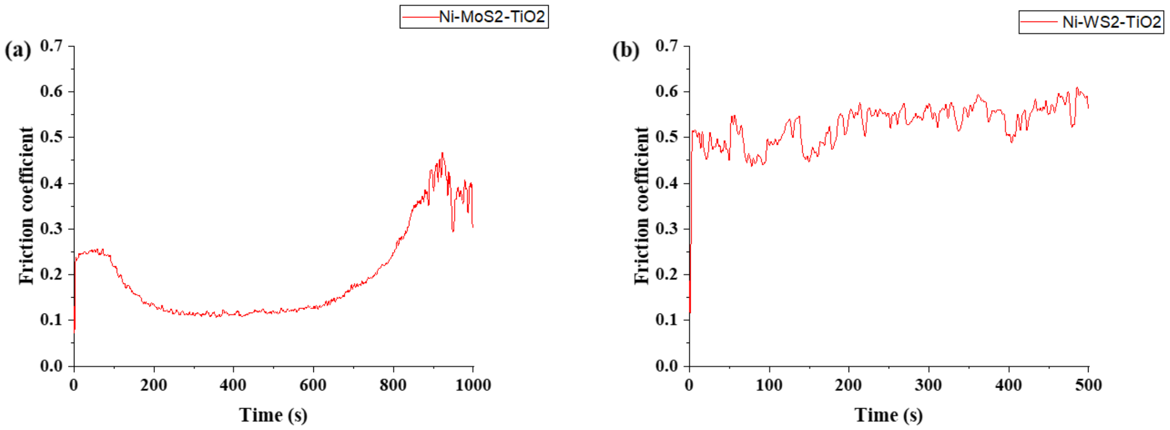

Figure 5.32 Friction coefficient as a function of time for (a) Ni-TiO_2-MoS_2 coating; (b) Ni-TiO_2-WS_2 coating.

The SEM images of wear tracks on Ni-TiO_2-MoS_2 and Ni-TiO_2-WS_2 coatings are displayed in **Figure 5.33**. Compared with the unworn surface shown in previous figure 4.12 (a), it can be seen that the porous Ni-TiO_2-MoS_2 coating was crushed, and the worn surface was covered with wear debris (**Figure 5.33 a**). Since the Ni-TiO_2-MoS_2 coating is rich in MoS_2 content, relatively low friction coefficient could be maintained initially due to the formation of tribofilm. However, as the friction test progressed, the porous coating structure could not provide firm support for the counterpart cylinder sliding and was easily worn out. Therefore, the friction coefficient experienced a sharp increase after 600 s of the test. On the other hand, coating delamination was observed, and the mild steel substrate was exposed on the worn surface of Ni-TiO_2-WS_2 coating (**Figure 5.33 b**). The poor tribological performance was attributed to the low WS_2 particle content in the coating, which could not provide effective self-lubrication.

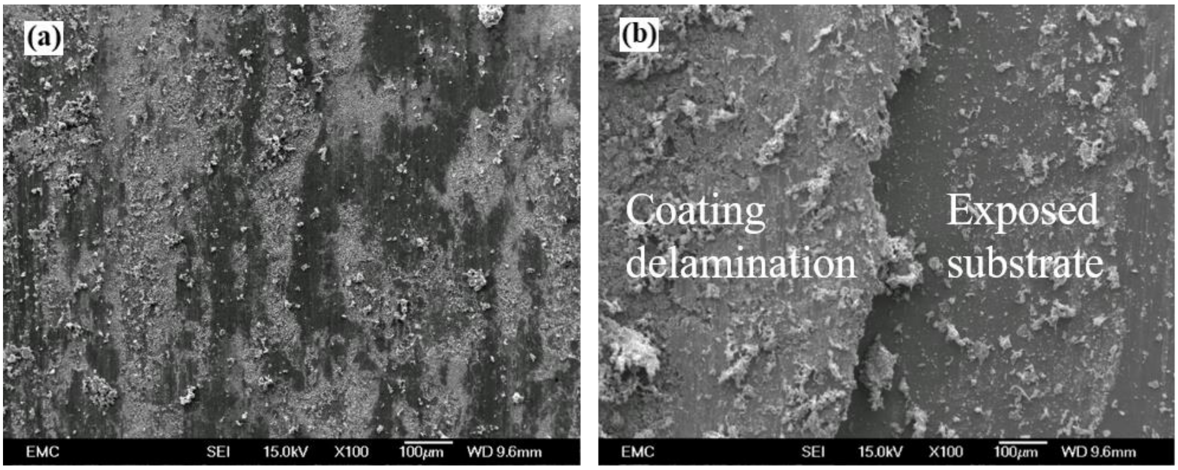

Figure 5.33 Secondary electron SEM images of wear tracks on (a) Ni-TiO_2-MoS_2 coating and (b) Ni-TiO_2-WS_2 coating.

The mechanical and tribological test results of Ni-TiO_2-MoS_2 and Ni-TiO_2-WS_2 coatings are shown in **Table 5.8**. Due to the porous structure of Ni-TiO_2-MoS_2 coating, hardness measurement is hard to be conducted on the cross-section. Moreover, as mentioned above, the porous coating structure is prone to wear, thereby resulting in a very deep wear track (303.6 μm). On the other hand, although the Ni-TiO_2-WS_2 coating possesses a dense structure and relatively high hardness (434.9 Hv), the low embedded WS_2 content (1.7 wt%) cannot provide sufficient lubrication during sliding contact motion and consequently lead to catastrophic coating damage.

Table 5.8 Mechanical and tribological properties of Ni-TiO_2-MoS_2 coating and Ni-TiO_2-WS_2 coating.

Sample	Hardness (Hv)	Friction coefficient	Wear depth (μm)
Ni-TiO_2-MoS_2	Too porous to be indented	Increasing from 0.11 to 0.45	303.6
Ni-TiO_2-WS_2	434.9 ± 28.5	Fluctuating between 0.50 to 0.55	Coating delamination

5.3 Discussion

5.3.1 Factors influencing the tribological performance

Many previous studies reported composite coatings containing high solid lubricant content could exhibit superior tribological performance [4, 14, 15]. However, in the current research, although the MoS_2 content in Ni-MoS_2 (10 g/L) coating is almost three times higher than that of Ni-MoS_2 (1 g/L) coating. The increasing solid lubricant content resulted in a higher friction coefficient (0.03 to 0.10) and wear depth (5.7 μm to 91.7 μm). The degradation in tribological performance is attributed to the porous coating structure (**Figure 5.6**) and rough coating surface (Ra = 18.1 μm). During the friction test, the counterpart cylinder easily crushed the porous Ni-MoS_2 (10 g/L) coating, leaving a deep wear track on the coating surface (**Figure 5.8 d**). Moreover, Ni-MoS_2 coating with porous structure could not provide firm support to form compact tribofilm. Consequently, a higher friction coefficient was observed on the Ni-MoS_2 coating when the particle concentration in the electroplating bath is 10 g/L or higher. Therefore, increasing solid lubricant content in the coating may not always lead to a lower friction coefficient. Coating structure and surface roughness can also affect the tribological performance.

This research aims to develop compact self-lubricating composite coatings through the co-deposition of mixed particles. **Table 5.9** compares self-lubricating composite coatings reported from the literature with nickel hybrid composite coatings prepared in this research. It can be noted that nickel single-particle composite coatings (i.e. Ni-MoS_2 and Ni-P-WS_2) exhibit coarse surface morphologies with roughness of 14.5 μm and 9.6 μm, respectively. In contrast, nickel hybrid composite coatings prepared in the current research show smooth surfaces. The roughness of Ni-SiC (40 nm)-MoS_2 and Ni-SiC-WS_2 are 3.2 μm and 6.3 μm. A similar effect of mixed particle co-deposition has been reported Wang et al. [204]. They found that the co-deposition of 10 g/L Al_2O_3 and 1 g/L MoS_2 into nickel could lead to a compact coating structure. The previous study claimed that the densification effect could be achieved by adding insulating particles (Al_2O_3) into a metal solid lubricant particle coating system [204]. However, in this study, the relatively lower roughness of Ni-SiC (40 nm)-MoS_2 and Ni-SiC-WS_2 coatings is attributed to the low co-deposition rate of MoS_2 or WS_2 particles ($\leq$ 2 wt%). Compared with Ni single-particle composite coatings (Ni-MoS_2 and Ni-WS_2), the low content of embedded MoS_2 or WS_2 particles in Ni-SiC (40 nm)-MoS_2 and Ni-SiC (40 nm)-WS_2 coatings prevents the dendritic growth of the coating structures.

However, the friction coefficient data in **Table 5.9** indicates that the addition of SiC particles to the nickel hybrid composite coating deteriorates its tribological performance. The friction coefficient of Ni-SiC-MoS_2 coatings is at least four times higher than that of Ni-MoS_2 coatings, both in this study and as reported in the literature [6]. In a previous study of Ni-SiC-MoS_2 coating [196], the friction coefficient was found to be higher (0.45-0.55) than this research. The lower friction coefficient of Ni-SiC (40 nm)-MoS2 prepared in the current research might be attributed to the compact structure as the previous study mentioned that the structure of Ni-SiC-MoS2 coating was porous due to excessive MoS_2 addition (12 g/L). For Ni-MoS_2-WS_2 coating, the tribological performance of is similar to that of Ni-MoS_2 coating. Both coatings exhibit low friction coefficient (< 0.1) and wear depth of about 12 μm.

Table 5.9 Comparison between single-particle composite coatings from the literature and nickel hybrid composite coating from the current research.

Coating types	Roughness (μm)	Friction coefficient	Wear depth (μm)	Data from
Ni-MoS_2	14.5	0.08	12.0	[6]
Ni-P-WS_2	9.6	0.20	Not given	[14]
Ni-SiC (2-3 μm)-MoS_2 (< 10 μm)	Not given	0.45-0.55	Not given	[205]
Ni-SiC (40 nm)-MoS_2 (1.2 μm)	3.2	0.35	7.7	This research
Ni-MoS_2-WS_2 (0.5 g/L CTAB)	5.6	0.07	12.3	This research

The better wear resistance of Ni-SiC (40 nm)-MoS_2 coating in the current research can be explained by Archard law. Theoretically, the wear volume can be calculated by Archard wear equation [202].

$$Q = \frac{KWL}{H} \quad \text{.......................................} 5.1$$

Where Q is the total volume of wear debris, K is a dimensionless constant, W is the applied load, L is the sliding distance, and H is the hardness of the softer contacting surface (in this case is the composite coating). From Archard's equation, the wear volume is inversely proportional to the hardness value. Therefore, it can be expected that Ni-SiC (40 nm)-MoS_2 coating with higher hardness (372.2 Hv) will have lower wear volume than Ni-MoS_2 coating (265.1 Hv). The relatively high friction coefficient of Ni-SiC (40 nm)-MoS_2 (0.35) is attributed to low MoS_2 content (2.0 wt%), which cannot provide lubrication during sliding contact motion. Based on the above discussion, it can be concluded that solid lubricant content, coating structure and surface roughness are three significant factors influencing tribological properties. Ni-SiC (40 nm)-MoS_2 coating prepared in the current research showed lower roughness and better wear resistance compared with Ni-MoS_2 coating in the literature. However, due to the low content of embedded MoS_2 (2.0 wt%), the friction coefficient of Ni-SiC (40 nm)-MoS_2 was relatively high. Further work will focus on reducing the friction coefficient of Ni-SiC (40 nm)-MoS_2 coating.

5.3.2 Effect of surfactant CTAB on the composite coatings

Section 5.3.2 shows that the addition of surfactant CTAB into the electroplating bath can affect both appearance and properties of Ni-MoS_2 and Ni-MoS_2-WS_2 coatings. However, little effect will be brought on Ni-WS_2 coating when the CTAB concentration increased from 0.1 g/L to 0.5 g/L. For Ni-MoS_2 coating, it can be observed that the holes found on Ni-MoS_2 coating deposited with 0.1 g/L CTAB addition disappeared with higher CTAB concentration (**Figure 5.15 a-c**). According to Ghazanlou et al. [233], the elimination of these holes might be attributed to the adsorption of redundant CTAB on the cathode, which disturbs the hydrogen evolution process. In addition, the EDS result in Figure **5.17 (a)** indicates that the embedded MoS_2 content in the composite coating will increase with higher CTAB concentration. This is in agreement with many previous studies [165, 167, 168]. Higher CTAB concentration can provide a greater positive charge on the suspended MoS_2 particles, thereby promoting the electrophoretic motion and enhancing the co-deposition rate.

However, for Ni-MoS_2-WS_2 coating, the embedded particle content (both MoS_2 and WS_2) decreased with higher CTAB concentration. A similar finding has also been reported by Ning et al. in the Cu-TiO_2 coating system [172]. One possible reason is that the optimum CTAB concentration for particle co-deposition in Ni-MoS_2-WS_2 coating system is lower than 0.1 g/L. Therefore, when the CTAB concentration exceeds 0.1 g/L, excessive CTAB could be adsorbed on the cathode surface. This adsorption would create a large repulsive force between particles and cathode, thereby reducing the deposition rate of particles.

On the other hand, a significant increase in hardness was observed on Ni-MoS_2 (from 16.3 Hv to 180.6 Hv) as CTAB concentration increased from 0.1 g/L to 0.5 g/L. The increase in hardness can be explained from two aspects. On the one hand, the porosity level of Ni-MoS_2 coatings dropped with increasing CTAB concentration (**Figure 5.18**). According to the physical modelling proposed by Ma et al. [234], the porous coating possesses a lower hardness than a dense one. Ni-MoS_2 coating prepared with 0.5 g/L CTAB exhibited a dense structure, and therefore a higher hardness. On the other hand, the addition of CTAB in the electroplating can cause a hardening effect on the nickel matrix. The previous research conducted by Hou et al. [166] revealed that the addition of CTAB in nickel sulfamate bath significantly increased the hardness of pure Ni deposit. However, the reason for this hardening effect is not understood.

Moreover, from **Figure 5.15**, **Figure 5.16** and **Figure 5.18** to **Figure 5.20**, it can be observed that for Ni-MoS_2 and Ni-MoS_2-WS_2 coatings, the surface morphologies became smoother, and the coating structure became denser when the CTAB addition in the electroplating bath increased from 0.1 g/L to 0.5 g/L. The phenomenon of coating densification by cationic surfactant addition has also been reported by Wang [173]. In Wang's study, it was suggested that cationic surfactant BAS adsorption on MoS_2 particles could partially reduce particle conductivity and promote uniform coating deposition. Therefore, it can be expected that the densification of Ni-MoS_2 and Ni-MoS_2-WS_2 coating was caused by a similar particle conductivity reduction effect of CTAB.

5.4 Summary of test results

1. Ni-MoS2 coatings have been successfully deposited from an electroplating bath containing different particle concentration. It was found that the amount of co-deposited MoS2 particles was not the only factor determining tribological performance. Ni-MoS_2 coating deposited from 1 g/L MoS_2 concentration showed sufficient MoS_2 content (16.7 wt%) to form tribofilm between coating and counterpart. Though the deposited Ni-MoS_2 (1 g/L) coating exhibited quite high surface roughness (Ra = 36.8 μm), the relatively high coating hardness (280 Hv) formed a firm support for the tribofim during friction test. Therefore, the lowest friction coefficient (0.03) and wear depth (5.7 μm) were obtained. On the other hand, the increase of MoS_2 concentration resulted in high MoS2 content up to 42.5 wt% in the deposited coating. However, the low coating hardness and porous structure was not able to support the formed tribofilm, which degraded the overall tribological performance.

2. The addition of CTAB in the electroplating bath could affect the surface morphologies and mechanical properties of Ni-MoS_2 and Ni-MoS_2-WS_2 coatings. When added at a sufficiently high concentration (0.5 g/L), CTAB was found to decrease the surface roughness of Ni-MoS2 and Ni-MoS2 coatings by 55.2% and 69.2% compared with the coatings deposited with 0.1 g/L CTAB. Additionally, both Ni-MoS_2 and Ni-MoS_2-WS_2 coatings exhibited a significant increase in hardness, reduction in friction coefficient, and reduction in wear depth when CTAB concentration increased from 0.1 g/L to 0.5 g/L.

3. The co-deposition of (40 nm) SiC particles into the Ni-MoS_2 coating system can develop a nickel hybrid composite coating with a dense and compact structure. Compared with the self-lubricating coating reported in the literature (Ni-MoS_2 coating), Ni-SiC (40 nm)-MoS_2 coating exhibits a much lower surface roughness (3.2 μm) and better wear resistance (wear depth of 7.7 μm). However, due to the low content of embedded MoS_2 particles (2.0 wt%), the friction coefficient was higher (0.35) than the Ni-MoS_2 coating reported in the literature (0.08).

6 Conclusion and future work

6.1 Overall conclusions

In this work, nickel single-particle composite coatings and nickel hybrid composite coatings have been successfully deposited for both superhydrophobic and tribological applications. Major challenges of poor abrasion resistance for superhydrophobic coatings and porous structure for self-lubricating coatings have been addressed. The main conclusions of this work are summarised as follows.

1. Nickel single-particle composite coatings (Ni-MoS_2 and Ni-WS_2) were successfully developed via electro-co-deposition. The Ni-WS_2 coating deposited with 1.1 µm WS_2 particles (Sample W4) exhibited the highest water contact angle of 158.8 ± 2.5°, demonstrating excellent superhydrophobic properties. However, due to its porous coating structure, as confirmed by cross-sectional analysis, the Ni-WS_2 coating lost its superhydrophobicity after a short abrasion distance of 450 cm under a load of 100 g.

2. Particle size plays an important role in determining surface morphologies and embedded particle content of composite coatings. For nickel single-particle composite coatings, either large (4.8 µm MoS_2) or small particles (275 nm WS_2) resulted in low particle content in the coating. Only medium-sized particles around 1 µm promoted a high co-deposition rate. For nickel hybrid composite coatings, the combination of micron-sized MoS_2 / WS_2 with nano-sized SiC (40 nm) contributed to a dense and compact coating structure with a low level of porosity. The lowest surface roughness of 3.2 ± 0.2 µm was observed on Ni-SiC (40 nm)-MoS_2 coating. However, the existence of nano-sized particles in the electroplating bath inhibited the co-deposition of solid lubricant particles (either MoS_2 or WS_2 content in the nickel hybrid composite coating is below 3 wt%).

3. With the addition of a third-phase ceramic particles, the abrasion resistance of nickel hybrid composite coatings was significantly enhanced. Ni-SiC (8.5µm)-WS_2 coating with highest water contact angle of 166.2 ± 0.7° maintained superhydrophobicity after a 2000 cm abrasion distance, which was four times better than Ni-WS_2 coating. The potentiodynamic polarisation test also confirmed the excellent anti-corrosion

performance of superhydrophobic Ni-SiC (8.5μm)-WS_2 coating with E_{corr} of -0.14 V and i_{corr} of 4.29×10^{-7} A/cm^2. The corrosion mechanism was further elucidated by EIS and demonstrated that the air layer formed on the hierarchical structure of Ni-SiC (8.5μm)-WS_2 coating inhibited the penetration of corrosive solution and provided a corrosion barrier for the substrate.

4. The long-term durability of superhydrophobicity was achieved by the development of Ni-TiO_2-MoS_2 coating. After being immersed in water for two days, the coating maintained the hydrophobicity. The excellent durability is attributed to the microporous and nanoporous structures, which retain air and form a layer of "air cushion" to prevent water penetration. This type of coating could solve the durability problem, which has been the major reason why superhydrophobic coatings have not achieved widespread commercial success.

5. Ni-MoS_2 coatings were deposited from baths containing different concentrations of MoS_2 particles. It was found that the self-lubricating property was not only determined by the content of embedded MoS_2 particles. Ni-MoS2 coating deposited from 10 g/L bath exhibited the highest MoS2 particle content of 42.5 wt%. However, high embedded MoS_2 content resulted in low hardness, which was prone to wear off during tribological tests. On the other hand, although Ni-MoS_2 coating deposited from 1 g/L MoS_2 concentration showed the lowest MoS_2 content and quite high surface roughness (Ra = 36.8 μm), the relatively high coating hardness formed a firm support for the tribofim. Therefore, the lowest friction coefficient (0.03) and wear depth (5.7 μm) were obtained.

6. CTAB concentration largely affected the structure and self-lubricating properties of the composite coatings. As the CTAB concentration increased from 0.1 g/L to 0.5 g/L, surface morphologies of Ni-MoS_2 and Ni-MoS_2-WS_2 coatings evolved from rough to smooth. The increase in CTAB concentration was also found to increase hardness, reduce friction coefficient, and improve wear resistance. However, the variation of CTAB concentration had little effect on Ni-WS_2 coatings.

7. The co-deposition of 5 g/L SiC particles (40 nm) and 5 g/L MoS_2 particles (1.2 µm) can develop a nickel hybrid composite coating with high compactness. Compared with Ni-MoS_2 coating reported in the literature, Ni-SiC (40 nm)-MoS_2 coating exhibited better wear resistance (wear depth of 7.7 µm). However, due to the low content of embedded MoS_2 particles (2.0 wt%), the friction coefficient is relatively high (0.35).

6.2 Future work

In this work, various types of hybrid coatings have been carried out to achieve a compact coating structure for the superhydrophobic or self-lubricating application. The future work will focus on the data analysis, mechanism elucidation and further experiment implementation to understand and build functional coatings from the following four aspects.

(1) Nickel hybrid composite coatings deposited with different particle ratios will be investigated. According to previous studies, the tribological performance of Ni-Al_2O_3-MoS_2 and Ni-P-Al_2O_3-PTFE coatings is dependent on the particle ratio. However, the work conducted to date only used the same ratio (5 g/L particle A + 5 g/L particle B, A and B represent different particle type). With this particle ratio, the co-deposited solid lubricant content in the nickel hybrid composite coatings (i.e. Ni- SiC (40 nm)-MoS_2 and Ni-SiC (40 nm)-WS_2) was very low (< 2.0 wt%), which resulted in a relatively high and unstable friction coefficient. In future work, mixed particle co-deposition with the addition of different particle ratio will be studied. The concentration of solid lubricant particle will be set to 5 g/L because Ni-MoS_2 coating deposited with this concentration shows sufficient MoS_2 content in the coating. The concentration of the 40 nm SiC will be lower (1 g/L, 2 g/L, 3 g/L and 4 g/L) as it was found to inhibit the co-deposition of solid lubricant particles. The variation of SiC (40 nm) concentration aims to obtain an optimum particle ratio. Hopefully, a nickel hybrid composite coating with dense structure and sufficient solid lubricant content could be developed with this optimum particle ratio.

(2) Although the structures of nickel-solid lubricant composite coatings have been densified by mixed particle co-deposition, the dendritic growth on the outmost layer can still be observed (**Figure 4.11**). From the literature, PC plating technique can avoid dendritic growth (**Figure 2.14**) and deposit Ni-WC coating without porosity. Therefore, to further smoothen the coating

surface, the PC plating technique will be used in future work. However, compared with DC plating, PC plating has more parameters to be considered (i.e. frequency, duty cycle, peak current density). A number of trails will be conducted to optimise electroplating parameters. PC electroplating will be conducted by varying the duty cycle and frequency of pulse current supply. According to a review article of PC and PRC [119], 33-50 % is taken as the minimum value of the duty cycle, and the frequency should be low enough (< 100 Hz) to allow the electrical double layer to fully discharge during the T_{OFF}.

(3) Cross-section of composite coatings after the friction test will be analysed to understand the behaviour of solid lubricant particles in the wear process. A focused ion beam (FIB) will be used to cut the cross-section sample from the worn surface using ‘lift-out’ technique. The reason for using FIB sample preparation is its advantage of high positioning accuracy for cross-sections. After FIB preparation, the sample will be observed under a transmission electron microscope (TEM). The combination of FIB and TEM aims to clarify the microstructure evolution of composite coating and particle behaviour within the metal matrix during the friction test, which helps to understand the self-lubrication mechanism.

(4) A model/mechanism will be set up to demonstrate how the size difference in hybrid particles contributes to the dense structure. To explore the effect of particle size on the microstructure of the composite coating, the researcher will use the COMSOL computer simulation software to calculate the current density distribution on the cathode. The simulation procedures will be similar to previous research of Cu-diamond coating conducted by Cho’s research group [235]. As the diamond particles do not conduct electricity, the electric field lines need to go around the diamond particles in their study. However, the electroplating process will be more complicated in my research because the electric field can be intensified at the MoS_2 or WS_2 adsorbed sites due to their conductive nature. Therefore, the simulation input parameters (e.g. diffusion coefficient, particle conductivity etc.) should be carefully selected. Hopefully, this model/mechanism will draw a quantified conclusion on the amount and types of solid lubricant doped in the solutions.

Reference

[1] I. Hutchings and P. Shipway, *Tribology: friction and wear of engineering materials*. 2nd edition, Butterworth-heinemann, Chapter 1, pp. 1-2, 2017.

[2] U. o. Edingurgh. "Materials study targets industry corrosion and wear." https://www.ed.ac.uk/news/2017/materials-study-targets-industry-corrosion-and-wea (accessed 9th Feb, 2021).

[3] M. R. Vazirisereshk, A. Martini, D. A. Strubbe, and M. Z. Baykara, "Solid lubrication with MoS2: a review," *Lubricants,* vol. 7, no. 7, p. 57, 2019.

[4] Y. He, S. Wang, F. Walsh, Y.-L. Chiu, and P. Reed, "Self-lubricating Ni-P-MoS2 composite coatings," *Surface and Coatings Technology,* vol. 307, pp. 926-934, 2016.

[5] Z. Chen *et al.*, "Surfactant-assisted electrodeposition of Au–Co/WS2 self-lubricating coating from WS2 suspended cyanide electrolyte," *Journal of Alloys and Compounds,* p. 154585, 2020.

[6] N. Zhou, S. Wang, and F. C. Walsh, "Effective particle dispersion via high-shear mixing of the electrolyte for electroplating a nickel-molybdenum disulphide composite," *Electrochimica Acta,* vol. 283, pp. 568-577, 2018.

[7] Q. Cheng, Z. Yao, F. Zhang, S. Zhang, and M. Oleksander, "Microstructure and tribological property of Ni–MoS2 composite coatings prepared by ultrasonic and mechanical stirring electrodeposition," *Materials Research Express,* vol. 6, no. 12, p. 126434, 2020.

[8] G. Fogg, "Diurnal fluctuation in a physical property of leaf cuticle," *Nature,* vol. 154, no. 3912, pp. 515-515, 1944.

[9] T. Darmanin, E. T. de Givenchy, S. Amigoni, and F. Guittard, "Superhydrophobic surfaces by electrochemical processes," *Advanced materials,* vol. 25, no. 10, pp. 1378-1394, 2013.

[10] S. H. Nguyen, H. K. Webb, P. J. Mahon, R. J. Crawford, and E. P. Ivanova, "Natural insect and plant micro-/nanostructsured surfaces: an excellent selection of valuable templates with superhydrophobic and self-cleaning properties," *Molecules,* vol. 19, no. 9, pp. 13614-13630, 2014.

[11] T. Le Mogne *et al.*, "Nature of super-lubricating MoS2 physical vapor deposition coatings," *Journal of Vacuum Science & Technology A: Vacuum, Surfaces, and Films,* vol. 12, no. 4, pp. 1998-2004, 1994.

[12] T. Scharf and S. Prasad, "Solid lubricants: a review," *Journal of materials science,* vol. 48, no. 2, pp. 511-531, 2013.

[13] G. Zhao *et al.*, "One-step electrodeposition of a self-cleaning and corrosion resistant Ni/WS 2 superhydrophobic surface," *Rsc Advances,* vol. 6, no. 64, pp. 59104-59112, 2016.

[14] Y. He, W. Sun, S. Wang, P. Reed, and F. Walsh, "An electrodeposited Ni-P-WS2 coating with combined super-hydrophobicity and self-lubricating properties," *Electrochimica Acta,* vol. 245, pp. 872-882, 2017.

[15] Y. He, S. Wang, W. Sun, P. A. Reed, and F. C. Walsh, "Synthesis and Properties of Electrodeposited Ni–Co/WS2 Nanocomposite Coatings," *Coatings,* vol. 9, no. 2, p. 148, 2019.

[16] L. H. Prado and S. Virtanen, "Cu–MoS2 Superhydrophobic Coating by Composite Electrodeposition," *Coatings,* vol. 10, no. 3, p. 238, 2020.

[17] S. Mirsaeedghazi, S. Allahkaram, S. Mahdavi, and A. Varmazyar, "Characteristics and properties of Cu/nano-SiC and Cu/nano-SiC/graphite hybrid composite coatings produced by pulse electrodeposition technique," *Canadian metallurgical quarterly,* vol. 57, no. 3, pp. 358-366, 2018.

[18] S. Pinate, P. Leisner, and C. Zanella, "Wear resistance and self-lubrication of electrodeposited Ni-SiC: MoS2 mixed particles composite coatings," *Surface and Coatings Technology,* p. 127400, 2021.

[19] K. Popov, B. Grgur, and S. S. Djokić, *Fundamental aspects of electrometallurgy*. Springer, 1st edition, Chapter 4, p. 108, 2007.

[20] K. I. Popov, P. M. Živković, and N. D. Nikolić, "A mathematical model of the current density distribution in electrochemical cells," *Journal of the Serbian Chemical Society,* vol. 76, no. 6, pp. 805-822, 2011.

[21] Y.-J. Tan and K. Y. Lim, "Understanding and improving the uniformity of electrodeposition," *Surface and Coatings Technology,* vol. 167, no. 2-3, pp. 255-262, 2003.

[22] K. I. Popov, S. S. Djokić, N. D. Nikolić, and V. D. Jović, *Morphology of electrochemically and chemically deposited metals*. Springer, 1st edition, Chapter 3, p. 114, 2016.

[23] W. Giurlani *et al.*, "Electroplating for decorative applications: Recent trends in research and development," *Coatings,* vol. 8, no. 8, p. 260, 2018.

[24] F. Hanna, Z. A. Hamid, and A. A. Aal, "Controlling factors affecting the stability and rate of electroless copper plating," *Materials letters,* vol. 58, no. 1-2, pp. 104-109, 2004.

[25] Z. Liu and W. Gao, "The effect of substrate on the electroless nickel plating of Mg and Mg alloys," *Surface and Coatings Technology,* vol. 200, no. 11, pp. 3553-3560, 2006.

[26] K. Helle and F. Walsh, "Electrodeposition of composite layers consisting of inert inclusions in a metal matrix," *Transactions of the IMF,* vol. 75, no. 2, pp. 53-58, 1997.

[27] C. Fink and J. Prince, "The codeposition of copper and graphite," *Trans. Am. Electrochem. Soc,* vol. 54, pp. 315-321, 1928.

[28] M. Ghorbani, M. Mazaheri, and A. Afshar, "Wear and friction characteristics of electrodeposited graphite–bronze composite coatings," *Surface and Coatings Technology,* vol. 190, no. 1, pp. 32-38, 2005.

[29] C. Liu, D. Wei, R. Xu, Y. Mai, L. Zhang, and X. Jie, "Electroplated Co-Ni/WS2 composite coating with excellent tribological and anticorrosion performance," *Tribology Transactions,* vol. 63, no. 5, pp. 857-866, 2020.

[30] D. Roy *et al.*, "Pulse current co-deposition of Ni-WS2 nano-composite film for solid lubrication," *Materials and Manufacturing Processes,* vol. 32, no. 4, pp. 365-372, 2017.

[31] E. S. Güler, E. Konca, and İ. Karakaya, "Investigation of the tribological behaviour of electrocodeposited Ni-MoS2 composite coatings," *International Journal of Surface Science and Engineering,* vol. 11, no. 5, pp. 418-432, 2017.

[32] Z.-w. Jia, W.-c. Sun, F. Guo, Y.-r. Dong, and X.-j. Liu, "Microstructure, friction and corrosion resistance properties of a Ni–Co–Al 2 O 3 composite coating," *RSC advances,* vol. 8, no. 22, pp. 12138-12145, 2018.

[33] B. Szczygieł and M. Kołodziej, "Composite Ni/Al2O3 coatings and their corrosion resistance," *Electrochimica Acta,* vol. 50, no. 20, pp. 4188-4195, 2005.

[34] S. Aruna, V. E. Selvi, V. W. Grips, and K. Rajam, "Corrosion-and wear-resistant properties of Ni–Al 2 O 3 composite coatings containing various forms of alumina," *Journal of Applied Electrochemistry,* vol. 41, no. 4, pp. 461-468, 2011.

[35] Q. Li, X. Yang, L. Zhang, J. Wang, and B. Chen, "Corrosion resistance and mechanical properties of pulse electrodeposited Ni–TiO2 composite coating for sintered NdFeB magnet," *Journal of Alloys and Compounds,* vol. 482, no. 1-2, pp. 339-344, 2009.

[36] P. Baghery, M. Farzam, A. Mousavi, and M. Hosseini, "Ni–TiO2 nanocomposite coating with high resistance to corrosion and wear," *Surface and Coatings Technology,* vol. 204, no. 23, pp. 3804-3810, 2010.

[37] F. Walsh and C. Larson, "Towards improved electroplating of metal-particle composite coatings," *Transactions of the IMF,* vol. 98, no. 6, pp. 288-299, 2020.

[38] C. Low, R. Wills, and F. Walsh, "Electrodeposition of composite coatings containing nanoparticles in a metal deposit," *Surface and Coatings Technology,* vol. 201, no. 1-2, pp. 371-383, 2006.

[39] N. Guglielmi, "Kinetics of the deposition of inert particles from electrolytic baths," *Journal of the Electrochemical Society,* vol. 119, no. 8, pp. 1009-1012, 1972.

[40] J.-P. Celis, J. Roos, and C. Buelens, "A mathematical model for the electrolytic codeposition of particles with a metallic matrix," *Journal of the Electrochemical Society,* vol. 134, no. 6, pp. 1402-1408, 1987.

[41] J. Fransaer, J.-P. Celis, and J. Roos, "Analysis of the electrolytic codeposition of non-brownian particles with metals," *Journal of the Electrochemical Society,* vol. 139, no. 2, p. 413, 1992.

[42] B. J. Hwang and C. S. Hwang, "Mechanism of codeposition of silicon carbide with electrolytic cobalt," *Journal of the Electrochemical Society,* vol. 140, no. 4, p. 979, 1993.
[43] I. Shao, P. Vereecken, R. Cammarata, and P. Searson, "Kinetics of particle codeposition of nanocomposites," *Journal of the Electrochemical Society,* vol. 149, no. 11, p. C610, 2002.
[44] P. Bercot, E. Pena-Munoz, and J. Pagetti, "Electrolytic composite Ni–PTFE coatings: an adaptation of Guglielmi's model for the phenomena of incorporation," *Surface and Coatings Technology,* vol. 157, no. 2-3, pp. 282-289, 2002.
[45] S. Huang, M. Samandi, and M. Brandt, "Abrasive wear performance and microstructure of laser clad WC/Ni layers," *Wear,* vol. 256, no. 11-12, pp. 1095-1105, 2004.
[46] T. Cao, Z. Zhu, and Y. Liu, "Preparation of a Self-Lubricating Cu/h-BN Coating on Cemented Carbide," *Advances in Materials Science and Engineering,* vol. 2018, 2018.
[47] B. Bhushan, "Solid lubricants and self-lubricating films," in *Modern Tribology Handbook, Two Volume Set*: CRC Press, 2001, pp. 817-856.
[48] K. Miyoshi, *Solid lubrication fundamentals and applications*. CRC Press, 2001.
[49] S. Fouvry and C. Paulin, "An effective friction energy density approach to predict solid lubricant friction endurance: Application to fretting wear," *Wear,* vol. 319, no. 1-2, pp. 211-226, 2014.
[50] K. P. Furlan, J. D. B. de Mello, and A. N. Klein, "Self-lubricating composites containing MoS2: a review," *Tribology International,* vol. 120, pp. 280-298, 2018.
[51] Q. Luo, "Tribofilms in solid lubricants," *Encyclopedia of Tribology,* pp. 3760-3767, 2013.
[52] T. Scharf and S. Prasad, "Solid lubricants: a review," *Journal of materials science,* vol. 48, pp. 511-531, 2013.
[53] M. R. Hilton and P. D. Fleischauer, "Applications of solid lubricant films in spacecraft," *Surface and Coatings Technology,* vol. 54, pp. 435-441, 1992.
[54] Y. Epshteyn and T. J. Risdon, "Molybdenum Disulfide in Lubricant Applications—A Review," in *12th Lubricating Grease Conference, Goa, India, Jan*, 2010, pp. 28-30.
[55] O. Faruk, A. K. Bledzki, H. P. Fink, and M. Sain, "Progress report on natural fiber reinforced composites," *Macromolecular Materials and Engineering,* vol. 299, no. 1, pp. 9-26, 2014.
[56] D. M. Mattox, "Physical vapor deposition (PVD) processes," *Metal Finishing,* vol. 100, pp. 394-408, 2002.
[57] E. García-Lecina, I. García-Urrutia, J. Díez, J. Fornell, E. Pellicer, and J. Sort, "Codeposition of inorganic fullerene-like WS2 nanoparticles in an electrodeposited nickel matrix under the influence of ultrasonic agitation," *Electrochimica Acta,* vol. 114, pp. 859-867, 2013.
[58] M. Redlich *et al.*, "Friction reduction and wear resistance of electro-co-deposited inorganic fullerene-like WS 2 coating for improved stainless steel orthodontic wires," *Journal of Materials Research,* vol. 23, no. 11, pp. 2909-2915, 2008.
[59] M. F. Cardinal, P. Castro, J. Baxi, H. Liang, and F. J. Williams, "Characterization and frictional behavior of nanostructured Ni–W–MoS2 composite coatings," *Surface and Coatings Technology,* vol. 204, no. 1-2, pp. 85-90, 2009.
[60] S. J. Shourije and M. Bahrololoom, "Effect of current density, MoS2 content and bath agitation on tribological properties of electrodeposited nanostructured Ni-MoS2 composite coatings," *Tribology-Materials, Surfaces & Interfaces,* vol. 13, no. 2, pp. 76-87, 2019.
[61] A. Devaraju, "A critical review on different types of wear of materials," *Int. J. Mech. Eng. Technol,* vol. 6, no. 11, pp. 77-83, 2015.
[62] M. Thakare, J. Wharton, R. Wood, and C. Menger, "Effect of abrasive particle size and the influence of microstructure on the wear mechanisms in wear-resistant materials," *Wear,* vol. 276, pp. 16-28, 2012.
[63] T. Quinn, "Review of oxidational wear: Part I: The origins of oxidational wear," *Tribology International,* vol. 16, no. 5, pp. 257-271, 1983.
[64] Y. Wei, L. Hongtao, and Z. Wei, "Preparation of anti-corrosion superhydrophobic coatings by an Fe-based micro/nano composite electro-brush plating and blackening process," *RSC Advances,* vol. 5, no. 125, pp. 103000-103012, 2015.
[65] C.-H. Xue, X.-J. Guo, J.-Z. Ma, and S.-T. Jia, "Fabrication of robust and antifouling superhydrophobic surfaces via surface-initiated atom transfer radical polymerization," *ACS applied materials & interfaces,* vol. 7, no. 15, pp. 8251-8259, 2015.

[66] L. B. Boinovich and A. M. Emelyanenko, "Anti-icing potential of superhydrophobic coatings," *Mendeleev Communications,* vol. 1, no. 23, pp. 3-10, 2013.

[67] K. Kubiak, Z. Khatir, P. Jimack, and T. Mathia, "Energy efficiency optimization of superhydrophobic surfaces for enhanced condensation heat transfer," in *Poster Papers*, 2015: SusTem, pp. 518-522.

[68] E. Jiaqiang *et al.*, "Wetting models and working mechanisms of typical surfaces existing in nature and their application on superhydrophobic surfaces: a review," *Adv. Mater. Interfaces,* vol. 5, no. 1, pp. 1701052-1701091, 2018.

[69] F. Borgioli, E. Galvanetto, and T. Bacci, "Influence of surface morphology and roughness on water wetting properties of low temperature nitrided austenitic stainless steels," *Materials Characterization,* vol. 95, pp. 278-284, 2014.

[70] S. Shibuichi, T. Onda, N. Satoh, and K. Tsujii, "Super water-repellent surfaces resulting from fractal structure," *The Journal of Physical Chemistry,* vol. 100, no. 50, pp. 19512-19517, 1996.

[71] Y. Yuan and T. R. Lee, "Contact angle and wetting properties," in *Surface science techniques*: Springer, 2013, pp. 3-34.

[72] T. Young, "III. An essay on the cohesion of fluids," *Philosophical transactions of the royal society of London,* no. 95, pp. 65-87, 1805.

[73] R. N. Wenzel, "Resistance of solid surfaces to wetting by water," *Industrial & Engineering Chemistry,* vol. 28, no. 8, pp. 988-994, 1936.

[74] R. Blossey, "Self-cleaning surfaces—virtual realities," *Nature materials,* vol. 2, no. 5, p. 301, 2003.

[75] A. Cassie and S. Baxter, "Wettability of porous surfaces," *Transactions of the Faraday society,* vol. 40, pp. 546-551, 1944.

[76] W. Barthlott and C. Neinhuis, "Purity of the sacred lotus, or escape from contamination in biological surfaces," *Planta,* vol. 202, no. 1, pp. 1-8, 1997.

[77] J. Jeevahan, M. Chandrasekaran, G. B. Joseph, R. Durairaj, and G. Mageshwaran, "Superhydrophobic surfaces: a review on fundamentals, applications, and challenges," *Journal of Coatings Technology and Research,* vol. 15, no. 2, pp. 231-250, 2018.

[78] L. Feng *et al.*, "Petal effect: a superhydrophobic state with high adhesive force," *Langmuir,* vol. 24, no. 8, pp. 4114-4119, 2008.

[79] M. Dickinson, "How to walk on water," *Nature,* vol. 424, no. 6949, pp. 621-622, 2003.

[80] M. Holdgate, "The wetting of insect cuticles by water," *Journal of Experimental Biology,* vol. 32, no. 3, pp. 591-617, 1955.

[81] X. Gao and L. Jiang, "Water-repellent legs of water striders," *Nature,* vol. 432, no. 7013, pp. 36-36, 2004.

[82] X.-Q. Feng, X. Gao, Z. Wu, L. Jiang, and Q.-S. Zheng, "Superior water repellency of water strider legs with hierarchical structures: experiments and analysis," *Langmuir,* vol. 23, no. 9, pp. 4892-4896, 2007.

[83] M. F. L. Shen, M. Qiu, W. Jiang and Z. Wang, "Superhydrophobic nickel coating fabricated by scanning electrodeposition," vol. 483, pp. 706-712, 2019.

[84] B. Han, Y. Yang, L. Fang, G. Peng, and C. Yang, "Electrodeposition of Super-Hydrophobic Nickel Film on Magnesium Alloy AZ31 and Its Corrosion Resistance," *Int J Electrochem Sci,* vol. 111123, pp. 9206-9215, 2016.

[85] R. Jain and R. Pitchumani, "Facile fabrication of durable copper-based superhydrophobic surfaces via electrodeposition," *Langmuir,* vol. 34, no. 10, pp. 3159-3169, 2017.

[86] H. Xiao, A. Hu, T. Hang, and M. Li, "Electrodeposited nanostructured cobalt film and its dual modulation of both superhydrophobic property and adhesiveness," *Applied Surface Science,* vol. 324, pp. 319-323, 2015.

[87] F. C. Walsh, S. Wang, and N. Zhou, "The electrodeposition of composite coatings: Diversity, applications and challenges," *Current Opinion in Electrochemistry,* vol. 20, pp. 8-19, 2020.

[88] M. Hashemzadeh, K. Raeissi, F. Ashrafizadeh, and S. Khorsand, "Effect of ammonium chloride on microstructure, super-hydrophobicity and corrosion resistance of nickel coatings," *Surface and Coatings Technology,* vol. 283, pp. 318-328, 2015.

[89] F. Soleimangoli, S. A. Hosseini, A. Davoodi, A. Mokhtari, and M. Alishahi, "Effect of NH4Cl on the microstructure, wettability and corrosion behavior of electrodeposited Ni–Zn coatings with hierarchical nano/microstructure," *Surface and Coatings Technology,* vol. 394, p. 125825, 2020.

[90] S. Khorsand, K. Raeissi, F. Ashrafizadeh, and M. Arenas, "Relationship between the structure and water repellency of nickel–cobalt alloy coatings prepared by electrodeposition process," *Surface and Coatings Technology,* vol. 276, pp. 296-304, 2015.

[91] T. Xiang *et al.*, "Effect of current density on wettability and corrosion resistance of superhydrophobic nickel coating deposited on low carbon steel," *Materials & Design,* vol. 114, pp. 65-72, 2017.

[92] Z. Chen, F. Tian, A. Hu, and M. Li, "A facile process for preparing superhydrophobic nickel films with stearic acid," *Surface and Coatings Technology,* vol. 231, pp. 88-92, 2013.

[93] S. Khorsand, K. Raeissi, F. Ashrafizadeh, and M. Arenas, "Super-hydrophobic nickel–cobalt alloy coating with micro-nano flower-like structure," *Chemical Engineering Journal,* vol. 273, pp. 638-646, 2015.

[94] Z. Yang, X. Liu, and Y. Tian, "Fabrication of super-hydrophobic nickel film on copper substrate with improved corrosion inhibition by electrodeposition process," *Colloids and Surfaces A: Physicochemical and Engineering Aspects,* vol. 560, pp. 205-212, 2019.

[95] A. Haghdoost and R. Pitchumani, "Fabricating superhydrophobic surfaces via a two-step electrodeposition technique," *Langmuir,* vol. 30, no. 14, pp. 4183-4191, 2014.

[96] Y. Fan, Y. He, P. Luo, X. Chen, and B. Liu, "A facile electrodeposition process to fabricate corrosion-resistant superhydrophobic surface on carbon steel," *Applied Surface Science,* vol. 368, pp. 435-442, 2016.

[97] Y. Xue, S. Wang, G. Zhao, A. Taleb, and Y. Jin, "Fabrication of NiCo coating by electrochemical deposition with high super-hydrophobic properties for corrosion protection," *Surface and Coatings Technology,* vol. 363, pp. 352-361, 2019.

[98] D. Zhang, L. Li, Y. Wu, B. Zhu, and H. Song, "One-step method for fabrication of bioinspired hierarchical superhydrophobic surface with robust stability," *Applied Surface Science,* vol. 473, pp. 493-499, 2019.

[99] R. Akbari, G. Godeau, M. Mohammadizadeh, F. Guittard, and T. Darmanin, "The influence of bath temperature on the one-step electrodeposition of non-wetting copper oxide coatings," *Applied Surface Science,* vol. 503, p. 144094, 2020.

[100] P. Liu, L. Cao, W. Zhao, Y. Xia, W. Huang, and Z. Li, "Insights into the superhydrophobicity of metallic surfaces prepared by electrodeposition involving spontaneous adsorption of airborne hydrocarbons," *Applied Surface Science,* vol. 324, pp. 576-583, 2015.

[101] S. Khorsand, K. Raeissi, and F. Ashrafizadeh, "Corrosion resistance and long-term durability of super-hydrophobic nickel film prepared by electrodeposition process," *Applied Surface Science,* vol. 305, pp. 498-505, 2014.

[102] L. Shen *et al.*, "A novel superhydrophobic Ni/Nip coating fabricated by magnetic field induced selective scanning electrodeposition," *Applied Surface Science,* vol. 489, pp. 25-33, 2019.

[103] W. Geng, A. Hu, and M. Li, "Super-hydrophilicity to super-hydrophobicity transition of a surface with Ni micro–nano cones array," *Applied Surface Science,* vol. 263, pp. 821-824, 2012.

[104] L. Richter, A. Cordner, and P. Brown, "Non-stick science: Sixty years of research and (in)action on fluorinated compounds," *Social Studies of Science,* vol. 48, no. 5, pp. 691-714, 2018.

[105] Z. Wang, I. T. Cousins, M. Scheringer, and K. Hungerbuehler, "Hazard assessment of fluorinated alternatives to long-chain perfluoroalkyl acids (PFAAs) and their precursors: status quo, ongoing challenges and possible solutions," *Environment international,* vol. 75, pp. 172-179, 2015.

[106] S. Choudhury, A. Kumar, and N. Kumar, "Silane: Risk assessment, environmental, and health hazard," in *Hazardous Gases*: Elsevier, 2021, pp. 353-362.

[107] A. P. Gaur, S. Sahoo, M. Ahmadi, S. P. Dash, M. J.-F. Guinel, and R. S. Katiyar, "Surface energy engineering for tunable wettability through controlled synthesis of MoS2," *Nano letters,* vol. 14, no. 8, pp. 4314-4321, 2014.

[108] M. Annamalai *et al.*, "Surface energy and wettability of van der Waals structures," *Nanoscale,* vol. 8, no. 10, pp. 5764-5770, 2016.

[109] J. G. Kim, W. S. Yoo, J. Y. Park, and W. J. Lee, "Quantitative analysis of contact angle of water on SiC: polytype and polarity dependence," *ECS Journal of Solid State Science and Technology,* vol. 9, no. 12, p. 123006, 2020.

[110] B. Bharti, S. Kumar, and R. Kumar, "Superhydrophilic TiO2 thin film by nanometer scale surface roughness and dangling bonds," *Applied Surface Science,* vol. 364, pp. 51-60, 2016.

[111] M. N. Abd Rahman, M. F. Dimin, M. Izani, and M. Mazliah, "Influence of Surface Treatment on the Surface Energy of Tungsten Carbide Inserts," *Applied Mechanics and Materials,* vol. 699, pp. 38-43, 2015.

[112] P. Maiya and J. Blakely, "Surface self-diffusion and surface energy of nickel," *Journal of Applied Physics,* vol. 38, no. 2, pp. 698-704, 1967.

[113] J. Zhou *et al.*, "Electroplating of non-fluorinated superhydrophobic Ni/WC/WS2 composite coatings with high abrasive resistance," *Applied Surface Science,* vol. 487, pp. 1329-1340, 2019.

[114] C. Kerr, D. Barker, F. Walsh, and J. Archer, "The electrodeposition of composite coatings based on metal matrix-included particle deposits," *Transactions of the IMF,* vol. 78, no. 5, pp. 171-178, 2000.

[115] F. Walsh and C. Ponce de Leon, "A review of the electrodeposition of metal matrix composite coatings by inclusion of particles in a metal layer: an established and diversifying technology," *Transactions of the IMF,* vol. 92, no. 2, pp. 83-98, 2014.

[116] M. Monev, L. Mirkova, I. Krastev, H. Tsvetkova, and W. Richtering, "Effect of brighteners on hydrogen evolution during zinc electroplating from zincate electrolytes," *Journal of applied electrochemistry,* vol. 28, no. 10, pp. 1107-1112, 1998.

[117] C. Liu, D. Wei, R. Xu, Y. Mai, L. Zhang, and X. Jie, "Electroplated Co-Ni/WS2 Composite Coating with Excellent Tribological and Anticorrosion Performance," *Tribology Transactions,* no. just-accepted, pp. 1-12, 2020.

[118] Y. Jeon, J. Byun, and T. Oh, "Electrodeposition and mechanical properties of Ni–carbon nanotube nanocomposite coatings," *Journal of Physics and Chemistry of Solids,* vol. 69, no. 5-6, pp. 1391-1394, 2008.

[119] M. Chandrasekar and M. Pushpavanam, "Pulse and pulse reverse plating—Conceptual, advantages and applications," *Electrochimica Acta,* vol. 53, no. 8, pp. 3313-3322, 2008.

[120] P. I. Nemes, M. Lekka, L. Fedrizzi, and L. M. Muresan, "Influence of the electrodeposition current regime on the corrosion resistance of Zn–CeO2 nanocomposite coatings," *Surface and Coatings Technology,* vol. 252, pp. 102-107, 2014.

[121] F. Mangolini, L. Magagnin, and P. Cavallotti, "Pulse plating of Mn–Cu alloys on steel," *Journal of the Electrochemical Society,* vol. 153, no. 9, p. C623, 2006.

[122] B. Tury, M. Lakatos-Varsányi, and S. Roy, "Effect of pulse parameters on the passive layer formation on pulse plated Ni–Co alloys," *Applied surface science,* vol. 253, no. 6, pp. 3103-3108, 2007.

[123] M. Stroumbouli, P. Gyftou, E. Pavlatou, and N. Spyrellis, "Codeposition of ultrafine WC particles in Ni matrix composite electrocoatings," *Surface and Coatings Technology,* vol. 195, no. 2-3, pp. 325-332, 2005.

[124] P. Leisner, G. Bech-Nielsen, and P. Møller, "Current efficiency and crystallization mechanism in pulse plating of hard chromium," *Journal of applied electrochemistry,* vol. 23, no. 12, pp. 1232-1236, 1993.

[125] L. Shao, L. Du, C. Liu, and L. Wang, "Microstructure and mechanical properties of nanocrystalline nickel prepared by pulse reverse microelectroforming," *Journal of Experimental Nanoscience,* vol. 9, no. 3, pp. 299-309, 2014.

[126] D. Weston *et al.*, "Co-electrodeposition of inorganic fullerene (IF-WS2) nano-particles with cobalt from a gluconate bath with anionic and cationic surfactants," *Electrochimica acta,* vol. 56, no. 19, pp. 6837-6846, 2011.

[127] T. Hielscher, "Ultrasonic production of nano-size dispersions and emulsions," *arXiv preprint arXiv:0708.1831,* 2007.

[128] R. E. Apfel, "7. Acoustic cavitation," in *Methods in experimental physics*, vol. 19: Elsevier, 1981, pp. 355-411.

[129] K. S. Suslick, *Ultrasound: its chemical, physical, and biological effects*. VCH Publishers, 1988.

[130] J. González-García, V. Sáez, I. Tudela, M. I. Díez-Garcia, M. Deseada Esclapez, and O. Louisnard, "Sonochemical treatment of water polluted by chlorinated organocompounds. A review," *Water,* vol. 2, no. 1, pp. 28-74, 2010.

[131] C. Walker and R. Walker, "Effect of ultrasonic agitation on some properties of electrodeposits," *Electrodeposition and Surface treatment,* vol. 1, no. 6, pp. 457-469, 1973.

[132] E. García-Lecina, I. García-Urrutia, J. Díez, J. Morgiel, and P. Indyka, "A comparative study of the effect of mechanical and ultrasound agitation on the properties of electrodeposited Ni/Al2O3 nanocomposite coatings," *Surface and Coatings Technology,* vol. 206, no. 11-12, pp. 2998-3005, 2012.

[133] C. Barnes and J. Ward, "The Use of Ultrasonic Agitation in Gold Plating for Electronic Applications," *Transactions of the IMF,* vol. 55, no. 1, pp. 101-103, 1977.

[134] P. Kristof and M. Pritzker, "Improved copper plating through the use of current pulsing & ultrasonic agitation," *Plat Surf Finish,* vol. 85, no. 11, pp. 237-240, 1998.

[135] Y. Choi, Y. Hahn, B. Seong, and M. Kim, "Study of the effect of ultrasonic agitation on the defects size in electro-deposited chromium layer by small-angle neutron scattering," *Physica B: Condensed Matter,* vol. 385, pp. 911-913, 2006.

[136] P. Prasad, R. Vasudevan, S. Seshadri, and S. Ahila, "The effect of ultrasonic vibration on nickel electrodeposition," *Materials letters,* vol. 17, no. 6, pp. 357-359, 1993.

[137] I. Tudela, Y. Zhang, M. Pal, I. Kerr, and A. J. Cobley, "Ultrasound-assisted electrodeposition of composite coatings with particles," *Surface and Coatings Technology,* vol. 259, pp. 363-373, 2014.

[138] N. Hari Babu, S. Tzamtzis, N. Barekar, J. Patel, and Z. Fan, "Fabrication of metal matrix composites under intensive shearing," in *Solid state phenomena*, 2008, vol. 141: Trans Tech Publ, pp. 373-378.

[139] J. Hashim, L. Looney, and M. Hashmi, "Particle distribution in cast metal matrix composites—part II," *Journal of Materials Processing Technology,* vol. 123, no. 2, pp. 258-263, 2002.

[140] N. Barekar, S. Tzamtzis, N. H. Babu, Z. Fan, and B. Dhindaw, "Processing of ultrafine-size particulate metal matrix composites by advanced shear technology," *Metallurgical and Materials Transactions A,* vol. 40, no. 3, p. 691, 2009.

[141] E. Pullicino, W. Zou, M. Gresil, and C. Soutis, "The effect of shear mixing speed and time on the mechanical properties of GNP/epoxy composites," *Applied Composite Materials,* vol. 24, no. 2, pp. 301-311, 2017.

[142] S. Bagherifard *et al.*, "Effects of nanofeatures induced by severe shot peening (SSP) on mechanical, corrosion and cytocompatibility properties of magnesium alloy AZ31," *Acta biomaterialia,* vol. 66, pp. 93-108, 2018.

[143] H.-W. Chang, P. Kelly, Y.-N. Shi, and M.-X. Zhang, "Thermal stability of nanocrystallized surface produced by surface mechanical attrition treatment in aluminum alloys," *Surface and Coatings Technology,* vol. 206, no. 19-20, pp. 3970-3980, 2012.

[144] Q. Yao, J. Sun, G. Zhang, W. Tong, and H. Zhang, "Enhanced toughness of nitrided layers formed on Ti-6Al-4V alloy via surface mechanical attrition pre-treatment," *Vacuum,* vol. 142, pp. 45-51, 2017.

[145] S. Eisner, "An Ultra High Speed Plating Process Utilizing Small Hard Particles," *Transactions of the IMF,* vol. 51, no. 1, pp. 13-16, 1973.

[146] Z. Ning, Y. He, and W. Gao, "Mechanical attrition enhanced Ni electroplating," *Surface and Coatings Technology,* vol. 202, no. 10, pp. 2139-2146, 2008.

[147] C.-l. BAN, S. Xin, M. Jie, and C. Hui, "Effect of mechanical attrition on microstructure and property of electroplated Ni coating," *Transactions of Nonferrous Metals Society of China,* vol. 22, no. 8, pp. 1989-1994, 2012.

[148] Z.-H. Ning and Y.-D. He, "Rapid electroplating of Cu coatings by mechanical attrition method," *Transactions of Nonferrous Metals Society of China,* vol. 18, no. 5, pp. 1100-1106, 2008.

[149] Z. Zhu, S. Wang, N. Qu, and D. Zhu, "Electrodeposition, assisted by abrasive polishing, of crack-free hard chromium with compressive stress," *Philosophical Magazine Letters,* vol. 96, no. 6, pp. 205-211, 2016.

[150] Y. He, H. Fu, X. Li, and W. Gao, "Microstructure and properties of mechanical attrition enhanced electroless Ni–P plating on magnesium alloy," *Scripta Materialia,* vol. 58, no. 6, pp. 504-507, 2008.

[151] Z. Ping, Y. He, C. Gu, and T.-Y. Zhang, "Mechanically assisted electroplating of Ni–P coatings on carbon steel," *Surface and Coatings Technology,* vol. 202, no. 24, pp. 6023-6028, 2008.

[152] P. Zhaoxia, Y. Juntao, H. Yedong, and L. Xiaogang, "Mechanical assisted electroless barrel-plating Ni-P coatings on magnesium alloy," *Acta Metallurgica Sinica (English Letters),* vol. 22, no. 3, pp. 225-232, 2009.

[153] C. Ban, F. Wang, J. Chen, and S. Zhu, "Effect of mechanical attrition on structure and property of electroplated Ni-P coating on magnesium alloy," *Electrochemistry,* vol. 87, no. 1, pp. 89-93, 2019.

[154] P. Zhaoxia, G. Cheng, and H. Yedong, "Ni-P-SiC composite coatings electroplated on carbon steel assisted by mechanical attrition," *Acta Metallurgica Sinica (English letters),* vol. 23, no. 2, pp. 137-146, 2010.

[155] G. Zhao, C. Ren, and Y. He, "Ni–P-multiwalled carbon nanotubes composite coatings prepared by mechanical attrition (MA)-assisted electroless plating," *Surface and Coatings Technology,* vol. 206, no. 11-12, pp. 2774-2779, 2012.

[156] T. Watanabe, *Nano-plating: microstructure control theory of plated film and data base of plated film microstructure*. Elsevier, 2004.

[157] D. Gabe, "The role of hydrogen in metal electrodeposition processes," *Journal of applied electrochemistry,* vol. 27, no. 8, pp. 908-915, 1997.

[158] J. Popić and D. Dražić, "Electrochemistry of active chromium: Part II. Three hydrogen evolution reactions on chromium in sulfuric acid," *Electrochimica acta,* vol. 49, no. 27, pp. 4877-4891, 2004.

[159] N. Imaz, M. Ostra, M. Vidal, J. Díez, M. Sarret, and E. García-Lecina, "Corrosion behaviour of chromium coatings obtained by direct and reverse pulse plating electrodeposition in NaCl aqueous solution," *Corrosion Science,* vol. 78, pp. 251-259, 2014.

[160] H. Khani and J. F. Brennecke, "Hard chromium composite electroplating on high-strength stainless steel from a Cr (III)-ionic liquid solution," *Electrochemistry Communications,* vol. 107, p. 106537, 2019.

[161] P. S. Kumar and P. K. Nair, "Studies on crystallization of electroless Ni□ P deposits," *Journal of Materials Processing Technology,* vol. 56, no. 1-4, pp. 511-520, 1996.

[162] K.-H. Hou, M.-C. Jeng, and M.-D. Ger, "The heat treatment effects on the structure and wear behavior of pulse electroforming Ni–P alloy coatings," *Journal of alloys and compounds,* vol. 437, no. 1-2, pp. 289-297, 2007.

[163] H.-C. Huang, S.-T. Chung, S.-J. Pan, W.-T. Tsai, and C.-S. Lin, "Microstructure evolution and hardening mechanisms of Ni–P electrodeposits," *Surface and coatings technology,* vol. 205, no. 7, pp. 2097-2103, 2010.

[164] X. Ji, S. Yang, J. Zhao, C. Yan, and L. Jiang, "Effect of heat treatment on slurry erosion wear resistance of amorphous Ni-P electrodeposits," *Tribology transactions,* vol. 55, no. 1, pp. 86-90, 2012.

[165] M.-D. Ger, "Electrochemical deposition of nickel/SiC composites in the presence of surfactants," *Materials Chemistry and Physics,* vol. 87, no. 1, pp. 67-74, 2004.

[166] K. Hou, M. Ger, L. Wang, and S. Ke, "The wear behaviour of electro-codeposited Ni–SiC composites," *Wear,* vol. 253, no. 9-10, pp. 994-1003, 2002.

[167] F. Kılıc, H. Gül, S. Aslan, A. Alp, and H. Akbulut, "Effect of CTAB concentration in the electrolyte on the tribological properties of nanoparticle SiC reinforced Ni metal matrix

composite (MMC) coatings produced by electrodeposition," *Colloids and Surfaces A: Physicochemical and Engineering Aspects,* vol. 419, pp. 53-60, 2013.

[168] C. Guo, Y. Zuo, X. Zhao, J. Zhao, and J. Xiong, "Effects of surfactants on electrodeposition of nickel-carbon nanotubes composite coatings," *Surface and Coatings Technology,* vol. 202, no. 14, pp. 3385-3390, 2008.

[169] S. Mohajeri, A. Dolati, and S. Rezagholibeiki, "Electrodeposition of Ni/WC nano composite in sulfate solution," *Materials Chemistry and Physics,* vol. 129, no. 3, pp. 746-750, 2011.

[170] A. Zarebidaki and S.-R. Allahkaram, "Effect of surfactant on the fabrication and characterization of Ni-P-CNT composite coatings," *Journal of Alloys and Compounds,* vol. 509, no. 5, pp. 1836-1840, 2011.

[171] M. Abdoli and A. S. Rouhaghdam, "Preparation and characterization of Ni–P/nanodiamond coatings: Effects of surfactants," *Diamond and related materials,* vol. 31, pp. 30-37, 2013.

[172] D. Ning, A. Zhang, M. Murtaza, and H. Wu, "Effect of surfactants on the electrodeposition of Cu-TiO2 composite coatings prepared by jet electrodeposition," *Journal of Alloys and Compounds,* vol. 777, pp. 1245-1250, 2019.

[173] L. Wang, "Effect of surfactant BAS on MoS 2 codeposition behaviour," *Journal of Applied Electrochemistry,* vol. 38, no. 2, pp. 245-249, 2008.

[174] L. Chen, L. Wang, Z. Zeng, and J. Zhang, "Effect of surfactant on the electrodeposition and wear resistance of Ni–Al2O3 composite coatings," *Materials Science and Engineering: A,* vol. 434, no. 1-2, pp. 319-325, 2006.

[175] G. Parida, D. Chaira, M. Chopkar, and A. Basu, "Synthesis and characterization of Ni-TiO2 composite coatings by electro-co-deposition," *Surface and Coatings Technology,* vol. 205, no. 21-22, pp. 4871-4879, 2011.

[176] R. J. Hunter, *Zeta potential in colloid science: principles and applications*. Academic press, 2013.

[177] M. Instruments, "Zeta potential: An Introduction in 30 minutes," *Zetasizer Nano Serles Tech. Note. MRK654,* vol. 1, no. 2, pp. 1-6, 2011.

[178] Y. He, S. Wang, F. Walsh, W. Li, L. He, and P. Reed, "The monitoring of coating health by in situ luminescent layers," *RSC Advances,* vol. 5, no. 53, pp. 42965-42970, 2015.

[179] T. F. Tadros, *Applied surfactants: principles and applications*. John Wiley & Sons, 2006.

[180] N. M. van Os, J. R. Haak, and L. A. M. Rupert, *Physico-chemical properties of selected anionic, cationic and nonionic surfactants*. Elsevier, 2012.

[181] G. Yasin *et al.*, "Effect of surfactant concentration in electrolyte on the fabrication and properties of nickel-graphene nanocomposite coating synthesized by electrochemical co-deposition," *RSC advances,* vol. 8, no. 36, pp. 20039-20047, 2018.

[182] M. Kartal, M. Uysal, H. Gul, A. Alp, and H. Akbulut, "Effect of surfactant concentration in the electrolyte on the tribological properties of nickel-tungsten carbide composite coatings produced by pulse electro co-deposition," *Applied Surface Science,* vol. 354, pp. 328-336, 2015.

[183] M. Rezaei-Sameti, S. Nadali, A. Falahatpisheh, and M. Rakhshi, "The effects of sodium dodecyl sulfate and sodium saccharin on morphology, hardness and wear behavior of Cr–WC nano composite coatings," *Solid state communications,* vol. 159, pp. 18-21, 2013.

[184] M. Sabri, A. A. Sarabi, and S. M. N. Kondelo, "The effect of sodium dodecyl sulfate surfactant on the electrodeposition of Ni-alumina composite coatings," *Materials Chemistry and Physics,* vol. 136, no. 2-3, pp. 566-569, 2012.

[185] S. Jiang, L. Yang, J. Pang, H. Lin, and Z. Wang, "Electrodeposition of Ni-Al2O3 composite coatings with combined addition of SDS and HPB surfactants," *Surface and Coatings Technology,* vol. 286, pp. 197-205, 2016.

[186] S. Aruna, P. Lashmi, and H. Seema, "The effect of additives on the properties of electrodeposited Ni–zircon composite coatings," *RSC advances,* vol. 6, no. 14, pp. 11185-11192, 2016.

[187] S. Hassani, K. Raeissi, and M. Golozar, "Effects of saccharin on the electrodeposition of Ni–Co nanocrystalline coatings," *Journal of Applied Electrochemistry,* vol. 38, no. 5, pp. 689-694, 2008.

[188] C. Ma, S. Wang, C. Low, L. Wang, and F. Walsh, "Effects of additives on microstructure and properties of electrodeposited nanocrystalline Ni–Co alloy coatings of high cobalt content," *Transactions of the IMF,* vol. 92, no. 4, pp. 189-195, 2014.

[189] A. Rashidi and A. Amadeh, "The effect of saccharin addition and bath temperature on the grain size of nanocrystalline nickel coatings," *Surface and Coatings Technology,* vol. 204, no. 3, pp. 353-358, 2009.

[190] T. Franklin, "Some mechanisms of action of additives in electrodeposition processes," *Surface and Coatings Technology,* vol. 30, no. 4, pp. 415-428, 1987.

[191] D. Mockute and G. Bernotiene, "The interaction of additives with the cathode in a mixture of saccharin, 2-butyne-1, 4-diol and phthalimide during nickel electrodeposition in a Watts-type electrolyte," *Surface and coatings technology,* vol. 135, no. 1, pp. 42-47, 2000.

[192] A. Ciszewski, S. Posluszny, G. Milczarek, and M. Baraniak, "Effects of saccharin and quaternary ammonium chlorides on the electrodeposition of nickel from a Watts-type electrolyte," *Surface and Coatings Technology,* vol. 183, no. 2-3, pp. 127-133, 2004.

[193] B. Szeptycka, "Effects of organic compounds on the electrocrystallization of nickel," *Russian journal of electrochemistry,* vol. 37, no. 7, pp. 684-689, 2001.

[194] V. Stankovic and M. Gojo, "Electrodeposited composite coatings of copper with inert, semiconductive and conductive particles," *Surface and Coatings Technology,* vol. 81, no. 2-3, pp. 225-232, 1996.

[195] C. Carpenter, P. Shipway, Y. Zhu, and D. Weston, "Effective dispersal of CNTs in the fabrication of electrodeposited nanocomposites," *Surface and Coatings Technology,* vol. 205, no. 20, pp. 4832-4837, 2011.

[196] T. He, Y. He, H. Li, Y. Fan, Q. Yang, and Z. He, "A comparative study of effect of mechanical and ultrasound agitation on the properties of pulse electrodeposited Ni-W/MWCNTs composite coatings," *Journal of Alloys and Compounds,* vol. 743, pp. 63-72, 2018.

[197] N. Elkhoshkhany, A. Hafnway, and A. Khaled, "Electrodeposition and corrosion behavior of nano-structured Ni-WC and Ni-Co-WC composite coating," *Journal of Alloys and Compounds,* vol. 695, pp. 1505-1514, 2017.

[198] G. Zhao *et al.*, "Robust Ni/WC superhydrophobic surfaces by electrodeposition," *RSC Advances,* vol. 7, no. 71, pp. 44896-44903, 2017.

[199] Z. Huang and D. Xiong, "MoS 2 PARTICLES MODIFIED WITH POLYSTYRENE FOR PRODUCING Ni–PS/MoS 2 COATINGS," *Surface Review and Letters,* vol. 15, no. 06, pp. 793-797, 2008.

[200] Z.-j. Huang and D.-s. Xiong, "MoS2 coated with Al2O3 for Ni–MoS2/Al2O3 composite coatings by pulse electrodeposition," *Surface and Coatings Technology,* vol. 202, no. 14, pp. 3208-3214, 2008.

[201] Z. J. Huang, D. S. Xiong, J. L. Li, and M. L. Liu, "Friction and wear characteristics of electrodeposited Ni-MoS2/Al2O3 composite coating," in *Advanced Materials Research*, 2011, vol. 189: Trans Tech Publ, pp. 173-176.

[202] J. Archard, "Contact and rubbing of flat surfaces," *Journal of applied physics,* vol. 24, no. 8, pp. 981-988, 1953.

[203] J. Archard, "Friction between metal surfaces," *Wear,* vol. 113, no. 1, pp. 3-16, 1986.

[204] Y. Wang, W. C. Sun, C. A. Wang, Y. Huang, and J. M. Xu, "Microstructure, friction, and wear properties of Ni-Al2O3-MoS2 composite coatings," *International Journal of Applied Ceramic Technology,* vol. 14, no. 5, pp. 889-898, 2017.

[205] M. Fazel, M. G. Jazi, S. Bahramzadeh, S. Bakhshi, and M. Ramazani, "Effect of solid lubricant particles on room and elevated temperature tribological properties of Ni–SiC composite coating," *Surface and Coatings Technology,* vol. 254, pp. 252-259, 2014.

[206] C. Suiyuan, S. Ying, F. Hong, L. Jing, L. Changsheng, and S. Kai, "Synthesis of Ni-P-PTFE-nano-Al2O3 composite plating coating on 45 steel by electroless plating," *Journal of composite materials,* vol. 46, no. 12, pp. 1405-1416, 2012.

[207] A. Tang, M. Wang, W. Huang, and X. Wang, "Composition design of Ni–nano-Al2O3–PTFE coatings and their tribological characteristics," *Surface and Coatings Technology,* vol. 282, pp. 121-128, 2015.

[208] Y. Huang, X. Zeng, I. Annergren, and F. Liu, "Development of electroless NiP–PTFE–SiC composite coating," *Surface and Coatings Technology,* vol. 167, no. 2-3, pp. 207-211, 2003.
[209] V. M. Pratiwi, "STUDY OF AISI 1020 STEEL CHARACTERIZATION BY ZINC-ELECTROPLATING TREATMENT," *MATERIALS RESEARCH COMMUNICATIONS,* vol. 1, no. 1, pp. 34-41, 2020.
[210] M. Schlesinger and M. Paunovic, *Modern electroplating*. John Wiley & Sons, 2011.
[211] X. Jia, "Robust superhydrophobic metal/ceramic coatings for antifouling," University of Southampton, 2018.
[212] B. Bakhit and A. Akbari, "Effect of particle size and co-deposition technique on hardness and corrosion properties of Ni–Co/SiC composite coatings," *Surface and Coatings Technology,* vol. 206, no. 23, pp. 4964-4975, 2012.
[213] P. Jin, C. Sun, C. Zhou, L. Shi, and C. Liu, "Effect of SiC particle size on structures and properties of Ni–SiC nanocomposites deposited by magnetic pulse electrodeposition technology," *Ceramics International,* vol. 45, no. 16, pp. 20155-20164, 2019.
[214] J. Long, A. Borissova, A. D. Wilson, and J. C. A.-B. Wilson, "Sample preparation of anodised aluminium oxide coatings for scanning electron microscopy," *Micron,* vol. 101, pp. 87-94, 2017.
[215] D. Murakami, H. Jinnai, and A. Takahara, "Wetting transition from the Cassie–Baxter state to the Wenzel state on textured polymer surfaces," *Langmuir,* vol. 30, no. 8, pp. 2061-2067, 2014.
[216] A. Milionis, E. Loth, and I. S. Bayer, "Recent advances in the mechanical durability of superhydrophobic materials," *Advances in colloid and interface science,* vol. 229, pp. 57-79, 2016.
[217] Z. Bai and B. Zhang, "Fabrication of superhydrophobic reduced-graphene oxide/nickel coating with mechanical durability, self-cleaning and anticorrosion performance," *Nano Materials Science,* vol. 2, no. 2, pp. 151-158, 2020.
[218] S. Ding *et al.*, "Fabrication of self-cleaning super-hydrophobic nickel/graphene hybrid film with improved corrosion resistance on mild steel," *Materials & Design,* vol. 117, pp. 280-288, 2017.
[219] X. Liu, T. C. Zhang, H. He, L. Ouyang, and S. Yuan, "A stearic Acid/CeO2 bilayer coating on AZ31B magnesium alloy with superhydrophobic and self-cleaning properties for corrosion inhibition," *Journal of Alloys and Compounds,* vol. 834, p. 155210, 2020.
[220] T. Xiang, D. Chen, Z. Lv, Z. Yang, L. Yang, and C. Li, "Robust superhydrophobic coating with superior corrosion resistance," *Journal of Alloys and Compounds,* vol. 798, pp. 320-325, 2019.
[221] Z. Lu and H. Owens, "A method to improve the quality of silica nanoparticles (SNPs) over increasing storage durations," *Journal of Nanoparticle Research,* vol. 20, no. 8, p. 213, 2018.
[222] I. Garcia, J. Fransaer, and J.-P. Celis, "Electrodeposition and sliding wear resistance of nickel composite coatings containing micron and submicron SiC particles," *Surface and Coatings Technology,* vol. 148, no. 2-3, pp. 171-178, 2001.
[223] M. Stern and A. L. Geary, "Electrochemical polarization: I. A theoretical analysis of the shape of polarization curves," *Journal of the electrochemical society,* vol. 104, no. 1, p. 56, 1957.
[224] S. M. Emarati and M. Mozammel, "Efficient one-step fabrication of superhydrophobic nano-TiO2/TMPSi ceramic composite coating with enhanced corrosion resistance on 316L," *Ceramics International,* vol. 46, no. 2, pp. 1652-1661, 2020.
[225] B. P. Singh, S. Nayak, K. K. Nanda, B. K. Jena, S. Bhattacharjee, and L. Besra, "The production of a corrosion resistant graphene reinforced composite coating on copper by electrophoretic deposition," *Carbon,* vol. 61, pp. 47-56, 2013.
[226] H.-K. Lee, H.-Y. Lee, and J.-M. Jeon, "Codeposition of micro-and nano-sized SiC particles in the nickel matrix composite coatings obtained by electroplating," *Surface and Coatings Technology,* vol. 201, no. 8, pp. 4711-4717, 2007.
[227] S. K. Kim and H. J. Yoo, "Formation of bilayer Ni–SiC composite coatings by electrodeposition," *Surface and coatings Technology,* vol. 108, pp. 564-569, 1998.

[228] T. J. Tuaweri and G. Wilcox, "Behaviour of Zn-SiO2 electrodeposition in the presence of N, N-dimethyldodecylamine," *Surface and Coatings Technology,* vol. 200, no. 20-21, pp. 5921-5930, 2006.

[229] R. Souto, L. Fernández-Mérida, S. González, and D. Scantlebury, "Comparative EIS study of different Zn-based intermediate metallic layers in coil-coated steels," *Corrosion Science,* vol. 48, no. 5, pp. 1182-1192, 2006.

[230] D. Mondal, S. Das, and N. Jha, "Dry sliding wear behaviour of aluminum syntactic foam," *Materials & Design,* vol. 30, no. 7, pp. 2563-2568, 2009.

[231] R. Elansezhian, B. Ramamoorthy, and P. K. Nair, "The influence of SDS and CTAB surfactants on the surface morphology and surface topography of electroless Ni–P deposits," *Journal of materials processing technology,* vol. 209, no. 1, pp. 233-240, 2009.

[232] R. E. Smallman and R. J. Bishop, *Modern physical metallurgy and materials engineering*. Butterworth-Heinemann, 1999.

[233] S. Imanian Ghazanlou, A. H. S. Farhood, S. Hosouli, S. Ahmadiyeh, and A. Rasooli, "Pulse and direct electrodeposition of Ni–Co/micro and nanosized SiO2 particles," *Materials and Manufacturing Processes,* vol. 33, no. 10, pp. 1067-1079, 2018.

[234] C. Ma, S. Wang, R. J. Wood, J. Zekonyte, Q. Luo, and F. Walsh, "Hardness of porous nanocrystalline Co-Ni electrodeposits," *Metals and Materials International,* vol. 19, no. 6, pp. 1187-1192, 2013.

[235] H. J. Cho, D. Yan, J. Tam, and U. Erb, "Effects of diamond particle size on the formation of copper matrix and the thermal transport properties in electrodeposited copper-diamond composite materials," *Journal of Alloys and Compounds,* vol. 791, pp. 1128-1137, 2019.

[236] J. Luo, A. Flewitt, S. Spearing, N. Fleck, and W. Milne, "Young's modulus of electroplated Ni thin film for MEMS applications," *Materials Letters,* vol. 58, no. 17-18, pp. 2306-2309, 2004.

Appendix A

Calculation of contact pressure

The roller-on-the plate line contact model is schematically shown in **Figure A.1**. The coating is considered as an infinite half-space.

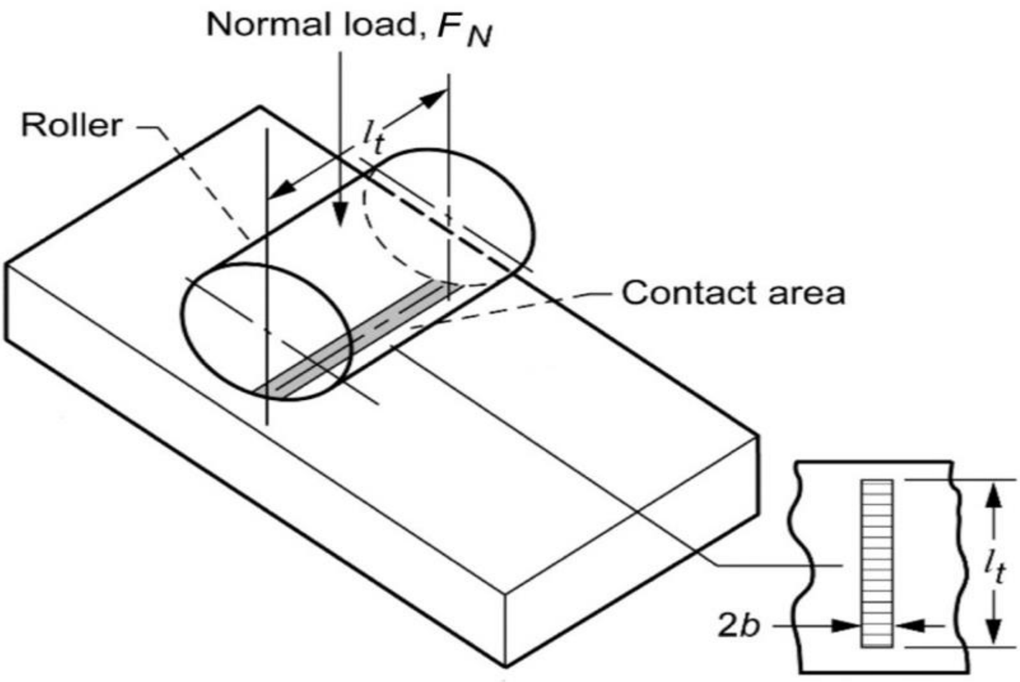

Figure A.1 A counterpart cylinder loaded on a flat plate. F_N is the normal load, l_t is the length of the cylinder, b is the half-width of the contact area.

According to Hertzian contact mechanics, the half-width of the contact area (b) and maximum contact pressure (P_{max}) can be calculated by the following equation [3].

$$b = \sqrt[3]{\frac{3F_N\left[\frac{1-v_1^2}{E_1}+\frac{1-v_2^2}{E_2}\right]}{4\left(\frac{1}{R_1}+\frac{1}{R_2}\right)}}$$

$$P_{max}=\frac{2F_N}{\pi b l_t}$$

Where F_N is the normal load applied on the counterpart cylinder, E_1 is Young's modulus of counterpart cylinder, V_1 is Poisson's ratio of counterpart cylinder, R1 is the radius of counterpart cylinder. E_2 is Young's modulus of coating, V_2 is Poisson's ratio of counterpart cylinder, R_2 is considered infinite for the coating surface. In this research, AISI-52100 stainless steel bearing cylinder roller was used as the counterpart, and parameters of pure nickel were used for the contact pressure calculation. Parameters of counterpart cylinder and coating are listed as below.

Table A.1 Parameters of pin and coating [236].

	AISI 52100 stainless steel cylinder	Pure Ni (coating)
Young's Modulus /GPa	207	205
Poisson's ratio	0.3	0.3
R / mm	3	∞

By substituting the parameters in **Table A.1** into the above equations, the maximum contact pressure was calculated to be 0.15 GPa.

Recommended Cut-off (ISO 4288-1996)

Periodic Profiles	Non-periodic profiles	Non-periodic profiles	Cut-off	Evaluation length
Spacing distance RSm (mm)	Rz (µm)	Ra (µm)	λc (mm)	L (mm)
> 0.013 to 0.04	To 0.1	To 0.02	0.08	0.4
> 0.04 to 0.13	> 0.1 to 0.5	> 0.02 to 0.1	0.25	1.25
> 0.13 to 0.4	> 0.5 to 10	> 0.1 to 2	0.8	4
> 0.4 to 1.3	> 10 to 50	> 2 to 10	2.5	12.5
> 1.3 to 4.0	> 50	> 10	8	40